

**CONTROLLING DIMENSIONS AND SHAPE
OF SUPRAMOLECULAR FIBERS BASED ON
1,3,5-BENZENETRISAMIDES**

DISSERTATION

zur Erlangung des akademischen Grades
einer Doktorin der Naturwissenschaften (Dr. rer. nat.)
an der Bayreuther Graduiertenschule für Mathematik
und Naturwissenschaften (BayNAT) der Universität Bayreuth

vorgelegt von

Melina Weber

geboren in Neuss
Bayreuth, 2024

Der experimentelle Teil der vorliegenden Arbeit wurde in der Zeit von Mai 2021 bis März 2024 am Lehrstuhl Makromolekulare Chemie I der Universität Bayreuth unter der Betreuung von Herrn Prof. Dr. Hans-Werner Schmidt angefertigt.

Vollständiger Abdruck der von der Bayreuther Graduiertenschule für Mathematik und Naturwissenschaften (BayNAT) der Universität Bayreuth genehmigten Dissertation zur Erlangung des akademischen Grades einer Doktorin der Naturwissenschaften (Dr. rer. nat).

Form der Dissertation: Monographie

Dissertation eingereicht am: 06.11.2024

Zulassung durch das Leitungsgremium: 13.11.2024

Wissenschaftliches Kolloquium: 17.03.2025

Amtierender Direktor: Prof. Dr. Jürgen Köhler

Prüfungsausschuss:

Prof. Dr. Hans-Werner Schmidt (Gutachter)

Prof. Dr. Andreas Greiner (Gutachter)

Prof. Dr. Markus Retsch (Vorsitz)

Prof. Dr. Jürgen Senker

“Das haben wir noch nie probiert, also geht es sicher gut.”

- Astrid Lindgren, Pippi Langstrumpf

List of publications

Die vorliegende Arbeit ist als Monographie verfasst.

Teile der Arbeit sind bereits publiziert und in der vorliegenden Arbeit mit der Literaturstelle [136] zitiert:

Melina Weber, Felix Bretschneider, Klaus Kreger, Andreas Greiner and Hans-Werner Schmidt
Mimicking Cacti Spines via Hierarchical Self-Assembly for Water Collection and Unidirectional Transport,

Adv. Mater. Interfaces, **2024**, 2400101

Weitere Publikationen sind im Rahmen der Promotion entstanden:

N. Raßmann, M. Weber, R. E. J. Glaß, K. Kreger, N. Helfricht, H.-W. Schmidt, G. Papastavrou,
Electrogelation: Controlled Fast Formation of Micrometer-Thick Films from Low-Molecular Weight Hydrogelators,

Langmuir, **2023**, 39, 17190-17200

A. Frank, M. Weber, C. Hils, U. Mansfeld, K. Kreger, H. Schmalz, H.-W. Schmidt,
Functional Mesostructured Electrospun Polymer Nonwovens with Supramolecular Nanofibers,
Macromol. Rapid Commun., **2022**, 43, 2200052

A. Frank, C. Hils, M. Weber, K. Kreger, H. Schmalz, H.-W. Schmidt,
Hierarchical Superstructures by Combining Crystallization-Driven and Molecular Self-Assembly,

Angew. Chem. Int. Ed. **2021**, 60, 21767 –2177

M. Weber, M. Schulze, G. Lazzara, A. P. Piccionello, A. Pace, I. Pibiri,
Oxadiazolyl-Pyridinium as Cationic Scaffold for Fluorinated Ionic Liquid Crystals,
Appl. Sci. **2021**, 11, 10347

List of abbreviations

Abbreviation	Description
AFM	Atomic force microscopy
BTA	1,3,5-benzenetricarboxamide
CTAC	<i>N,N,N</i> -Trimethyl-1-hexadecan-aminiumchloride
1-D	One-dimensional
3-D	Three-dimensional
DMF	Dimethylformamide
DNA	Deoxyribonucleic acid
DSC	Differential Scanning Calorimetry
ESEM	Environmental Scanning Electron Microscopy
EtOH	Ethanol
FF	Diphenylalanine
LiCl	Lithium chloride
LIT	Lock-in Thermography
MEK	Methyl ethyl ketone
MeOH	Methanol
MgO ₂	Magnesium peroxide
MS	Mass spectrometry
NMR	Nuclear magnetic resonance
<i>O. microdasys</i>	<i>Opuntia microdasys</i>
PA	Polyamide
PDMS/MS	Polydimethylsiloxane/microsphere
PdNPs	Palladium Nanoparticles
PET	Polyethyleneterephthalate
PLA	Poly lactide
PP	Polypropylene
PS	Polystyrene
rt	Room temperature
SEDMA	Polystyrene- <i>block</i> -polyethylene- <i>block</i> -poly(<i>N,N</i> -dimethyl-aminoethyl methacryl-amide)
SEM	Scanning Electron Microscopy
T _{clearing}	Clearing temperature
T _{cloud}	Cloud temperature
THF	Tetrahydrofurane
TMPTA	<i>N, N', N''</i> -tris(3-methylpyridyl)-trimesic amide

List of symbols and units

Abbreviation	Description
Å	Ångström
2α	Apex angle
α	Thermal diffusivity
β	Angle of the polarizer
$\delta(C_{ar})$	Aromatic band of the ring deformation
λ	Wavelength
b.p.	Boiling point
c	Concentration
CA	Contact angle
C ₃	Carbon atom position 3
°C	Celsius
°C min ⁻¹	Celsius per minute
cm	Centimeter [1 x 10 ⁻² m]
cm s ⁻¹	Centimeter [1 x 10 ⁻² m] per second
d	Diameter
D	Distance
F _{Laplace}	Driving force Laplace
f _{lock-in}	Lock-in frequency
¹ H	Proton (hydrogen)
h	Hour
Hz	Hertz [s ⁻¹]
IR	Infrared
kJ mol ⁻¹	Kilo Joule per mole
K min ⁻¹	Kelvin per minute
kV	Kilo volt [1 x 10 ³ V]
kV cm ⁻¹	Kilo volt per centimeter
L	Liter
l/d	Aspect ratio
mg	Milligram [1 x 10 ⁻³ g]
mm	Millimeter [1 x 10 ⁻³ m]
mm ² s ⁻¹	Millimeter square per second
m s ⁻¹	Meter per second

Abbreviation	Description
mW	Milliwatts [$1 \times 10^{-3} \text{ W}$]
μW	Microwatts [$1 \times 10^{-6} \text{ W}$]
nm	Nanometer [$1 \times 10^{-9} \text{ m}$]
Pa	Pascal [1 N m^{-2}]
P_L	Laplace pressure
ppm	Parts per million
μ	Dipole moment, macrodipole
μl	Micro liter [$1 \times 10^{-6} \text{ L}$]
μm	Micrometer [$1 \times 10^{-6} \text{ m}$]
$\mu\text{m s}^{-1}$	Micrometer per second
r	Roughness
R	Substituent, Radius
rpm	Revolutions per minute
s	Second
WD	Working Distance
wt. %	Weight percentage
γ	Surface tension [$\text{mN}\cdot\text{m}^{-1}$]
γ_{SV}	Surface tension of the solid-vapor
γ_{SL}	Surface tension of the solid-liquid
γ_{LV}	Surface tension of the liquid-vapor
θ	Contact angle value

Table of contents

Summary	1
Zusammenfassung	3
1 Introduction	7
1.1 Hierarchical self-assembly	8
1.2 Non-covalent interactions and fabrication techniques on different length scales	15
1.3 1,3,5-benzenetrisamides a versatile class of supramolecular building blocks	17
1.4 Self-assembly of 1,3,5-benzenetrisamides	21
1.5 Hierarchical superstructures with supramolecular fibers	39
2 Motivation of the thesis	43
3 Controlled preparation of supramolecular fibers	47
3.1 Background to self-assembly under controlled conditions	47
3.2 Controlled preparation of supramolecular fibers	51
3.2.1 Selection of 1,3,5-benzenetrisamides.....	51
3.2.2 Self-assembly experiments with BTA 1	52
3.2.3 Development of the custom-made experimental set-up for self-assembly	56
3.2.4 Sample preparation for scanning electron microscopy measurements	58
3.3 Self-assembly experiments under controlled conditions.....	60
3.3.1 Self-assembly experiments with BTA-1	60
3.3.2 Self-assembly experiments with BTA 2	71
3.3.3 Self-assembly experiments with BTA 3	77
3.4 Conclusion to controlled preparation of supramolecular fibers	81
4 Electrostatic flocking of supramolecular fibers	83
4.1 Background to electrostatic flocking	83
4.2 Material selection for suitable supramolecular fibers	90

4.3	Development of electrostatic flocking of supramolecular fibers	93
4.3.1	Electrostatic flocking device and process.....	93
4.3.2	Electrostatic flocking of neat supramolecular fibers	94
4.3.3	Optimization of the electrostatic flocking process	97
4.3.4	Electrostatic flocking of equipped BTA fibers	106
4.4	Electrostatic flocking with optimized conditions	111
4.4.1	Influence of the flocking time	112
4.4.2	Orientation of the supramolecular fibers	114
4.4.3	Properties of the supramolecular flock.....	115
4.5	Conclusion to electrostatic flocking of supramolecular fibers.....	116
5	Self-assembly of supramolecular fibers within polymer flocks	119
5.1	Material selection of BTAs.....	121
5.2	Solubility and self-assembly studies of the selected BTAs	122
5.2.1	Solubility studies of the selected BTAs in polar solvents	122
5.2.2	Self-assembly studies of the selected BTAs upon solvent evaporation	129
5.3	Site-specific self-assembly in polymer flocks	133
5.3.1	Selection and preparation of a polymer flock substrate.....	133
5.3.2	Self-assembly studies of the BTAs within polyamide flocks upon solvent evaporation	135
5.3.3	Influencing parameter of the site-specific self-assembly	140
5.4	Supramolecular spines	148
5.4.1	Proposed mechanism to site-specific supramolecular spine formation.....	148
5.4.2	Hierarchical level of the supramolecular spines	150
5.4.3	Morphology of the hierarchical structured supramolecular spines	154
5.4.4	Similarities of supramolecular spines to natural cactus spines and biomimetic concept.....	156
5.5	Background to natural cactus spines and their water interaction	158
5.6	Water interaction studies on supramolecular spines	165
5.6.1	Water condensation on supramolecular spines	165
5.6.2	Unidirectional water transport on supramolecular spines	169
5.7	Conclusion to self-assembly of supramolecular fibers within polymer flocks	172

6	Thermal diffusivity of supramolecular fibers	173
6.1	Background to lock-in thermography	173
6.2	Preparation of supramolecular fibers for lock-in thermography measurements	178
6.2.1	Preparation of suitable supramolecular fibers	179
6.2.2	Material selection for thermal diffusivity measurements	180
6.2.3	Sample preparation for lock-in thermography measurements	183
6.3	Properties of selected self-assembled BTAs	184
6.4	Thermal diffusivity measurements of selected BTAs	189
6.4.1	Frequency sweep	190
6.4.2	Power Sweep	191
6.4.3	Dependency on BTA fiber diameter	192
6.4.4	Lock-in thermography measurements on supramolecular fibers	195
6.5	Conclusion to thermal diffusivity of supramolecular fibers	197
7	Experimental Part.....	199
7.1	Methods.....	199
7.2	Experimental procedure	203
7.2.1	Controlled preparation of supramolecular fibers.....	203
7.2.2	Electrostatic flocking of supramolecular fibers	205
7.2.3	Self-assembly of supramolecular fibers within polymer flocks	207
7.2.4	Thermal diffusivity of supramolecular fibers	209
7.3	Synthesis and characterization of 1,3,5-benzenetrisamides	211
8	Appendix.....	223
	Appendix A	223
	Appendix B	229
	Appendix C	235
9	References.....	245
	Danksagung	261
	(Eidesstattliche) Versicherungen und Erklärungen	263

Summary

1,3,5-benzenetrisamides (BTAs) represent a well-established class of materials known to form supramolecular fibers driven by three strands of directed hydrogen bonds. However, precisely controlling the dimensions in the μm -range, particular the length and diameter with narrow distributions of both is rarely achieved in a controlled manner. This hampers the use of such supramolecular microfibers in certain applications. The goal of this thesis was to understand and control the processing conditions of the self-assembly process in view of the preparation and application of supramolecular microfibers with defined dimensions and morphology.

The first part, aimed at the *controlled preparation of 1,3,5-benzenetricarboxamides fibers* in solution on the liter-scale upon cooling. For this, an experimental set up was developed and optimized, which enabled the investigation of the self-assembly of three selected BTAs in view of the fibers shape and dimensions depending on non-linear and linear cooling rates, different stirring rates and concentrations. It was found that the cooling rate has a significant impact on the fiber diameter and length distribution if no stirring is applied. With a non-linear cooling profile, the BTA fibers show a broad distribution whereas linear cooling rates results in a narrower distribution. Stirring also has a major influence on the diameter and length, with faster stirring leading to narrower distributions and shorter BTA fibers. Only the selected different concentrations, appears to have a limited impact on the mean fiber diameter and length. In particular, for the BTA based on trimesic acid with cyclohexyl side groups, the fiber diameter can be tuned from 4 to 15 μm and the length from 160 to 500 μm . These dimensions are prerequisite for electrostatic flocking presented in the following chapter.

The second part, aimed for the first time at the preparation of densely packed and vertically aligned *supramolecular microfibers of BTAs by electrostatic flocking*. Electrostatic flocking is an industrial technique that accelerate and align short cut polymer microfibers in an electric field ultimately promoting their perpendicular arrangement on substrates used for various applications. One key requirement for electrostatic flocking is a suitable aspect ratio and very defined dimensions, both are challenging to achieve for supramolecular fibers by self-assembly. Here, specifically strongly rigid BTA fibers with a cyclohexyl periphery and narrowly distributed diameters and lengths from the first part were selected. In particular, the defined fiber lengths with narrow distributions were successfully achieved by developing a straightforward non-destructive sieving process. Neat BTA fibers without additives can be successfully flocked supporting the hypothesis that their intrinsic macrodipole moment

facilitates fiber alignment within an electric field. Efforts to optimize the free-flowing properties of the BTA fibers to transport single fibers in the electric field, also combined with conductivity-enhancing materials to improve acceleration, resulted in higher flocking densities and more vertical fiber alignment.

The third part, explored the *self-assembly of supramolecular fibers within polymer flocks* with the aim to prepare novel morphologies. This work was performed in collaboration with Felix Bretschneider (Macromolecular Chemistry II, Prof. Dr. Greiner). For this, a polyamide flock was prepared by electrostatic flocking and exposed to solutions of three selected BTAs. It was found, that for distinct BTAs and proper processing conditions the polyamide flock serves as structure-directing substrate comprising capillary effects along the vertically aligned microfibers and transporting the solutions towards the polyamide heads. This results in a remarkable site-specific self-assembly, where the BTA microfibers develop mostly on top of the polyamide flocks. Surprisingly, the BTA fibers feature a unique conical shape with microstructured surfaces arising from the hierarchical order of the supramolecular fibers. The conical shape with its structural features including microgrooves and structural gradients mimics that of natural cactus spines in form and function and enables the nucleation and directional transport of water towards the spine's base. Environmental scanning electron microscopy reveal that these artificial BTA spines feature a superhydrophilic surface, which further improves water transport. Here, a water droplet velocity of $150 \mu\text{m s}^{-1}$ was found, exceeding those of the natural cactus *Opuntia microdasys* by more than a factor of ten.

Finally, the last part, aimed for the first time to investigate the *thermal diffusivity of BTA fibers* determined using lock-in thermography. This work was performed in collaboration with Ina Klein (Physical Chemistry I, Prof. Dr. Retsch). Essentially, this study requires high aspect ratio BTA fibers with suitable diameter in the μm -range and length up to centimeters. This was achieved by self-assembling BTAs from DMF via slow solvent evaporation. Fibers of eight structurally different BTAs, all with anisotropic columnar arrangement, were successfully prepared for a comparative study. Our findings indicate that the thermal characteristics improve with increasing strength of the hydrogen bonds and order in the fibers. The thermal diffusivities of these fibers were found to be in the range of 0.080 to $0.114 \text{ mm}^2 \text{ s}^{-1}$ and is similar to that of thermal insulators.

Zusammenfassung

1,3,5-Benzoltriamide (BTAs) sind eine etablierte Materialklasse, die für ihre Fähigkeit bekannt ist, supramolekulare Fasern zu bilden. Diese sind stabilisiert durch drei gerichtete Wasserstoffbrückenbindungen. Die präzise Kontrolle der Dimensionen der Fasern im μm -Bereich, insbesondere der Länge und des Durchmessers mit engen Verteilungen, ist jedoch nur selten in einem kontrollierten Verfahren möglich. Dies erschwert den Einsatz solcher supramolekularen Mikrofasern in bestimmten Anwendungen. Ziel dieser Arbeit war es, die Prozessbedingungen des Selbstorganisationsprozesses zu verstehen und zu kontrollieren, um supramolekulare Mikrofasern mit definierten Dimensionen und Morphologie herzustellen und anwendungsspezifisch einzusetzen.

Im ersten Teil der Arbeit wurde ein Verfahren zur kontrollierten Herstellung von 1,3,5-Benzoltriamid-Fasern im Litermaßstab aus Lösung und unter Abkühlung entwickelt. Dafür wurde ein experimentelles Setup optimiert, das die Untersuchung der Selbstorganisation von drei ausgewählten BTAs ermöglicht. Hierbei wurden die Form und Dimensionen der Fasern in Abhängigkeit von nicht-linearen und linearen Abkühlraten, verschiedenen Rührgeschwindigkeiten und Konzentrationen analysiert. Es wurde festgestellt, dass die Abkühlrate einen erheblichen Einfluss auf den Durchmesser und die Längenverteilung der Fasern hat, insbesondere wenn kein Rühren erfolgt. Bei einem nicht-linearen Abkühlprofil weisen die BTA-Fasern eine breite Verteilung auf, während eine lineare Abkühlrate zu einer schmalen Verteilung führt. Homogenes Rühren hat einen signifikanten Einfluss auf die Durchmesser- und Längenverteilung, wobei schnellere Rührgeschwindigkeiten zu schmalen Verteilungen und kürzeren BTA-Fasern führen. Die Variation der Konzentration beeinflusste hingegen nur begrenzt die Dimensionen der Fasern. Besonders für BTA-Fasern auf Basis von Trimesinsäure mit Cyclohexyl-Seitengruppen ließ sich der Faserdurchmesser zwischen 4 und 15 μm sowie die Länge zwischen 160 und 500 μm einstellen. Diese Dimensionen sind entscheidend für die im nächsten Kapitel beschriebene elektrostatische Beflockung.

Das Ziel im zweiten Teil dieser Arbeit war die erstmalige Herstellung dicht gepackter und vertikal ausgerichteter supramolekularer Mikrofasern von BTAs auf einem Substrat durch elektrostatische Beflockung. Diese industriell genutzte Technik beschleunigt und richtet kurzgeschnittene Polymermikrofasern in einem elektrischen Feld aus, sodass sie letztlich senkrecht auf Substraten angeordnet werden – ein Verfahren, das vielseitig anwendbar ist. Eine wesentliche Voraussetzung für diese Technik ist ein geeignetes Verhältnis von Länge zu Durchmesser sowie präzise definierte Dimensionen, was grundsätzlich bei supramolekularen Fasern durch Selbstorganisation schwer zu erzielen ist. Daher wurden in diesem Zusammenhang gezielt starre BTA-Fasern mit Cyclohexyl- Seitengruppen sowie eng verteilten Durchmessern aus dem vorherigen Kapitel ausgewählt. Die definierten Faserlängen mit schmalen Verteilungen wurden erfolgreich durch die Entwicklung eines einfachen, schonenden Siebverfahrens erreicht. Es zeigte sich, dass reine BTA-Fasern ohne Zusatzstoffe erfolgreich geflockt werden können, was die Hypothese stützt, dass ihr intrinsisches Makrodipolmoment die Ausrichtung der Fasern im elektrischen Feld fördert. Durch gezielte Optimierungen zur Verbesserung der Rieselfähigkeit der BTA-Fasern und der Transportfähigkeit einzelner Fasern im elektrischen Feld, konnten eine höhere Flockdichte sowie eine verbesserte vertikale Ausrichtung der Fasern erreicht werden. Die Kombination mit leitfähigkeitssteigernden Materialien erwies sich dabei als vorteilhaft für die Rieselfähigkeit als auch den Beflockungsprozess.

Im Gegensatz dazu wird im dritten Teil dieser Arbeit ein innovativer Selbstorganisationsansatz untersucht, bei dem Polymerflocks als Substrat für die Bildung supramolekularer BTA-Fasern dienen. Diese Arbeit wurde in Zusammenarbeit mit Felix Bretschneider (Makromolekulare Chemie II, Prof. Dr. Greiner) durchgeführt. Dazu wurde ein Polyamid-Flock mittels elektrostatischer Beflockung hergestellt und mit Lösungen von drei ausgewählten BTAs in Kontakt gebracht. Für bestimmte BTAs und geeignete Prozessparameter zeigt sich, dass der Polyamid-Flock als strukturrichtendes Substrat wirkt. Die Kapillareffekte entlang der vertikal ausgerichteten Mikrofasern transportieren die Lösungen zu den Flockköpfen, was zu einer ortsspezifischen Selbstorganisation führt, bei der sich die BTA-Mikrofasern hauptsächlich an den Spitzen der PA-Flocks bilden. Erstaunlicherweise nehmen die BTA-Fasern eine einzigartige konische Form mit mikrostrukturierter Oberfläche an, die durch die hierarchische Anordnung der supramolekularen Fasern entsteht. Diese konische Form der BTA Faser mit ihren strukturellen Eigenschaften, wie Mikrorillen und strukturellen Gradienten, imitiert Kaktusstacheln in Form und Funktion, da sie die Nukleation und den gerichteten Transport von

Wasser zur Basis der Stacheln fördert. Mit einem speziellen Rasterelektronenmikroskop wurde die Interaktion der BTA Stacheln mit Wasser untersucht und die Ergebnisse zeigen eine superhydrophile Oberfläche, die eine Nukleation und den unidirektionalen Wassertransport entlang der BTA-Stacheln ermöglicht. Bemerkenswert ist, dass die gemessenen Tropfengeschwindigkeiten von $150 \mu\text{m s}^{-1}$ die der natürlichen Kaktusart *Opuntia microdasys* um mehr als das Zehnfache übersteigen.

Im letzten Teil dieser Arbeit wird erstmals die thermische Diffusivität von BTA-Fasern mittels Lock-in-Thermografie untersucht. Diese Arbeit entstand in Zusammenarbeit mit Ina Klein (Physikalische Chemie I, Prof. Dr. Retsch). Die Studie erforderte BTA-Fasern mit hohem Aspektverhältnis, einem geeigneten Durchmesser im μm -Bereich und einer Länge bis zu einem Zentimeter. Diese Voraussetzungen an die Dimensionen der Fasern wurden durch Selbstassemblierung der BTAs aus DMF unter langsamer Lösungsmittelverdampfung erreicht. Für eine vergleichende Analyse wurden Fasern aus acht strukturell unterschiedlichen BTAs erfolgreich hergestellt. Alle acht BTAs weisen Anisotropie und einen säulenartigen Aufbau auf. Die Ergebnisse zeigen, dass sich die thermischen Eigenschaften mit zunehmender Stärke der Wasserstoffbrückenbindungen und einer höheren Ordnung der Fasern verbessern. Die gemessenen thermischen Diffusivitäten der Fasern liegen zwischen $0,080$ und $0,114 \text{ mm}^2 \text{ s}^{-1}$, was im Bereich der Wärmeisolatoren liegt.

1 Introduction

Jean-Marie Lehn as pioneer and one of Nobel Prize winners in 1987 defined supramolecular chemistry as “*chemistry beyond the molecule*”.^[1] He understood the self-assembly process as the self-organization of low molecular weight building blocks which are held together by non-covalent intermolecular interactions.^[2,3] For example, organic molecules can undergo interactions such as donor acceptor interactions, electrostatic, van der Waals or hydrogen bonding.^[3] The self-assembly is initiated in a state of lower organization such as a solution, disordered aggregate, or random coil, and evolves towards an organized final state, like a crystal or folded macromolecule resulting in supramolecular architectures.^[4] The formation into such complex and organized state through non-covalent interactions is primarily guided by the molecular structures of the monomeric building blocks, their functional groups, and specific environmental conditions. Depending on these conditions, the fundamental advantage of the non-covalent interactions lies in their reversibility enabling an in situ assembly of monomers into the supramolecular structures.^[5] The resulting intermolecular bonding between the building blocks provides the opportunity for the design and fabrication of complex supramolecular structures with unique and unprecedented properties and functionality. Coupled with the advances in synthetic chemistry and characterization methods, structure and morphology determination and microscopy over the past decades, a more rigorous understanding of the structure at the molecular level, the self-assembly process and the intermolecular bonding was generated.^[6] Today, a level of control over the self-assembly process at the molecular level is achieved which enables the control at the macroscopic level as well and facilitating the adjustment of bulk material properties.^[5] The resulting structures cover biological and chemical as well as physical features greater than the single monomeric building block resulting in high complexity and novel functional properties.^[3] As a highly interdisciplinary field, supramolecular chemistry bridges physical, chemical, biological and material science.^[3,5] Some key areas where the supramolecular functional architectures make an important impact are applications such as membranes,^[7] supramolecular nanoelectronics,^[8] delivery agents,^[5] sensors^[9] and nucleating agents for semi-crystalline polymers.^[10] Hence, till to date, supramolecular chemistry remains a field for generating novel functional materials.

1.1 Hierarchical self-assembly

Hierarchical self-assembly is a process of multilevel organization into complex structures that cover several length scales ranging from molecular to macroscopic scale.^[4] These structures then serve as the foundational elements for constructing more intricate and multifunctional entities at subsequent level(s). Nature uses hierarchical self-assembly as fundamental concept to create such multilevel-organized structures with unique properties and functionality. Self-assembled biological structures can be as simple as the dimerization of two small building blocks driven by hydrogen bonding or as complicated as DNA, viruses and cell membranes being considered as supramolecular architectures.^[4,11] One prominent example in natural living systems is the double-stranded DNA as schematically depicted in Figure 1-1 A.^[12] The complementary nucleic base pairs (adenine and thymine, guanine and cytosine) held together *via* multiple hydrogen bonding (blue dashed lines) as shown in Figure 1-1 B.

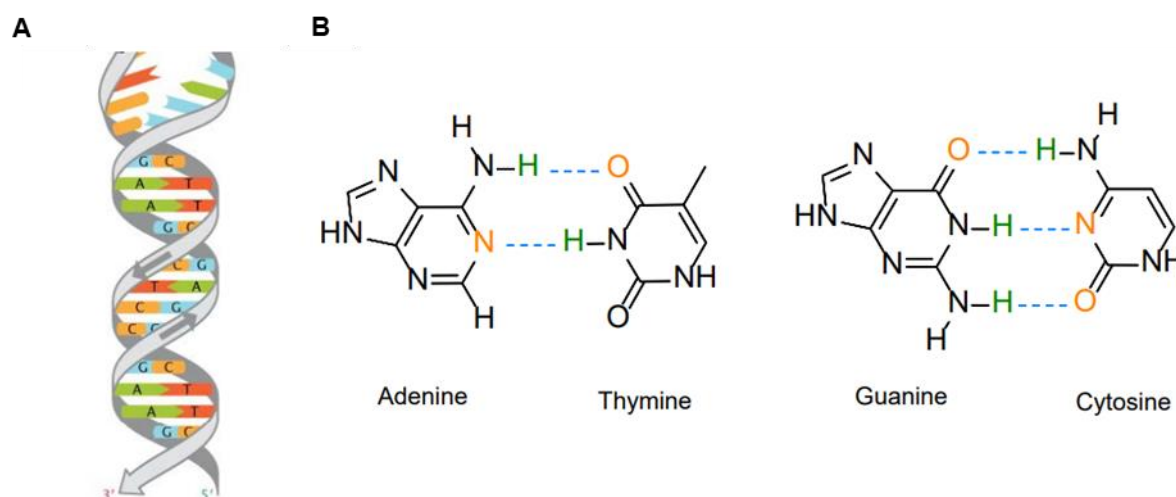


Figure 1-1. **Double stranded DNA with complementary base pairing.** **A:** DNA double helix and **B:** complementary DNA nucleic base pairs adenine and thymine as well as guanine and cytosine with multiple hydrogen bonding (blue dashed lines). Figure adapted and reproduced with from Ref.^[13] Copyright © 2008 Nature Education.

Some other examples for multi-level organized hierarchical materials from nature are spider silk,^[14] crustaceans,^[14] wood,^[14,15] human teeth (enamel)^[16] or bone^[14,17,18]. Figure 1-2 depicts some of these examples with hierarchical order from the nanoscale (< 100 nm) to the macroscale (> 0.1 mm). Functionality arises as a result of high level of organization and hierarchy on the macroscale. Complex structures in form of fibers, helicoids or layered walls are made of building blocks that self-assemble within the nanoscale which further aggregate to nanocrystals or fibrils on the next hierarchical level.

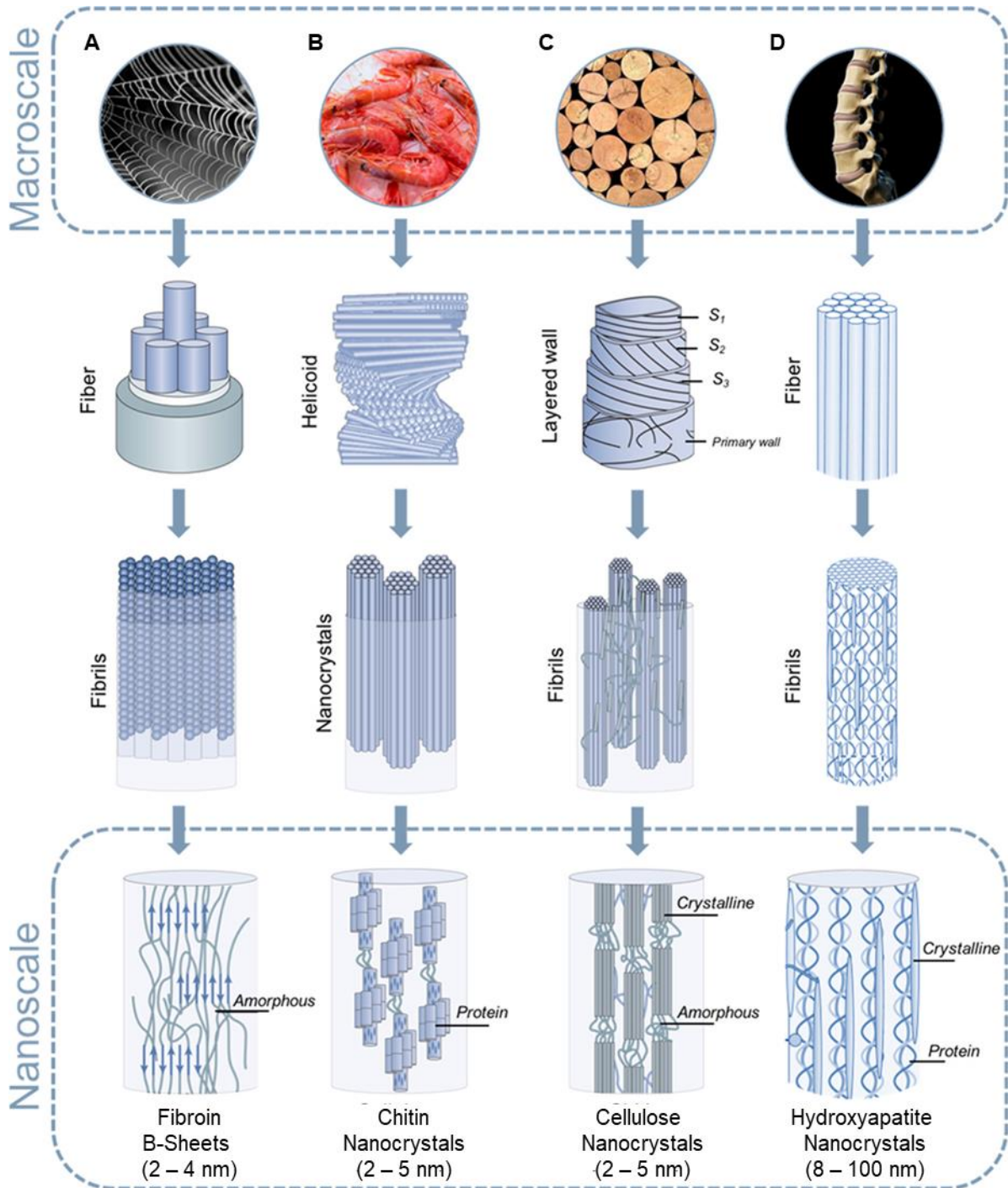


Figure 1-2. **An overview of various hierarchical materials in nature and their assembled structures from the macroscale down to the nanoscale:** Schematic representations of **A:** spider silk exhibits a multi-hierarchical structure in which silk fibroin is the primary component. **B:** The scaffold of crustacean exoskeletons contains chitin, which is organized hierarchically. **C:** Wood that exhibits a hierarchical structure, with a significant role played by cellulose nanocrystals. **D:** Bone has a hierarchical structure and is based on hydroxyapatite crystals and collagen protein. Figure adapted and reproduced with permission from Ref.^[14] Copyright © 2018, American Chemical Society.

A different illustration of the hierarchical levels of human tissue such as tendons and bones with its length scale are schematically shown in Figure 1-3. Tissues are a multi-hierarchically ordered composite made of collagen and mineral nanoparticles.^[15] On the first hierarchical level the *amino acids* as monomeric subunits are polymerized into peptide chains. Three peptide chains self-assemble and wind together, forming a triple helix arranged into the so called triple helical *collagen molecule* with lengths of about 300 nm. Collections of collagen molecules then aggregate both laterally and longitudinally to the next hierarchical level forming thin *collagen fibrils* with a uniform diameter of around 100 nm. However, in tissues like tendons, there is a wide-ranging distribution of fibril diameters, spanning from 100 to 500 nm. In bone tissue, the fibrils contain tiny hydroxyapatite crystals. These crystals provide the stiffness and resistance to compressive loads that are characteristic of bone tissue. The modified collagen fibrils further bundle into a complex *collagen fiber* morphology and finally made up the bone tissue resulting in the macroscopic level.^[18] Due to the complex hierarchy, a broad range of mechanical functionalities are introduced which cannot be achieved just by a single collagen molecule alone.

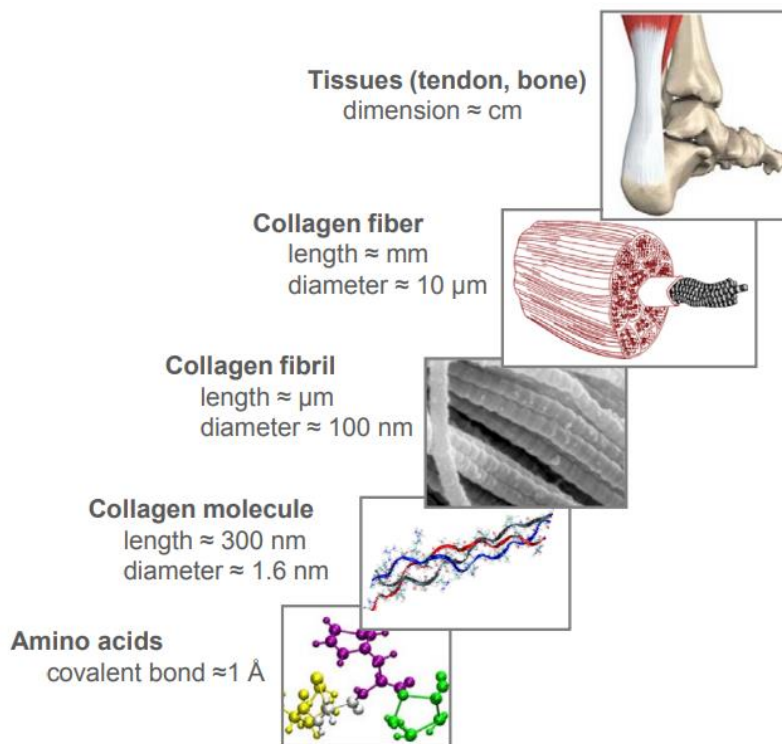


Figure 1-3. **The hierarchical structure of collagen protein materials exhibiting several levels of organization.** Each collagen molecule is composed of three peptide chains made of amino acids that wind together to form a triple helix with approximately 300 nm length. Collections of collagen molecules aggregate both laterally and longitudinally to form thin fibrils with a uniform diameter of around 100 nm. In tendons and ligaments, multiple fibrils come together to form a collagen fiber.^[17,18] Figure adapted and reproduced with permission from Ref.^[18] Copyright © 2011, American Chemical Society.

Figure 1-4 schematically illustrates the different levels of structural organization of polypeptides as macromolecular subunits, which are composed of amino acids as their smallest monomeric units. The amino acid sequence is the *primary structure* of a polypeptide chain (Figure 1-4 A). Electrostatic and hydrogen bonds between the N-H and the C=O groups of the amino acids lead to folding and twisting into a variety of shapes resulting in a *secondary structure* (Figure 1-4 B). The three-dimensional structure of a β -polypeptide is shown as the *tertiary structure* of the protein (Figure 1-4 C). The tertiary structure is determined by the distribution of the substituents along the chain and their interactions with each other such as ionic interactions, sulfur bridges, van der Waals forces or hydrogen bonds. The *quaternary structure* is a complex of polypeptide chains in its tertiary structure and thus can be only found in proteins that have more than one polypeptide chain (Figure 1-4 D).^[19] These non-covalent interactions are essential to achieve such a high level of organization and hierarchy in the final structure, which provides the function.

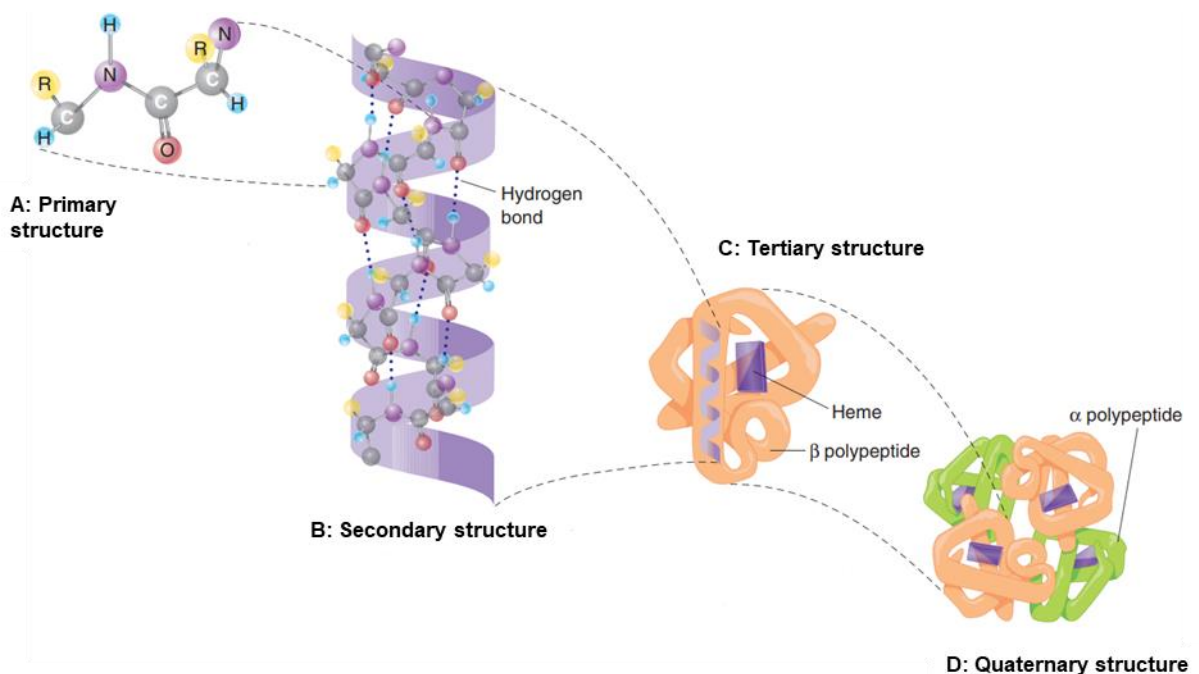


Figure 1-4. **The different levels of structural organization of proteins.** **A:** Primary structure of a polypeptide chain consisting of amino acids building blocks. **B:** Secondary structure arises from hydrogen bonding and resulting in a variety of shapes. **C:** Tertiary structure depicted as three-dimensional structure of a β -polypeptide and **D:** quaternary structure as a complex of several peptide chains. Figure adapted and reproduced with permission from Ref.^[19] Copyright © 2024 Pearson Benelux B.V.

Another interesting example of a multi-hierarchical organization process is found with the dipeptide diphenylalanine as a low molecular weight building block (Figure 1-5 A).^[20-22] Diphenylalanine has been reported to self-assembles into various morphologies such as nanotubes,^[23] nanofibers,^[24] nanowires,^[25] and hexagonal microtubes depending on the applied set of conditions during the self-assembly.^[26] Yan et al.^[26] investigated hierarchically structured diphenylalanine tubes by scanning electron microscopy and revealed the self-assembly and organization process of the diphenylalanine building blocks into the hexagonal microtubes as depicted in Figure 1-5. At the beginning, individual molecular building blocks (Figure 1-5 A) self-assemble into a hexagonal packing of six diphenylalanine molecules (Figure 1-5 B). Further hexagonal packing lead to the first stacking units which form the nanotube seeds (Figure 1-5 C and D). Hexagonal packing of nanotubes is the beginning stage for the formation of the hexagonal microtubes (Figure 1-5 E). The self-organization of the nanotubes results in the final hierarchical structure of hexagonal microtubes (Figure 1-5 F). The hierarchical self-assembly covers several length scales from the monomeric building block to the resulting hexagonal microtube consisting of ordered nanotube arrays with long range order. These microtubes exhibit diameters in the order of micrometers and can reach several millimeters in length (Figure 1-5 G). A hexagonal cross-section (Figure 1-5 H) spanning several magnitudes of hierarchy is visible at a fractured tube in Figure 1-5 D.

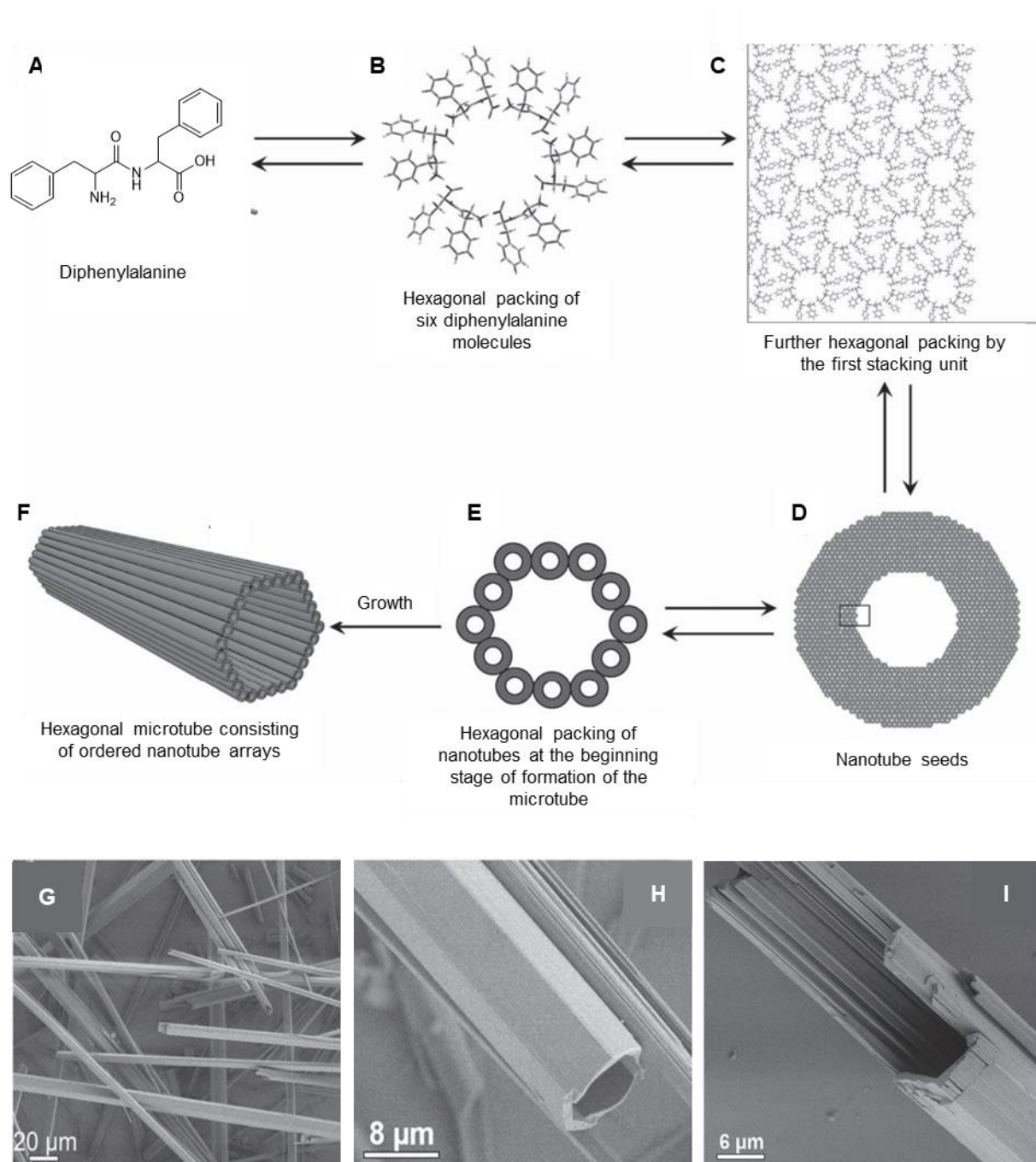


Figure 1-5. **Schematic formation of the self-assembly process of diphenylalanine into hexagonal microtubes.** **A:** Diphenylalanine building block. **B:** First assembly of six diphenylalanine monomers into a hexagonal pattern. **C and D:** Further hexagonal packing into nanotube seeds. The panel C shows an enlarged view of the area in D indicated with a black rectangle. **E and F:** show the beginning stage and further spontaneously organization into hexagonal microtubes. **G-I:** Scanning electron microscopy micrographs of hexagonal diphenylalanine microtubes with **H:** higher magnification and **I:** as fractured tube. Figure adapted and reproduced with permission from Ref.^[26] Copyright © 2011 WILEY-VCH Verlag GmbH & Co. KGaA, Weinheim

The resulting length scales from 1 Å to 1 mm and through self-assembly into hierarchical structures are illustrated in Figure 1-6.^[4,20] Here, the self-assembly into hierarchical structures starting from elementary amino acid molecules to secondary structures such as α -helix or β -sheets of peptides towards fibers and fiber bundles as well as oriented crystalline sheets is guided by several intermolecular interactions from short to long-range order.^[20] The interplay and balance of different non-covalent interactions such as hydrogen-bonds, van-der-Waals interactions and electrostatic interactions as well as surface tension forces/dewetting determines the resulting overall hierarchical morphology into nanostructures such as the formation of nanofibers, nanoribbons or nanosheets.^[21] The self-assembly of the peptides is typically spontaneous, rapidly and reproducible under given conditions. Moreover, by systematically varying the chemical structure, such as the size and nature of amino acids, fine-tuning of the self-assembling characteristics of the building blocks is possible and allow the preparation for a wide range of diverse nanostructures.^[4]

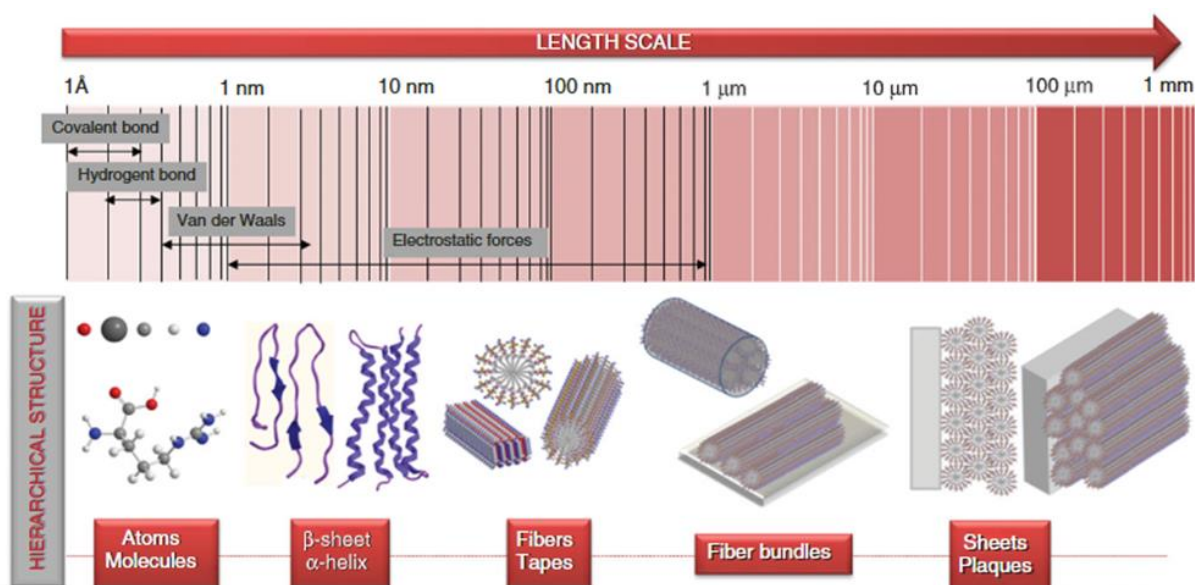


Figure 1-6. **The intermolecular interactions involved in multiscale hierarchical self-assembly of peptides.** Various intermolecular interactions play pivotal roles in the multiscale hierarchical self-assembly of peptides. These interactions serve distinct functions at different scales, starting from elementary molecules and progressing to secondary structures like β -sheets and α -helices, then extending to fibers and tapes, fiber bundles, and even crystalline structures. Figure adapted and reproduced with permission from Ref.^[4] Copyright © 2013 Wiley Periodicals, Inc.

1.2 Non-covalent interactions and fabrication techniques on different length scales

The binding energies for covalent bonds can vary based on whether the element is bonding with itself, forming single, double, or triple bonds, or bonding with other elements, typically hydrogen or oxygen. For instance, a single carbon-carbon bond usually has a binding energy of 346 kJ mol^{-1} , while double and triple carbon-carbon bonds have binding energies of 602 kJ mol^{-1} and 835 kJ mol^{-1} , respectively. In comparison, a single carbon-hydrogen bond has a binding energy of 411 kJ mol^{-1} . For carbon-oxygen bonds, the binding energies are 358 kJ mol^{-1} for a single bond and 799 kJ mol^{-1} for a double bond.^[27] Non-covalent interactions between individual molecules can be significantly weaker such as van-der-Waals binding energies are found to be below 5 kJ mol^{-1} , however, ion-ion interactions such as in NaCl can reach higher binding energies up to 350 kJ mol^{-1} .^[6] Binding energies in hydrogen bonding depending on the properties of the hydrogen bonds such as lengths, strengths and geometries. Hydrogen bonds can be as strong as some covalent bonding energies (HF complexes) or as low as reported for hydrophobic effects (for example C-H...O).^[28] Even though non-covalent interactions can be weaker than covalent bonds, in sufficient assembled number they can generate stable assemblies as demonstrated with the mentioned examples. The common non-covalent interactions involved in supramolecular chemistry are summarized in Table 1-1.

Table 1-1. Non-covalent interactions with their binding energies involved in supramolecular chemistry.^[6]

Non-covalent interactions	Binding energies (kJ mol^{-1})
Ion-Ion	100-350
Ion-Dipole	50-200
Hydrogen bonding	4-120
Dipole-Dipole	5-50
π - π	2-50
Hydrophobic effects	<5

In addition, new technologies are able to fabricate structures achieving functions or properties similar to those found in biological materials. For example, techniques such as 3-D printing, layer-by-layer or self-assembly as shown in Figure 1-7, have enabled the fabrication of various complex structures such as artificial blood vessels (3-D printing), microporous scaffolds (layer-by-layer), and DNA origami (self-assembly) covering length scales from nano-to macroscale.^[29]

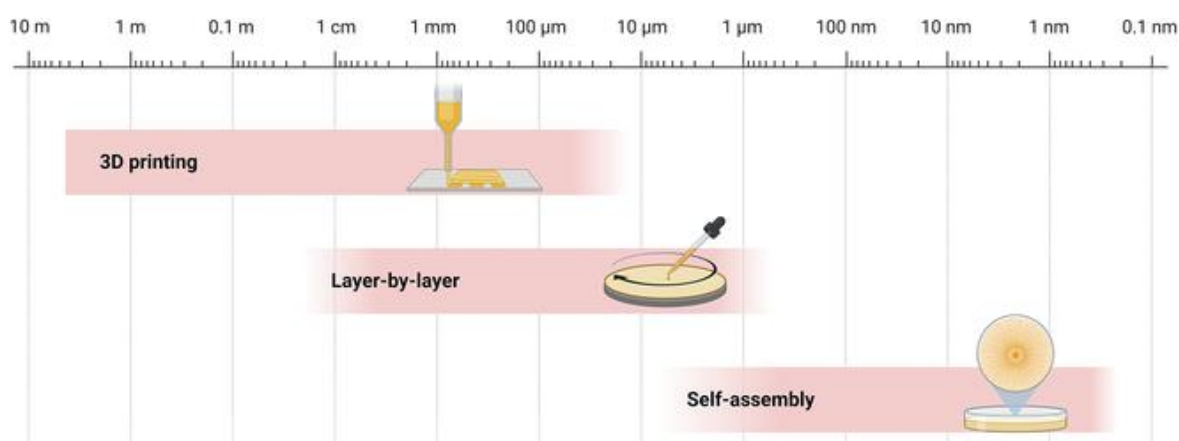


Figure 1-7. **Fabrication techniques for different applications including 3-D printing, layer-by-layer and self-assembly covering length scales from nano-to macroscale.** Figure adapted and reproduced with permission from Ref.^[29] Copyright © 2023 Jingjiang Wei et al..

In summary, the presented examples for hierarchical structures from nature demonstrate that their multiple levels of organization and hierarchy contribute to the overall properties and functions. Nature provides crucial insights in utilizing supramolecular chemistry to also be applied to rational design of artificial molecular building blocks in terms of size, the molecular structure, geometry, orientation and strength of interactions.

This knowledge is more frequently used in the scientific community to design new materials for various applications in engineering, materials science and biomimicry via supramolecular chemistry. Choosing an appropriate material system and suitable preparation methods enable the fabrication of artificial hierarchical structures. Despite the example of amino acids as small building blocks there exists a multitude of other building blocks being able to undergo self-assembly into hierarchically structured materials. For example, benzimidazole derivatives which self-assemble into nanofibers or microflower structures via metal-interactions,^[30] 3,5-dimethyl-4-iodopyrazole that shows self-assembly into fibrils, sheets and tubular fibers through hydrogen and halogen bonding^[31] or perylene diimide derivatives forming multilayered nanobelts merely through π - π -stacking.^[32]

Another well-established self-assembling system based on small building blocks is the class of 1,3,5-benzenetrisamides (BTAs). These molecules are able to self-assemble into a variety of hierarchical structures depending on the molecular design and self-assembly parameters. This class represents the structural motif used within this thesis and is described in detail in the following chapters.

1.3 1,3,5-benzenetrisamides a versatile class of supramolecular building blocks

The class of 1,3,5-benzenetrisamides (BTAs) represents a prominent supramolecular motif as small building blocks capable to form hierarchical structures.^[33–37] Their molecular design will be explained in the following. The general chemical structure of such a BTA is depicted in Figure 1-8 and can be divided into three structural elements: *i)* a central core, *ii)* amide linkages and *iii)* the peripheral groups. The depicted BTA consists of a planar benzene ring as core and symmetrical substituted amide groups in 1, 3 and 5 position leading to a C_3 -symmetry. The amide groups enable directed hydrogen bonding resulting in threefold hydrogen bond strands.^[35,37] However, the self-assembly behavior can be finetuned by changing the peripheral substituents. Due to the great variety of the possible peripheries (e.g. linear and branched alkyl chains of different length, chiral, chromophoric or polar and ionic substituents), the solubility in different media and thus self-assembly behavior can be adjusted concerning the desired supramolecular structures for different applications.

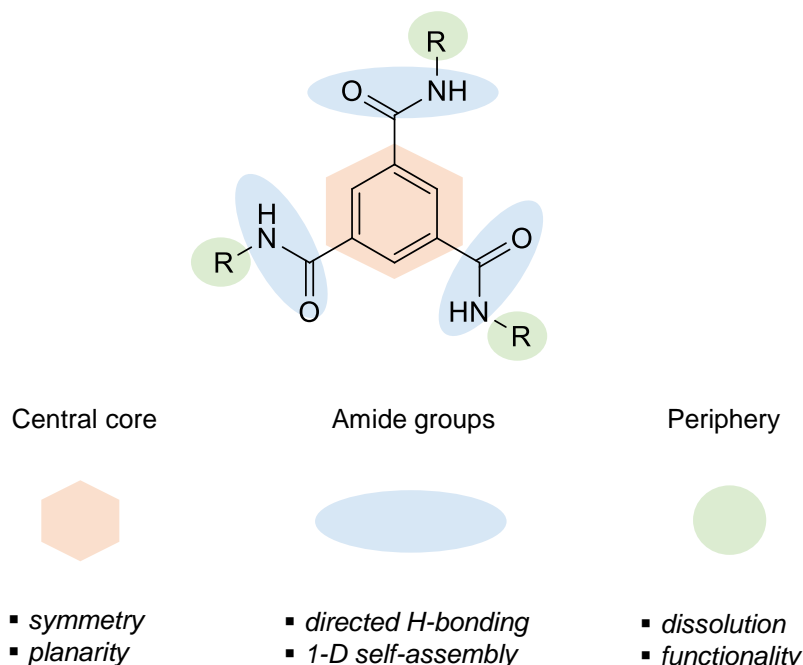


Figure 1-8. **Structural elements of 1,3,5-benzenetricboxamides with a C-centered amide connectivity.** The central core provides symmetry and planarity, the amide groups are responsible for directed H-bonding and the 1-D self-assembly and the periphery allows to finetune the self-assembly and morphology of the supramolecular entities.

There exist four basic structural variations of benzenetrisamides as depicted in Figure 1-9. The amide linkages are either over the carbon atom of the C=O bond, so called C-centered or over the NH-bond so called N-centered or even a mixture of them to the benzene core. Coupled with variations in the periphery, a library of 1,3,5-benzenetricarboxamides became available making these motifs a versatile system in supramolecular chemistry. The trisamides used in this work are based on a benzene core with either N- or C-centered amide connectivity, thus the self-assembly behavior of these derivatives is described in more detail in the following chapters.

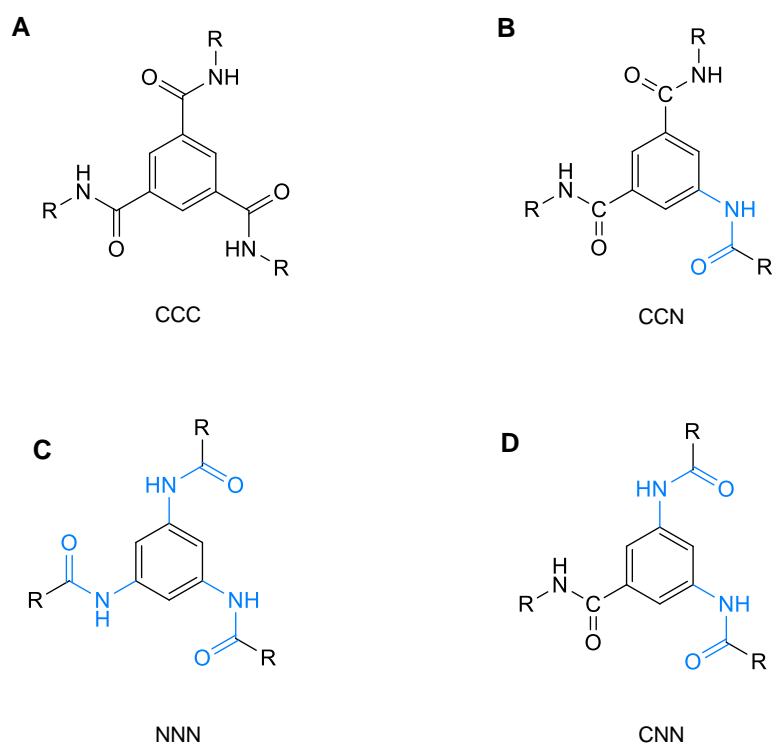


Figure 1-9. **Molecular structures of trisamides with variation in their amide connectivity.** **A:** 1,3,5-benzenetricarboxamide with all C-centered amide connectivity, annotated as *CCC*. **B:** 1,3,5-benzenetrisamide with two C-centered and one N-centered amide connectivity (*CCN*). **C:** 1,3,5-benzenetrisamide with one C-centered and two N-centered amide connectivity (*CNN*). **D:** 1,3,5-benzenetrisamide with all N-centered amide connectivity, annotated as *NNN*. Blue marked amid linkages represent the N-centered amide connectives.

In addition, there exists another structural variation using a cyclohexane ring as core.^[38-40] These molecules typically feature less solubility in polar solvents. Thus, they are not further described in detail in this thesis.

The ability of BTAs to self-assemble arises from the formation of a threefold intermolecular hydrogen bonding helix as schematically shown in Figure 1-10.^[37] One BTA molecule is considered as a molecular building block. The molecular building blocks start to self-assemble and can form supramolecular stacks which can be considered as columnar aggregates. The self-assembly into such columnar aggregates has been revealed by crystallographic structure analysis^[41–44] and experimental studies on their self-assembly behavior.^[45–48] As a result of the columnar self-assembly of the triple hydrogen bonding per molecule BTA a directional alignment of the polar NH and C=O bonds takes place creating a macrodipole (μ) along the columnar axis.^[39,40,49,50]

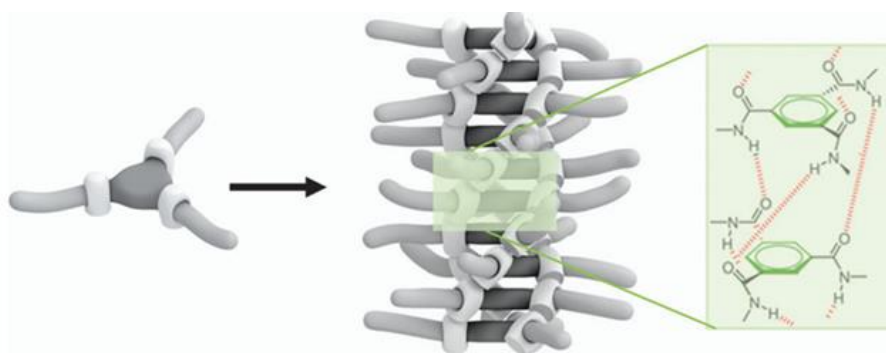


Figure 1-10. **Schematic illustration of supramolecular columnar aggregates.** BTA with C-centered amide connectivity and its self-assembled structure driven by the formation of a threefold intermolecular hydrogen bonding helix. Figure adapted and reproduced with permission from Ref.^[37] Copyright © Royal Society of Chemistry 2012.

In detail, the supramolecular building block itself is planar as schematically shown in Figure 1-11 A. Due to the formation of the intermolecular triple hydrogen bonding helix in an oligomer, the amide and carbonyl linkages start to orient themselves resulting in a dipole moment which adds up to a macrodipole (μ) as schematically described in Figure 1-11 B. The addition of building blocks to the stack has been proven to be favorable with each monomer added showing a positive cooperativity among hydrogen bonds.^[39] The total dipole moment of the stack increases with growing stack size. However, if two columns arrange, they prefer an anti-parallel alignment, i.e. opposite direction of the macrodipole. This is shown in Figure 1-11 C where two stacks of BTA are depicted in a space-filling model view in an antiparallel orientation due to the electrostatic interactions. The black and white hexagons indicate the macrodipole direction with either up or down. The steric restraints of the peripheral groups of a BTA influence the arrangement of the stacks and thus having an impact on the macrodipole interaction. An example is shown in Figure 1-11 D of seven stacks in a hexagonal rod packing.^[50] This packing of neighboring columns for BTAs offers dense packing favorable for van der Waals forces.^[51] However, in such a hexagonal rod packing it is not possible to achieve

an antiparallel alignment of all macrodipoles as exemplarily shown with the black, white and grey hexagons. As a consequence, the macrodipole interaction between the stacks becomes frustrated relative to their nearest neighbor resulting in a reduced impact of the macrodipole interaction in the lattice energy and increased impact of the steric restraints.^[50]

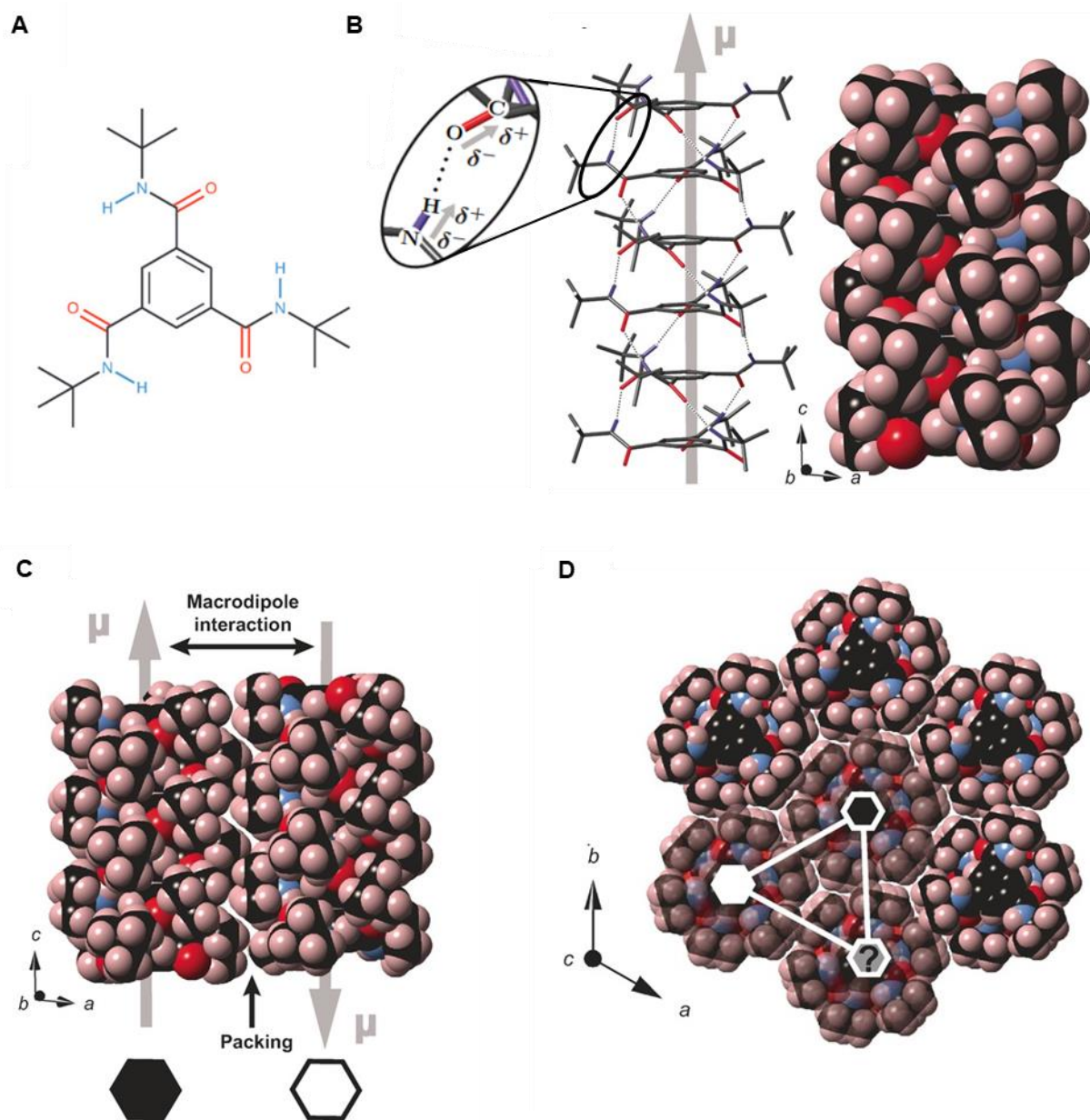


Figure 1-11. Schematic presentation of the dipole formation of BTA stacks and the resulting geometric frustration. **A:** Chemical structure of a BTA with tert-butyl moieties. **B:** Left: a columnar stack with six BTA molecules showing hydrogen bonding (dotted lines). The gray arrow indicates the macrodipole μ . Right: space-filling model of the same stack. **C:** Two stacks of BTA depicted in space-filling model view in an antiparallel orientation. The black and white hexagons indicate the macrodipole direction. **D:** Display of the geometric frustration arising from seven stacks in a hexagonal rod packing. Figure adapted and reproduced with permission from Ref.^[50] © 2017 The Authors. Published by Wiley-VCH Verlag GmbH & Co. KGaA.

1.4 Self-assembly of 1,3,5-benzenetrisamides

To achieve desired supramolecular structures and morphology of BTAs from self-assembly one has to consider several parameters which influence the self-assembly process that are: *i) the molecular structure, ii) the selected medium, iii) the concentration and temperature* and *iv) the applied self-assembly method* (Figure 1-12). For example, for a given molecular structure, the medium such as the choice of the right solvent, the right concentration and temperature determine the solubility. Suitable self-assembly methods will determine and allow for the preparation of tailored self-assembled structures and to control the dimensions and shape. Thus, for a given application each BTA has an own processing window and set of conditions for its self-assembly. The different influencing parameters are discussed in detail in the following.

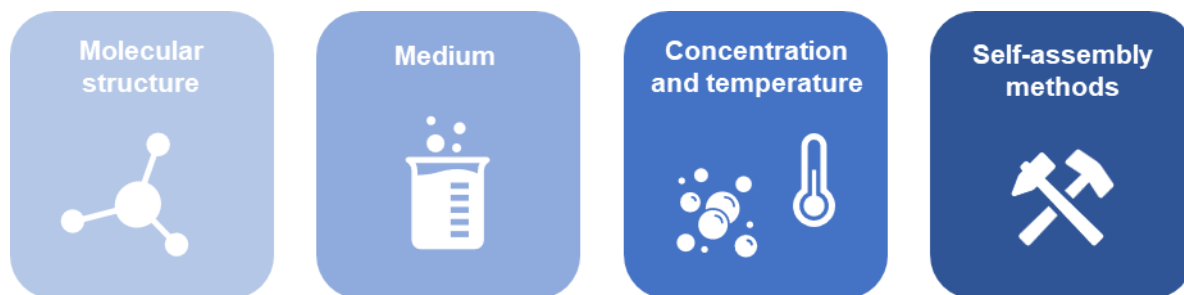


Figure 1-12. **Parameter that influence the solution-based self-assembly of BTAs.** The interplay of the molecular structure, medium, concentration and temperature and self-assembly methods influences the self-assembly of BTAs into supramolecular structures. Source: University of Bayreuth, Macromolecular Chemistry I.

i) Molecular structure:

The molecular structure of the BTA, i.e. the core (benzene or cyclohexane based), the amide connectivity (C- or N-centered) and the periphery strongly determines the crystal packing and thus the self-assembled structures. For example, the difference of a benzene or cyclohexane core has a significant influence on the disc-to-disc distance as well as the hydrogen bonding in the self-assembled stacks. The molecules with a cyclohexane core, which is more flexible, will stack with a disc distance of 0.47 nm.^[38] As described in literature, the three carbonyl groups can easily align parallel to each other and perpendicular to the cyclohexane ring. This conformation allows the three carbonyl oxygens ideally positioned to interact with the three NH-groups of the adjacent molecule and thus almost linear hydrogen bonds are formed.^[41,44] Due to the linear hydrogen bonding pattern, the peripheral groups have enough space to be stacked on top of each other. In contrast to that, tricarboxamides with a planar benzene core

usually stack with a disc distance of 0.347 nm being one third smaller than the cyclohexane core derivatives.^[38,39,43,52] This is reflected directly in the stacking of such BTA derivatives. A twist angle of 60° is observed between consecutive discs resulting in an out-of-plane rotation of the amide groups and consequently building a helix of threefold hydrogen bond strands.^[46,52]

The next molecular structure element to be discussed is the arrangement of the amide linkages, i.e. the amide connectivity, which can either C- or N-centered (or a mixture). The pattern of the amide connectivity has an influence on the strength and direction of the hydrogen bonding and thus, directly on the self-assembly.^[37] Regardless the connectivity and the resulting different symmetry, the threefold hydrogen bonding is always formed. Regarding amide connectivity for BTA derivatives, N-centered connectivity leads to more planarized carbonyl groups. The intermolecular hydrogen bonds exhibit a larger distance indicating a lower strength resulting to an overall reduced macrodipole. This further leads to weakened macrodipole-macrodipole interactions between two stacks and predominantly grow in one direction (long axis).^[39] This phenomenon is observed regardless the amount of N-centered amide connectivity (only one, two or all three amide groups) however the effect becomes more pronounced with each shift toward more N-centered connectivity. Conversely, when all three amide groups are in a C-centered connection, a significant macrodipole is established.^[39,50]

The last component of the molecular structure – the periphery- can be either used to introduce functionality (such as favorable groups for nanoparticle adsorption^[53,54]) or moieties which will react to external triggers such as pH-change,^[52,55–58] temperature^[59,60] or light.^[61] Moieties reported in literature are versatile ranging from length and size, e.g. linear and branched alkyl,^[46,62] aryl,^[33,52,63,64] pyridyl,^[55,65] triphenyl^[66] as well as amino acid,^[48,67–70] peptide^[71,72] to benzo crown ethers^[59] and many more.^[60,73–76] Studies about the crystal packing of short aliphatic chains such as R = methyl,^[77] R = ethyl^[78] or R = propyl^[78] show sheet-like hydrogen bond patterns or three-dimensional networks instead of columnar stacking. However, introducing larger groups ($n \geq 4$) with higher sterically hindrance lead to columnar stacking.^[41–43,67] Larger aliphatic peripheral groups rather influence the macrodipole along the axis, however contribute to the macrodipole-macrodipole interactions between two columnar stacks. The larger distance between two stacks will eventually weakened the interactions and leading to a predominantly grow along the axis resulting in long fibers rather than thick ones.^[39] Long and flexible peripheral groups often resulting in liquid crystalline behavior.^[38,62,79]

ii) Medium:

The choice of the medium is crucial for the self-assembly process and can lead to a variety of supramolecular structures differing in dimensions and shape for the same molecular building block. For example, self-assembly in *bulk* of BTAs is studied and mostly liquid crystalline behavior is observed if the BTAs are meltable.^[38,62,79] Changing towards *solvents* the BTAs show selective solubilities (in dependence of concentration, temperature and polarity of the solvent) which can be used to finetune self-assembly in solution. Many groups report BTA gelation either from water^[58–60,80] and water mixtures^[81–83] or from organic solvents^[54,64,77,84–86]. Self-assembly into fibrous structures from different kind of solvents are observed for various BTA derivatives, specific examples are given in the next chapters.^[60,69,73,87–93] Further research dealt with the self-assembly in polymer *melts* resulting in self-assembly into fibrous structures and thus nucleation in the polymer melt.^[10,42,74] Mostly, the different applications dictate in which media the BTAs are self-assembled.

iii) Concentration and temperature:

For a given BTA the concentration and temperature play an important role to control the dimensions and shape of the supramolecular structures and governs the solubility of the BTA in a given solvent. The concentration has an impact on the size of the self-assembled hierarchical structures. At higher concentrations, the more likely bundling and formation of larger aggregates is observed followed by gel formation and solid as a function of concentration.^[46] Due to the dependence of temperature and concentration on the solubility in a given solvent, there exists a phase diagram (temperature vs. concentration) for BTAs and the selected solvent, showing either too good solubility (no self-assembly in the concentration range), self-assembly in the right window or only partial solubility. With this knowledge, the self-assembly and dimensions and shape of the hierarchical structures can be controlled and tuned in a reversible and highly reproducible manner. More details are described later in the section a) Self-assembly in solution at a constant concentration.

iv) Self-assembly methods:

The self-assembly methods (Figure 1-13) have also an influence on the dimensions and shape of the resulting supramolecular structures. Common methods for the preparation of supramolecular structures are: self-assembly in a given medium at a constant concentration, self-assembly upon solvent evaporation, self-assembly in solvent mixtures or stimuli responsive self-assembly (pH change or light) to name a few. For example, using self-assembly in solution

at constant concentration is mainly governed by processing parameters such as the stirring and temperature profile. Here constant stirring at a defined stirring rate in a solution result in a more homogenous distribution of the fiber diameter. Thinner fibers can be generated by applying a higher stirring rate. The temperature profile plays a significant role, too. Using the same reactor, cooling profile and stirring eventually lead to a high reproducibility of the obtained fibrous structures.^[90,94] These methods can be considered as one tool to achieve a dedicated dimensions and shape of the supramolecular structures and thus, functionality and application. The different self-assembly methods and the resulting hierarchical structures will be described in more detail in the upcoming chapters.

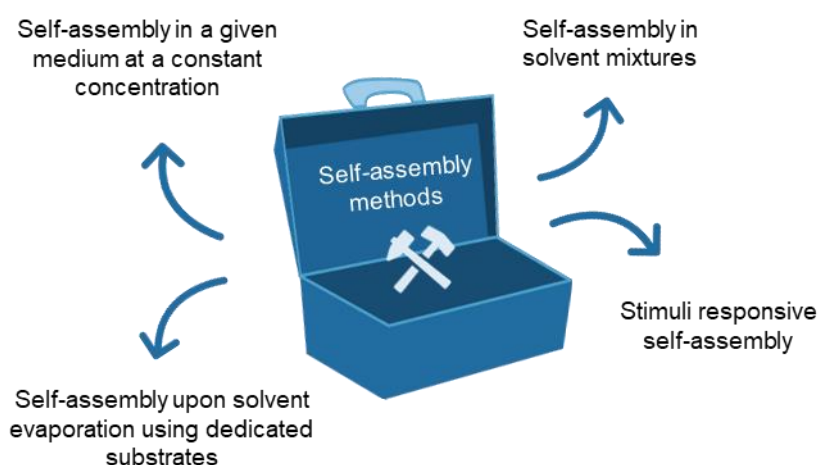


Figure 1-13. **Different self-assembly methods.** These self-assembly methods can be considered as tools to prepare dedicated dimensions and shapes of 1,3,5-benzenetrisamides.

To summarize, the self-assembly behavior in bulk or the solubility and self-assembly of a molecule in a specific medium is determined by the combination of its structural elements and the final molecular structure. Consequently, each BTA exhibits a unique processing window influenced by the interplay of molecular structure, solvent, concentration, temperature, and self-assembly methods. Thorough investigations of these combinations are required to achieve tailored functional materials and to control the dimensions and shape of the resulting supramolecular structures.

In the following a) self-assembly in solution at a constant concentration, b) self-assembly in solvent mixtures, c) self-assembly during solvent evaporation and d) stimuli responsive self-assembly triggered by pH change will be discussed. For each method examples from literature will be given.

a) Self-assembly in solution at a constant concentration

One typical solution-based self-assembly process of 1,3,5-benzenetrisamides into supramolecular fibers at a constant concentration is depicted in Figure 1-14 (A). The process is dependent on the change in temperature, concentration and the solubility of the BTA in the given solvent. Starting from the molecularly dissolved state (a_1), the initiation of self-assembly occurs upon cooling leading to the formation of supramolecular fibers (a_2) held together by hydrogen bonding. Figure 1-14 B depicts the hierarchical level of the formed supramolecular fibers (b_1) composed of fiber bundles with dimensions of $> 0.1 \mu\text{m}$ (b_2). The fiber bundles are made of single BTA molecules which feature a columnar arrangement with typical dimensions ranging from 1-3 nm (b_3), depending on the peripheral substituents of the utilized BTA. The supramolecular fibers can exhibit various dimensions (e.g. aspect ratios) and shapes, contingent on the molecular structure and self-assembly conditions.

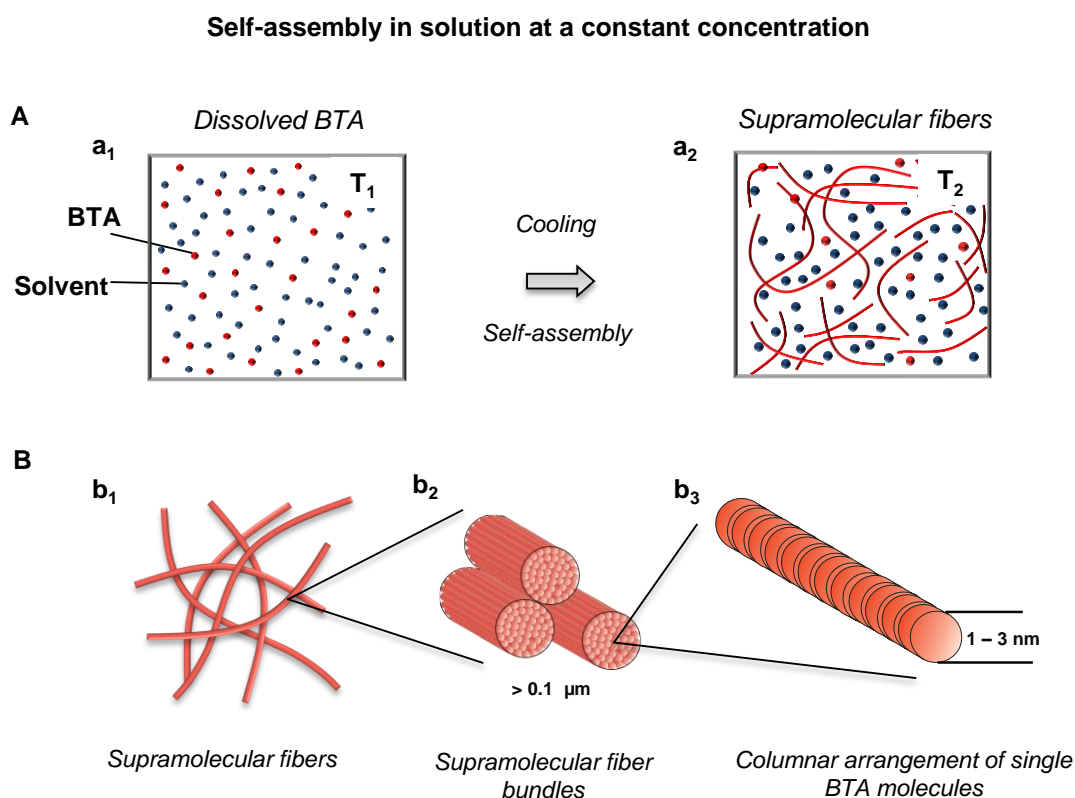


Figure 1-14. **Schematic presentation of the formation process of supramolecular fibers from solution at a constant concentration.** **A:** Self-assembly process from dissolved BTA towards supramolecular fibers upon cooling with the depiction of a_1 : Complete molecularly dissolved BTA molecules (red dots) in a selective solvent (blue dots) at elevated temperatures (T_1) and a_2 : initiation of hierarchical self-assembly and the creation of supramolecular fibers upon cooling (T_2). **B:** The resulting hierarchical supramolecular fibers (b_1) are composed of b_2 : supramolecular fiber bundles which further consists of b_3 : a columnar arrangement of the single BTA molecules. Source: Macromolecular Chemistry I, University of Bayreuth.

Due to the dependency on concentration and temperature, one can generate a phase diagram for a selected BTA and solvent. The phase diagram of a BTA can be divided into three important regions that are caused by the solubility of the BTA molecules at constant concentration. Such a phase diagram is schematically depicted in Figure 1-15.

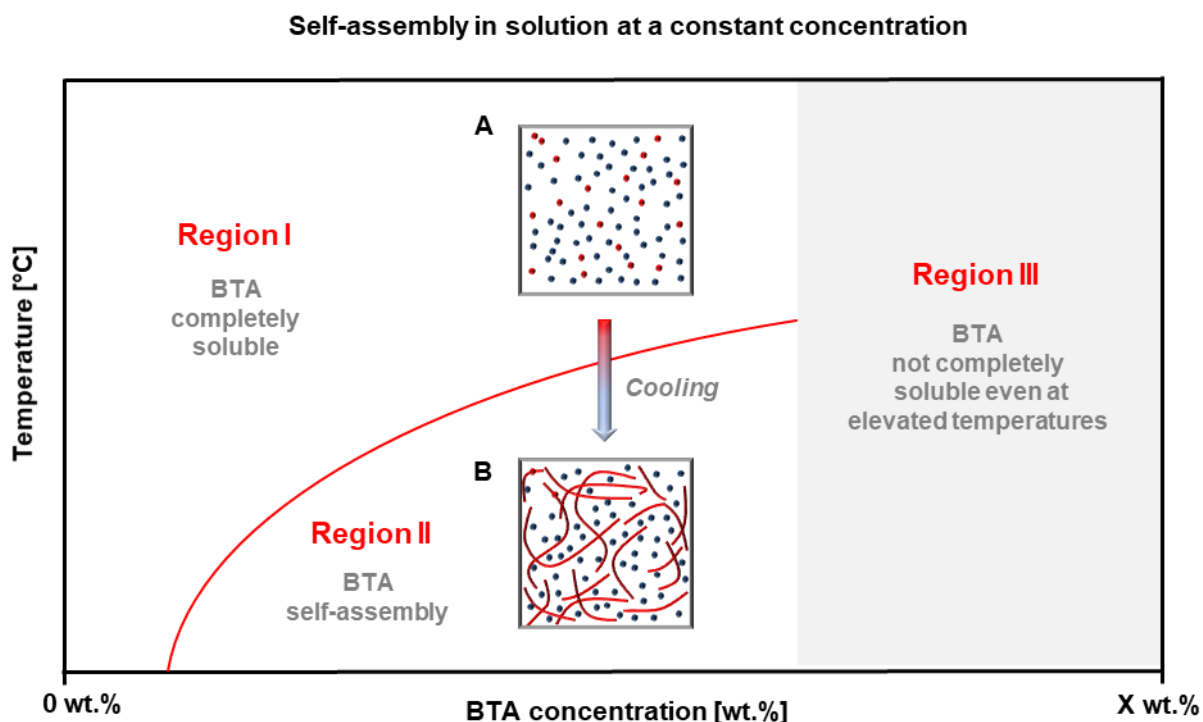


Figure 1-15. **Schematic representation of the self-assembly process of 1,3,5-benzenetrisamides in solution at constant concentration.** Self-assembly in solution at constant concentration with **A**: Complete molecularly dissolved BTA molecules (red dots) in a selective solvent (blue dots) at elevated temperatures and **B**: hierarchical self-assembly and creation of supramolecular fibers upon cooling. The phase diagram exhibit three regions: Region I: BTA completely soluble, Region II: BTA self-assembly and Region III: BTA not completely soluble even at elevated temperatures. The end concentration of X wt.% is a variable depending on the selected BTA/solvent system. Source: Macromolecular Chemistry I, University of Bayreuth.

- Region I: Region I refer to *BTA completely soluble*. The BTA molecules (red dots) are completely dissolved at the molecular level in the solvent (blue dots) and no self-assembly occurs in the region I as depicted in Figure 1-15 A. The relationship between temperature and concentration affecting the solubility is illustrated by the red dotted line. At low concentrations, the BTA remains molecularly dissolved even at room temperature.
- Region II: Region II refer to *BTA self-assembly*. This region represents the right conditions of temperature and concentration to reproducible self-assemble BTA molecules to supramolecular fibers. During the process *the concentration remains constant*. Consequently, self-assembly is only induced through a change in temperature. An example is shown in Figure 1-15 A where the BTA is molecularly dissolved at elevated temperatures at a given concentration thus being in Region I. Subsequent cooling of the molecularly dissolved solution causes a decrease in the BTA solubility, the red line is crossed resulting in supersaturation. At this point, the self-assembly starts and supramolecular aggregates are formed via hydrogen bonding. The resulting suspension of supramolecular fibers in the selective solvent is shown in Figure 1-15 B. Thus, Region II – *BTA self-assembly* can be achieved by crossing the solubility line in the phase diagram.
- Region III: Region III refer to *BTA not completely soluble even at elevated temperatures*. This region is characterized by a higher concentration of BTA molecules and here the BTA is not entirely soluble anymore at elevated temperatures. Self-assembly may occur upon cooling the solution, because not dissolved BTAs are still present in the solution, acting as nuclei and trigger further growth. This results in a mixture of bulk material and supramolecular fibers. Thus, even if self-assembly occurs, the region (grey) is considered as not completely soluble as a whole. This solubility limit is often restricted by the boiling points of the used solvents and depends on the selected BTA.

Self-assembly in solution at constant concentration has been used widely and several groups reported their work on systems that are triggered by solubility changes upon cooling. In the following literature examples of BTA derivatives in pure organic solvents and water are described using the temperature change as trigger.^[37,46,85,95,96] BTA motifs have been extensively studied in organic solvents being able to form also gels consisting of a network of fibrous assemblies.^[64,70,73,84–86,97] Similarly, Kumar et al.^[85] investigated a *BTA derivative bearing L-phenylalanine* as substituent being able to form an organogel in toluene or xylene upon cooling the molecularly dissolved solution from elevated temperatures. The chemical structure of the BTA derivative is depicted in Figure 1-16 A. The morphology of the xerogel from toluene reveals entangled fibers (Figure 1-16 B) with a twisted morphology of the individual fiber bundles (Figure 1-16 C).

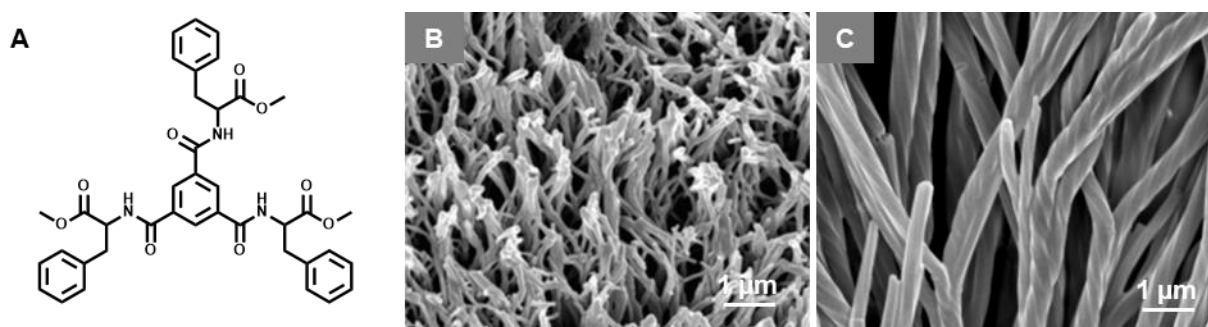


Figure 1-16. **Self-assembly behavior of L-phenylalanine substituted BTA derivative in organic solvents.** **A:** Chemical structure of the L-phenylalanine substituted BTA derivative and **B:** scanning electron microscopy images as xerogel showing entangled fibers and **C:** the twisted morphology of the supramolecular fibers. Figure adapted and reproduced with permission from Ref.^[85] Copyright ©The Royal Society of Chemistry 2021.

For example, Paikar et al.^[70] reported a *BTA derivative containing γ -aminobutyric acid* which self-assembles into an organogel in xylene or toluene due to an entangled supramolecular fiber network after heating, subsequent cooling and ageing the solution at room temperature.

Other groups focus on self-assembly in aqueous media. For example, the group Meijer designed water soluble *BTA derivatives with ethylene glycol motifs in the periphery* that form micrometer sized supramolecular fibrillar aggregates. Minimal changes in molecular structures caused significant changes in the internal packing of the aggregates.^[93] The work of the group of Palmans and a lot of work together with Meijer was published aiming to understand the self-assembly behavior of BTAs in aqueous solution.^[98–102] In general, water-solubility can be achieved by introducing polar sidegroups into the BTA structure with aliphatic chains as

shielding units for the central hydrogen bonding groups. The systematic investigation from Besenius et al.^[48] showed that the larger the hydrophobic spacer between the amide groups and the polar sidegroups, the stronger the aggregation of BTAs in aqueous media. This is caused by a more effective shielding of the amide groups from water molecules. Another example is given by Huang et al.^[92] who investigated *BTA derivative with sulfonic acid* headgroups regarding the formation of structures in water with varying concentrations. They found that with increasing concentration, the molecules assemble first into stable clusters of seven molecules followed by the formation of robust columns and final arrangement into nanofibers. Increasing the concentration further led to microfibers and fiber bundles.

In our group, self-assembly in solution at constant concentration has been investigated for example by Frank et al.^[54,60] Here, a *BTA derivative bearing peripheral tertiary N,N-diethylethylamino substituents* shows water-solubility up to 10 wt.% at room temperature. However, a special self-assembly behavior was observed. Heating the molecularly dissolved solution at room temperature resulted in clouding of the sample and reversible self-assembly into microtubes. Another derivative of this family, namely the *N,N-diisopropylethylamino substituted BTA derivative (iPr-BTA)* shows poor water solubility of 0.01 wt.%, however self-assembly in solution at constant concentration in 2-propanol is observed for various concentrations as depicted in Figure 1-17. Evolution of cloud and clearing points of *iPr-BTA* in 2-propanol reveal three distinct regions as shown in Figure 1-17 A. In region I the *iPr-BTA* remains dissolved at low concentrations within the investigated temperature range. In region II the concentration increases and the *iPr-BTA* forms a gel upon cooling and fully dissolves upon heating. In region III the *iPr-BTA* is not completely soluble anymore at higher concentrations. An example of the shape and dimensions of the self-assembled structures is shown in Figure 1-17 B. The scanning electron microscope micrograph reveals long, uniform supramolecular nanofibers with a diameters of about 320 nm.^[54]

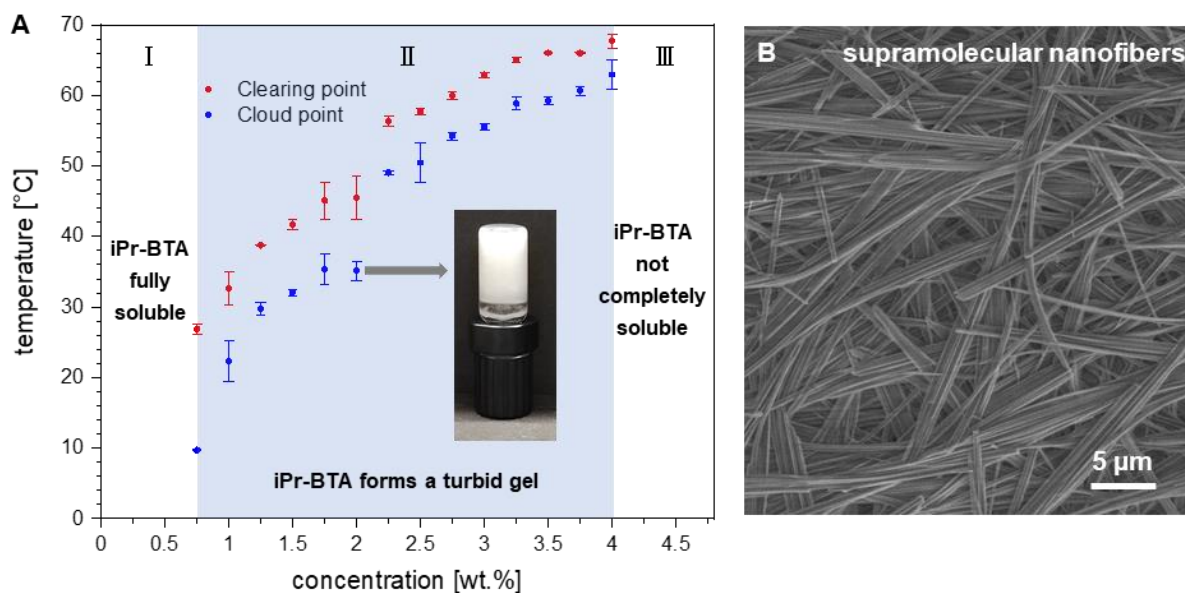


Figure 1-17. **Self-assembly process of *N,N*-diisopropylethylamino substituted BTA derivative (*iPr*-BTA) in solution at constant concentration and corresponding supramolecular structures.** **A:** Evolution of cloud and clearing points of *iPr*-BTA in 2-propanol. Three distinct regions are present. In region I at low concentrations up to 0.75 wt.% the *iPr*-BTA remains dissolved within the investigated temperature range. As the concentration increases the *iPr*-BTA forms a gel upon cooling and fully dissolves upon heating (region II). At very high concentrations the *iPr*-BTA is not completely soluble even at elevated temperatures (region III). **B:** A scanning electron microscope micrograph of a dried gel from a 2.0 wt.% solution of *iPr*-BTA reveals long, uniform supramolecular nanofibers with a diameter of approximately 320 nm for the single fibers. Figure adapted and reproduced with permission from Ref.^[54] Copyright © 2022 The Authors. *Macromolecular Rapid Communications* published by Wiley-VCH GmbH.

b) Self-assembly in solvent mixtures

Despite the BTA derivatives that are able to form nano- or microfibers in single organic solvents, research interest concerns BTA derivatives that self-assemble in solvent mixtures. For example, organic solvents with addition of water with the aim to reduce solubility and allow self-assembly.^[64,73,97,103]

For instance, adding small amounts of the anti-solvent leads to instantaneous gelation and is reported for a *L*-glutamic acid based BTA derivative as shown by Cao et al.^[73] While gelation in pure organic solvents were obtained within 2 h, gelation took place within seconds when certain amount of the anti-solvent (water) is added to an acetone, dimethyl sulfoxide (DMSO) or dimethylformamide (DMF) solution. Tubular structures with a hexagonal cross-section of nano- and micrometer size were revealed by electron microscopy after removing the solvent.

Furthermore, Nagajaran and Pedireddi^[64] prepared *N,N',N''-tris-(4-alkylphenyl)-1,3,5-benzenetricarboxamide derivatives* with varying length of the alkyl chain from methyl to butyl. The gelation ability of these derivatives was investigated in DMSO. Despite the butyl substituted BTA, all derivatives show gelation in DMSO within 96 hours and a fibrous morphology revealed by investigations from the xerogels. The addition of a small amount of water rapidly accelerated the gel formation within seconds.

On the other hand the aqueous solution can be the main part and the organic solvent are co-solvents.^[65,83,90,104] as shown by Palmans et al.^[65] who investigated *BTAs with pyridyl substituents* and their ability to form hydrogels in mixtures of water with MeOH, EtOH, DMSO or DMF upon cooling. Hexagonal hollow shaped microtubes have been reported from a BTA derivative with pyridyl substituents in H₂O-THF solutions. During the self-assembly into microtubes, they observed a gel like state. If the BTA concentration is increased, larger tubes have been observed.^[83]

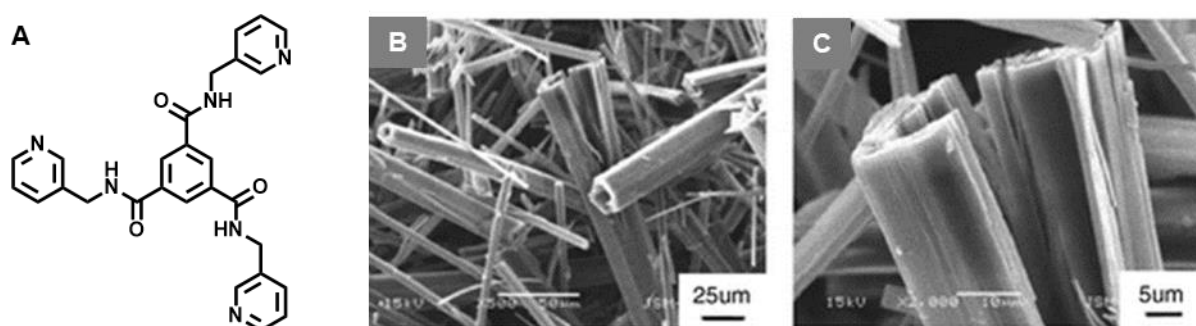


Figure 1-18. **Self-assembly behavior of a pyridyl substituted BTA derivative in a solvent mixture H₂O-THF.** **A:** Chemical structure of the L-phenylalanine substituted BTA derivative and **B** and **C:** scanning electron microscopy images of the hexagonal microtubes obtained in the solvent mixture of H₂O-THF. Figure adapted and reproduced with permission from Ref.^[83] Copyright © The Royal Society of Chemistry and the Centre National de la Recherche Scientifique 2008.

c) Self-assembly during solvent evaporation

Another method of a self-assembly process into fibrous structures involves the self-assembly triggered during solvent evaporation. In this process, the BTA molecules (red dots) need to be molecularly dissolved in the solvent (blue dots) as depicted in Figure 1-19 A. Experimentally this is typically achieved by heating the BTA solution. For lower concentrations the molecularly dissolved state can be achieved without heating. The self-assembly can be induced in two different process routes:

Process route 1: Cooling a molecularly dissolved solution from elevated temperatures to room temperature and subsequent solvent evaporation

The phase diagram of process route 1 is schematically shown in Figure 1-19 with three regions and four states (Figure 1-19 A-D). In region I of the self-assembly phase diagram, namely *BTA completely soluble*, the solution remains molecularly dissolved as depicted in Figure 1-19 A. The subsequent step involves the crossing of the red solubility line in the phase diagram from region I to region II – initiating the *BTA self-assembly*. For this, the solution is dropped onto a substrate at room temperature, allowing the solvent to evaporate. During evaporation of the solvent, the concentration locally increases resulting in a crossing of the solubility line due to supersaturation of the solution and thus initiation of the self-assembly. Coexistence of solvent and fibrous structures can be observed (Figure 1-19 B). Further drying (Figure 1-19 C) resulting in 100 % completely dried supramolecular fibers (Figure 1-19 D). Region III of the self-assembly phase diagram represents the condition namely *BTA not completely soluble even at elevated temperatures*. Upon cooling from this region, the solubilized BTA molecules will self-assemble resulting in a mixture of bulk and self-assembled structures. However, region III is not relevant for this process route as typically lower concentrations are selected.

Self-assembly during solvent evaporation (Process route 1)

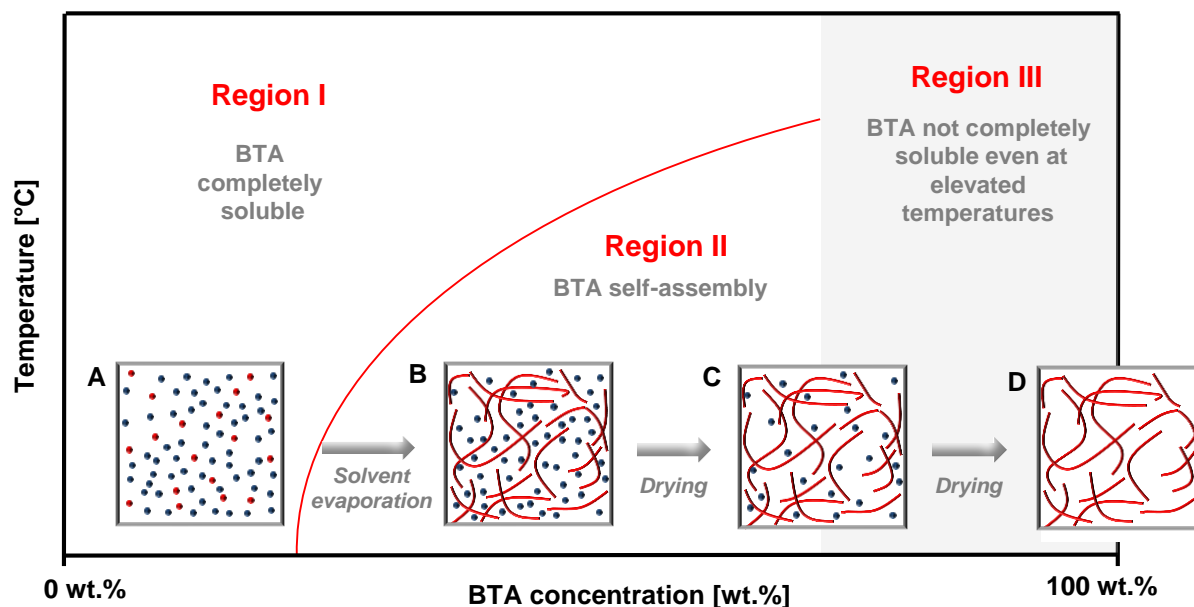


Figure 1-19. **Schematic representation of the self-assembly process of 1,3,5-benzenetrisamides (BTAs) for solvent evaporation.** **A:** Complete molecularly dissolved BTA molecules (red dots) in a selective solvent (blue dots) at room temperature at constant concentration. **B:** Solvent evaporation resulting in a crossing of the red solubility line and subsequent self-assembly. Supramolecular fibers are illustrated in red coexisting with remaining solvent illustrated as blue dots. **C:** Further drying of the solvent. **D:** Complete solvent evaporation results in dried supramolecular fibers. The phase diagram exhibit three regions: Region I: BTA completely soluble, Region II: the BTA self-assembly and Region III: BTA not completely soluble even at elevated temperatures. Source: Macromolecular Chemistry I, University of Bayreuth.

Process route 2: Simultaneous cooling and solvent evaporation of a molecularly dissolved solution from elevated temperatures.

The second process route as depicted in Figure 1-20 begins with the same initial state as process route 1— a molecularly dissolved solution here at an elevated temperature (Figure 1-20 A). Simultaneous cooling and solvent evaporation occur in the next step, causing the crossing of the solubility line from region I to II at higher temperatures than room temperature. This has the advantage that higher BTA concentrations can be achieved and that the evaporation of the solvent is faster. This simultaneous process also leads to a supersaturation in the drying solution and consequently to self-assembly, resulting in fibrous assemblies (Figure 1-20 B) with further drying (Figure 1-20 C) and resulting ultimately in the dried supramolecular fibers (Figure 1-20 D).

Self-assembly during simultaneously cooling and solvent evaporation (process route 2)

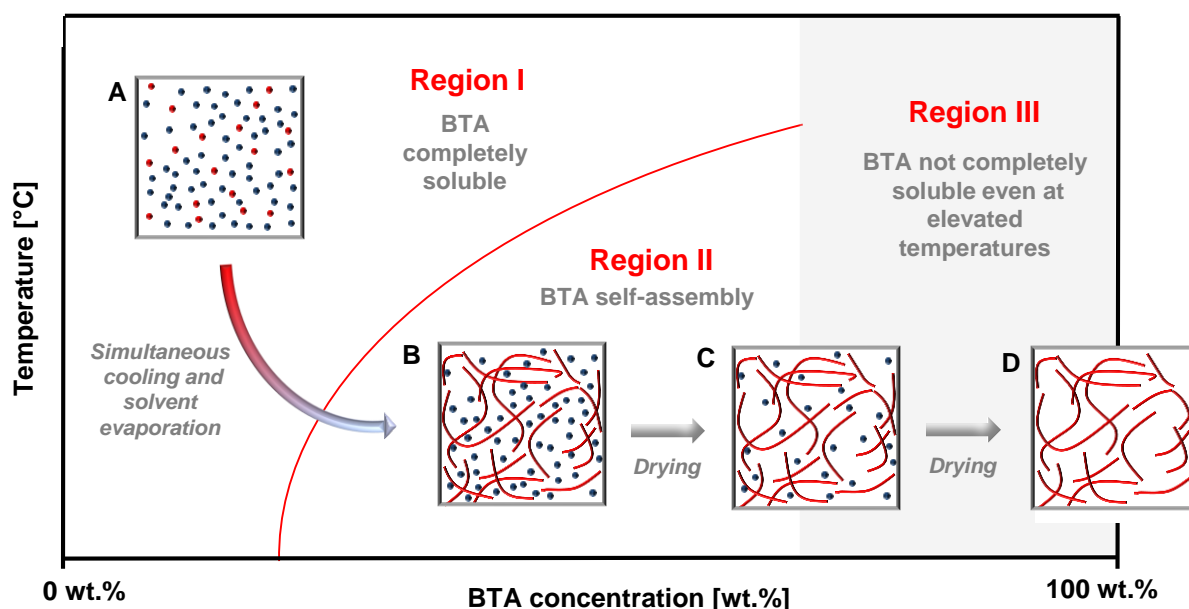


Figure 1-20. **Schematic representation of the self-assembly process of 1,3,5-benzenetrisamides (BTAs) for simultaneous cooling and solvent evaporation.** **A:** Complete molecularly dissolved BTA molecules (red dots) in a selective solvent (blue dots) at elevated temperatures and **B:** Supramolecular fibers (red lines) coexisting with remaining solvent (blue dots) after simultaneous cooling and solvent evaporation. **C:** State after further drying. **D:** Complete solvent evaporation results in dried supramolecular fibers. The phase diagram exhibit three regions: Region I: BTA completely soluble, Region II: the BTA self-assembly and Region III: BTA not completely soluble at elevated temperatures. Source: Macromolecular Chemistry I, University of Bayreuth.

The difference between the first and the second process route lies in the resulting fibers, which are illustrated as the same in the figures, however may differ in their dimensions and shape depending of the used BTA. Both routes can be employed in combination with any substrate or porous system, thus open the way for different outcomes and morphological variations.

Self-assembly upon solvent-evaporation is often used to create self-assembled structures either on simple flat substrates or more advanced porous substrates such as nonwovens. An example for supramolecular structures from solvent evaporation prepared via the first process route is shown in Figure 1-21. The molecular structure of the used *BTA derivative N, N', N''-tris(3-methylpyridyl)-trimesic amide* is depicted in Figure 1-21 A. The supramolecular structures are formed via solvent evaporation from the solvent THF on a glass slide. The self-assembled structures feature a hexagonal hollow fiber morphology as shown in the SEM images in Figure 1-21 B and C.^[83]



Figure 1-21. **Example of supramolecular structures prepared during solvent evaporation.** **A:** Molecular structure of the BTA derivative *N,N',N''*-tris(3-methylpyridyl)-trimesic amide. **B:** Scanning electron microscopy images of the supramolecular structures obtained by self-assembly via solvent evaporation from a drop of the BTA THF solution on a glass slide. **C:** magnification of the self-assembled structure. Figure adapted and reproduced with permission from Ref.^[83] Copyright © The Royal Society of Chemistry and the Centre National de la Recherche Scientifique 2008.

An example of self-assembly via simultaneous cooling and solvent evaporation can be given from our group. Misslitz et al.^[105] investigated for the first time the self-assembly behavior of the *BTA derivative N, N', N''-tris(2-ethylhexyl)-1,3,5-benzenetricarboxamide* in a porous substrate of viscose/polyester nonwoven. The molecular structure of the used BTA is depicted in Figure 1-22 A and the corresponding self-assembled structures prepared from different concentrations in Figure 1-22 B, C and D. Here the simultaneous cooling and solvent evaporation within the nonwoven microfibers results in a nanofiber-microfiber composite.^[105] Using different concentrations of the initial BTA solution prior solvent evaporation led to different density of BTA fibers within the nonwoven demonstrating the importance of concentration and the self-assembly conditions with respect to the final structure.

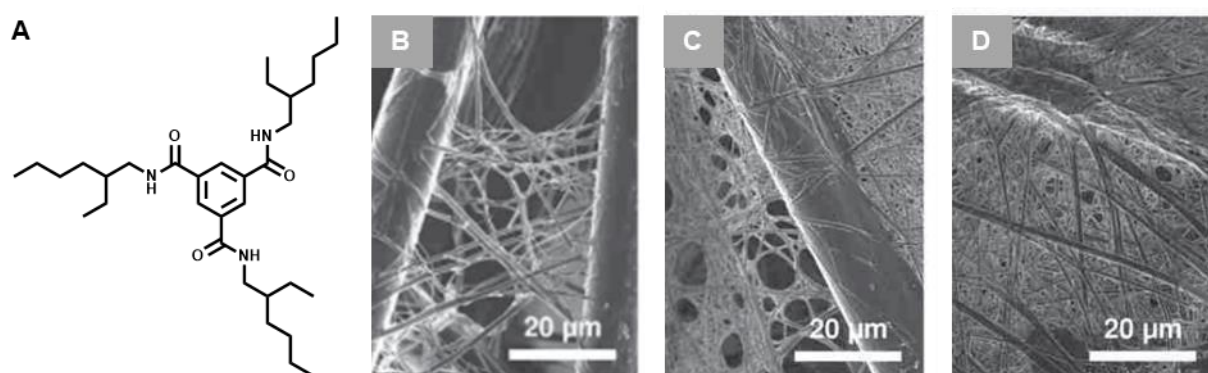


Figure 1-22. **Example of supramolecular structures prepared via solvent evaporation method 2 (simultaneous cooling and solvent evaporation).** **A:** Molecular structure of the BTA derivative *N, N', N''*-tris(2-ethylhexyl)-1,3,5-benzenetricarboxamide. **B-D:** Scanning electron microscopy images of self-assembled BTA fibers within a viscose/polyester nonwoven from solvent evaporation of a **B:** 0.4 wt.%, **C:** 0.6 wt.%, and **D:** 1.0 wt.% 2-butanone solution, respectively. Figure adapted and reproduced with permission from Ref.^[105] Copyright © 2013 Wiley-VCH Verlag GmbH & Co. KGaA, Weinheim.

d) Stimuli responsive self-assembly triggered by pH change

Using the external trigger of pH-change has been used by different groups to achieve supramolecular structures from aqueous solution where a temperature/concentration change is not sufficient to induce self-assembly.^[52,55–58,72] For instance, VandenBerg et al.^[72] present an *BTA with glutamic acid residues* that are sensitive to pH change and form supramolecular structures which vary according to the rate of pH stimulus alteration. The molecular structure of the BTA is depicted in Figure 1-23 A. The initial stage of sample growth triggered by HCl, exhibits a thick and branching fibrillar nanomorphology is shown in Figure 1-23 B. After one hour the sample is composed of a dense network with thick fibrillar bundles (Figure 1-23 C).^[72]

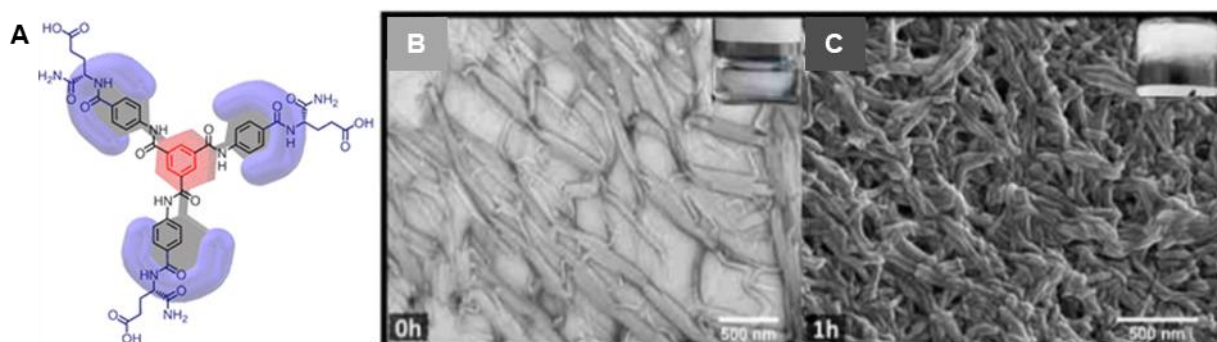


Figure 1-23. **Example of a pH responsive BTA structure and resulting self-assembly.** **A:** Molecular structure of the BTA derivative with glutamic acid residues. **B:** Transmission scanning electron microscopy image from the initial stage of sample growth triggered by HCl, exhibiting a thick and branching fibrillar nanomorphology. **C:** Scanning electron microscopy image after 1 hour depicts a dense network composed of thick fibrillar bundles. Figure adapted and reproduced with permission from Ref.^[72] Copyright © 2020 American Chemical Society.

Ionic self-assembly of *BTAs with sulfonic acid peripheral groups* has been observed by Iwan et al.^[106] Here the resulting structures are supramolecular aggregations in form of spherulite-like or feather-like morphologies.

Other work focused on *BTA derivatives with sodium carboxylate peripheral groups* which exhibits liquid crystalline properties in solution. The ionic BTA derivatives self-assemble into cylinder assemblies in aqueous solutions and by addition of glucono-delta-lactone.^[80,88,107,108]

A similar *BTA derivative N, N', N''-tris(4-carboxyphenylene)-1,3,5-benzenetricarboxamide* has been investigated in our group by Bernet et al.^[52] who used the pH-sensitivity of the molecule to induce self-assembly into a photoluminescent supramolecular hydrogel by addition of the acid glucono-delta-lactone.

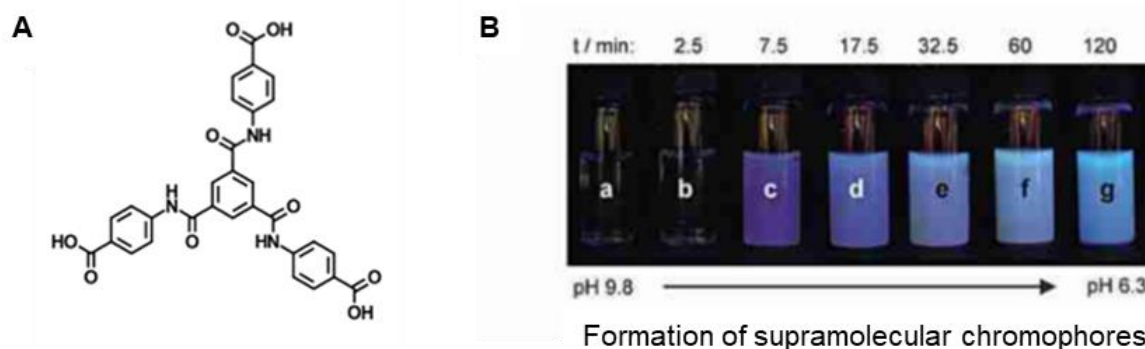


Figure 1-24. **Formation of supramolecular chromophores from BTAs.** **A:** Chemical structure of the BTA derivative *N, N', N''*-tris(4-carboxyphenylene)-1,3,5-benzenetricarboxamide. **B:** Photographs of the hydrogel samples of aqueous BTA solution with a) before and b) to g) after addition of glucono- δ -lactone. Figure adapted and reproduced with permission from Ref. [52] Copyright © The Royal Society of Chemistry 2012.

In a collaboration work with Helfricht et al.^[56] from the physical department the feature of reversibility of the supramolecular hydrogel is used to pattern the specific BTA. Once the film is formed, it can be locally dissolved under alkaline conditions. By a combination of atomic force microscopy (AFM) and nanofluidics – so called FluidFM, “chemical writing” into the hydrogel is achieved by dissolving the supramolecular structures. In detail, the BTA hydrogel can be locally dissolved when an alkaline solution is ejected through the aperture of a hollow AFM-cantilever which is connected to a nanofluidic controller. The chemical writing and the resulting writing lines are depicted in Figure 1-25.

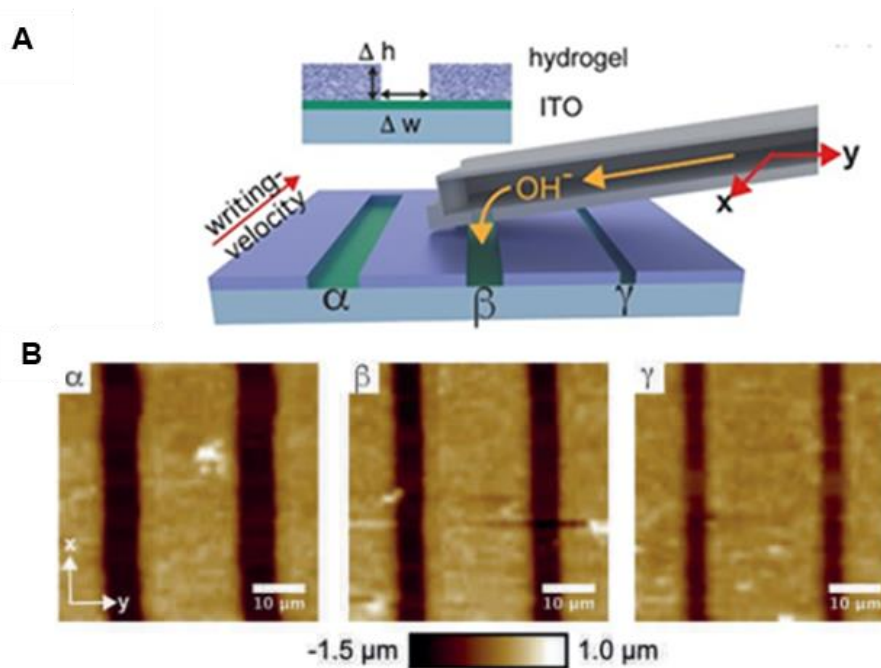


Figure 1-25. **Chemical writing into BTA hydrogel films.** **A:** Schematic illustration of the chemical writing with the FluidFM by selectively dissolving BTA films. **B:** Resulting line patterns after the chemical writing into the BTA hydrogel. Figure adapted and reproduced with permission from Ref. [56] Copyright © 2017 Wiley-VCH Verlag GmbH & Co. KGaA, Weinheim

The formation of the hydrogel was then further intensively studied by Raßmann et al.^[57] For this an *in-situ* nano-indentation technique was developed that was integrated in an electrochemistry AFM fluid cell and allowed for the deposition of the BTA hydrogel on a conductive layer within seconds. The film thickness is a function of the BTA concentration, the applied potential and the gelation time. The BTA film formation is illustrated in Figure 1-26. The process, also referred to as electrogelation, relies on a localized change in pH resulting from the electrolysis of water at the electrode. The protonation of the BTA sodium salt depicted in Figure 1-26 A induces the self-assembly into supramolecular fibrous hydrogel. Figure 1-26 B illustrates the self-assembly of the BTA into a hydrogel induced by local acidification in the vicinity of the working electrode in a three-electrode electrochemical setup. The local decrease in pH results from proton generation by the oxygen evolution reaction at the working electrode.^[57]

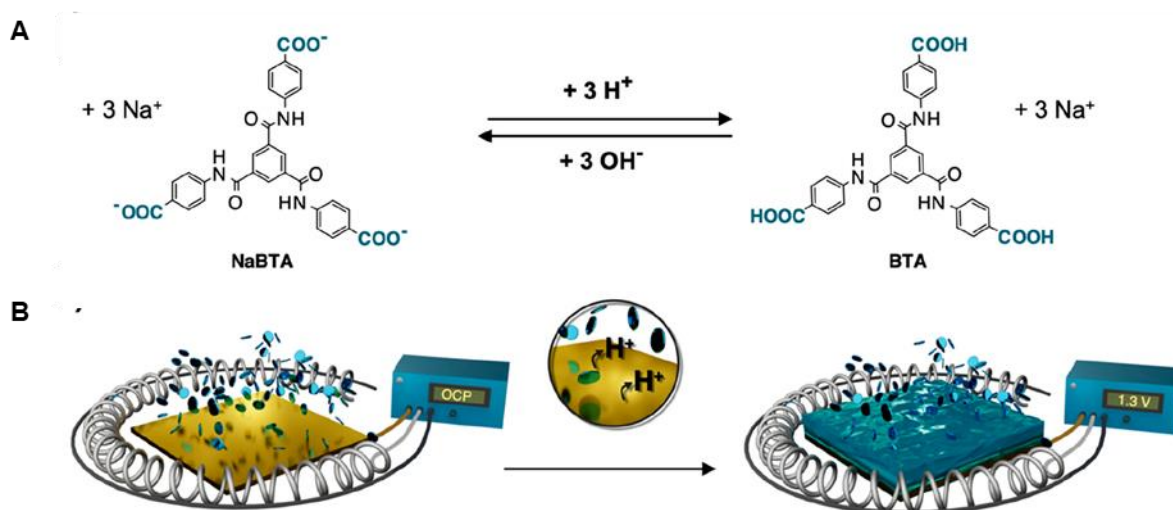


Figure 1-26. **Electrogelation process of the BTA derivative *N, N', N''*-tris(4-carboxyphenylene)-1,3,5-benzenetricarboxamide into a fibrous hydrogel.** **A:** The three carboxyl groups of the soluble trisodium salt of the BTA derivative (NaBTA) undergo protonation under acidic conditions. The protonated BTA molecules assemble into a fibrous hydrogel. The assembly process can be reversed by shifting the pH back to the alkaline regime. **B:** The assembly of the BTA into a hydrogel can be induced by local acidification in the vicinity of the working electrode in a three-electrode electrochemical setup. The local decrease in pH results from proton generation by the oxygen evolution reaction at the working electrode. Figure adapted and reproduced with permission from Ref.^[57] Copyright © 2023, American Chemical Society.

1.5 Hierarchical superstructures with supramolecular fibers

In the literature, the term "superstructure" has been applied to a variety of morphologies, leading to its use for any supramolecular structures that exhibit hierarchical morphology. This includes copolymer micelles^[109] that form a multitude of hierarchical superstructures depending on their polymer composition, self-assembly of small organic molecules into micro- and nanohierarchical,^[110] fibrous^[111] or tubular^[112] superstructures. In the following *hierarchical superstructures* refer to a combination of two systems: top-down and bottom-up.

One example for hierarchical superstructures is the collaboration work of Burgard et al.^[113] where they fabricated mesostructured nonwovens and studied the nonwovens in the context of filtration. They achieve a penguin downy feather-like morphology by combining electrospinning and self-assembly resulting in electrospun fibers with off-standing supramolecular nanostructures. The process involves coaxial electrospinning of a polystyrene and BTA *N,N,N''-tris(1-(methoxymethyl)propyl)benzene-1,3,5-tricarboxamide* solution as schematically show in Figure 1-27 A resulting in electrospun polystyrene fibers with BTA seeds (B). Combination of the electrospun polystyrene fibers with a the BTA solution and subsequent solvent evaporation leads to seeded growth of the BTAs and off-standing supramolecular fibers.

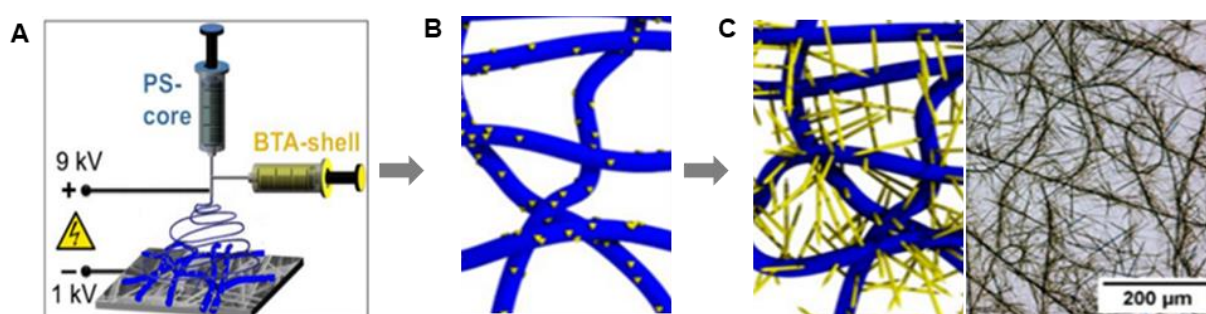


Figure 1-27. **Illustration of the fabrication process for mesostructured nonwoven with penguin downy feather-like morphology.** **A:** the coaxial electrospinning of a polystyrene solution (PS) and a BTA solution. **B:** The resulting polystyrene nonwoven (blue) featuring BTA seeds (yellow dots) on the surface. **C:** Mesostructured nonwoven after an BTA immersion process and subsequent seeded growth into fibers (yellow) - left image. Corresponding optical microscopy of the mesostructured nonwoven fibers with seeded BTA fibers grown from the PS fibers surface - right image. Figure adapted and reproduced with permission from Ref.^[113] Copyright © 2019 WILEY-VCH Verlag GmbH & Co. KGaA, Weinheim.

Coaxial electrospinning and seeded self-assembly has been also used in our group by Frank et al.^[114] to fabricate well-defined hierarchical fir-tree-like superstructures. Here, polymer fibers are decorated with patchy micelles via coaxial electrospinning of a micellar dispersion composed of patchy polystyrene-*block*-polyethylene-*block*-poly(*N,N*-dimethylaminoethyl methacryl-amide) (SEDMA) worm-like crystalline-core micelles and a polystyrene solution resulting in patchy SEDMA fibers as shown in Figure 1-28 A. The patchy SEDMA fibers are located on aluminum foil. After immersion of the patchy SEDMA fibers into an aqueous *N¹,N³,N⁵-tris[2-(dimethylamino)ethyl]-1,3,5-benzenetricarboxamide* solution and subsequent solvent evaporation hierarchical superstructures are created as depicted in B and C. Here, the patchy micelles are used to induce the molecular self-assembly of the BTA. For this, a chemical match of the functional groups in the micelle patches and the peripheral groups of the BTA is crucial. The seeded self-assembly of the BTA is a result of accessibility of the patch for the BTA and a local increase of BTA concentration at the corresponding patch.

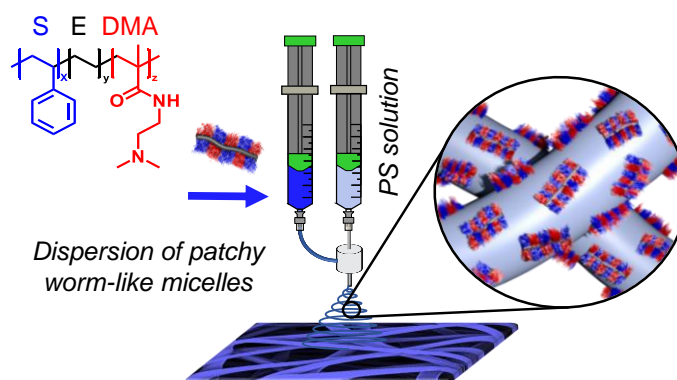
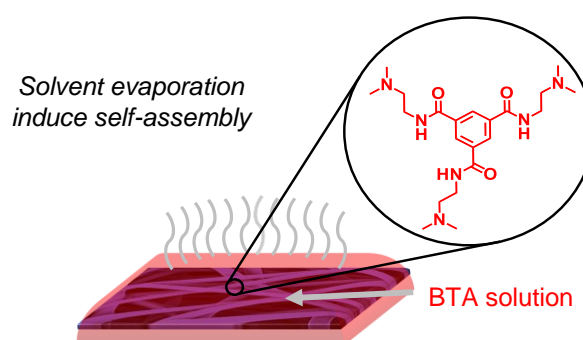
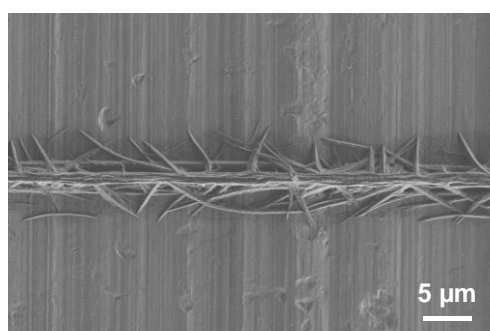
A: Preparation of patchy PS_{core} / SEDMA fibres via coaxial electrospinning**B: BTA self-assembly onto patchy PS_{core} / SEDMA fibres****C: Resulting hierarchical fir tree-like superstructures**

Figure 1-28. Formation of hierarchical superstructures by combining patchy electrospun fibers and self-assembly of BTAs. **A:** Schematic representation of the coaxial electrospinning process of a polystyrene (PS) solution and a dispersion of patchy worm-like polystyrene-block-polyethylene-block-poly(*N,N*-dimethylaminoethyl methacrylamide) (SEDMA) triblock terpolymer micelles to prepare patchy fibers. **B:** Immersion of the patchy fibers into an aqueous *N*¹,*N*³,*N*⁵-tris[2-(dimethylamino)ethyl]-1,3,5-benzenetricarboxamide solution. Seeded self-assembly of the BTA onto the patchy fibers occurs upon solvent evaporation. **C:** Scanning electron microscopy image of the final hierarchical superstructures after complete solvent evaporation. Figure adapted and reproduced with permission from Ref.^[114] Copyright © 2021 The Authors. *Angewandte Chemie International Edition* published by Wiley-VCH GmbH.

As the patchy micelles are predestined to induce the seeded self-assembly of BTAs if chemical matching groups of the patchy micelle and the BTA are chosen, this approach is further used for a BTA and patchy micelle with chemical matching *N,N*-diisopropylaminoethyl substituents (see Figure 1-29 A).^[54] A nonwoven is fabricated with the corresponding patchy micelles which is then combined with a chemical matching BTA solution. Subsequent solvent evaporation results in hierarchically mesostructured nonwoven. The functional BTA fibers in this hierarchically mesostructured nonwoven contribute to an increased active surface area, enabling effective immobilization of metal nanoparticles as shown in Figure 1-29 B.

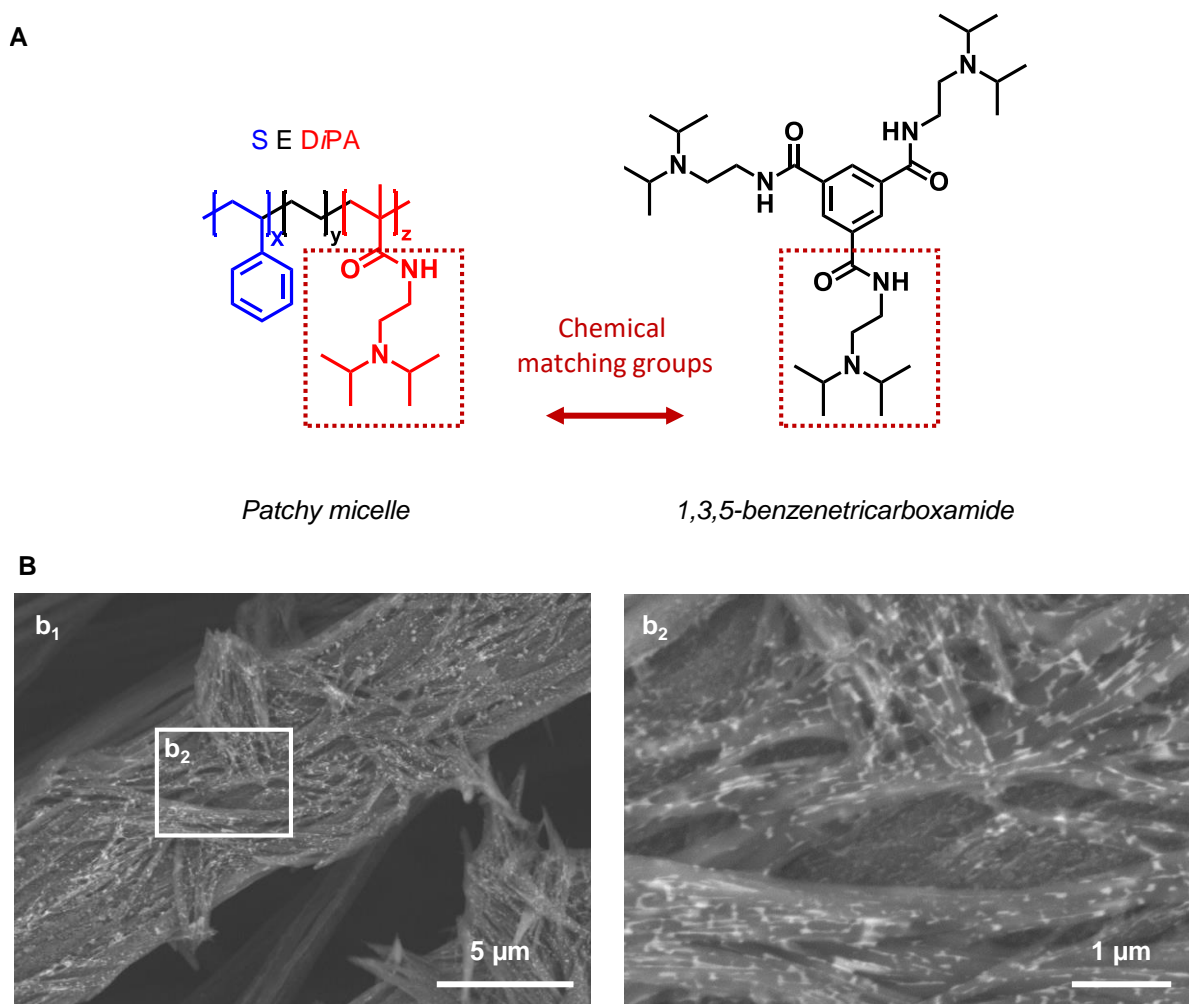


Figure 1-29. **Functional mesostructured nonwovens.** **A:** Chemical structures of the SEDiPA patchy micelles and chemical matching BTA featuring *N,N*-diisopropylaminoethyl substituents (red dotted box). **B:** Scanning electron microscopy images of hierarchically mesostructured nonwovens with immobilized palladium nanoparticles (PdNPs). The mesostructured nonwovens were prepared by immersion of patchy nonwovens into BTA solutions of 0.50 wt.% in 2-propanol and subsequent drying at ambient conditions. PdNPs were immobilized by immersion of the mesostructured nonwovens into aqueous PdNP dispersions for 3 h at room temperature and subsequent drying at ambient conditions. Figure adapted and reproduced with permission from Ref.^[54] Copyright © 2022 The Authors. Macromolecular Rapid Communications published by Wiley-VCH GmbH.

2 Motivation of the thesis

Supramolecular chemistry known as “chemistry beyond the molecule” enables the preparation of objects with tailored dimensions and shapes and thus unique properties and functions. Specifically, 1,3,5-benzenetrisamides (BTAs) represent a thoroughly investigated class of materials known to form supramolecular (nano)fibers guided by three strands of directed hydrogen bonds. These directed hydrogen bonds results in a highly organized columnar arrangement of the molecular building blocks featuring a macrodipole along the columns. Depending on the self-assembly conditions and macrodipole interactions between the columns, the self-assembly process enables the realization of various anisotropic morphologies with different hierarchical levels, shapes and dimensions. This thesis aims for the preparation of highly ordered and anisotropic (micro)fibers from BTAs with control over shape and dimensions such as diameter and length and their morphology necessary for specific applications. The thesis comprises four parts as illustrated in Figure 2-1. Their individual motivations are described in the following:

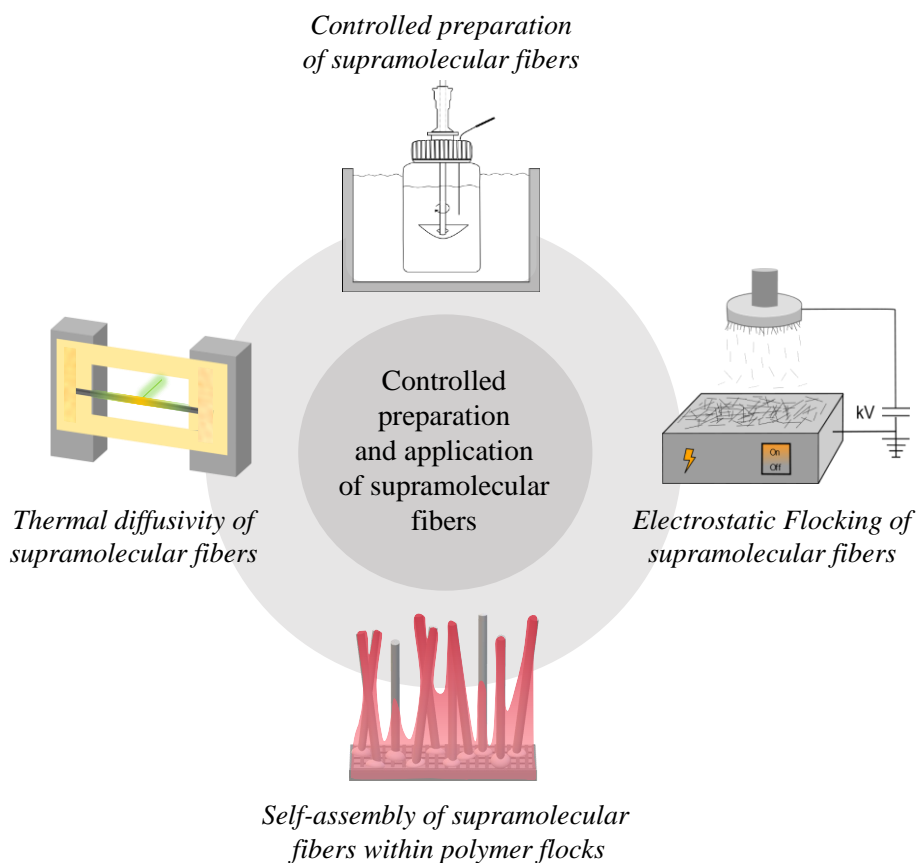


Figure 2-1. **Graphical overview of the four parts of the thesis covering the controlled preparation and application of supramolecular (micro)fibers.** Development of a controlled preparation process of supramolecular fibers with tailored shape and dimensions. First time electrostatic flocking of supramolecular fibers with defined dimensions. Novel site-specific self-assembly process using BTA solutions within polymer flocks. First time measurements of thermal diffusivity in supramolecular fibers.

I. **Controlled preparation of supramolecular fibers**

The first part of the thesis aims for the controlled preparation of supramolecular BTA microfibers on the liter-scale upon cooling. This requires the development of a custom-made set-up for the self-assembly process that enables the identification and precise control of the relevant processing parameters for supramolecular fibers with dimensions in the micrometer range in a reproducible manner. Due to the unique processing window of each BTA, determined by factors such as molecular structure, solvent, concentration and temperature, a comprehensive investigation of each parameter is essential for achieving control over the shape and dimensions. Beyond the previous work in our group from D. Weiss^[94] an advanced custom-made experimental set-up will be built and optimized with a focus on adjustable linear and non-linear cooling rates and constant stirring to analyze the influencing parameter individually. Three different BTAs will be selected for this study and the processing parameters during the self-assembly process to supramolecular fibers will be systematically varied including cooling rates, stirring rates and concentrations. The dimensions of the supramolecular fibers will mainly be characterized and analyzed by scanning electron microscopy to evaluate and optimize the impact of each parameter on the resulting BTA fibers dimensions. Control over the BTA dimensions are a prerequisite for electrostatic flocking, which will be part in the following.

II. **Electrostatic flocking of supramolecular fibers**

Based on the findings from the first part, the objective of the second part is to achieve electrostatic flocking using supramolecular fibers for the first time. Electrostatic flocking is an industrial technique that align short cut polymer fibers in an electric field ultimately promoting their perpendicular arrangement for various applications. Importantly, successful flock preparation requires rigid fibers with defined dimensions and aspect ratios. However, precisely controlling the dimensions, in particular the length, of supramolecular fibers in the micrometer range is a challenging task. Thus, a critical aspect to prepare well-defined flocks with high fiber density is to use rigid BTA fibers with well-defined dimensions, including uniform diameter and length. For this, supramolecular fibers with suitable morphology, from the previous chapter will be used. Special focus will be given on achieving defined fiber lengths with narrow distributions by implementing a novel non-destructive sieving process. Another challenge is related to their post-isolation handling and processing parameters for electrostatic flocking. This includes for example their free-flowing properties that facilitates transport of single fibers along the electric field. The addition of conductive additives will be also considered to create optimized, densely packed flocks with highly aligned supramolecular BTA fibers.

III. Self-assembly of supramolecular fibers within polymer flocks

Differently to the electrostatic flocking of supramolecular fibers, this part of the thesis deals with substrates comprising vertically aligned polymer flocks and how BTA solutions self-assemble within these flocks. Previous studies have demonstrated that the shape and dimensions of self-assembled BTA fibers on various fibrous substrates can be tuned by using prior deposited nuclei and seeds. However, the supramolecular fibers typically form randomly along the polymer fibers, depending on the seeds' locations.^[54,113,114] Therefore, the primary objective here is to explore how capillary forces within aligned polymer flocks act as structure-directing substrate by driving the transport of the solution to the top of the flock. Together with a distinct solvent evaporation profile from the polymer flocks top, this leads to a concentration gradient and potentially to a site-selective self-assembly process of BTAs resulting in novel supramolecular fiber morphologies. To address all these questions, this part of the thesis deals with a thoroughly investigation of the self-assembly behavior of BTAs within polymer flocks. In particular numerous parameters such as, the choice of *i*) the flocking material and *ii*) the BTA together with *iii*) the application technique, *iv*) the solvent properties, *v*) the BTA concentration and *vi*) the drying method have to be considered. Evaluating the data by various microscopy techniques should provide a better understanding how these various conditions control and direct the self-assembly process. This research was performed in a joint collaboration with Felix Bretschneider (Macromolecular Chemistry II, Prof. Dr. Greiner).

IV. Thermal diffusivity of supramolecular fibers

The final part of this thesis aims at the preparation of highly ordered, columnar and anisotropic BTA microfibers, which shall be used to investigate the time-dependence of the temperature distribution in supramolecular fibers, i.e., thermal diffusivity for the first time. The thermal diffusivity will be determined with the lock-in thermography method, which requires high aspect ratio BTA fibers with suitable diameters in the μm -range and length in the cm-range. Thus, a main target of this part is the elaboration of a suitable self-assembly method that can consistently produce supramolecular fibers with these large dimensions for BTAs, while the order and columnar arrangement will be maintained to a very high degree. Since it is unclear how thermal diffusivity is related to the hydrogen packing and order, several BTAs with distinct structural variations will be selected, processed to supramolecular microfibers and their impact within the BTAs on their thermal diffusivity will be analyzed. This research was carried out in collaboration with Ina Klein (Physical Chemistry I, Prof. Dr. Retsch).

3 Controlled preparation of supramolecular fibers

3.1 Background to self-assembly under controlled conditions

Controlled self-assembly in solution at a constant concentration to produce well-defined BTA fibers is of great interest as it allows to tailor the fiber morphology including shape and dimensions, e.g. diameter and length. An example to address the controlled self-assembly was given by D. Weiss et al.^[90] in which they investigated the influence of the stirring rate in a custom-made experimental set-up for a solution-based self-assembly process as summarized in Figure 3-1. The custom-made experimental set-up includes a 250 mL screw-mountable glass bottle as vessel with a modified cap for the insertion of the mechanical stirrer and a thermocouple. The investigated BTA alkoxy substituents in the periphery is shown in Figure 3-1 A. The vessel with the BTA solution was then heated in a water bath to 70 °C until the BTA was completely dissolved. After that, it was directly transferred into a cryostat with a fixed temperature which was set between -5 °C to 25 °C to achieve different non-linear cooling profiles. Furthermore, the stirring rates were varied from 0 rpm to maximum 450 rpm (Figure 3-1 B). It was shown that the diameter of the alkoxy-substituted BTA in a water/2-propanol (80/20) mixture can be tuned by the stirring rate. The higher the stirring rate, the thinner the BTA fibers, which is also exhibit an increasingly smaller distribution of the fiber diameter. Without stirring the solution during the cooling process led to a broad distribution of the fiber diameter with a mean fiber diameter of 1459 nm as shown in the histogram depicted in (Figure 3-1 C). In contrast, applying a stirring rate of 300 rpm eventually led to the narrowest distribution with a mean fiber diameter of 344 nm (Figure 3-1 D). Keeping the stirring rate constant at 300 rpm but varying the temperature of the cooling bath to 25 °C, 15 °C and 5 °C leads to thinner BTA fibers and narrower fiber diameter distribution, respectively. Nonetheless, due to the non-linear nature of the cooling rates, the solvent experiences an initially rapid cooling, reaching room temperature within the first 5 minutes, especially when at high stirring rates. The subsequent 20 minutes of stirring contribute to a gradual attainment of the set temperature of 5 °C. However, there is no information provided regarding the temperature at which the self-assembly initiates in the given solvent mixture. While the cooling rates are reproducible with the set temperatures, the initial rapid cooling coupled with the fast stirring rate may impact the fiber morphology. Consequently, the consideration of both parameters cannot be observed individually with this type of set-up.

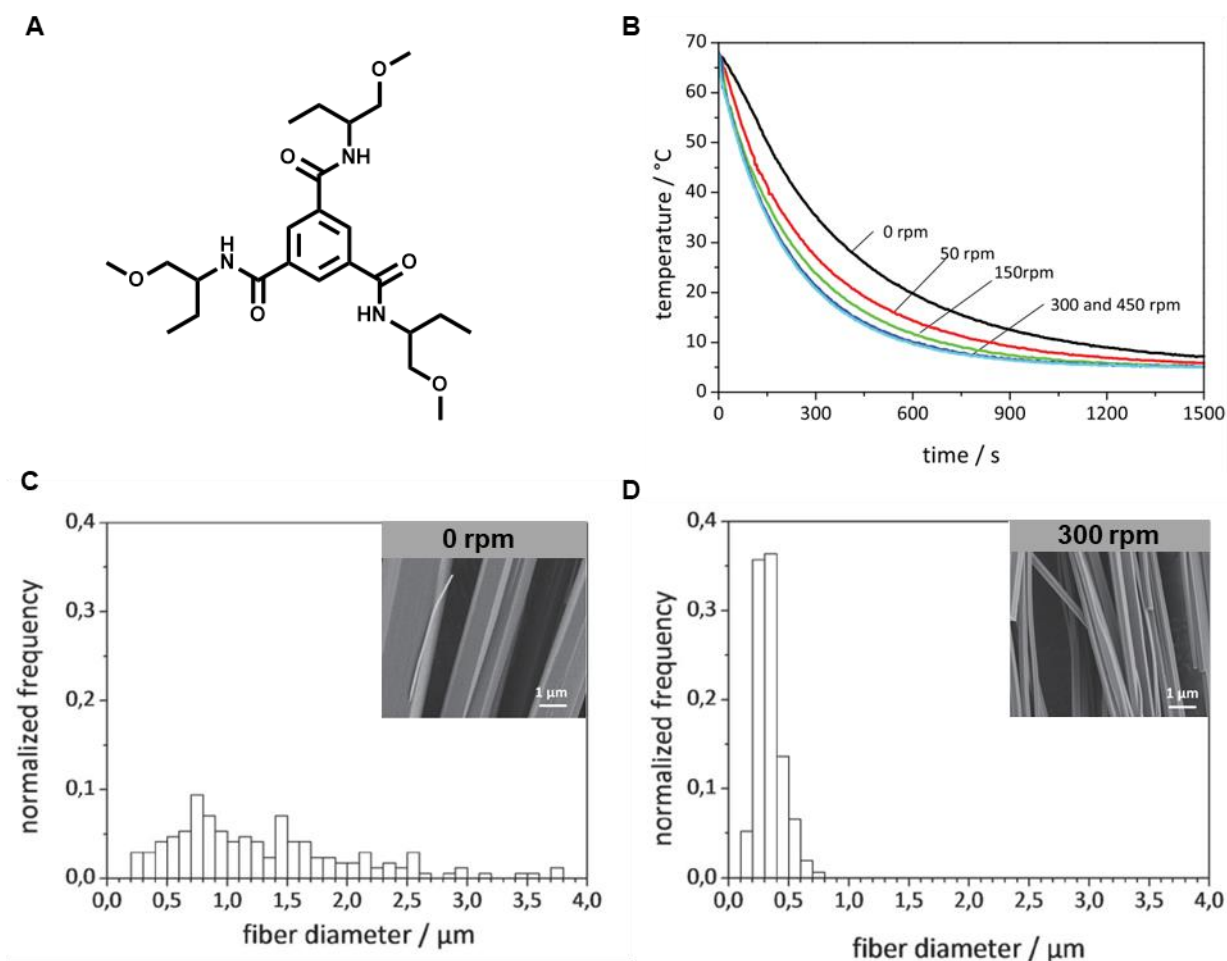


Figure 3-1. **Results from the thermally induced self-assembly under controlled conditions by Weiss et al.^[90]** **A:** Chemical structure of the BTA. **B:** Tailored cooling profiles by applying different stirring rates of 0 rpm, 50 rpm, 150 rpm, 300 rpm and 400 rpm. **C and D:** Resulting BTA fiber diameter histograms in dependence of the stirring rate of 0 rpm (C) and 300 rpm and (D). Figure adapted and reproduced with permission from Ref.^[90] Copyright © 2016 WILEY-VCH Verlag GmbH & Co. KGaA, Weinheim

Furthermore, Steinlein et al.^[91] have shown that the aspect ratio of a selected BTA can be controlled by ultrasonication. In this work, the BTA derivative 1,3,5-tris(2,2-dimethylpropionylamino) benzene has been used which forms rigid supramolecular submicron fibers from the solvent Marlotherm[®] SH, a mixture of dibenzyltoluene isomers. Supramolecular fibers prior the sonification process exhibit fiber length of $150 \pm 57 \mu\text{m}$ and diameter of $0.59 \pm 0.41 \mu\text{m}$. Utilizing a sonification protocol allows for the reduction and control of fiber length. With increased sonification time, the BTA fibers become shorter, reaching an average length of $0.14 \mu\text{m}$. The aspect ratio is also diminished, decreasing from 10.3 after 1 minute of sonification to 2.4 after 90 minutes. The sonification process acts as a cutting mechanism and influences the overall fiber morphology, particularly the homogeneity of fibers, as it produces very small BTA fragments that adhere to existing larger fibers.

Approach in this thesis for the controlled preparation of supramolecular fibers

Supramolecular fibers exhibit unique properties, which differ significantly from those of the individual supramolecular building blocks and thus being interesting for a multitude of applications. However, tailoring the dimensions such as length and diameter and ultimately the aspect ratio of self-assembled fibers is challenging. Achieving control over the diameter and length distribution of BTA fibers requires the consideration of the set of conditions such as the molecular design and the chosen processing parameters including the solvent, concentration, stirring and cooling rate. With this, supramolecular fibers can be produced on large-scale in an efficient manner. In contrast to the described method of Weiss et al.,^[94] the custom-made experimental set-up will be optimized with a focus on adjustable linear cooling rates and at a constant stirring rate to analyze the influencing parameter individually.

Prior to the preparation of supramolecular fibers under controlled conditions, the temperature-dependent self-assembly and disassembly behavior is explored. For this, selected BTAs are investigated using the crystallization system Crystal16® device, which allows the simultaneous observation of multiple samples with respect to the solubility and self-assembly behavior in solution in small scale (1 mL). The findings are then transferred to the optimized custom-made experimental set-up with larger scale of 1 L with the aim to achieve control over the dimensions of the supramolecular fibers in a reproducible manner by adjusting the critical self-assembly conditions.

The detailed description of the approaches in this thesis to comprehensively investigate the controlled preparation of BTA fibers are summarized in the following:

- i)* Selecting suitable BTAs with different molecular designs and self-assembly behavior in polar organic solvents to prepare supramolecular fibers with varying dimensions. Here it is aimed to validate the general applicability of this approach across different BTA/solvent systems.
- ii)* Solubility studies of the selected BTAs at a constant concentration in crystallization system Crystal16® device. Based on these results, the findings of solubility and self-assembly behavior are transferred to the experimental set-up.

- iii) Development and optimization of the experimental set-up to conduct self-assembly in solution at constant concentration with linear temperature profiles and constant stirring.
- iv) Extensive investigation of the processing parameter such as the temperature profile, the stirring rate and concentration of one selected BTA regarding the influence on the dimensions, e.g. diameter and length distribution of the resulting BTA fibers.
- v) Implementation of the findings from the optimized self-assembly conditions onto two other BTA systems and validation of the experimental set-up across the different BTA/solvent systems.

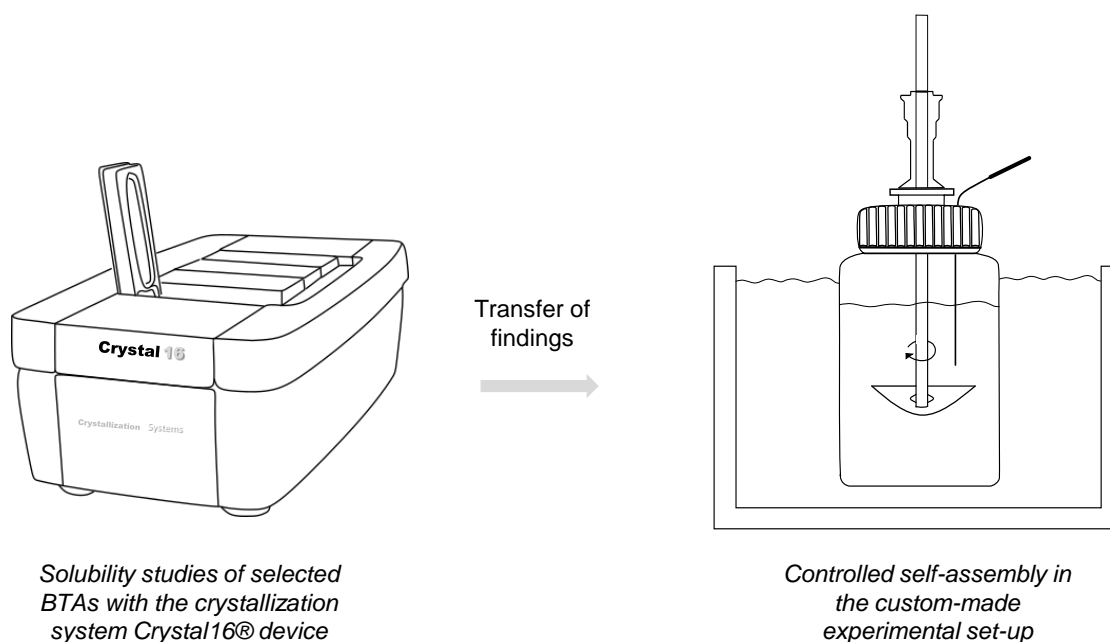


Figure 3-2. **Schematic illustration of the two main parts in this chapter of controlled preparation of supramolecular fibers.** Findings of solubility studies of selected BTAs with crystallization system Crystall16® device are transferred to the controlled self-assembly in the custom-made experimental set-up.

3.2 Controlled preparation of supramolecular fibers

3.2.1 Selection of 1,3,5-benzenetrisamides

For the study of controlled self-assembly in solution at constant concentration, suitable BTAs need to be selected that show variety in their molecular design as well as in their self-assembly behavior. As previously stated, the formation of fibers through self-assembly is significantly influenced by the molecular design of the BTA and the selected processing parameters, such as solvent and concentration. Rigid supramolecular fibers are typically achieved when employing BTAs with short or aliphatic moieties that lack heteroatoms. In contrast to that, BTAs with heteroatoms in their periphery or longer aliphatic peripheral side chains typically self-assemble into more flexible and long aggregates.^[39] Based on 7 different BTAs differing in their peripheral groups (functionalized and non-functionalized), pre-experiments resulted in the final selection of three BTAs exhibiting a variety in their chemical structures and self-assembly behavior in polar organic solvents. The three selected BTAs are depicted in Figure 3-3. The BTA-1 (A) features a cyclohexyl periphery and self-assembles into rigid and thick fibers whereas the BTA-2 (B) with a 2,4,4-trimethylpentan-2-yl periphery shows self-assembly into long, thin fibers (gel-like). The third BTA-3 has a methionine methyl ester periphery and complete the material selection with self-assembly behavior into short, thin fibers.

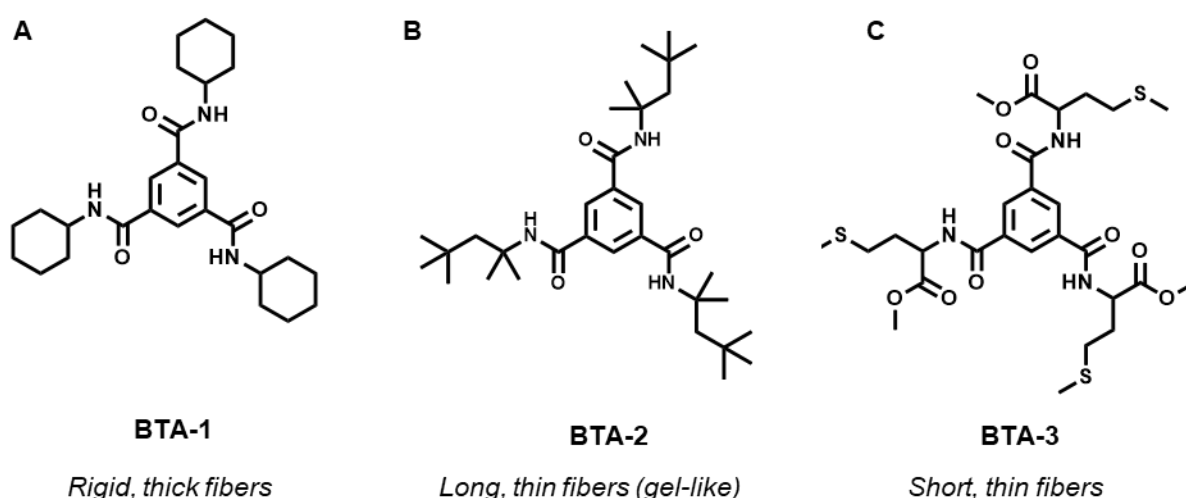


Figure 3-3. **Chemical structure of selected BTAs as suitable candidates for self-assembly in solution at constant concentration.** **A:** BTA featuring cyclohexyl periphery self-assembles into rigid, thick fibers. **B:** BTA featuring a 2,4,4-trimethylpentan-2-yl periphery self-assembles into long, thin fibers (gel-like). **C:** BTA featuring methionine methyl ester periphery self-assembles into short, thin fibers. All molecular building blocks can be self-assembled from polar organic solvents using appropriate conditions.

3.2.2 Self-assembly experiments with BTA 1

BTA-1 is selected for detailed investigation in the subsequent chapters to screen parameters for the self-assembly process. The gained knowledge is then transferred and implemented for BTA-2 and BTA-3 in the section *Implementation of controlled self-assembly on other BTAs*.

At first, investigations in view of the solubility of BTA-1 in different solvents are done to elaborate the optimal solvent for the self-assembly in solution. For this purpose, temperature-dependent turbidity measurements were performed with the crystallization system Crystal16® device to determine the cloud and clearing points by means of transmittance revealing the self-assembled or solution state, respectively. The change in transmittance upon cooling from 100 % to 0 % is defined as cloud point and indicates the presence of turbid solutions due to the self-assembly of BTAs. In contrast, the change in transmittance upon heating from 0 % to 100 % is defined as clearing point since dissolution results in a clear solution. Here, cloud and clearing points were determined at 50 % of transmittance upon heating or cooling. Table 3-1 summarizes the solubility tests of BTA-1 in selected solvents that qualify for the use in the controlled experimental set-up. For example, the BTA-1 was tested with respect to the solubility at room temperature and at the boiling points of the used solvents. It was found that BTA-1 shows no solubility in water and toluene at room temperature and no change was observed upon heating. In the solvent methanol, ethanol, MEK and 2-propanol, BTA-1 exhibits also no solubility at room temperature, but it is completely dissolved when heated close to the boiling points of the solvents. In THF and 1-butanol BTA-1 shows already good solubility at room temperature. Furthermore, the minimal concentration to start the self-assembly (first turbidity detected) and the maximal concentration soluble was determined (upper concentration limit). The BTA-1 exhibits the best solubility in 1-butanol with an upper solubility limit of 1.8 wt.% at 80 °C showing complete dissolution. Concentrations > 1.8 wt.% were not soluble anymore and the self-assembly upon cooling was not investigated for higher concentrations. The lowest concentration which still shows self-assembly upon cooling water determined with 0.80 wt.%. Thus, the self-assembly region for 1-butanol upon cooling start at concentrations of 0.80 wt.% and ends at the solubility limit at 1.8 wt.%. In THF the solubility limit is reached at 1.0 wt.% but no self-assembly occurs upon cooling the sample. The lowest solubility was observed for MEK with 0.35 wt.%. However, self-assembly at the lowest concentration occurs at 0.125 wt.% resulting in rigid fibers.

Table 3-1. Solubility of BTA-1 in selected solvents at rt and at the b.p. of the solvent with determined lowest concentration detected for self-assembly upon cooling and maximal concentration soluble at b.p. of the solvent (concentrations given in wt.%).

Solvent	Solubility at rt	Solubility at b.p. of solvent	Lowest concentration detected for self-assembly upon cooling [wt.%]	Maximal concentration soluble at b.p. of solvent [wt.%]
Water	✗	✗	-	-
Methanol	✗	✓	0.40	1.0
Ethanol	✗	✓	0.50	1.3
MEK	✗	✓	0.125	0.35
2-Propanol	✗	✓	0.45	1.0
THF	✓	✓	-	1.0
1-Butanol	✓	✓	0.80	1.8
Toluene	✗	✗	-	-

✓ = completely soluble, ✗ = no solubility, b.p. = boiling point

After investigation of the fiber morphology from the different solvents, the most promising results regarding the formed fiber morphology and dimension were obtained from MEK. Thus, the temperature-dependent turbidity measurements obtained from the crystallization system Crystal16® device in MEK will be described in more detail as an example. For this, concentrations of 0.05 wt.% up to 4.0 wt.% in MEK were prepared at room temperature. The samples were heated to 75 °C and hold at this temperature for 30 minutes at 400 rpm to ensure complete dissolution of the BTA. Samples with a concentration > 3.5 wt.% showed no clear solution at these conditions and were considered as “not completely soluble”. After the isothermal step and first dissolution, the temperature-dependent transmittance of each sample was recorded for three cycles upon heating and cooling with a rate of 0.50 C min⁻¹ in the range from 75 °C to 5 °C while stirring with 400 rpm. The change in transmittance upon cooling from 100 % to 0 % indicates clouding of the sample and thus the self-assembly of BTAs into self-assembled fibers. The cloud points (T_{cloud}) were determined at 50 % of transmittance. In contrast, the change in transmittance upon heating from 0 % to 100 % indicates dissolution of the self-assembled fibers resulting in a clear solution. The so-called clearing points (T_{clearing}) were determined at 50% of transmittance, too. Exemplarily, the 2nd cooling and 2nd heating temperature-dependent transmittance curves of a 0.20 wt.% BTA-1 in MEK sample are shown in Figure 3-4. Upon cooling to 5 °C, clouding of the solution occurs at around 42 °C (T_{cloud})

and fibers are formed. Heating the sample back to 75 °C, the fibers dissolve and a clear solution is observed at around 51 °C (T_{clearing}). A hysteresis of ~10 °C is observed between the cloud and clearing point. This process is completely reversible and all three heating and cooling cycles resulted in dissolution and clouding, respectively.

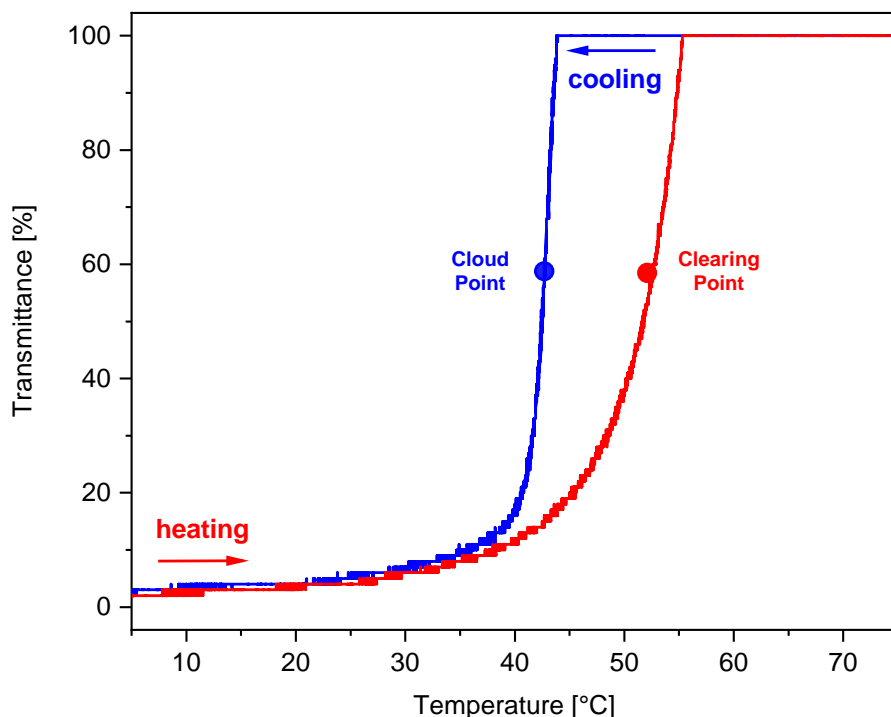


Figure 3-4. **Temperature-dependent transmittance curve.** The 2nd heating and 2nd cooling of a 0.2 wt.% BTA-1 sample in MEK with a scanning rate of 0.50 C min⁻¹. Upon cooling, the sample starts to self-assemble into rigid fibers (Cloud Point, $T_{\text{cloud}} = 42$ °C). Upon heating, dissolution of the fibers leads to clearing of the sample (Clearing Point, $T_{\text{clearing}} = 51$ °C). The process is fully reversible.

The concentration-dependent course of the cloud and clearing points of BTA-1 in MEK as mean values including the standard deviation from the applied three heating and cooling cycles were obtained. With this data a phase diagram from 5 to 75 °C can be created as depicted in Figure 3-5. The phase diagram can be divided into three regions:

- Region I: *In this region, no self-assembly takes place.* Here, the BTA-1 is fully soluble in MEK at low concentrations in the investigated temperature range from 5 °C to 75 °C. This is valid for concentrations up to 0.125 wt.%.
- Region II: *In this region, controlled self-assembly takes place.* The BTA-1 self-assembly yielding in a turbid solution upon cooling and reversibly dissolves upon heating the sample back to 70 °C. This is observed for concentrations of 0.125 wt.% - 0.30 wt.%. The cloud points increase from 21 °C (0.125 wt.%) to 62 °C

(0.30 wt.%) with increasing concentration. The clearing points raising from 32 °C (0.125 wt.%) to 68 °C (0.30 wt.%). Above the clearing points, the BTA-1 is completely dissolved again. The high reproducibility of the self-assembly process is indicated by the small error bars of the mean values for the cloud and clearing points.

- **Region III:** *In this region, no controlled self-assembly takes place.* For concentrations larger than 0.30 wt.% in MEK, BTA-1 is not completely soluble anymore at elevated temperatures. Self-assembly occurs upon cooling the solution, because not dissolved BTAs are still present in the solution, acting as nuclei and trigger further growth. This results in a mixture of bulk material and supramolecular fibers.

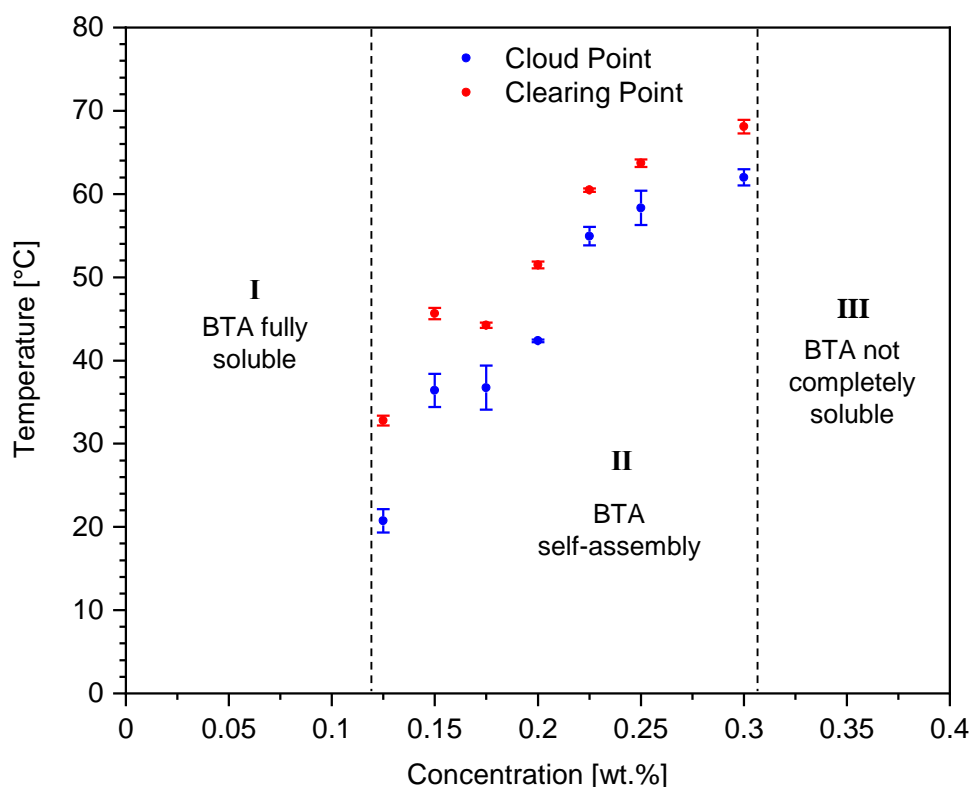


Figure 3-5. **Phase-diagram of the BTA-1 with a cyclohexyl periphery in MEK.** The concentration-dependent development of the cloud and clearing points of BTA in MEK as mean values including the standard deviation from the applied three heating and cooling cycles with a scanning rate of 0.50 C min⁻¹. Region I: No self-assembly takes place as the BTA is fully soluble in MEK at low concentrations up to 0.125 wt.% in the given temperature range. Region II: Controlled self-assembly of the BTA self-assembles into fibers upon cooling and reversibly dissolves upon heating the sample. Region III: No controlled self-assembly takes place as the BTA-1 is not completely soluble anymore at elevated temperatures for concentrations > 0.3 wt.%.

3.2.3 Development of the custom-made experimental set-up for self-assembly

After the determination for the optimal solvent and concentration range to prepare fibers from BTA-1, the next step involves the transfer of these findings from small scale (1 mL) to large scale (1 L) using a custom-made experimental set-up. The set-up is designed in a way, that evaporation of the solvent is prevented during the self-assembly process and controlled self-assembly in solution at constant concentration can be realized. Furthermore, the set-up is able to stir with an adjustable and reproducible stirring rate as well as defined linear cooling rates during the self-assembly process.

The custom-made experimental set-up is schematically shown with all components numerically marked from 1 to 10 in Figure 3-6. A screw-mountable 1 L vessel (laboratory glass bottle DURAN GLS 80) (1) has been chosen to be filled with the BTA at a given concentration in a selected solvent (2). The cap (3) of the vessel is modified for the insertion of a mechanical stirrer (4) and a temperature sensor (5) to prevent evaporation. The temperature sensor is immersed in the solution and is linked the thermometer (6) to record time-dependent temperature profiles which are saved with a custom-made software on the computer (7). The vessel is almost completely placed in a water bath (8) of a cryostat (9), to ensure heating and cooling with a defined linear heating and cooling rate ($^{\circ}\text{C min}^{-1}$), respectively. Furthermore, a camcorder (9) is set in a way, that it records the experiment to determine the self-assembly point visually upon cooling the solutions. In a general procedure, the solvent and the BTA has been weighed in the vessel which was then sealed and placed into the custom-made set-up. At this point, the BTA was not dissolved. The mixture was then heated up to 75°C and isothermally hold for about 30 minutes with rigorous stirring until all BTA was molecularly dissolved. The cooling profile was then started and the BTA solution was cooled down to 15°C with a chosen linear cooling rate and defined stirring rate.

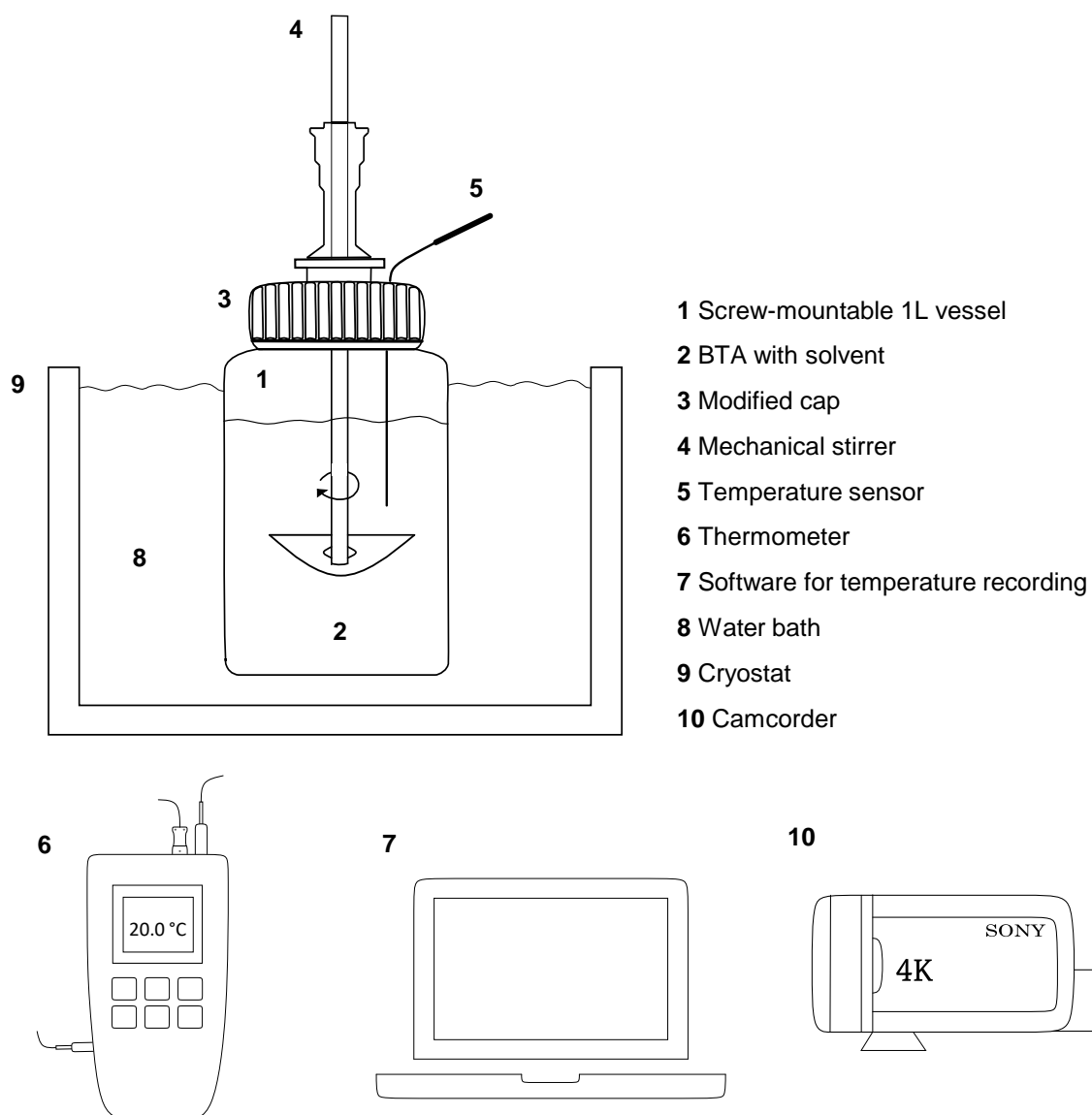


Figure 3-6. **Schematic presentation of the custom-made experimental set-up for controlled self-assembly in solution with all the components numerically marked.** The set-up consists of a screw-mountable 1 L vessel (1) filled with the BTA in a selected solvent (2), a modified cap (3), a mechanical stirrer (4), a temperature sensor immersed in the solution (5) linked to a thermometer (6) and a custom-made software for temperature recording (7), a water bath (8) associated of a cryostat (9) and a camcorder (10).

3.2.4 Sample preparation for scanning electron microscopy measurements

To determine the dimensions, i.e. diameter and length of the resulting BTA fibers, suitable samples need to be prepared and investigated by scanning electron microscopy (SEM). The obtained SEM-images can then be evaluated by means of ImageJ regarding the fiber's diameter and length. In a typical procedure, the dispersion with BTA fibers are drop-casted often resulting into dense and accumulated fibers on the substrate during the drying process, which significantly hampers proper evaluation of the SEM images.

To avoid dense fiber accumulation, a new process was implemented as schematically shown in Figure 3-7. Here, the fibers in the dispersion are isolated by a glass pipette (A) and deposited on a mesh with mesh-size of 50 μm . The solvent passes the mesh and the BTA fibers are statistically deposited on the mesh (B) without leading to a coffee stain effect. The deposited BTA fibers are then washed with water (C) to remove the remaining BTA in solution and prevent further self-assembly upon solvent evaporation. After drying of the BTA fibers, they are transferred to SEM stub (D), which is equipped with a conductive adhesive layer ensuring the fixation by stamping.

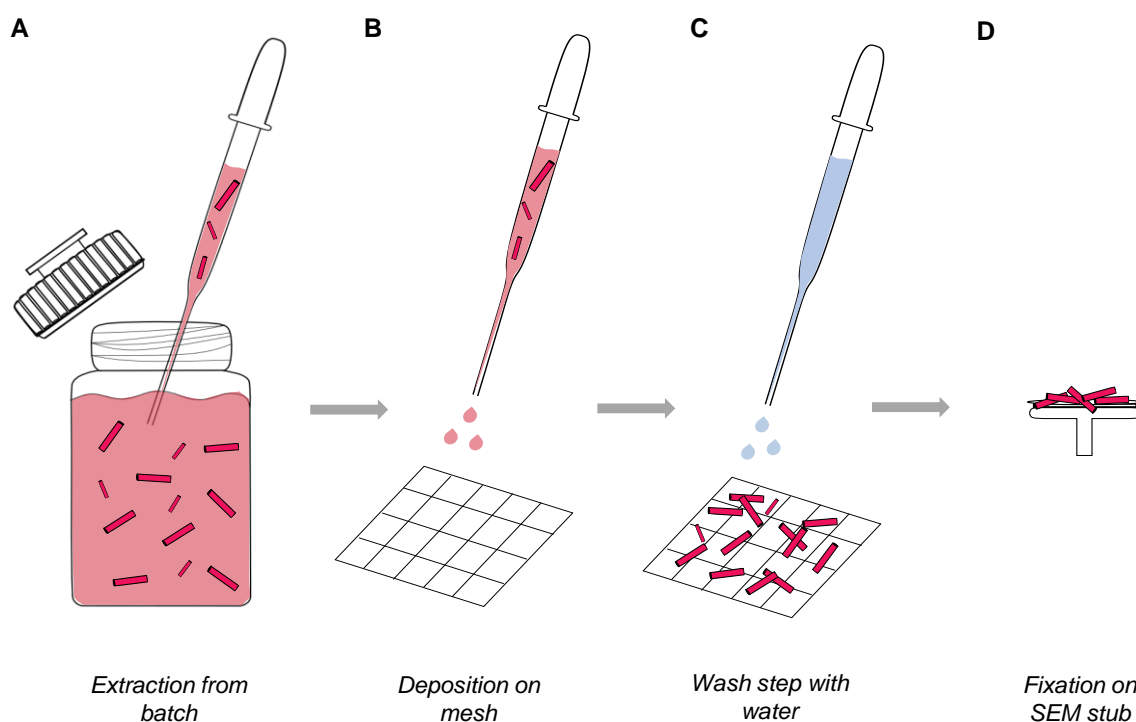
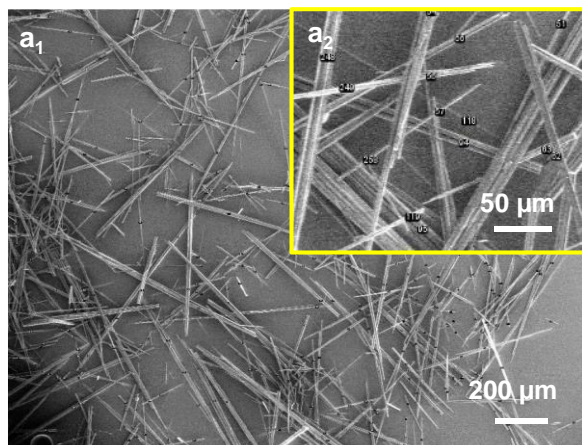


Figure 3-7. **Schematic illustration of the sample preparation for the investigation of BTA fibers with scanning electron microscopy.** The sample preparation includes **A**: isolation of the BTA fibers and **B**: deposition on a mesh, **C**: a wash step with water and **D**: further fixation on a SEM stub via stamping for the investigation with SEM.

An example of the well distributed BTA-1 fibers isolated with the new method, analyzed with SEM and evaluated by ImageJ is shown in Figure 3-8. The diameter and length are determined for the same fibers from the same image as depicted in Figure 3-8 A and B.

A: Evaluation of the fiber diameter



B: Evaluation of the fiber length

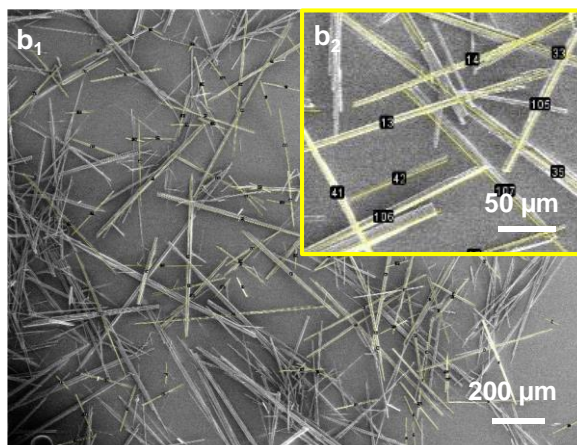


Figure 3-8. SEM images of BTA-1 fibers for the evaluation of the fiber diameter (A) and length (B). The diameter and length of the fibers are evaluated by ImageJ using the same SEM image. **a₁** and **b₁**: overview of the sample. **a₂** and **b₂**: Magnification of a sample spot used for evaluation.

3.3 Self-assembly experiments under controlled conditions

3.3.1 Self-assembly experiments with BTA-1

As demonstrated before, MEK is a proper solvent for BTA-1 in which the BTA self-assembles into rigid fibers in solution at a constant concentration. Thus, MEK is used in all following experiments in the custom-made set-up, in which a variety of other parameters can now be considered. The following chapter deals, therefore, with the investigation of the influence of cooling rates, stirring rates and varying concentrations on the fiber dimensions. In the following the a) influence of the cooling rate, b) influence of the stirring rate and c) the influence of the concentration are described.

a) Influence of the cooling rate

The next set of experiments deals with the investigation of the cooling rate on the BTA-1 fiber's morphology. From the solubility studies, the concentration of 0.175 wt.% is identified for the initial experiments, as this concentration marks the middle between the metastable dissolved solution and the upper solubility limit. In the first set of experiments three different cooling rates has been investigated without stirring the solution. These experiments aim to investigate the influence of cooling rates individually. The first experiment correlates to the experimental method from Weiss^[94] without stirring. The BTA-1 is heated to 75 °C and isothermally hold for 30 minutes to guarantee complete dissolution of the BTA-1 in MEK. The vessel is then taken out of the water bath from the cryostat and placed on the bench to cool down to room temperature. Here, no linear cooling rate is realized and the solution is allowed to cool from 75 °C until room temperature is reached. In contrast, in the second and third experiment the linear cooling rate of 0.50 °C min⁻¹ and 0.25 °C min⁻¹, was chosen, respectively. In both cases, the solution was cooled from 75 °C to 15 °C. The corresponding temperature profiles recorded during all three self-assembly processes are depicted in Figure 3-9. As expected, when the vessel is taken out of the water bath and cooled by the surrounding temperature, the cooling profile shows a comparable non-linear cooling rate as reported by Weiss et al.^[90] Despite no stirring for all three samples, the solution was able to be cooled with the set cooling rate when the vessel is placed within the cryostat. Note, that the thermocouple is fixated in a way in the middle of the vessel.

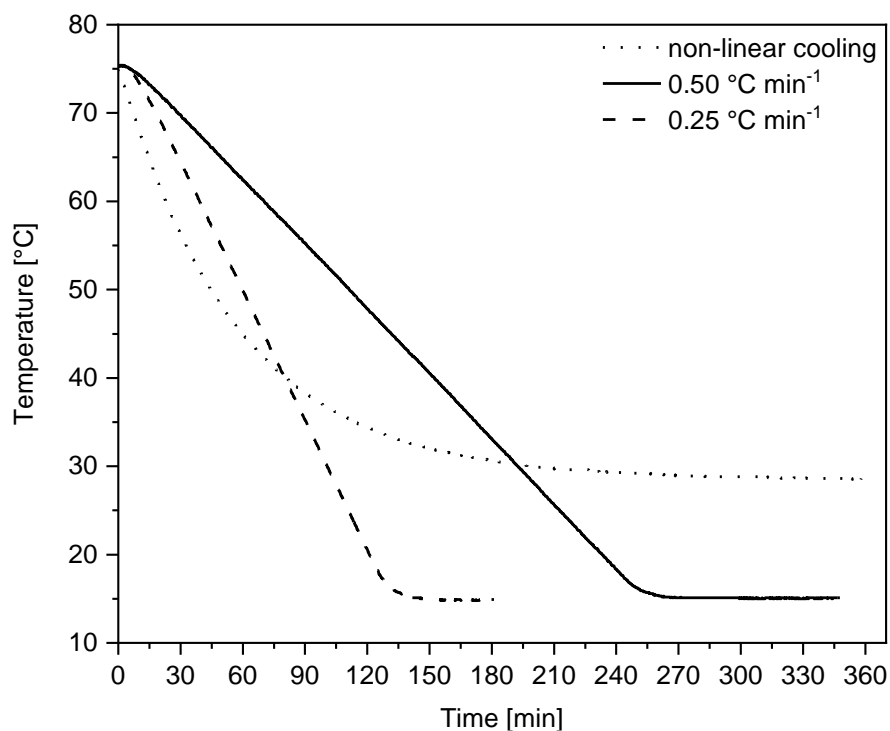


Figure 3-9. **Temperature profiles recorded during the self-assembly process of a BTA solution in MEK with 0.175 wt.% and no stirring.** The diagram shows three temperature profiles with a non-linear cooling, a cooling rate of 0.50 °C min^{-1} and 0.25 °C min^{-1} .

After the self-assembly process, a sample for SEM investigation was prepared as described before. The results of the SEM images are depicted in Figure 3-10 for the three cooling profiles (see a₁-c₁). The BTA-1 fibers show a rigid fibrous morphology for all three profiles, which, however, differ in their dimensions. The results of the fiber diameter and length distributions of all three cooling profiles are summarized in Figure 3-10 (a₂-c₂). The non-linear cooling profile shows a BTA-1 fiber diameter of $32.5 \pm 21.6\ \mu\text{m}$ with the highest distribution. Using a linear cooling rate of 0.50 °C min^{-1} leads to a narrower distribution of the diameter. The fibers exhibit a mean fiber diameter of $15.3 \pm 7.7\ \mu\text{m}$. Choosing an even lower cooling rate of 0.25 °C min^{-1} results in the thinnest fibers with a mean diameter of $9.4 \pm 6.1\ \mu\text{m}$. From these findings can be concluded, that the cooling rate has a significant influence on the fibers morphology. With a non-linear cooling profile, the BTA-1 fibers show a broad distribution arising from the very fast cooling at the beginning within the first minutes leading to a multitude of nuclei growing rates from supercooling. Compared to that, with a linear cooling rate of 0.50 °C min^{-1} , the slow homogenous cooling results in a narrower distribution, however still spanning several micrometers. Slowing the cooling process even more, results in thinner BTA-1 fibers.

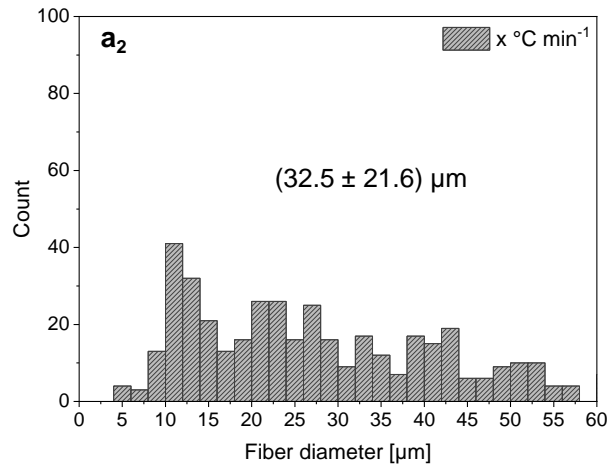
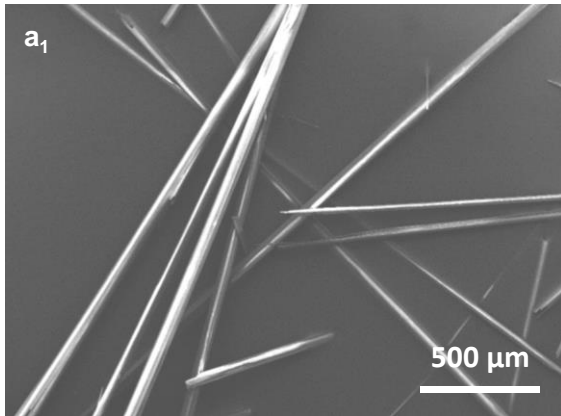
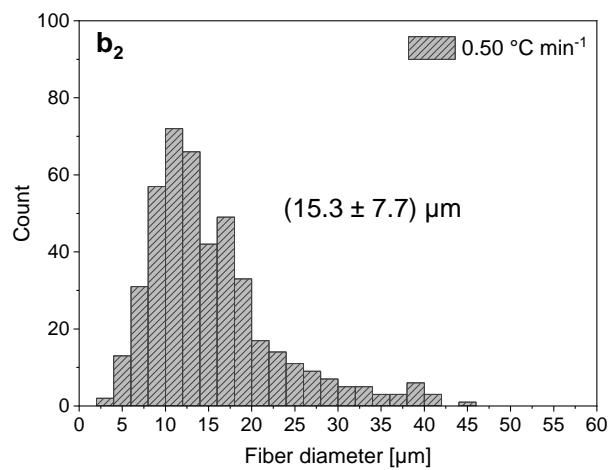
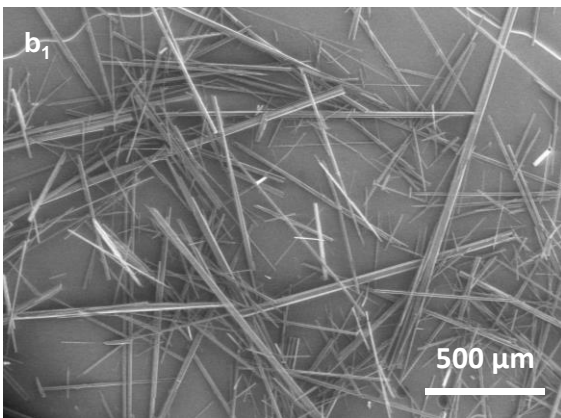
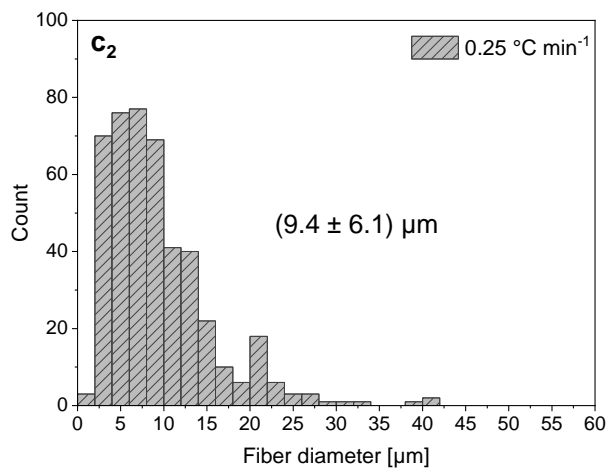
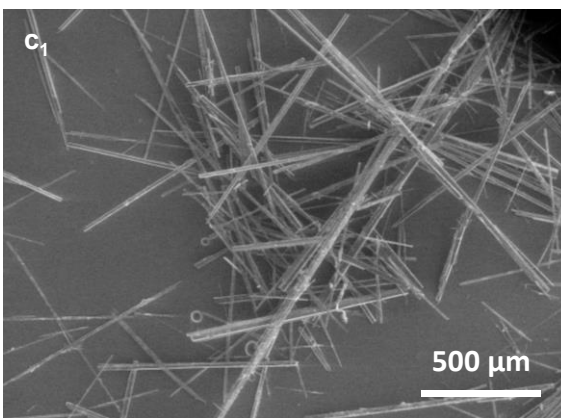
A: 0 rpm stirring rate, non-linear cooling rate**B: 0 rpm stirring rate, 0.50 °C min⁻¹ cooling rate****C: 0 rpm stirring rate, 0.25 °C min⁻¹ cooling rate**

Figure 3-10. **Diameter histograms and corresponding scanning electron microscopy images of self-assembly BTA-1 fibers from a 0.175 wt.% solution in MEK treated with different cooling rates without stirring. A:** No stirring and non-linear cooling profile. **B:** No stirring and cooling rate of 0.50 °C min⁻¹ and **C:** No stirring and cooling rate of 0.25 °C min⁻¹. **a₁-c₁:** SEM images of the prepared fibers and **a₂-c₂:** corresponding histograms of the fiber diameter distribution.

b) Influence of the stirring rate

The next experiments aim to examine the influence of the stirring rate on the fiber dimension during the self-assembly process. In these experiments, the BTA-1 concentration is kept constant at 0.175 wt.% and the linear cooling rates of $0.50\text{ }^{\circ}\text{C min}^{-1}$ and $0.25\text{ }^{\circ}\text{C min}^{-1}$ are applied. To investigate the influence of stirring, the stirring rates are varied from 0 rpm, 25 rpm, 100 rpm to 200 rpm. The results of the fiber diameter and length distribution from the self-assembly experiments are exemplarily shown in Figure 3-11 and Figure 3-12 for the parameter set of $0.50\text{ }^{\circ}\text{C min}^{-1}$ as cooling rate, a BTA-1 concentration of 0.175 wt.% in MEK at different stirring rates. Employing a linear cooling rate without any stirring results in a mean diameter of $15.3 \pm 7.7\text{ }\mu\text{m}$ with a wide range of mean diameters from $3\text{ }\mu\text{m}$ up to $56\text{ }\mu\text{m}$. Applying a low stirring rate of 25 rpm leads to a narrower distribution of BTA-1 fiber diameter. The BTA-1 fibers show a reduced mean fiber diameter of $8.1 \pm 2.8\text{ }\mu\text{m}$ with a minimum fiber diameter of $3\text{ }\mu\text{m}$ and a maximum of $22\text{ }\mu\text{m}$. Increasing the stirring rates to 100 rpm or 200 rpm leads to a slight decrease of the mean diameter of the BTA-1 fibers to $7.6 \pm 3.2\text{ }\mu\text{m}$ for 100 rpm and $7.1 \pm 2.8\text{ }\mu\text{m}$ for 200 rpm, respectively further. However, the distribution shifts towards smaller mean fiber diameters with higher stirring rates. The broad fiber distribution observed when no stirring is applied can be attributed to the temperature gradient which is formed during cooling. The solution near the cooling side of the vessel wall cools faster than the solution inside the vessel, in which is mainly attributed to the formation of numerous nuclei at different times. This may lead to larger fibers forming on the outside of the vessel (more time to grow) and smaller fibers on the inside (less time to grow), creating a wide distribution in fiber diameter. Once stirring is introduced, the temperature gradient is reduced, and the distribution becomes narrower. With faster stirring, the cooling process remains consistent when applying a linear cooling rate of $0.50\text{ }^{\circ}\text{C min}^{-1}$. The slight reduction in diameter with increasing stirring may be explained by the assumption that, with a constant cooling profile, other factors such as homogeneous nuclei formation, nuclei quantity per time, and fiber growth are impacted differently. As the distribution narrows with faster stirring, it can be assumed that nuclei form more uniformly, with most of the nuclei forming simultaneously during the self-assembly process. A smaller diameter suggests an increased number of nuclei, as the concentration remains constant.

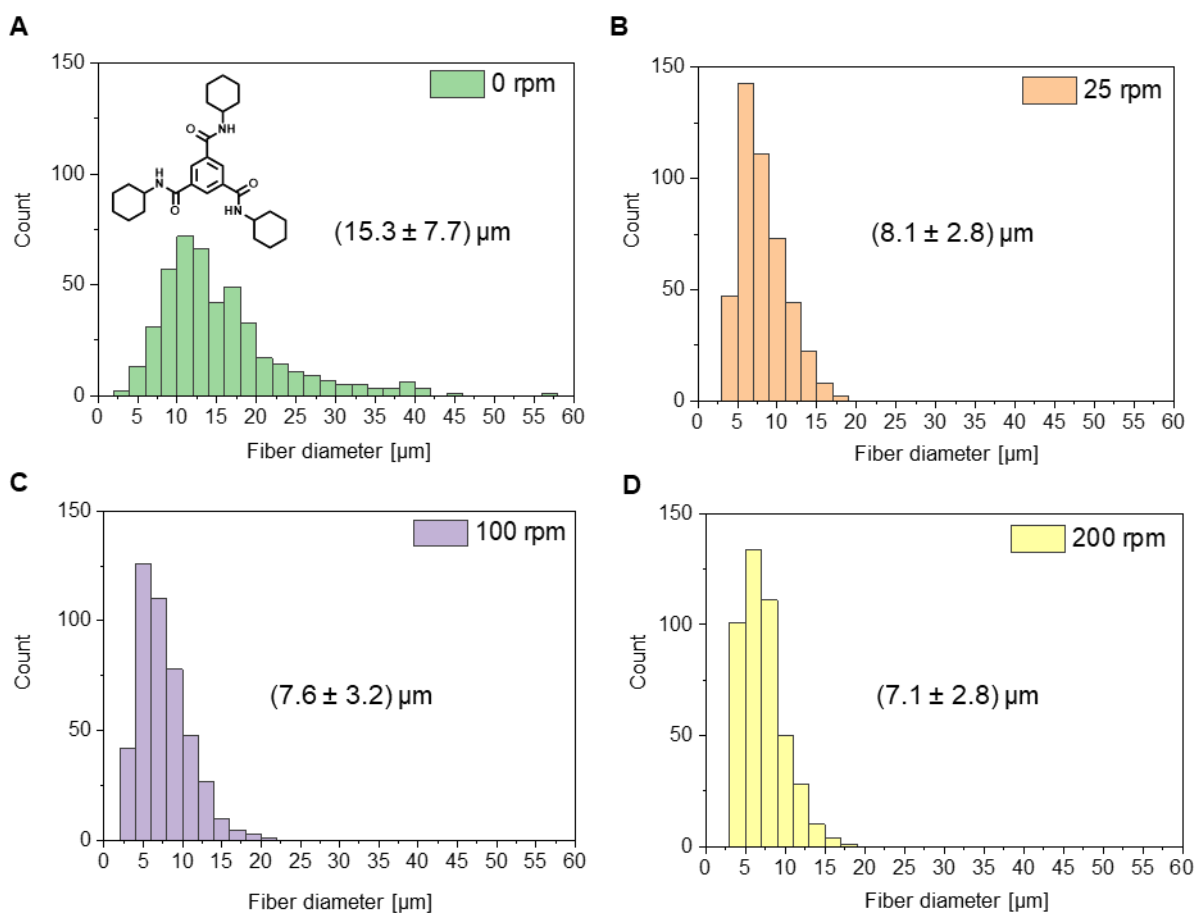


Figure 3-11. **Fiber diameter histograms of BTA fibers fabricated from a 0.175 wt.% solution in MEK, constant cooling rate of 0.50 °C min⁻¹ and different stirring rates. A:** Chemical structure of BTA-1 and stirring rate of 0 rpm, **B:** 25 rpm, **C:** 100 rpm and **D:** 200 rpm. The histograms of the diameter and length are based on 450 fibers.

A more pronounced impact is observed on the length distribution of the BTA-1 fibers as shown in Figure 3-12. No stirring leads to a mean fiber length of $505 \pm 386 \mu\text{m}$ with a wide distribution ranging from short BTA fibers measuring less than $100 \mu\text{m}$ up to a length of 2 mm. Inducing mild stirring of 25 rpm leads to a narrower distribution of BTA fiber length. Here, the mean fiber length is $274 \pm 182 \mu\text{m}$ with a minimum fiber length of $55 \mu\text{m}$ and a maximum of $875 \mu\text{m}$. Higher stirring at 100 rpm results in a mean length of $201 \pm 120 \mu\text{m}$ and 200 rpm in $162 \pm 100 \mu\text{m}$. Stirring $> 100 \text{ rpm}$ leads to a greater number of smaller fibers. In general, a trend is noticeable, where the distribution becomes narrower with the introduction of stirring into the self-assembly process. The resulting length of the BTA-1 fibers shows a significant dependence on faster stirring. The faster the stirring, the shorter the BTA-1 fibers become. This can be similarly explained as discussed for the fiber diameter reduction. The fiber length distribution narrows with faster stirring due to a more homogeneous nuclei formation. Additionally, the fibers become shorter at a constant concentration, likely because of the increased number of

nuclei and fewer remaining building blocks available to form large supramolecular assemblies. Moreover, shearing forces may contribute to the length distribution, particularly with fast stirring at 200 rpm, thus restricting the growth into larger assemblies.

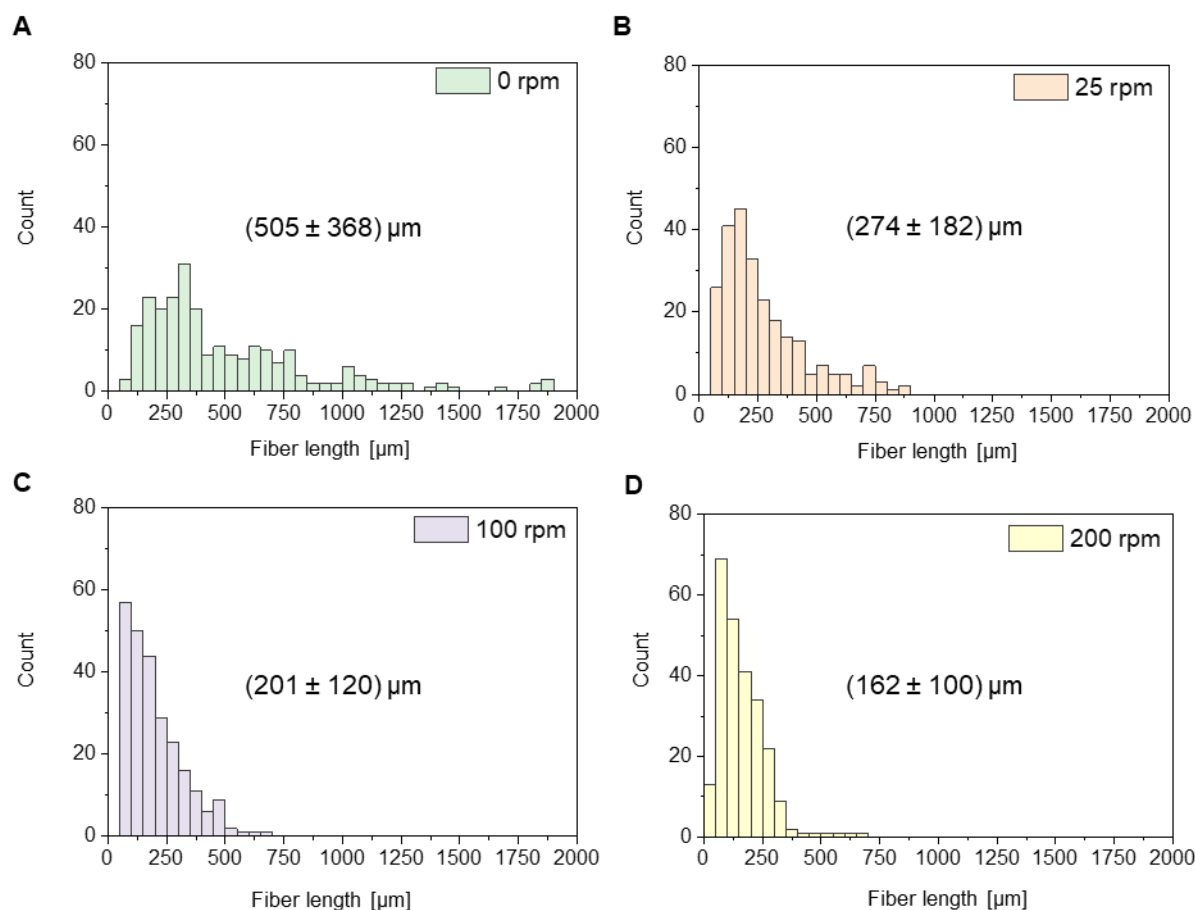


Figure 3-12. **Fiber length histograms of BTA fibers fabricated from a 0.175 wt.% solution in MEK, constant cooling rate of $0.50\text{ }^{\circ}\text{C min}^{-1}$ and different stirring rates. A: of 0 rpm, B: 25 rpm, C: 100 rpm and D: 200 rpm. The histograms of the diameter and length are based on 450 fibers.**

To proof the reproducibility of the experimental set-up and the self-assembling system, the parameter of 25 rpm, 0.175 wt.% and $0.50\text{ }^{\circ}\text{C min}^{-1}$ as cooling rate were repeated ($n=10$) and the mean diameter and length of each sample were evaluated. A graphical representation is given in Figure 3-13. The mean value of all samples results in a fiber diameter of $6.5 \pm 1.3\text{ }\mu\text{m}$ and a fiber length of $238 \pm 37\text{ }\mu\text{m}$.

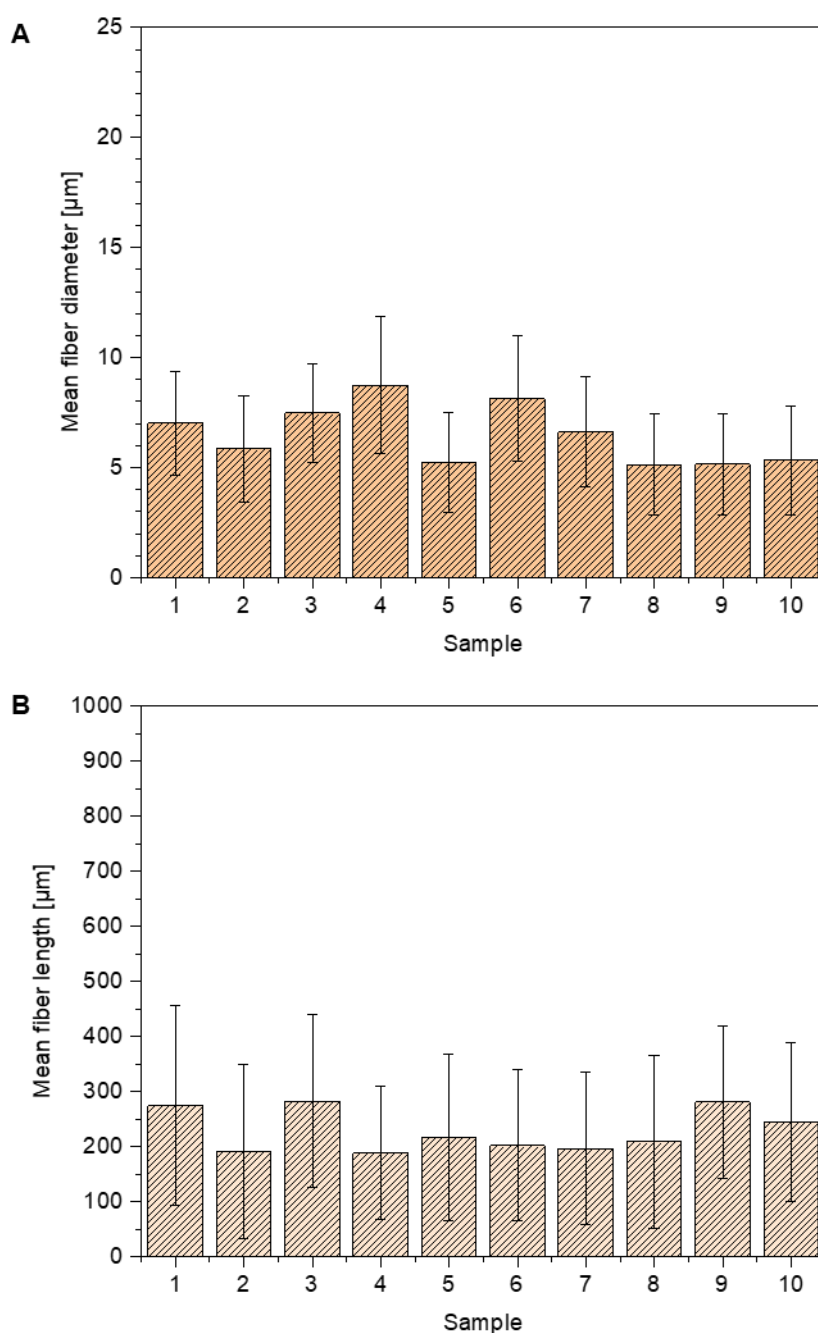


Figure 3-13. **Mean diameter (A) and length (B) of BTA fibers of n=10 samples treated by the same self-assembly profile.** Parameters: 25 rpm, 0.175 wt.% in MEK and a cooling rate of $0.50\text{ }^{\circ}\text{C min}^{-1}$.

Further experiments were conducted with the linear cooling rate of $0.25\text{ }^{\circ}\text{C min}^{-1}$ employing different stirring rates at a constant concentration of 0.175 wt.% in MEK. The histograms of the fiber diameter and length are summarized in *Appendix A* Figure 8-1 and Figure 8-2, respectively. The values of the fiber diameter and length distribution for this parameter set are summarized in Table 3-2. Similar as seen for the linear cooling rate of $0.50\text{ }^{\circ}\text{C min}^{-1}$, the

introduction of stirring has a great impact on the diameter and length distribution. A pronounced difference in the mean diameter and distribution is noticeable when comparing no stirring (0 rpm) to a stirring rate of 25 rpm. Whereas no stirring results in a broad distribution and mean diameter of $9.4 \pm 6.1 \mu\text{m}$, stirring with 25 rpm results in a narrower distribution with a mean diameter of $6.4 \pm 2.9 \mu\text{m}$. Increasing the stirring rate results in a decreased mean fiber diameter of $5.3 \pm 2.6 \mu\text{m}$ for 100 rpm and $4.6 \pm 2.2 \mu\text{m}$ for 200 rpm, respectively. However, for the linear cooling rate of $0.25 \text{ }^\circ\text{C min}^{-1}$ as well, the length of the BTA fibers is notably affected by the stirring rates, decreasing from a mean length of $383 \pm 311 \mu\text{m}$ with a broad distribution for no stirring (0 rpm) to $188 \pm 133 \mu\text{m}$ with a narrower distribution when stirred with 200 rpm

Table 3-2. Mean fiber diameter and length in dependence of different cooling rates ($0.25 \text{ }^\circ\text{C min}^{-1}$ and $0.50 \text{ }^\circ\text{C min}^{-1}$) and stirring rates (0, 25, 100 and 200 rpm) with a constant concentration of 0.175 wt.%.

Stirring [rpm]	$0.25 \text{ }^\circ\text{C min}^{-1}$		$0.50 \text{ }^\circ\text{C min}^{-1}$	
	Diameter [μm]	Length [μm]	Diameter [μm]	Length [μm]
0	9.4 ± 6.1	383 ± 311	15.3 ± 7.7	505 ± 368
25	6.4 ± 2.9	262 ± 186	8.1 ± 2.8	274 ± 182
100	5.3 ± 2.6	213 ± 179	7.6 ± 3.2	201 ± 120
200	4.6 ± 2.2	188 ± 133	7.1 ± 2.8	162 ± 100

In conclusion, the greatest impact on the mean fiber diameter and on the mean fiber length of the BTA-1 fibers has stirring. If no stirring is applied, the distribution of the mean fiber diameter and length is broad and very large and thick fibers are obtained for BTA-1. In contrast, if stirring is applied, even for low stirring rates of 25 rpm, the mean fiber diameter and length distribution is narrower and both diameter and length are reduced to smaller values. Higher stirring rates steadily decrease the mean fiber diameter and length, however, the impact is rather low. Note, by applying the highest stirring rate of 200 rpm, the mean fiber diameter and length can be reduced by ~50 % compared to no stirring. However, 25 rpm are sufficient to generate a narrower distribution of the BTA fibers diameter while applying a linear cooling rate. Furthermore, comparing both linear cooling rates ($0.50 \text{ }^\circ\text{C min}^{-1}$ and $0.25 \text{ }^\circ\text{C min}^{-1}$) with each other, the impact on the mean fiber diameter and

c) Influence of the concentration

The next experiments aim to study the influence of the concentration on the fiber morphology. For this, the linear cooling rate of $0.50\text{ }^{\circ}\text{C min}^{-1}$ is used and additionally to the concentration of 0.175 wt.%, the two concentrations 0.20 wt.% and 0.25 wt.% are investigated. These two concentrations are within the lower and upper concentration limits of the BTA-1 in MEK investigated by the solubility studies with the crystallization system Crystal16® device. All experiments were performed and evaluated as described before. The histograms of the diameter and length distribution in dependence of the stirring rates for both concentrations are summarized in *Appendix A* Figure 8-5 - Figure 8-6, respectively. An example of the impact of the concentration on the BTA-1 fibers dimension is shown in Figure 3-14 for samples treated by a stirring rate of 25 rpm and a linear cooling rate of $0.50\text{ }^{\circ}\text{C min}^{-1}$. The mean fiber diameter slightly increases from $8.1 \pm 2.8\text{ }\mu\text{m}$ with 0.175 wt.% to $8.6 \pm 3.1\text{ }\mu\text{m}$ for 0.20 wt.% and $10.3 \pm 4.4\text{ }\mu\text{m}$ with 0.25 wt.%. Additionally, the distribution of the fiber diameter is wider for the higher concentrations.

The fiber length is largely unaffected using different concentrations and a stirring rate of 25 rpm. The mean fiber length is $274 \pm 182\text{ }\mu\text{m}$ for the 0.175 wt.% sample, $270 \pm 178\text{ }\mu\text{m}$ for the 0.20 wt.% sample and $241 \pm 161\text{ }\mu\text{m}$ for the 0.25 wt.% sample. The distribution of the fiber diameters of the different samples is also very similar leading to the conclusion that the concentration does not affect the fiber dimension significantly for a given set of conditions.

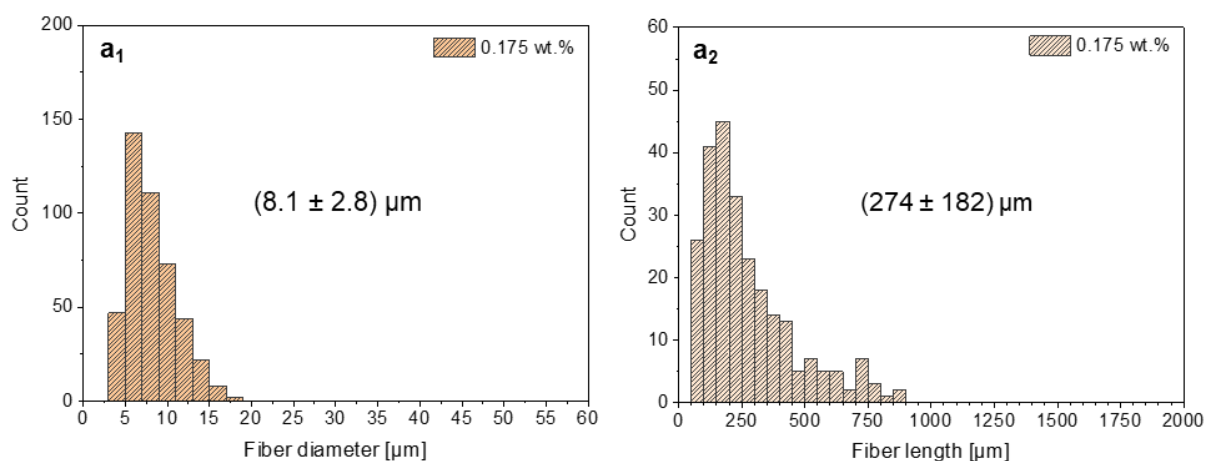
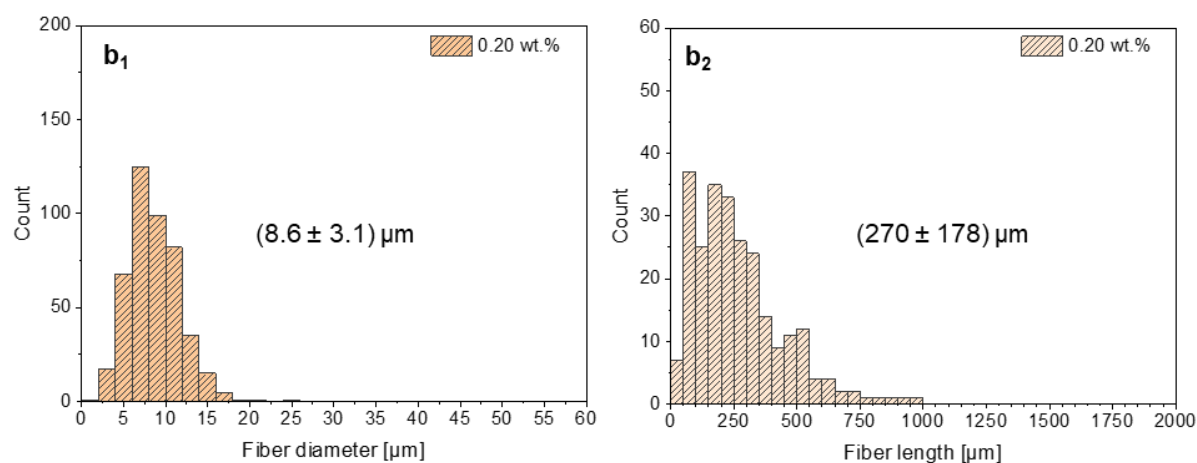
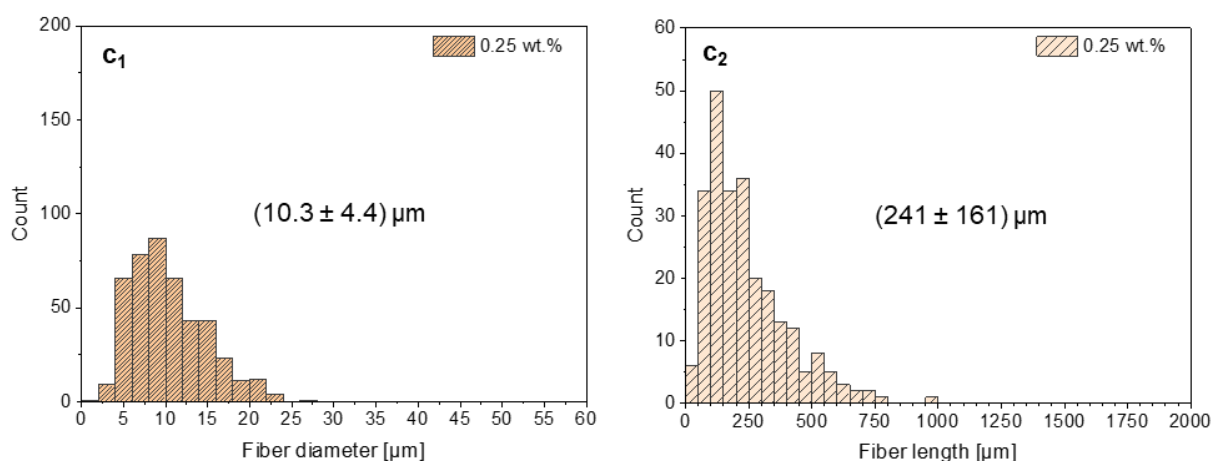
A: Concentration of 0.175 wt.%**B: Concentration of 0.20 wt.%****C: Concentration of 0.25 wt.%**

Figure 3-14. **Diameter and length histograms of BTA-1 fibers in dependence of BTA concentration.** Parameters: stirring rate of 25 rpm, a constant cooling rate of $0.50 \text{ }^\circ\text{C min}^{-1}$ from different concentration (**A**: 0.175 wt.%, **B**: 0.20 wt.% and **C**: 0.25 wt.% in MEK). **a₁-c₁**: depicts the fiber diameter distribution and **a₂-c₂**: the fiber length distribution.

The mean fiber diameter and length of the BTA fibers fabricated with constant cooling rate of $0.50\text{ }^{\circ}\text{C min}^{-1}$ in dependence of concentration and stirring rate are summarized in Table 3-3. Additionally, to the exemplarily shown parameter set of 25 rpm stirring for the three concentrations, the mean diameter and length are only affected slightly comparing each data of the different stirring rates.

Table 3-3. Mean fiber diameter and length in dependence of different concentrations (0.175 wt.%, 0.20 wt.% and 0.25 wt.%) and stirring rates (0, 25, 100 and 200 rpm) with a constant cooling rate of $0.50\text{ }^{\circ}\text{C min}^{-1}$.

Stirring [rpm]	0.175 wt.%		0.20 wt.%		0.25 wt.%	
	Diameter [μm]	Length [μm]	Diameter [μm]	Length [μm]	Diameter [μm]	Length [μm]
0	15.3 ± 7.7	505 ± 368	11.6 ± 5.8	326 ± 289	14.9 ± 7.9	326 ± 205
25	8.1 ± 2.8	274 ± 182	8.6 ± 3.1	270 ± 178	10.3 ± 4.4	241 ± 161
100	7.6 ± 3.2	201 ± 120	6.8 ± 3.6	213 ± 172	8.9 ± 3.5	227 ± 148
200	7.1 ± 2.8	162 ± 100	6.0 ± 2.3	233 ± 155	6.7 ± 3.0	211 ± 153

From this data can be concluded, that the stirring rate has a higher impact rather than the concentration. The mean fiber diameter and length of the supramolecular fibers are quite similar using the same cooling rate and stirring for each concentration. The most significant difference is observed in the diameter and length distributions of the fibers, which become narrower with higher stirring rates, regardless of the concentration as explained previously is a result of the homogeneously formation of nuclei and growth into supramolecular fibers.

3.3.2 Self-assembly experiments with BTA 2

The second BTA derivative (BTA-2) is also based on trimesic acid and feature a branched aliphatic periphery, i. e. N^1,N^3,N^5 -tris(2,4,4-trimethylpentan-2-yl) benzene-1,3,5-tricarboxamide. The chemical structure is depicted in Figure 3-15. This derivative shows good solubility in polar solvents and self-assembly ability into fibrous gel-like structures. For the upcoming experiments, 2-propanol is chosen as solvent, because with 2-propanol the solubility and self-assembly behavior is highly uniform within the solubility studies with the crystallization system Crystal16® device.

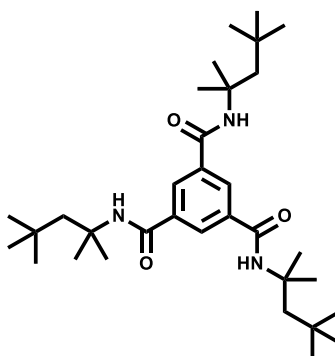


Figure 3-15. Chemical structure of a N^1,N^3,N^5 -tris(2,4,4-trimethylpentan-2-yl) substituted BTA (BTA-2).

a) Solubility studies and self-assembly behavior in solution at constant concentration for BTA-2

To get more detailed information about the solubility and the self-assembly behavior of BTA-2 at a constant concentration, temperature-dependent turbidity measurements were performed to determine the cloud and clearing points by means of transmittance revealing the self-assembled or solution state, respectively. The concentration-dependent development of the cloud and clearing points of the BTA-2 in 2-propanol is summarized in a phase diagram from 0 °C to 75 °C (Figure 3-19). The phase diagram can be divided into three regions:

- **Region I:** *In this region, no self-assembly takes place.* Here, the BTA-2 is fully soluble in 2-propanol at low concentrations in the investigated temperature range. This is valid for concentrations up to 0.09 wt.%.
- **Region II:** *In this region, controlled self-assembly takes place.* The BTA-2 self-assembles into entangled fibers upon cooling and reversibly dissolves upon heating the sample. This is observed for concentrations of 0.09 wt.% - 0.25 wt.%. The cloud points increase from 30 °C (0.09 wt.%) to 65 °C (0.25 wt.%) with increasing concentration of the BTA-2. The clearing points raising from 40 °C (0.09 wt.%) to 69 °C (0.25 wt.%). Above the clearing points, the BTA-2 is completely dissolved again. The high reproducibility of the self-assembly process is indicated by the small error bars of the mean values for the cloud and clearing points.
- **Region III:** *In this region, no controlled self-assembly takes place.* For concentrations larger than 0.25 wt.% in 2-propanol, BTA-2 is not completely soluble anymore at elevated temperatures. Self-assembly occurs upon cooling the solution, because not dissolved BTAs are still present in the solution, acting as nuclei and trigger further growth. This results in a mixture of bulk material and supramolecular fibers.

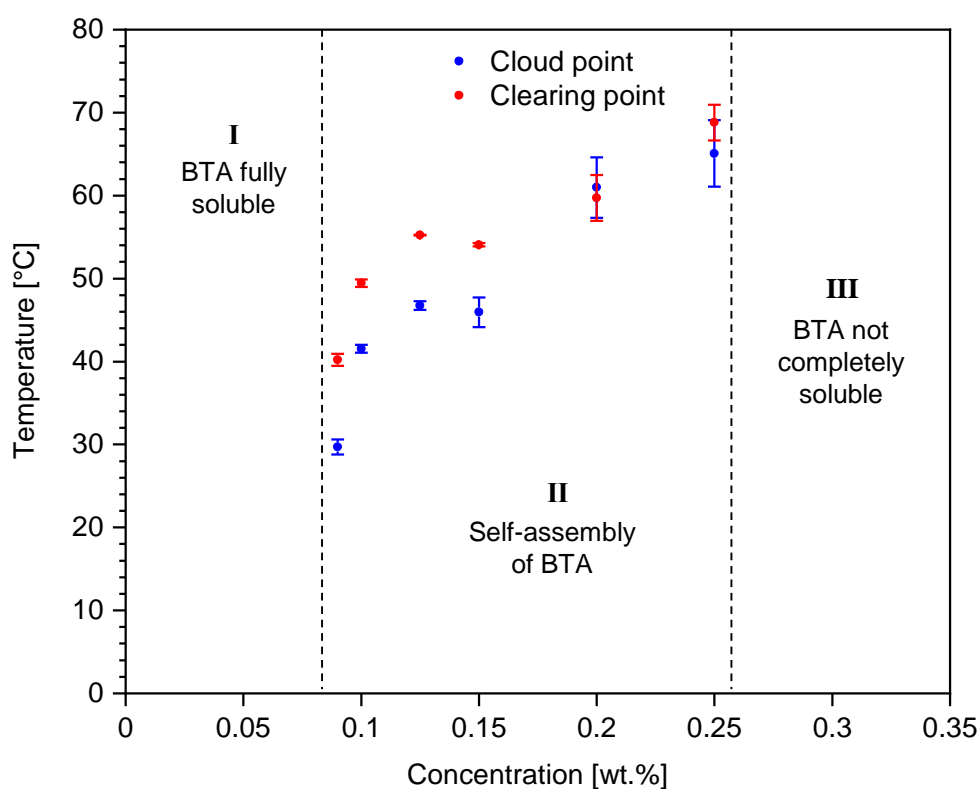


Figure 3-16. **Phase-diagram of N^1, N^3, N^5 -tris(2,4,4-trimethylpentan-2-yl) substituted BTA (BTA-2) in 2-propanol.** The concentration-dependent development of the cloud and clearing points of the BTA in 2-propanol as mean values including the standard deviation from the applied three heating and cooling cycles with a scanning rate of $0.50\text{ }^\circ\text{C min}^{-1}$. Region I: No self-assembly takes place as the BTA-2 is fully soluble in 2-propanol at low concentrations up to 0.09 wt.% in the given temperature range. Region II: Controlled self-assembly of the BTA-2 self-assemble into gel-like fibrous structures upon cooling and reversibly dissolves upon heating the sample for concentrations 0.09 wt.% - 0.25 wt.%. Region III: No controlled self-assembly takes place as the BTA-2 is not completely soluble anymore for concentrations > 0.25 wt.%.

b) Self-assembly under controlled conditions for BTA-2

The solubility studies enabled the selection of a proper concentration for the experiments for the controlled self-assembly in the custom-made 1-liter scale set-up. The chosen concentration for BTA-2 in 2-propanol is 0.15 wt.%. Under these conditions, BTA-2 self-assembles into very long and thin fibers with some entanglement resulting into macroscopically gel-like state. Therefore, BTA-2 has been selected to complement the BTA selection, aiming to verify whether the controlled self-assembly parameters are applicable for such entangled fibers. To analyze the influence of the different parameter settings during the self-assembly and to analyze whether the prior determined stirring rates and cooling rates will influence the BTA-2 fibers diameter in a similar manner, three different parameter settings are chosen: First, no stirring and non-linear cooling profile is applied to investigate the self-assembly in an uncontrolled manner. The two other experiments are conducted by introducing stirring as well as a linear cooling rate to investigate the controlled self-assembly. Thus, the second experiment is conducted by using a defined stirring rate of 25 rpm and a cooling rate of $0.50\text{ }^{\circ}\text{C min}^{-1}$ and the third experiment with a stirring rate of 100 rpm and a cooling rate of $0.50\text{ }^{\circ}\text{C min}^{-1}$.

The results of the obtained fiber morphology are depicted in the SEM images in Figure 3-17 (a₁-c₁) for the three settings, respectively. The BTA-2 assemblies show a fibrous morphology for all three profiles, being very flexible and bending. As they are flexible and bending, the length cannot be correctly determined. Thus, the following evaluation concentrates on the fiber diameter distribution. The diameter distributions of the fibers are depicted in Figure 3-17 (a₂-c₂). The non-linear cooling profile paired with no stirring shows a slightly broader distribution of the BTA-2 fiber's diameter with $1.4 \pm 0.53\text{ }\mu\text{m}$ with a minimum diameter of 372 nm and a maximum of 2.9 μm . Using a linear cooling rate of $0.50\text{ }^{\circ}\text{C min}^{-1}$ and introducing stirring leads to a slightly narrower distribution of the diameter. The fibers treated with 25 rpm stirring rate exhibit a mean diameter of $1.2 \pm 0.44\text{ }\mu\text{m}$ within a diameter range from 500 nm to 2.5 μm including one fiber with a larger diameter of 3.5 μm . Faster stirring with 100 rpm results in an even narrower distribution and smaller mean diameter of $1.0 \pm 0.35\text{ }\mu\text{m}$ with a minimum diameter of 413 nm and a maximum of 2.3 μm . Despite the stirring and cooling rate, the BTA intrinsically forms much thinner fibers than the BTA-1. However, introducing stirring and cooling with a linear rate results in the self-assembly in a controlled manner and tuning possibilities of the fiber diameter into smaller dimensions.

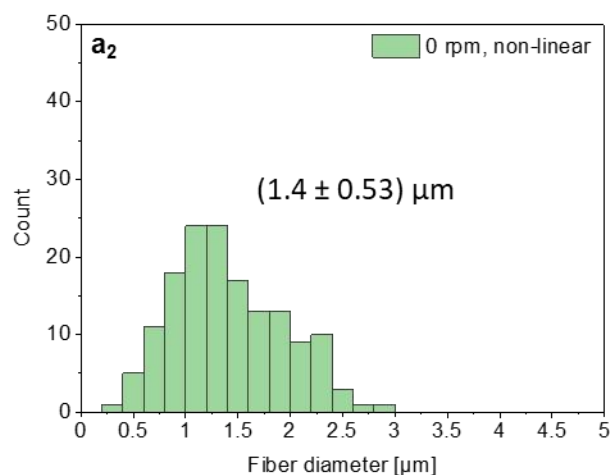
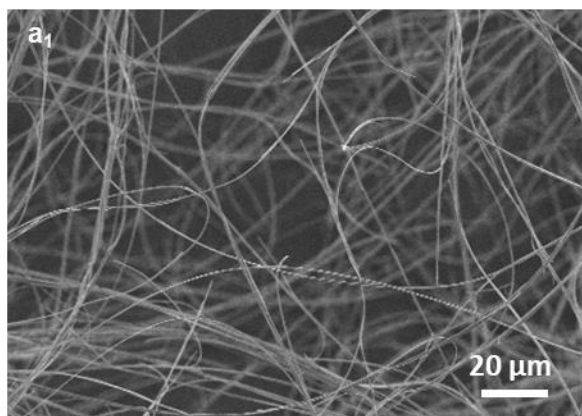
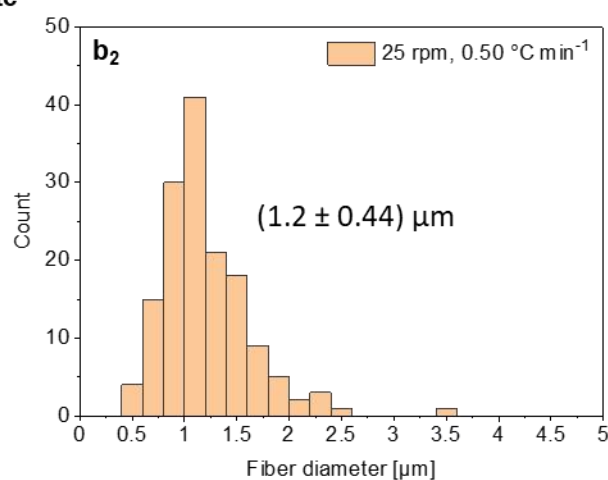
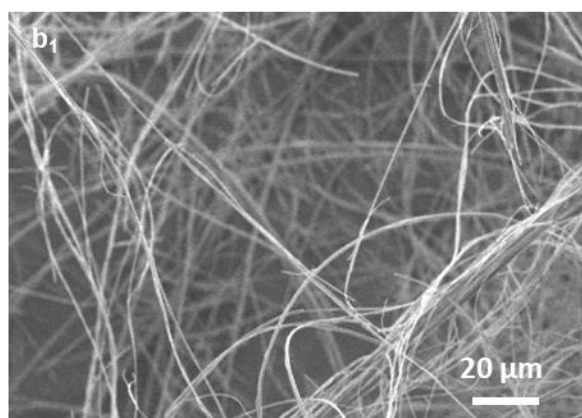
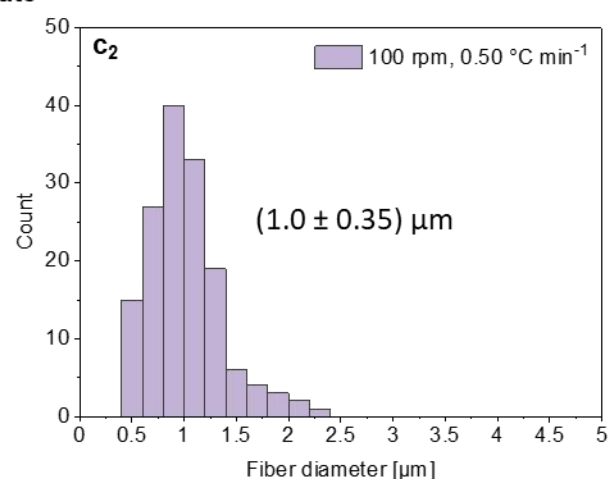
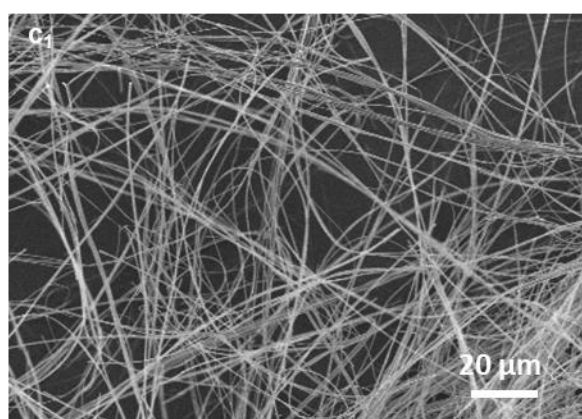
A: 0 rpm stirring rate, non-linear cooling rate**B: 25 rpm stirring rate, 0.50 °C min⁻¹ cooling rate****C: 100 rpm stirring rate, 0.50 °C min⁻¹ cooling rate**

Figure 3-17. Diameter histograms and corresponding scanning electron microscopy images of self-assembly BTA-2 fibers from a 0.150 wt.% solution in 2-propanol treated with different cooling rates and stirring rates. **A:** No stirring and non-linear cooling profile. **B:** 25 rpm as stirring rate and cooling rate of 0.50 °C min⁻¹ and **C:** 100 rpm as stirring rate and cooling rate of 0.50 °C min⁻¹. **a₁-c₁:** SEM images of the prepared fibers and **a₂-c₂:** corresponding histograms of the fiber diameter distribution.

3.3.3 Self-assembly experiments with BTA 3

The third BTA derivative BTA-3 is a sulfur-containing BTA derivative as depicted in Figure 3-18. This derivative shows good solubility in polar solvents and self-assembly ability into fibrous structures. 1-Propanol was found to be the most suitable solvent and, therefore, chosen as solvent for the upcoming experiments.

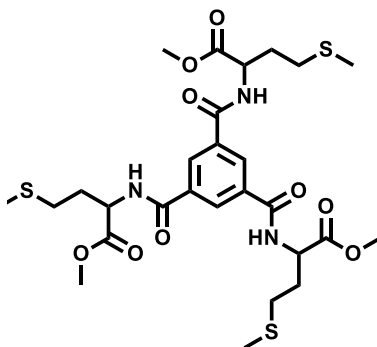


Figure 3-18. Chemical structure of a methionine methyl ester substituted BTA (BTA-3).

a) Solubility studies and self-assembly behavior in solution at constant concentration for BTA-3

At first, the temperature-dependent turbidity measurements were performed in 1-propanol to determine solubility of the BTA-3 derivative. Based on all solubility measurements, the concentration-dependent development of the cloud and clearing points of the BTA-3 in 1-propanol were obtained and a phase diagram from 5 to 75 °C created as depicted in Figure 3-19. The phase diagram shows three regions:

- Region I: *In this region, no self-assembly takes place.* Here, the BTA-3 is fully soluble in 1-propanol at low concentrations in the temperature range from 5 °C to 75 °C. This is valid for concentrations up to 0.10 wt.%.
- Region II: *In this region, controlled self-assembly takes place.* The BTA-3 self-assembles into fibers upon cooling and reversibly dissolves upon heating the sample. This is observed for concentrations of 0.10 wt.% - 1.75 wt.%. The cloud points increase from 13 °C (0.10 wt.%) to 60°C (1.75 wt.%) with increasing concentration of the BTA-3. Concentrations > 0.750 wt.% result in a fibrous gel-like structure of the

BTA-3. The clearing points raising from 21 °C (0.10 wt.%) to 64 °C (1.75 wt.%). Above the clearing points, the BTA-3 is completely dissolved again. The high reproducibility of the self-assembly process is indicated by the small error bars of the mean values for the cloud and clearing points.

- **Region III:** *In this region, no controlled self-assembly takes place.* For concentrations larger than 1.75 wt.% in 1-propanol, BTA-3 is not completely soluble anymore at elevated temperatures. Self-assembly occurs upon cooling the solution, because not dissolved BTAs are still present in the solution, acting as nuclei and trigger further growth. This results in a mixture of bulk material and supramolecular fibers.

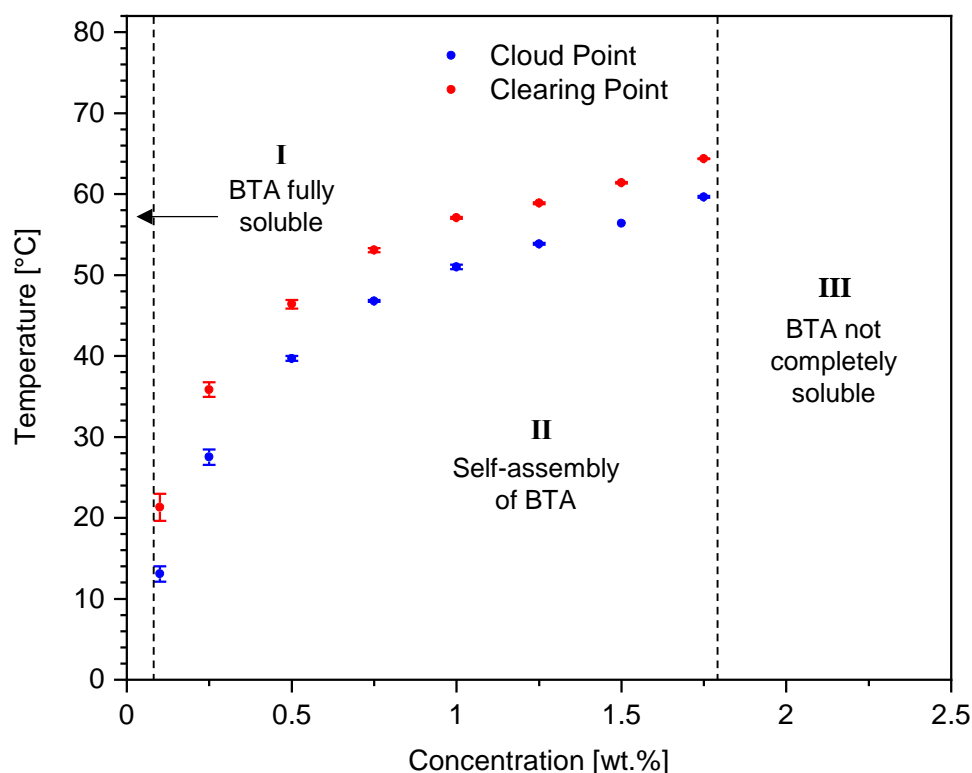


Figure 3-19. **Phase-diagram of methionine methyl ester substituted BTA (BTA-3) in 1-propanol.** The concentration-dependent development of the cloud and clearing points of the BTA-3 in 1-propanol as mean values including the standard deviation from the applied three heating and cooling cycles with a scanning rate of 0.50 °C min⁻¹. Region I: No self-assembly takes place as the BTA-3 is fully soluble in 1-propanol at low concentrations up to 0.10 wt.% in the given temperature range. Region II: Controlled self-assembly of the BTA-3 into fibers upon cooling and reversibly dissolves upon heating the sample for concentrations 0.10 wt.% - 1.75 wt.%. Region III: No controlled self-assembly takes place as the BTA-3 is not completely soluble anymore at elevated temperatures for concentrations > 1.75 wt.%.

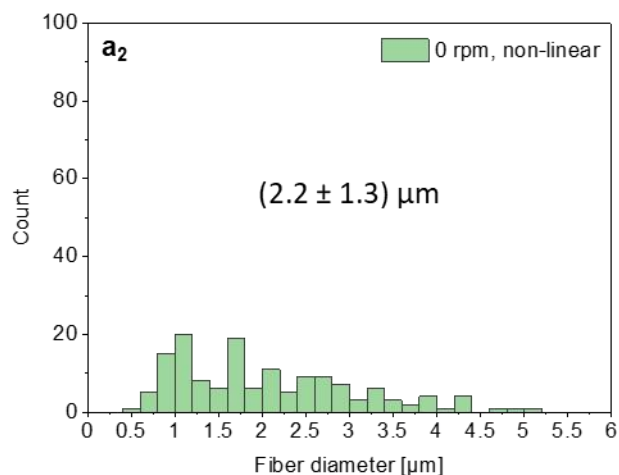
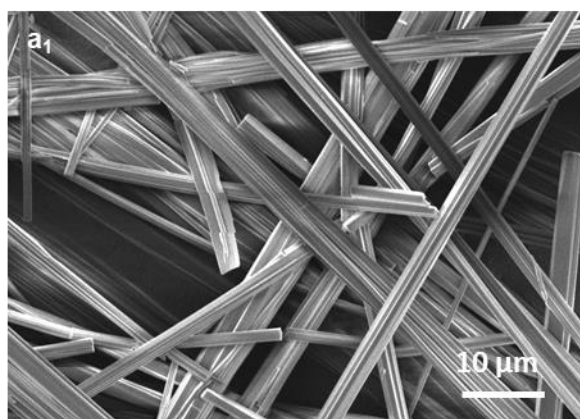
b) Self-assembly under controlled conditions for BTA-3

The solubility studies enabled the selection of a proper concentration for the experiments of the controlled self-assembly in the custom-made 1-liter scale set-up. 0.30 wt.% was chosen as constant concentration for BTA-3 in 1-propanol in all experiments. At this concentration, BTA-3 self-assembles into thin fibers prior the formation of gel-like structures. The BTA-3 was investigated regarding three parameter settings: *i)* no stirring, non-linear cooling profile, *ii)* 25 rpm as stirring rate and linear cooling rate of $0.50\text{ }^{\circ}\text{C min}^{-1}$ and *iii)* 100 rpm and $0.50\text{ }^{\circ}\text{C min}^{-1}$.

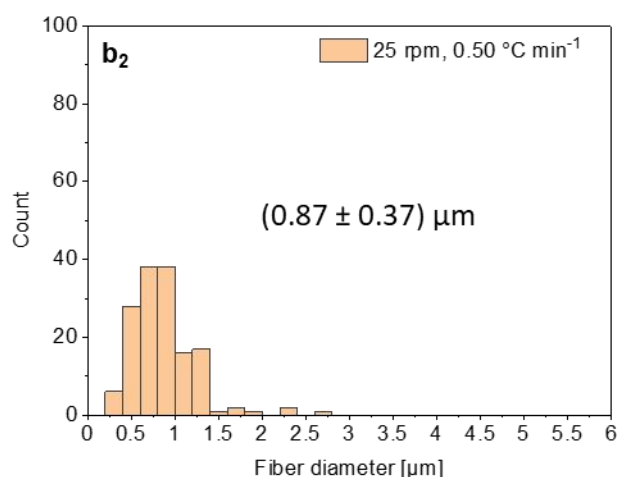
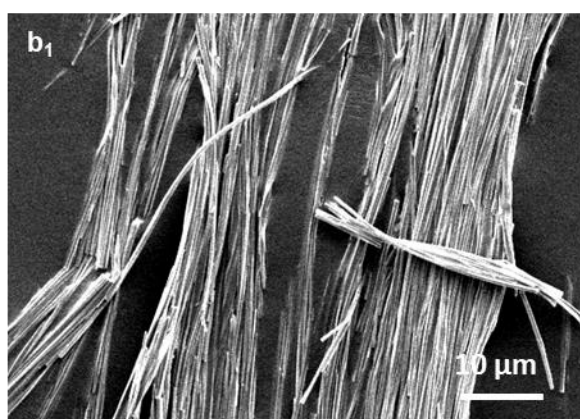
The results are depicted in the SEM images in Figure 3-20 (a₁-c₁) showing the morphology of the BTA-3 derivative for the three settings, respectively. The aggregates of BTA-3 exhibit a fibrous morphology in all three profiles. The resulting fibers treated without stirring and a non-linear cooling rate appear stiffer and less flexible compared to the fibers treated with stirring and controlled cooling. However, self-assembly during stirring seems to yield a large amount of agglomerates, which are deposited in a highly oriented manner. Thus, the accurate determination of length is challenging due to insufficient statistics. From the non- or less-agglomerated structures it seems that the fibers are shorter with faster stirring, which is consistent with the findings for BTA-1 and BTA-2. Therefore, the subsequent evaluation focuses only on the diameter distribution. The diameter distributions of the fibers are illustrated in Figure 3-20 (a₂-c₂).

As found before for BTA-1 and BTA-2, the non-linear cooling profile paired with no stirring shows the broadest distribution of the BTA-3 fibers. The BTA-3 mean fiber diameter was determined to be $2.2 \pm 1.3\text{ }\mu\text{m}$ with a minimum diameter of 414 nm and a maximum of 9.6 μm . Using a linear cooling rate of $0.50\text{ }^{\circ}\text{C min}^{-1}$ and applying a stirring rate of 25 rpm leads to a narrower distribution of the diameter. Experiments with 25 rpm results in fibers with a mean diameter of $0.87 \pm 0.37\text{ }\mu\text{m}$ with a minimum diameter of 276 nm and a maximum of 2.7 μm . Faster stirring with 100 rpm results in an even narrower distribution and smaller mean diameter of $0.39 \pm 0.13\text{ }\mu\text{m}$ with a minimum diameter of 156 nm and a maximum of 779 nm. In contrast to BTA-2, a very strong dependence on the stirring rate is observed as well as a morphology change with respect to the dimensions.

A: 0 rpm stirring rate, non-linear cooling rate



B: 25 rpm stirring rate, 0.50 °C min⁻¹ cooling rate



C: 100 rpm stirring rate, 0.50 °C min⁻¹ cooling rate

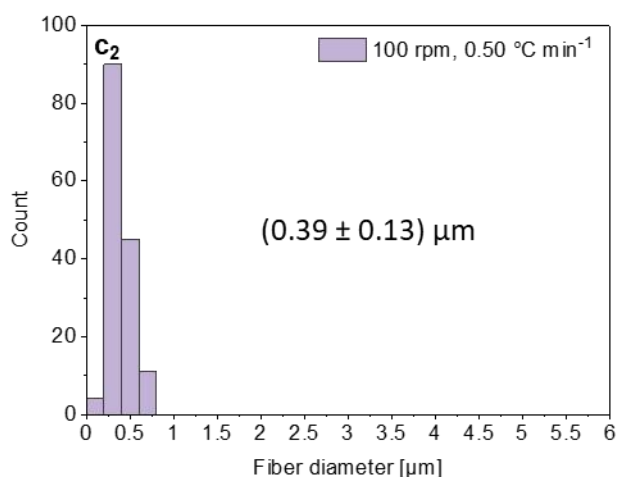
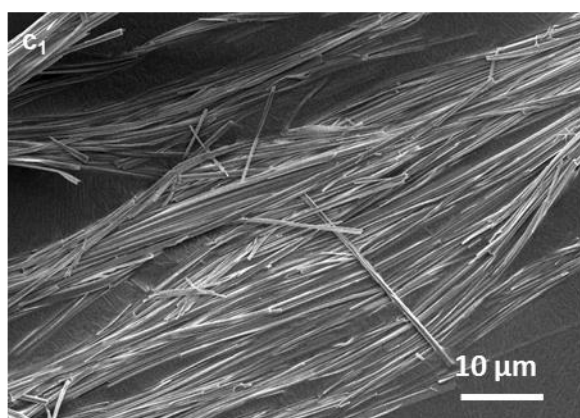


Figure 3-20. Diameter histograms and corresponding scanning electron microscopy images of self-assembly BTA-3 fibers from a 0.30 wt.% solution in 1-propanol treated with different cooling rates and stirring rates. **A:** No stirring and non-linear cooling profile. **B:** 25 rpm as stirring rate and cooling rate of 0.50 °C min⁻¹ and **C:** 100 rpm as stirring rate and cooling rate of 0.50 °C min⁻¹. **a₁-c₁:** SEM images of the prepared fibers and **a₂-c₂:** corresponding histograms of the fiber diameter distribution.

3.4 Conclusion to controlled preparation of supramolecular fibers

This chapter aimed at the *controlled preparation of 1,3,5-benzenetricarboxamides fibers* in solution on the liter-scale upon cooling. For this, an experimental set-up was developed and optimized, which enabled the investigation of the self-assembly of three selected BTAs in view of the fibers shape and dimensions depending on non-linear and linear cooling rates, different stirring rates and concentrations. Due to the unique processing window of each BTA, determined by factors such as molecular structure, solvent, concentration and temperature, a comprehensive investigation of each parameter is essential for achieving control over the shape and dimensions. Prior to the preparation of supramolecular fibers under controlled conditions in the custom-made experimental set-up, the temperature-dependent self-assembly and disassembly behavior was explored. For this, the selected BTAs are investigated using the crystallization system Crystal16® device, which allows to identify a suitable BTA/solvent-system and to determine the solubility and self-assembly behavior in solution at different concentrations on a mL-scale. Subsequently, experiments with the custom-made set-up on the 1-liter scale were performed and relevant self-assembly parameters including the temperature profile, stirring rate and concentrations were systematically varied.

It was found that the cooling rate has a significant impact on the fiber diameter and length distribution if no stirring is applied. With a non-linear cooling profile, the BTA fibers show a broad distribution whereas linear cooling rates results in a narrower distribution. Stirring also has a major influence on the diameter and length, with faster stirring leading to narrower distributions and shorter BTA fibers. Only the selected different concentrations, appears to have a limited impact on the mean fiber diameter and length. For BTA 2 and BTA 3 flexible fibers with diameters of about 1 μm and below were found. For BTA 1, which is based on trimesic acid and linked via amide groups to cyclohexyl side groups, the fiber diameter can be tuned from 4 to 15 μm and the length from 160 to 500 μm . These rigid microfibers with defined dimensions are of particular interest to be used in an electrostatic flocking process, as it will be demonstrated in the following chapter.

4 Electrostatic flocking of supramolecular fibers

4.1 Background to electrostatic flocking

In the following introduction part, the process of electrostatic flocking will be introduced. In this context, the most important influences on the process, application and materials for electrostatic flocking are addressed.

Electrostatic flocking process

Flocking is a process of depositing fine objects onto an adhesive-coated surface.^[115] Electrostatic flocking is an industrial technique that align fibers in an electric field ultimately promoting their perpendicular arrangement as schematically illustrated in Figure 4-1. The electric field is established by applying a voltage between a positive electrode and a grounded electrode. Here, the fibers reservoir which is connected to the electrode results in partially charging the fibers. Subsequently, the charged fibers orient themselves with respect to their long axes along the electric field lines. Typical voltages applied in the electrostatic flocking process are 5-70 kV depending on the flocking device.^[115-117] The field lines of the electrostatic field lead to the repulsion and alignment of the flock fibers along these lines.^[118] Consequently, a dense flock is generated as the majority of fibers are oriented perpendicularly on the surface. The flocking process can be divided into several steps including 1) pre-treatment of the substrate if necessary, 2) application of adhesive layer, 3) the flocking, 4) cleaning 5) drying/curing of the adhesive and 6) final treatment such as cleaning.^[115,116] The flock fibers exhibit length of approximately 0.5 – 3.0 mm.^[119] Typically used flock fibers are made of cotton, rayon, acrylic, nylon or polyester.^[116,119-121] The polymer flock fibers usually exhibit low electrical conductivities and thus would not be aligned within the electrical field. Therefore, the fibers are equipped using coding products, metal salts, tannic acids, or similar substances that enhance conductivity.^[118]

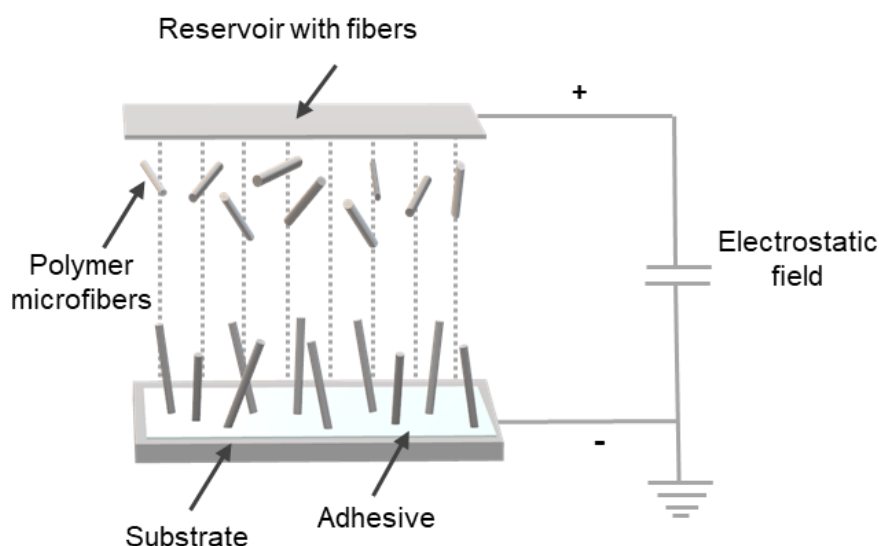


Figure 4-1. **Schematic illustration of the electrostatic flocking.** Under applied voltage the polymer microfibers are accelerated and aligned in the electrostatic field resulting in a perpendicularly alignment on a substrate covered with an adhesive. Figure adapted and reproduced with permission from Ref ^[136] Copyright © 2024 The Authors. *Advanced Materials Interfaces* published by Wiley-VCH GmbH.

There exist two different configurations of electrostatic flocking as schematically shown in Figure 4-2. The first configuration is based on a bottom-to-top (A) configuration that has a charging electrode at the top where the flock fibers are deposited. Here, the fibers are accelerated against gravity towards the top substrate. Throughout the bottom-to-top process, the flock fibers move back and forth between the two poles until it is either anchored in the adhesive or falls out of the field. Another configuration is the top-to-bottom (B) that uses a charged sieve box at the top where the flock fibers are brushed through.^[117]

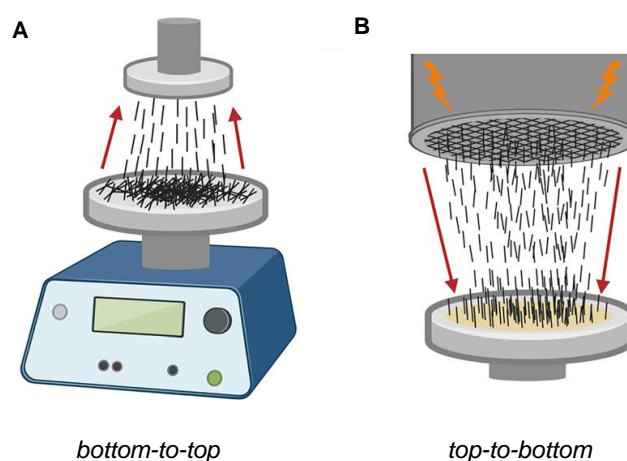


Figure 4-2. **Schematic representation of a bottom-to-top and top-to-bottom electrostatic flocking configuration.** **A:** The bottom-to-top configuration has a charging electrode where the flock fibers are deposited. **B:** The top-to-bottom configuration uses a charged sieve box where the flock fibers are brushed through. Figure adapted and reproduced with permission from Ref. ^[117] Rights managed by AIP Publishing.

Several parameters influence the flocking process. For example, the distance between the electrode and the substrate plays a significant role in the flocking process. Larger distances between the positive and negative (grounded) poles can complicate flocking and lead to worse results. However, this issue can be countered by elevating the voltage. Essentially, a higher voltage is required with increased distance between the electrode and the substrate. Factors affecting an ideal flocking outcome involve the preparation and chemical treatment of the flock fiber, air conditions, and as mentioned above the distance between the electrode and the substrate.^[116,118] These parameters are interconnected and influence each other. To achieve the best flocking results, it's essential for the flock fibers to exhibit proper electrical conductivity. In general, fiber charging is achieved through contact charging when a direct current is applied to the electrodes. Fibers placed on the positively charged electrode accumulate positive charge on their surfaces. The longer the voltage is applied, the more charge is generated between the two differently charged electrodes. With the fibers possessing equal positive charge, repulsion occurs between them and the electrode. Once the electrostatic force surpasses the force of gravity, the fibers accelerate towards the negatively charged electrode and adhere to the substrate which is typically covered with adhesive.^[117,122–124] While in flight within the electric field, the fiber experiences forces from electrostatic repulsion, air resistance, gravity, and the electric field as well as rotational and translational rotation.^[125] If the distance between the two electrodes is too small, fibers may not rotate sufficiently, and their angle with respect to the substrate will be well below 90°. Therefore, a high conductivity of the fibers is necessary. The calculated theoretical maximum occupied area of the substrate is 53 %. However, if the fibers randomly hit the substrate or do not adhere perpendicularly, the theoretical flock density is significantly reduced. This reduction is attributed to the coulombic repulsion of the fibers within the flock, which occupies a portion of the area around each fiber.^[125,126] Generally, around 10% of the surface is actually covered with flock fibers after flocking process. The limited coverage of the substrate can be explained by the electrostatic charge of each individual flock fiber. Each fiber to create an electrostatic field around itself due to the applied voltage. Consequently, the next fiber can only adhere at a specific distance to the already adhered fiber. The size of this field depends on the length of the flock fiber i.e. longer fibers possess larger electrostatic fields. Furthermore, once the initial fibers are anchored in the adhesive or on the substrate, they generate additional field lines that extend upwards, similar to the field lines around them. These lines also play a role in determining the spacing between the fibers.^[118]

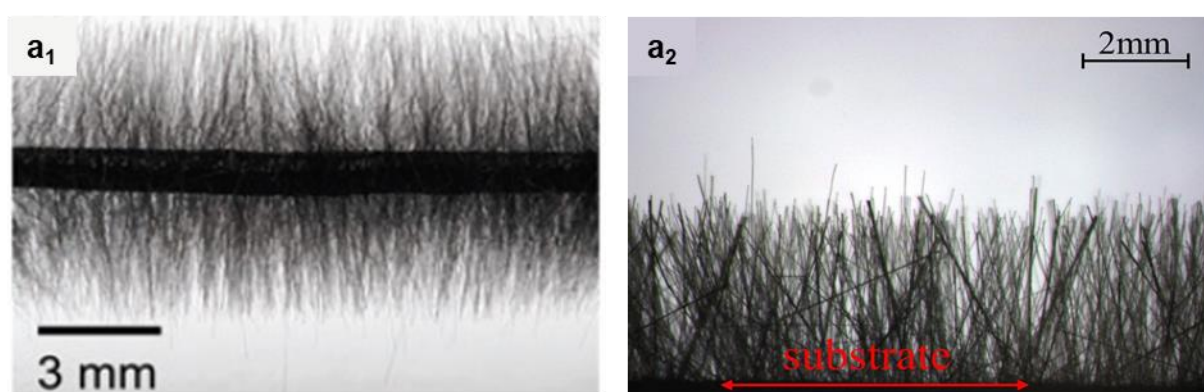
Application of flocked fibers

Electrostatic flocking is applied across a broad spectrum of applications to manufacture a variety of flocked products. Flocked products are used in the medical and automotive sector, in cosmetics, fabrics and clothing, in the decorative sector, in tissue engineering as composite materials.^[117,118,122,123,127–129] For example, in the medical sector, flocked swabs of Nylon are used for extraction of samples^[129] such as the swabs used for the corona tests of Covid 19. A large application field is the automotive sector, where polymer flocks are used in the glove compartment and the center console. The flocked surfaces provide a visually high-quality finish and improve the haptics and reduce noise. In cosmetics the polymer flocks serve as applicators or as finishing of various packaging. The most prominent area of flock application is the fashion industry with the application of various polymer flocks and sizes for T-shirts. Furthermore, flocking is known in the decoration sector, especially for toys.^[118] However, besides the industrial application of flocking, it has become popular in the scientific field where flocking is used for wound healing applications^[128] or thermal conductivity thermal interface materials.^[123] For all of these applications, whether industrial or scientific, the chosen material and the dimensions of the flocks are crucial for the electrostatic flocking process and the final finish of the flocked product.

New materials for electrostatic flocking

In addition to traditional polymer fibers, several researchers have directed their attention toward exploring new materials such as carbon fibers or inorganic materials for electrostatic flocking to discover novel applications. Several works were dealing with carbon fibers as flocking material for applications such as low reflection microwave shielding material,^[130] elastomeric thermal interface material,^[123,131] ultrasensitive airflow sensor,^[132] three-dimensional stretchable fabric-based electrode for supercapacitors.^[133] Another work investigated the use of MgO₂ nanofibers for electrostatic flocking to obtain an electrode for long-term stable supercapacitors with high cycling rates.^[134] Examples of two different examples from long fibers (> 3 mm) and nanofibers are shown in Figure 4-3 represented by flocked carbon fibers (A) and MgO₂ nanofibers (B).

A: Flocked carbon fibers



B: Flocked MnO₂ nanofibers

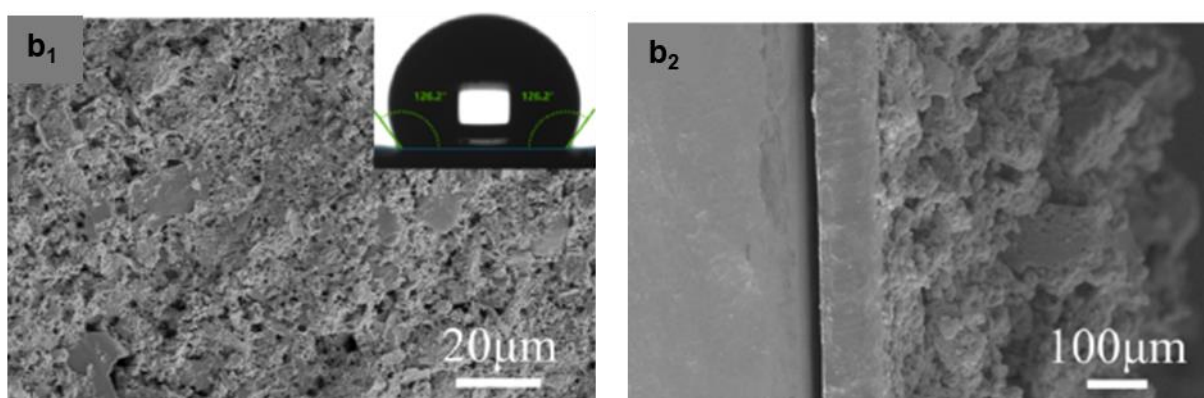


Figure 4-3. **Examples of flocked carbon fibers and MgO₂ nanofibers.** **A:** Flocked carbon fibers with length exceeding 3 mm **a₁**: as ultrasensitive airflow sensor^[132] and **a₂**: as low reflection microwave shielding material.^[130] **B:** MgO₂ nanofibers for electrostatic flocking to obtain an electrode for supercapacitors.^[134] **b₁**: Presentation with contact angle on flocked MgO₂ nanofibers and **b₂**: Cross-section of the flocked MgO₂ nanofibers. Figure adapted and reproduced with permission from Refs.^[130,132,134] Copyright © 2020 Elsevier Ltd. All rights reserved, © The Royal Society of Chemistry 2022 and © 2022 John Wiley & Sons Ltd.

Approach for electrostatic flocking of supramolecular fibers

Apart from the above-mentioned carbon fiber-based and inorganic materials, electrostatic flocking is a method where typically polymer microfibers with conductive-enhancing materials are aligned in an electric field and adhered, mostly perpendicular, to a surface giving a dense pile finish. This is an already established industrial method with applications e.g. in biomedicine, textile and automobile section.^[117] In this context, supramolecular BTA microfibers exhibit a high potential to be flocked, because these fibers intrinsically feature a macrodipole, arising from their hierarchical structure and thus might be suitable for an alignment in an electric field.

This chapter deals with self-assembled BTA fibers from solution, which will be isolated and sieved to achieve defined fiber dimensions with defined aspect ratio (l/d). Subsequently these small fibers will be processed in an electric field to obtain a vertical BTA array.

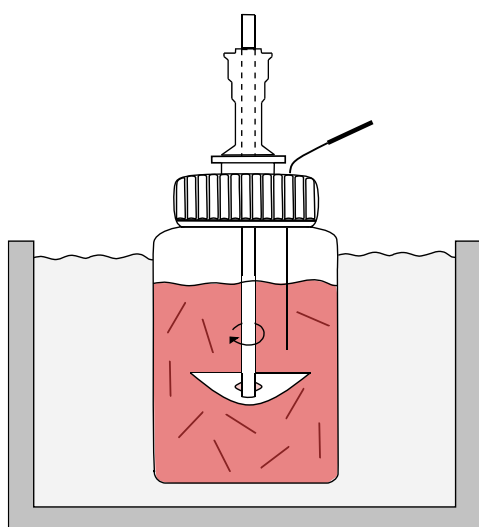
For this, BTA fibers need to be prepared in the first step being suitable for electrostatic flocking. The following requirements need to be considered:

- i)* suitable and homogenous dimensions of the fibers,
- ii)* certain stiffness and
- iii)* free-flowing properties after isolation from the self-assembled solution.

Thus, the chapter can be divided into two parts as schematically shown in Figure 4-4. Part I covers the controlled self-assembly in solution in the custom-made experimental set-up elaborated in Chapter 3 *Controlled preparation of supramolecular fibers* to produce the BTA fibers with suitable and homogeneous dimensions. The next step addresses the isolation and drying process of the BTA fibers to generate free-flowing fibers. Part II deals with the experiments for the electrostatic flocking set-up with the aim to orientate the BTA fibers and produce an aligned BTA fiber array.

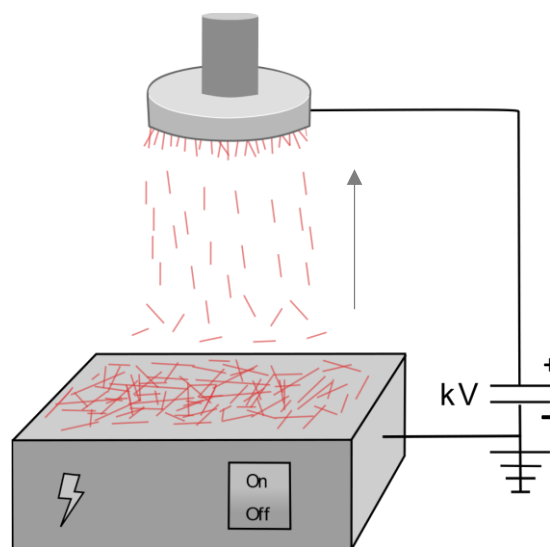
Part I: Preparation of flockable BTA fibers

Part II: Electrostatic flocking of BTA fibers



Controlled self-assembly complexity:

- Solubility and concentration of the BTA in the selected solvent
- Cooling rate
- Stirring rate



Electrostatic flocking complexity:

- Electric field (distance to electrode)
- Fiber properties (dimensions and shape, conductivity, free-flowing properties)
- Flocking time

Figure 4-4. **Schematic illustration of the two main parts of chapter 4.** Part I: Experimental set-up elaboration for the preparation of BTA fibers suitable for electrostatic flocking. Part II: Subsequent use of prepared supramolecular fibers in an electrostatic flocking set-up top obtain a vertically aligned BTA microfiber array.

To comprehensively investigate the suitability of selected BTA fibers for electrostatic flocking, this chapter covers the following objectives:

- i) Material selection of a suitable BTA
- ii) Preparation of BTA fibers featuring suitable characteristics for electrostatic flocking such as stiffness, aspect ratio and possibility to isolate and handle from solution
- iii) Equipment of processing additives on the BTA fibers surface such as conductivity-enhancing materials to improve free-flowing properties and electrostatic flocking process
- iv) Electrostatic flocking of BTA fibers and characterization of the BTA flocks

4.2 Material selection for suitable supramolecular fibers

This chapter deals with the preparation of supramolecular BTA fibers that exhibit properties being suitable for electrostatic flocking. This requires short supramolecular fibers, which feature a certain stiffness and defined dimensions. For electrostatic flocking, it is favorable to use fibers of similar diameter and similar length resulting in a defined aspect ratio, as too much variety causes a density reduction (flock per cm²) of the flocked material as well as a non-regular surface modulation in terms of fiber height. If a fiber with a larger length will be adhered first, it creates a larger electrostatic field around itself due to the applied voltage. Consequently, the next fiber can only adhere at a specific distance to the already adhered fiber. To avoid such a phenomenon, it is favorable to use homogenous dimensions of the fibers. Thus, the controlled self-assembly in solution at a constant concentration is considered as it allows for the adjustment of the BTA fiber diameter. As elaborated in Chapter 3 *Controlled preparation of supramolecular fibers*, the use of a selected set of conditions BTAs results in a control over the BTA fibers diameter and distribution. Another crucial requirement is that the fibers should exhibit minimal agglomeration, improving the "free-flowing" properties to ensure successful flocking. For instance, if the BTA fibers exhibit nanometer-scale diameters, they tend to agglomerate during drying procedures, which hinders the proper alignment and perpendicular deposition of single fibers during the electrostatic flocking process. Consequently, the choice of an appropriate BTA focuses on stiffness, which is associated with small peripheral groups and fiber diameters in the micrometer range. The studied BTA-1 from Chapter 3 exhibits both of these characteristics and is therefore selected for the upcoming preparation and flocking experiments. The chemical structure of BTA-1 is depicted in Figure 4-5.

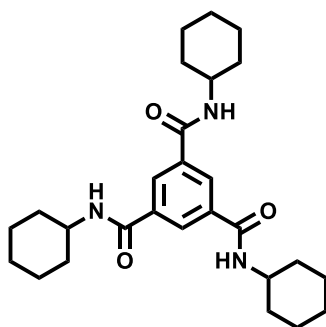


Figure 4-5. **Chemical structure of the selected BTA for electrostatic flocking experiments.** The BTA-1 exhibits a cyclohexyl periphery and self-assembles into rigid microfibers.

For the controlled self-assembly at a constant concentration in solution the following set of conditions is chosen: *i*) a concentration of 0.20 wt.% in MEK resulting in about 1 g BTA-1 fibers each charge, which is suitable for comprehensive and various experiments using the same batch, *ii*) a cooling rate of $0.50\text{ }^{\circ}\text{C min}^{-1}$ and *iii*) a constant stirring at 25 rpm. Fibers produced with these parameters in the custom-made experimental set-up from chapter 3 are shown in Figure 4-6.

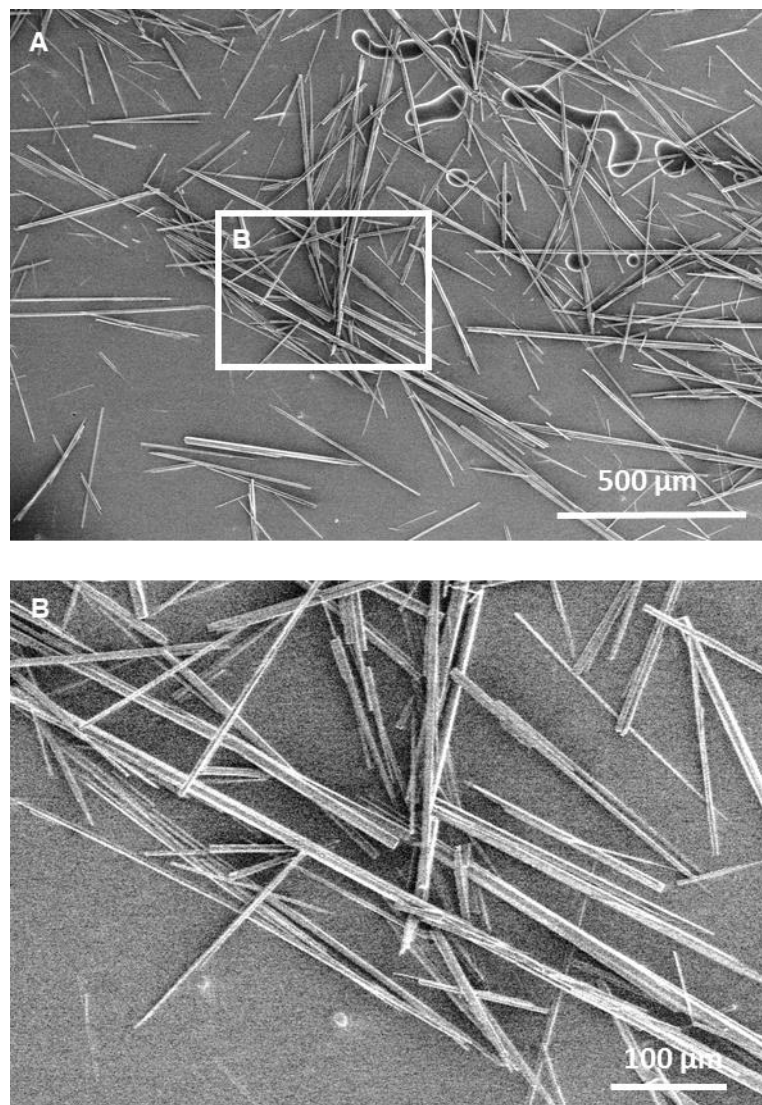


Figure 4-6. **Scanning electron microscopy images of BTA-1 fibers.** **A:** Overview of the prepared BTA fibers. **B:** Magnification of the white box. Set of conditions: concentration of 0.20 wt.% in MEK, cooling rate of $0.50\text{ }^{\circ}\text{C min}^{-1}$ and constant stirring at 25 rpm.

The corresponding histograms were prepared with respect to the fiber diameter and length based on 450 fibers are depicted in Figure 4-7 A and B, respectively. The supramolecular microfibers of BTA-1 show a mean fiber diameter of $8.6 \pm 3.1 \mu\text{m}$ and a mean length of $270 \pm 178 \mu\text{m}$.

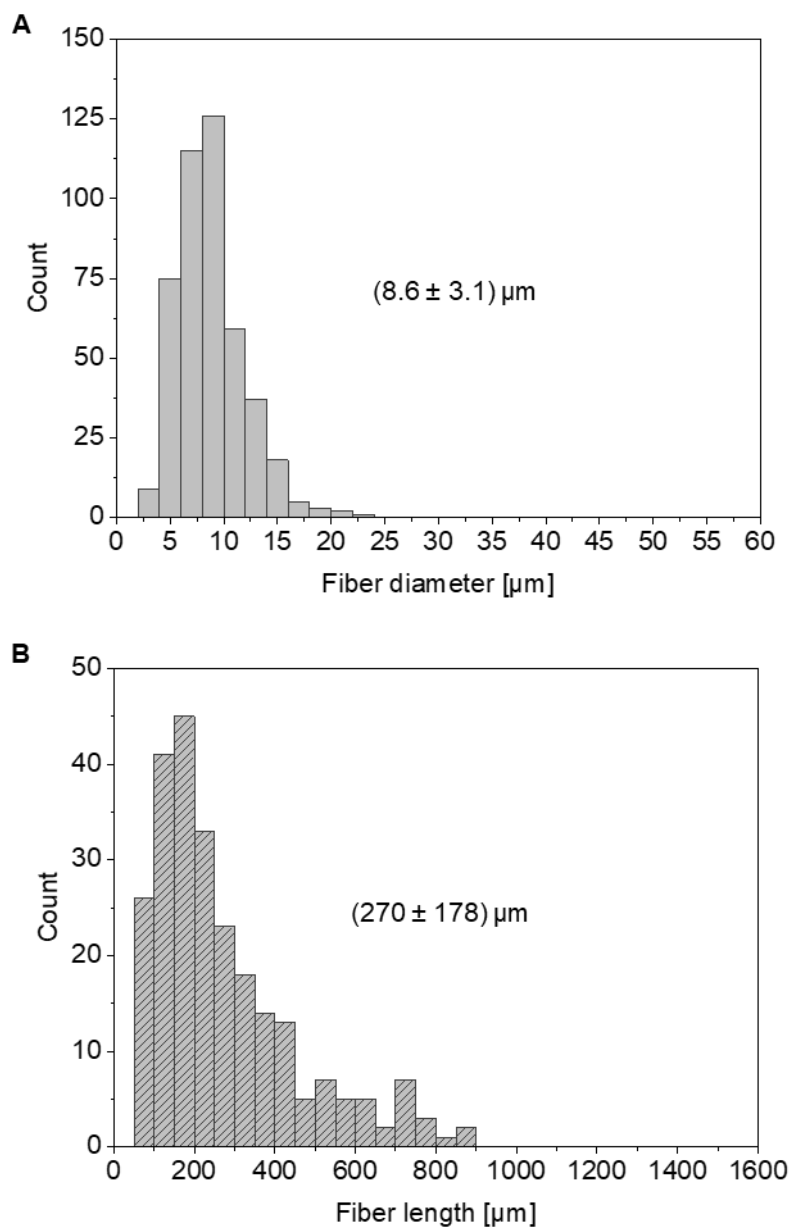


Figure 4-7. **Diameter and length histograms of BTA-1 fibers.** **A:** Fiber diameter distribution. **B:** Fiber length distribution. Set of conditions: stirring rate of 25 rpm, concentration of 0.20 wt.% in MEK and a constant cooling rate of $0.50 \text{ }^\circ\text{C min}^{-1}$.

4.3 Development of electrostatic flocking of supramolecular fibers

4.3.1 Electrostatic flocking device and process

The experimental set-up is based on a WWScenics Pro Grass Applicator Device as depicted in Figure 4-8 and used for the electrostatic down-top flocking process. The electrostatic flocking device consists of a large surface area electrode (~12 cm x 10 cm) and an alligator clamp acting as the ground electrode. The larger area electrode is covered with aluminum foil. Two glass slides are placed at the left and right end to fixate the aluminum foil ensuring a complete contact of the aluminum foil with the electrode. The supramolecular BTA fibers for flocking process are subsequently placed on the aluminum foil (Figure 4-8 A). A SEM stub is clamped to the ground electrode, which acts as substrate where the fibers should be flocked onto (Figure 4-8 B). An adhesive conductive carbon layer is placed on the SEM stub. Thus, flocking is achieved on the surface of the conductive stub, whereas the supramolecular fibers are directly fixated in the adhesive layer. Furthermore, this flocked samples can be directly used for SEM measurements for screening purposes to investigate the flocking morphology on local scale as well as the overall appearance of the flocked sample.

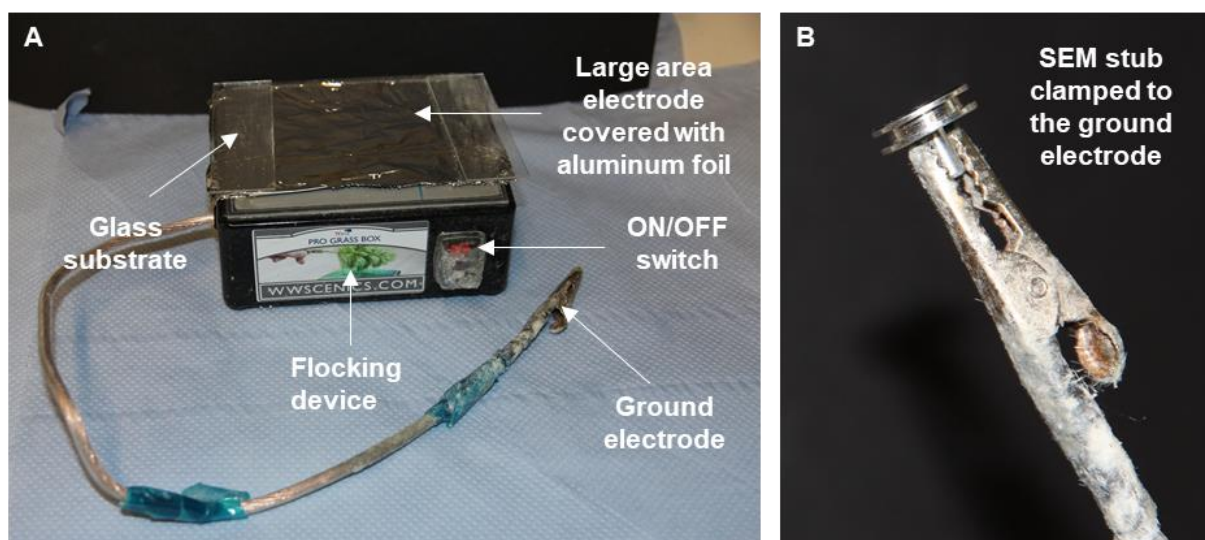


Figure 4-8. **Optical images of the flocking machine and the substrate used for the flocking process.** **A:** Flocking WWScenics Pro Grass Applicator Device with the components: large area electrode covered with aluminum foil and glass substrates to ensure complete contact, ON/OFF switch and the ground electrode. **B:** SEM stub (substrate) clamped to the ground electrode.

4.3.2 Electrostatic flocking of neat supramolecular fibers

The first flocking experiment aims to demonstrate the principal flockability of BTA fibers. Normally, nonconductive material cannot be accelerated in an electric field due to the missing intrinsic charges or no possibility to be charged on the electrode. Typically, fiber charging is achieved through contact charging when a direct current is applied to the electrodes. Fibers placed on the positively charged electrode accumulate positive charge on their surfaces.^[117,122-124] To obtain fiber charging for nonconductive materials the use of conductive-enhancing additives as done for conventional polymers is one common procedure.

As the BTA fibers exhibit a macrodipole, there exists a possibility to be charged on the electrode which lead to the investigation for flockability of neat BTA fibers without any additives. In the first step, the self-assembled BTA fibers need to be isolated from the solution. Figure 4-9 shows the process from self-assembled fibers in solution towards the drying procedure. The self-assembled BTA fibers in the vessel after the controlled self-assembly are depicted in Figure 4-9 A. Most of the solvent MEK can be decanted as the BTA fibers settle down after a while in the solution. This solution is then given through a PET net with a mesh size of 50 μm which is fixated and spanned between two round-shaped magnetic 3-D printed polypropylene holder (Figure 4-9 B) to filter off the self-assembled fibers. The fibers are then washed with water to remove the MEK with residual dissolved BTA as depicted in Figure 4-9 C. The latter step prevents that residual dissolved BTA molecules self-assemble upon drying resulting in an undesired different BTA fiber morphology.

The BTA fibers were isolated from the MEK solution as described above and subsequently dried at 80 °C overnight. The resulting fibers with a mean length of 270 μm and a mean diameter of 8.6 μm still showed some extend of agglomeration after drying.

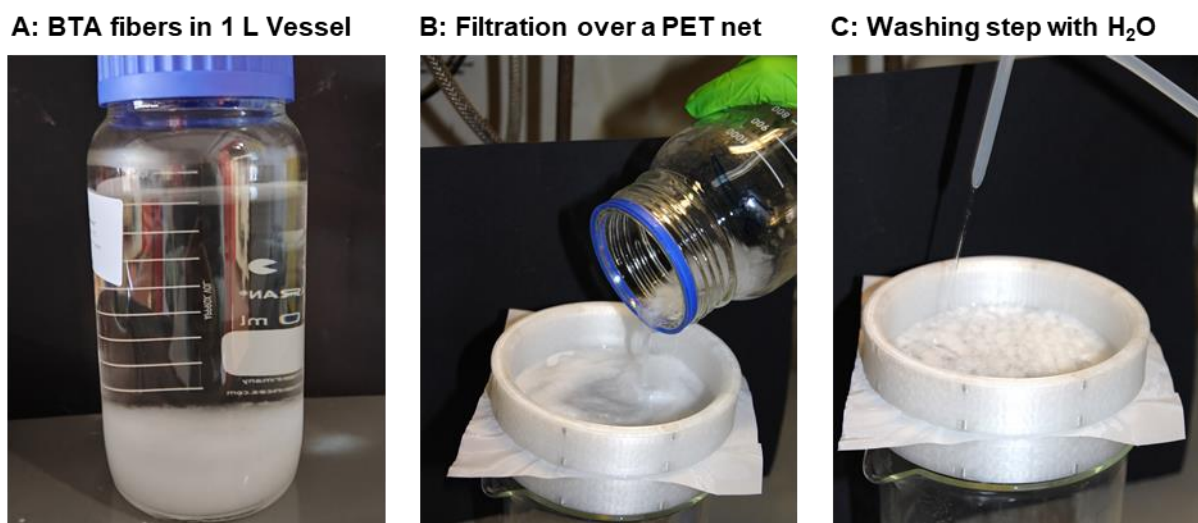


Figure 4-9. **Optical images of the isolation process of BTA fibers after the controlled self-assembly.** **A:** Shows the 1 L vessel with settled BTA fibers after the controlled self-assembly. **B:** Filtration of the BTA fibers over a PET net with a mesh size of 50 μm . **C:** Subsequent washing step with deionized water to remove the residual MEK with dissolved BTA.

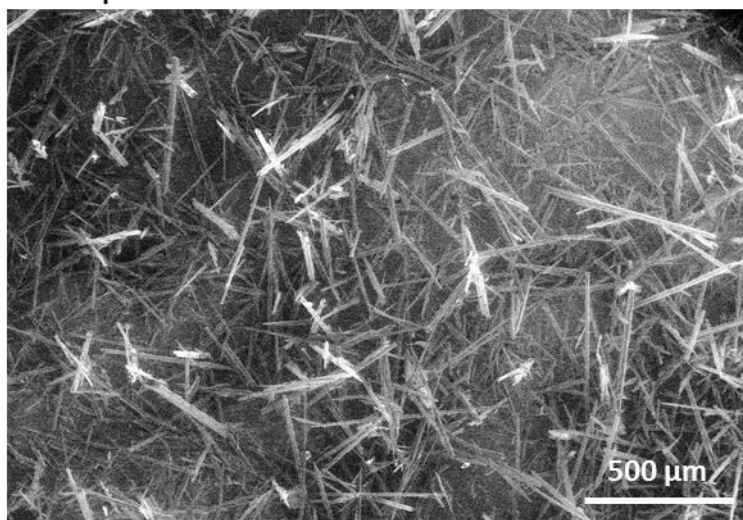
To check the above mentioned expectations that the BTA fibers might be accelerated in an electric field, a first set of experiments was done with the isolated neat BTA fibers. For this, the BTA fibers are deposited on the aluminum foil electrode and The SEM stub connected to the ground electrode was placed at a distance of 3 cm over the aluminum foil. The electric field was applied for 10 seconds. It can be observed, that within the first few seconds, no BTA fibers are accelerated towards the SEM Stub. However, after typically 4-6 seconds the BTA fiber agglomerates start to be transported in the electric field. This indicates that fiber charging took place and that the BTA fibers placed on the positively charged electrode accumulate positive charges on their surfaces. Furthermore, for bottom-to-top processes, it has been observed that the flock fibers move back and forth between the two poles until it is either anchored in the adhesive or falls out of the field.^[117] Exactly this phenomenon has been observed for the BTA agglomerates.

The results of the flocked sample are shown Figure 4-10. It is visible that the BTA fibers are generally flockable and were accelerated within the electric field towards the substrate. However, the flocked BTA fibers on the SEM stub were mostly composed of less-defined agglomerates resulting in most of the fibers laying on the adhesive layer rather than they were vertically aligned. This is a result of the whole agglomerates being accelerated towards the

electrode instead of single BTA fibers. Only some of the fibers are vertically aligned (bright color in the SEM images).

The most important finding here is that supramolecular BTA fibers can be generally accelerated in an electric field without using additives. However, the appearance is not optimal when compared to standard polymer flocks which show higher density and degree of order. Thus, the next step focusses on optimization steps to enhance the flockability and finishing density and the appearance of the BTA fibers.

A: Sample area I



B: Sample area II

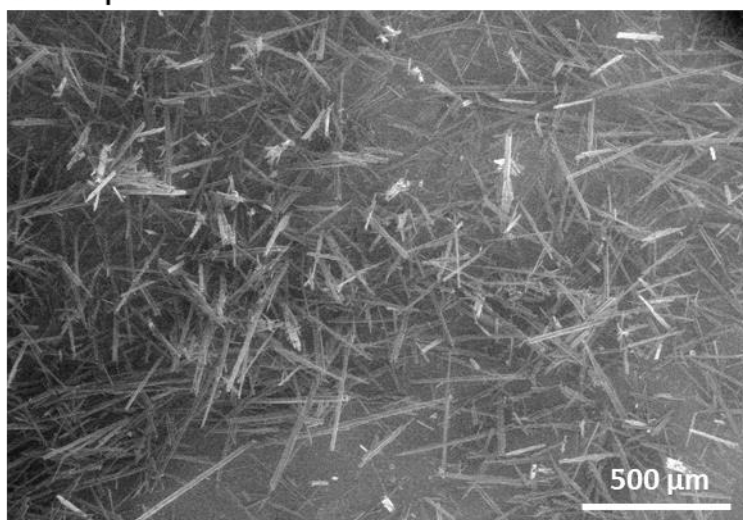


Figure 4-10. **Scanning electron microscopy images of flocked neat BTA fibers on the SEM stub (top view).** BTA fibers were deposited on the electrode as agglomerates. **A** and **B**: different sample areas of the sample.

4.3.3 Optimization of the electrostatic flocking process

For the optimization, two main influences of the electrostatic flocking process are considered: *i*) the dependency on the fiber length and *ii*) the free-flowing properties. Large fiber distribution in length and diameter will reduce the density and appearance of the flock in terms of orientation.^[116] Thus, narrowing fiber length and diameter distributions are promising to optimize the flocking process. Thus, the fiber length distribution of the BTA fibers is tried to be narrowed by a fractionation process as the controlled self-assembly already narrowed the diameter distribution of the supramolecular fibers. Furthermore, to realize flocking of individual BTA fibers, which is a requirement to achieve homogeneous flocks, agglomeration of the BTA fibers to larger less-defined bundles has to be prevented. Very fine, non-agglomerated objects can often freely move through the air and are therefore often regarded as “free-flowing” solids. To prevent agglomeration, salts or charged materials can be used. These materials are known to be conductive-enhancing thus improving the acceleration in the electric field and they increase the free-flowing properties due to less agglomeration.^[117]

a) Development of a size-selection process

The BTA fiber fractionation process using woven fabrics with defined mesh sizes and the corresponding histograms of the BTA fiber length distributions from the fractions are shown in Figure 4-11. The woven fabrics consist of polyethyleneterephthalate (PET) and feature defined mesh sizes ranging from 400 μm , 100 μm to 50 μm . The fractionation process starts from the initial fiber length distribution of $270 \mu\text{m} \pm 178 \mu\text{m}$ obtained after the controlled self-assembly (A). The dispersion of the fibers is filtrated through an assembly of the PET nets of the different sizes (B). Using the fabric with 400 μm mesh size, most of the very long fibers can be retained. However, a significant number of small fibers adhere to the larger ones, resulting in a broad distribution of $439 \mu\text{m} \pm 197 \mu\text{m}$ (C). The fibers collected from the 100 μm mesh have a mean length of $184 \mu\text{m} \pm 84 \mu\text{m}$ (D) and the fibers collected from the 50 μm mesh have a mean fiber length of $110 \mu\text{m} \pm 52 \mu\text{m}$ (E). The fractionation process and the resulting dimensions of the fibers is most successful with mesh size of 100 μm which is considered for the upcoming experiments. The sample of the 50 μm net is not considered due to high agglomeration tendency. Furthermore, scanning electron microscopy images reveal very fine, small fibers adhering on the larger BTA fibers. A more homogenous picture is obtained from the 100 μm net samples. This sieving technique allows a non-destructive fractioning for the BTA length.

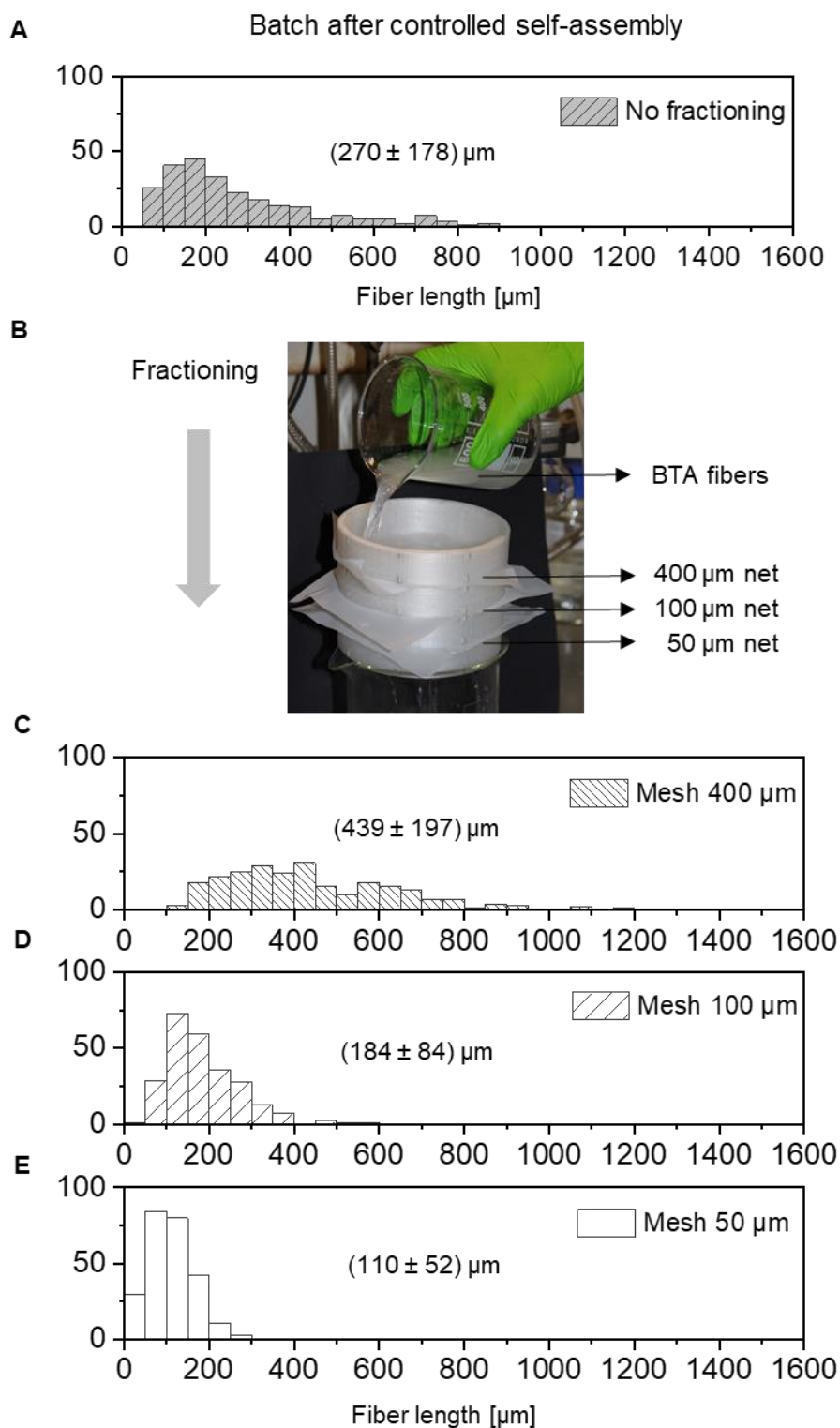


Figure 4-11. **Fractionation process using nets of various mesh sizes (400 μm , 100 μm and 50 μm) and the corresponding histograms of the BTA fiber length distribution from the fractions.** The mean fiber length of the collected fibers on the different nets is summarized for each mesh size in the histograms. **A:** Mean fiber length histogram of the batch after controlled self-assembly with set of conditions: stirring rate of 25 rpm, concentration of 0.20 wt.% in MEK and a constant cooling rate of 0.50 $^{\circ}\text{C min}^{-1}$. **B:** Fractionation process. **C-E:** Mean fiber length histograms of the fractions from the different nets.

b) Equipment with salt and tenside

As described in the previous chapter *Electrostatic flocking of neat supramolecular fibers*, neat BTA fibers can be accelerated within the electric field. However, agglomeration of the BTA fibers prevent an optimal flock appearance. Inspired by the conventional processing of polymer fibers, the next step includes the equipment of BTA fibers with salt. Due to the nonpolar nature of the chosen BTA, the equipment of salt on a BTA fiber from an aqueous solution requires a tenside. The use of a tenside results in a homogeneous dispersion. Here, ammonium sulfate $(\text{NH}_4)_2\text{SO}_4$ was selected as salt to increase the conductivity of the BTA fibers and *N,N,N*-Trimethyl-1-hexadecan-aminiumchloride (CTAC), a cationic tenside was chosen to improve the dispersibility of the BTA in the aqueous solution. The chemical structure of the tenside CTAC is depicted in Figure 4-12.

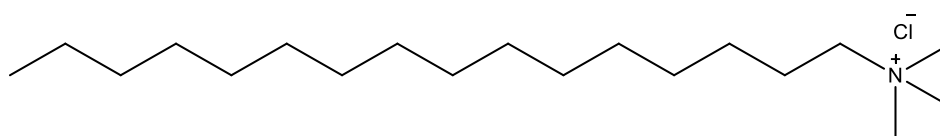


Figure 4-12. Chemical structure of the tenside *N,N,N*-Trimethyl-1-hexadecan-aminiumchloride (CTAC).

The equipment procedure of the BTA fibers is shown in Figure 4-13. After the controlled self-assembly, a batch of about 1 g of all self-assembled BTA fibers is isolated and filtrated over a PET mesh with 50 μm mesh size (Figure 4-13 B). The PET mesh with the BTA fibers is then put into the $(\text{NH}_4)_2\text{SO}_4/\text{CTAC}$ mixture as shown in Figure 4-13 C. The BTA fibers are subsequently transferred into the $(\text{NH}_4)_2\text{SO}_4/\text{CTAC}$ mixture. The resulting homogenous dispersion of BTA fibers equipped with the additives $(\text{NH}_4)_2\text{SO}_4/\text{CTAC}$ in 500 mL deionized water is shown in Figure 4-13 D. In the next step, the fibers are passed through a consecutive series of PET nets as depicted in Figure 4-13 E for sieving. Here, three different PET meshes with mesh size of 400, 100 and 50 μm are assembled from top to bottom each fixated by a magnetic 3-D-printed PP holder. With this method, the BTA fibers with the additives are selected in size as described before. Furthermore, this procedure has the advantage that less BTA fibers are at each net and thus reducing agglomeration. The PET meshes with the defined fibers with additives are dried in an oven at 80 $^\circ\text{C}$ overnight (Figure 4-13 F). The dried equipped BTA fibers are then used for the flocking experiments.

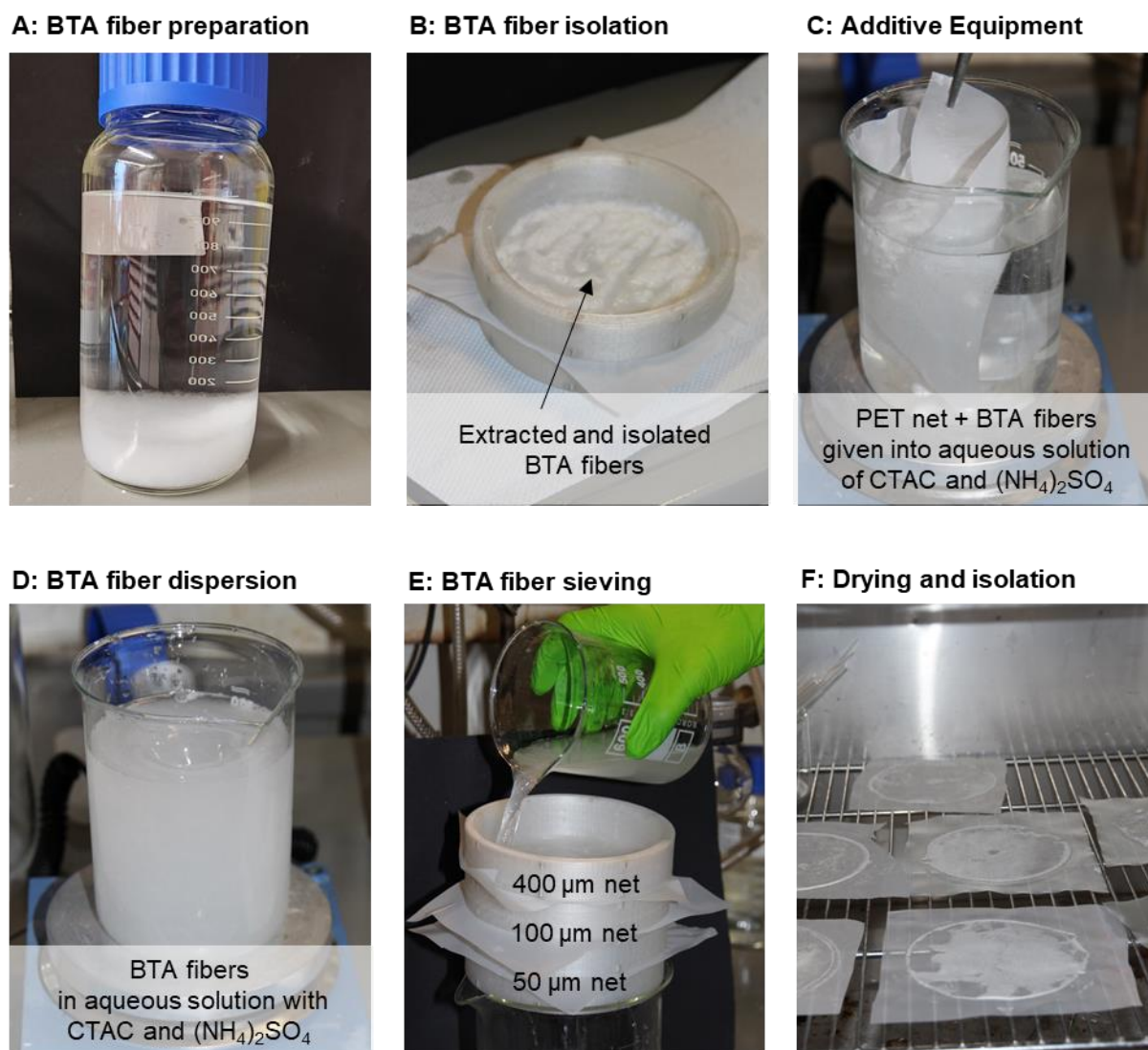


Figure 4-13. **Equipment procedure of BTA fibers with salt $(\text{NH}_4)_2\text{SO}_4$ and tenside (CTAC).** **A:** Defined amount of $(\text{NH}_4)_2\text{SO}_4$ and CTAC are dissolved in 500 mL deionized water. **B:** The prepared BTA fibers under controlled conditions are filtrated through a 50 μm PET net and subsequently washed with deionized water. Image shows the isolated BTA fibers. **C:** The PET net with the deposited BTA fibers is transferred into the $(\text{NH}_4)_2\text{SO}_4$ /CTAC solution. As soon as the BTA fibers are transferred into the solution, the PET net is taken out. **D:** Homogenous BTA fiber dispersion (BTA fibers/ $(\text{NH}_4)_2\text{SO}_4$ /CTAC 500 mL deionized water). **E:** The dispersion is filtrated through an assembly of PET nets (400 μm , 100 μm and 50 μm). **F:** The PET nets with deposited BTA fibers are dried in the oven at 80°C overnight.

To reveal structure-property relations and to identify optimal conditions, several samples were prepared with respect to varying the concentration of $(\text{NH}_4)_2\text{SO}_4$ and CTAC. The investigated different ratios of $(\text{NH}_4)_2\text{SO}_4$ and CTAC to BTA fibers are summarized in Table 4-1. First, the dispersibility in solution and the free-flowing properties resulting after equipment and drying of the BTA fibers were in focus of this study. The concentration of the $(\text{NH}_4)_2\text{SO}_4$ was varied in the range from 0.00 to 2.50 g/L and the CTAC from 0.00 to 1.0 g/L, whereas the amount of BTA fibers were kept constant at 2.00 g/L in all cases. In a first series, a large $(\text{NH}_4)_2\text{SO}_4$

concentration (2.50 g/L) was used and kept constant and the CTAC concentration was lowered successively. It was observed, that 0.10 g of CTAC is sufficient to achieve a homogeneous dispersibility of the BTA fibers. However, the high $(\text{NH}_4)_2\text{SO}_4$ content lead to even more agglomeration than neat BTA fibers, thus the free-flowing properties are low. In the second series the CTAC concentration was kept constant at 0.20 g/L and the amount of $(\text{NH}_4)_2\text{SO}_4$ were lowered successively. With the concentration of 0.20 g/L of CTAC, the dispersibility was good for each sample. Reducing the $(\text{NH}_4)_2\text{SO}_4$ amount eventually lead to better free-flowing properties. A concentration of 0.20 g/L of $(\text{NH}_4)_2\text{SO}_4$ and CTAC is considered as good for dispersibility as well as free-flowing properties. Interestingly, only CTAC as additive leads to good free-flowing properties and thus less agglomerates, too. A sample with only CTAC (increased amount of 0.50 g) and no $(\text{NH}_4)_2\text{SO}_4$ was prepared which showed good dispersibility and free-flowing properties of the BTA fibers, too. In contrast, when using only $(\text{NH}_4)_2\text{SO}_4$ (0.50 g) and no CTAC, the solution is not well-dispersed and big agglomerates of BTA fibers are observed when a sample is dried. This is also valid if no additives are used and the BTA fibers are dried from the MEK solution.

In contrast to the conventional equipment of polymer flock with salt, the results for the equipment of BTA fibers shows that a high amount of $(\text{NH}_4)_2\text{SO}_4$ is counterproductive in terms of the free-flowing properties. Furthermore, it has been tried to break the BTA agglomerates before the flocking process by different methods. Transferring the fibers into a vial and try to loosen up the agglomerates with a spatula results in smaller fibers, however agglomerates are still present. Mixing or shaking the fibers within the vial does not result in better free-flowing properties of the $(\text{NH}_4)_2\text{SO}_4$ equipped samples. Even though free-flowing properties could be enhanced, the samples still show some extend of agglomerates.

Table 4-1. Amount of additives tenside (CTAC) and salt ((NH₄)₂SO₄) in 500 mL water and ~1 g BTA fibers and corresponding dispersibility in solution and free-flowing properties in the dried state.

	CTAC/500 mL H ₂ O	(NH ₄) ₂ SO ₄ /500 mL H ₂ O	Dispersibility	Free-flowing properties
Series I	0.50 g	1.25 g	✓	~
	0.25 g	1.25 g	✓	~
	0.10 g	1.25 g	✓	~
Series II	0.10 g	1.00 g	✓	~
	0.10 g	0.75 g	✓	~
	0.10 g	0.50 g	✓	~
	0.10 g	0.25 g	✓	~
	0.10 g	0.10 g	✓	✓
	0.10 g	0.00 g	✓	✓
Series III	0.50 g	0.00 g	✓	✓
	0.00 g	0.50 g	~	~
	0.00 g	0.00 g	~	~

c) Application methods onto the electrode

In the conventional top-down electrostatic flocking process of polymer fibers a big brush transfers the fibers through a net which are then subsequently accelerated in the electric field towards the substrate. Even though conventional flock fibers are mostly free-flowing due to the equipment of additives, agglomerates can be present. Transferring through a net ensures that single fibers are accelerated in the electric field rather than agglomerated fibers. Similarly, to polymer fibers, BTA fibers tend to agglomerate. This may already occur in the storage vials in solution and especially after drying.

Whereas tensides reduces the agglomeration, the next step addresses the application method to transfer the BTA fibers directly onto the electrode of the flocking machine with the aim to further reduce agglomeration. Inspired by the top-down electrostatic flocking process, this should lead to an increased number of single BTA fibers on the electrode, less agglomerates and thus better behavior in the flocking process.

At first, the BTA fibers were brushed through a metal net onto the electrode. However, this method seems to cause too much abrasion. Thus, a new method has been implemented to reduce the amount agglomerated BTA fibers and being non-disruptive. Here, two brushes are used as exemplarily shown in Figure 4-14. The bigger brush is used to collect the BTA fibers (A) and the smaller brush is used to deposit the BTA fibers onto the electrode by going over the bigger brush with BTA fibers (B) resulting in deposition of BTA fibers onto the electrode (C). Big agglomerates which have been deposited too are removed before the flocking process. The agglomerates which are still visible by eye will either loosen up during the flocking process or not accelerated towards the substrate.

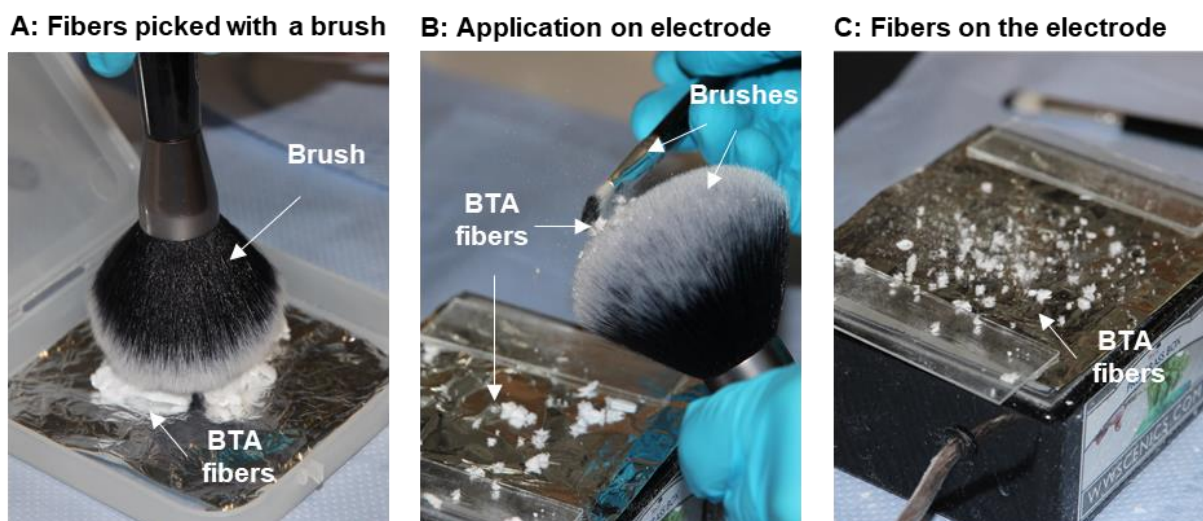
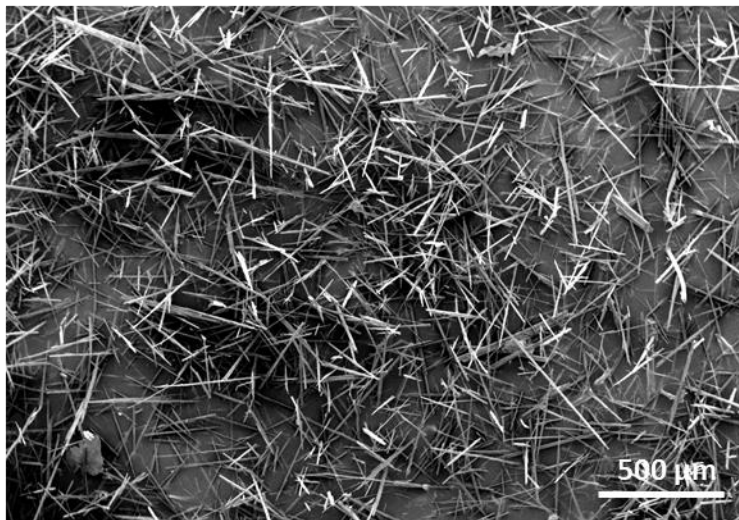


Figure 4-14. **Deposition of BTA fibers onto the electrode of the flocking machine using two brushes.** **A:** The agglomerated BTA fibers are picked up and deposited on the bigger brush. **B:** The BTA fibers are brushed onto the electrode with the help of a second brush. **C:** Deposited BTA fibers on the aluminum covered electrode.

An example of BTA fibers flocked with this method is shown Figure 4-15. For this, the equipped BTA fibers with a concentration of 0.20 g/L of each additive (CTAC and $(\text{NH}_4)_2\text{SO}_4$) are used. The overall appearance shows a reduced density of BTA fibers. Most of the fibers are standing in the substrate proving the successful flocking. During the process, it was observed that the fibers accelerate towards the substrate after a few seconds when the power was switched on. Similar as seen for the neat BTA fibers, which could be explained by the necessary fiber charging at the beginning of the process.

A: Sample area I



B: Sample area II

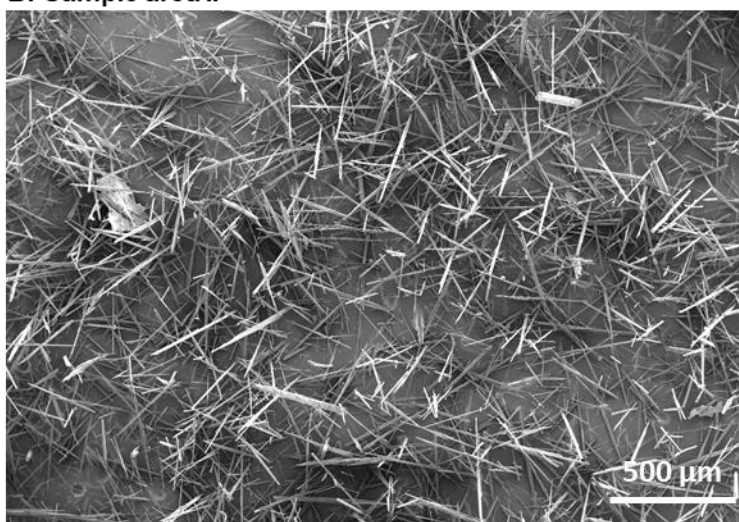


Figure 4-15. **Top view of scanning electron microscopy images of flocked BTA fibers equipped with 0.20 g/L of CTAC and $(\text{NH}_4)_2\text{SO}_4$. BTA fibers were deposited on the electrode by the two-brush method. A and B: show two different sample areas.**

4.3.4 Electrostatic flocking of equipped BTA fibers

In the next step, all samples of the equipped BTA fibers with different $(\text{NH}_4)_2\text{SO}_4$ and CTAC concentrations were tried to be flocked. For this, supramolecular BTA fibers with dimensions of typically 184 ± 84 are used (fraction from 100 μm PET net). The results are summarized in Table 4-2. The flocked samples were analyzed by scanning electron microscopy to state the appearance. From Table 4-2 can be seen that samples prepared from solution with high $(\text{NH}_4)_2\text{SO}_4$ content of 2.50 g/L (series I) and 2.00 g/L (series II) are not flockable, which means that the agglomerates were not accelerated in the electric field. This was expected as the prior equipment tests have shown no sufficient free-flowing properties. The fibers have a strong tendency to form strongly bonded agglomerates and are clumped together. These agglomerates cannot be easily broken up and therefore almost no single fibers deposited on the substrate during the flocking process despite the amount of reduced CTAC within the series.

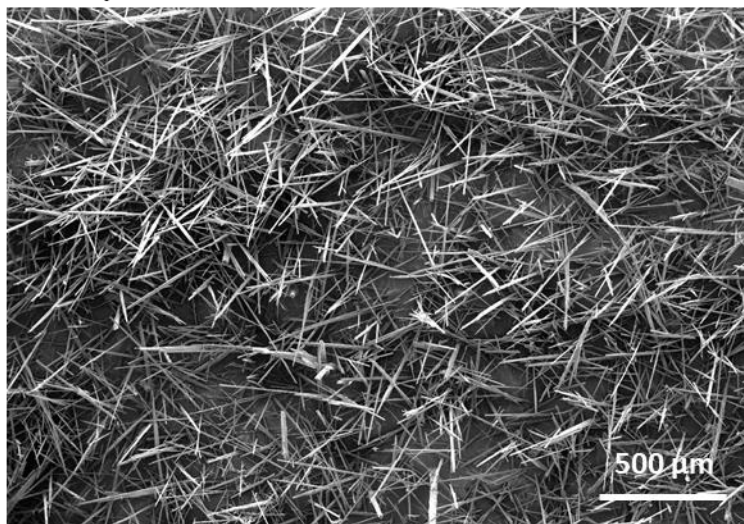
The free-flowing properties can be enhanced by using less $(\text{NH}_4)_2\text{SO}_4$ amount in the dispersions and 0.20 g/L and constant CTAC concentration of 0.20 g/L (series II) and directly correlates with the flockability. Here, electrostatic flocking was possible for $(\text{NH}_4)_2\text{SO}_4$ concentrations of 1.50 g/L and lower. Interestingly, the appearance of the flocked BTA fibers varied in dependency of the salt content. With higher $(\text{NH}_4)_2\text{SO}_4$ amount, most of the BTA fibers were adhered to the ground instead of the desired vertically alignment in the adhesive. The lower the $(\text{NH}_4)_2\text{SO}_4$ amount, the better the flockability and appearance of the flock in terms of density and fiber orientation. Good flocking performance was obtained for the sample with 0.20 g/L of CTAC and $(\text{NH}_4)_2\text{SO}_4$. Here, good coverage and vertically aligned fibers were obtained (see Figure 4-15) which can be explained to good free-flowing properties. Interestingly, when reducing the $(\text{NH}_4)_2\text{SO}_4$ amount to zero with a CTAC concentration of 0.20 g/L, the coverage decreases again. This might be explained by the reduced charges without $(\text{NH}_4)_2\text{SO}_4$. Nevertheless, it was observed that the fibers with only CTAC were mostly vertically aligned.

Table 4-2. Summary of the amount of the used additives (CTAC and CTAC / (NH₄)₂SO₄) for BTA fiber equipment in dependency of flockability and flock appearance.

	CTAC / (NH ₄) ₂ SO ₄ in g/L	Flockability and Appearance
Series I	1.00 / 2.50	Not flockable
	0.50 / 2.50	Not flockable
	0.20 / 2.50	Not flockable
Series II	0.20 / 2.00	Not flockable
	0.20 / 1.50	Flockable, few fibers
	0.20 / 1.00	Flockable, few fibers
	0.20 / 0.50	Flockable, few fibers
	0.20 / 0.20	Flockable, good coverage
	0.20 / 0.00	Flockable, few fibers
Series III	1.00 / 0.00	Flockable, best performing
	0.00 / 1.00	Not flockable
	0.00 / 0.00	Flockable, few fibers

In the last series, the BTA fibers are equipped with only one of the additives with concentrations of 1.00 g/L each. While only (NH₄)₂SO₄ equipment lead to no flockability due to agglomerates, the sample with CTAC shows best performing flocking properties. The agglomerates of this sample were easy to break up, showing good free-flowing properties. The overall appearance shows an increased density of BTA fibers as depicted in Figure 4-16. The BTA fibers stand mostly vertically aligned. The flocking density increase of the sample with 1.00 g/L CTAC compared to the sample with 0.20 g/L of CTAC and (NH₄)₂SO₄ might be explained by combination of two effects: free-flowing properties and fiber charging. The free-flowing properties are increased and less agglomerates are observed for the sample with only CTAC. Furthermore, it is assumed that the CTAC is easier attached to the BTA fibers due to the tenside character with a nonpolar chain and a polar headgroup. As the BTA features a nonpolar nature, it is assumed that the nonpolar tenside part likely attach to the BTA fibers and the polar head facing outwards.

A: Sample area I



B: Sample area II

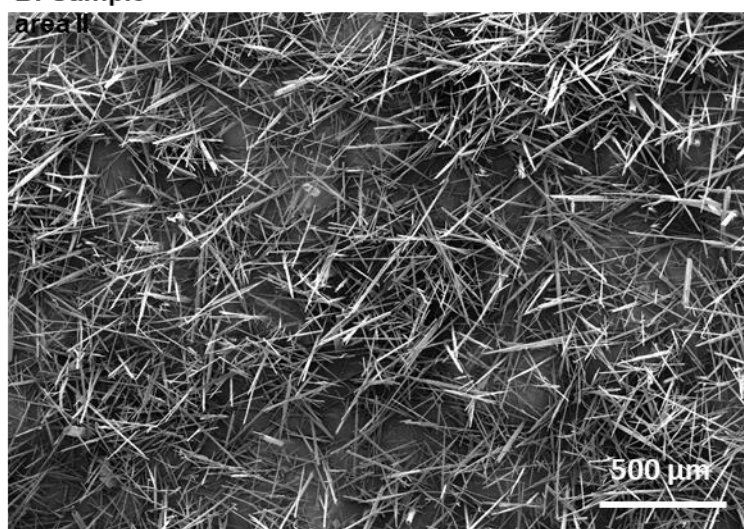
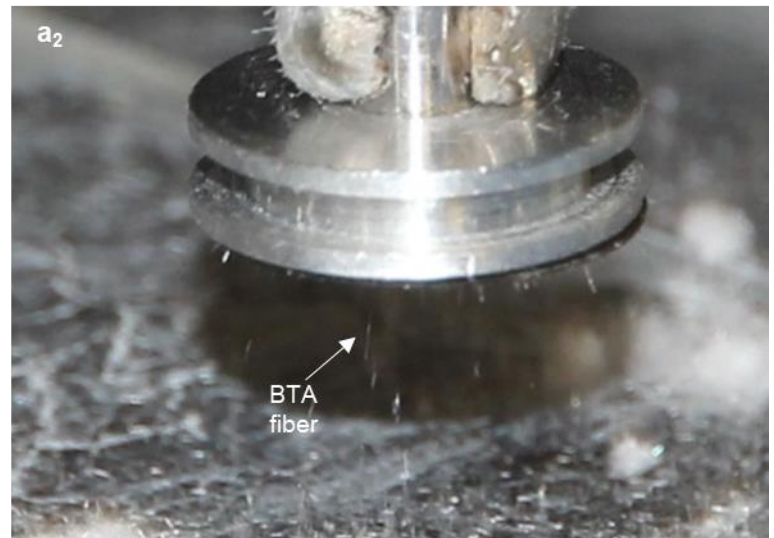
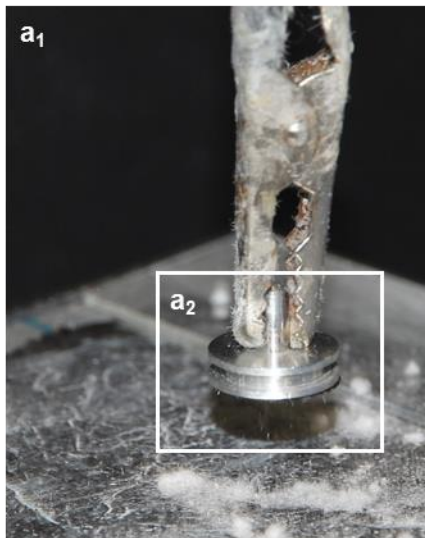


Figure 4-16. **Top view of scanning electron microscopy images of flocked BTA fibers equipped with 1.00 g/L of CTAC.** BTA fibers were deposited on the electrode by the two-brush method. **A** and **B**: show two different sample areas.

During the electrostatic flocking process, the BTA fibers seem to be accelerated easily and mostly single fibers are flying towards the SEM stub. The process and evolution of the flocking process was captured with a single-lens reflex camera and is depicted in Figure 4-17. Single BTA fibers are accelerated towards the SEM stub which can be seen in Figure 4-17 A after the electric field is switched on for 6 seconds. Two seconds later (8 seconds into flocking process), the BTA fibers are still accelerating towards the SEM stub. It can be clearly seen, that the BTA fibers are adhered in the carbon layer of the substrate on the SEM stub (Figure 4-17 B).

A: 6 seconds into flocking



B: 8 seconds into flocking

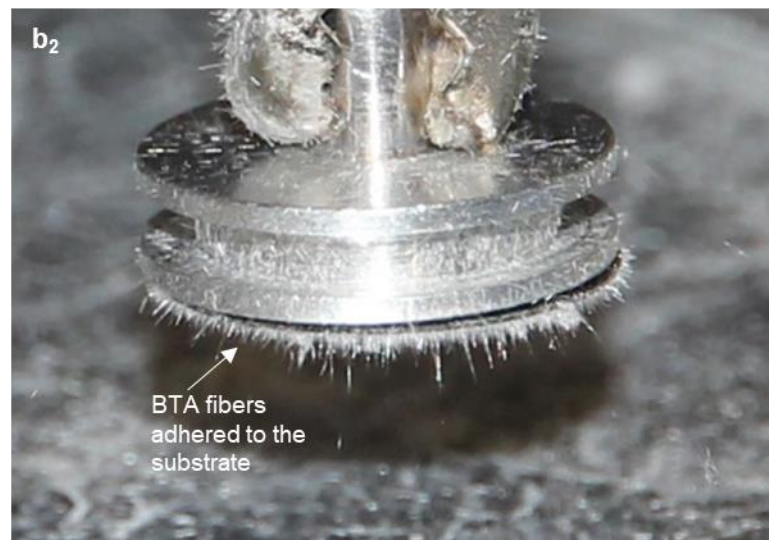
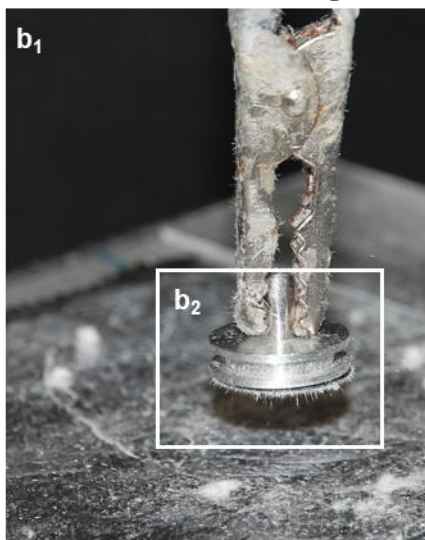


Figure 4-17. **The process and evolution of the flocking process obtained using equipped BTA fibers with 1.00 g/L CTAC. A:** single BTA fibers are accelerated towards the SEM stub after 6 seconds when the electric field is switched on. **a₁:** Overview and **a₂:** magnification. **B:** Two seconds later (8 seconds into flocking process), the BTA fibers are still accelerating towards the SEM stub and the BTA fibers are adhered in the carbon layer on the SEM stub. **b₁:** Overview and **b₂:** magnification

The last sample in the series III are the neat BTA fibers, i.e. no additives. As known from the previous chapter, neat BTA fibers can be flocked, however, the agglomeration leads to less free-flowing properties and most BTA fibers laying in the adhesive. As the two-brush method seem to be the most promising to deposit the BTA fibers onto the electrode and loosen up agglomerates, neat BTA fibers has been tested with this method, too. The results are shown in the SEM images of Figure 4-18. The density seems to be quite similar to the samples deposited without the two-brush method, however the overall appearance regarding the alignment is optimized. Nevertheless, samples treated with CTAC still have best performing flocking properties and thus are used in the upcoming chapter for the optimized electrostatic flocking.

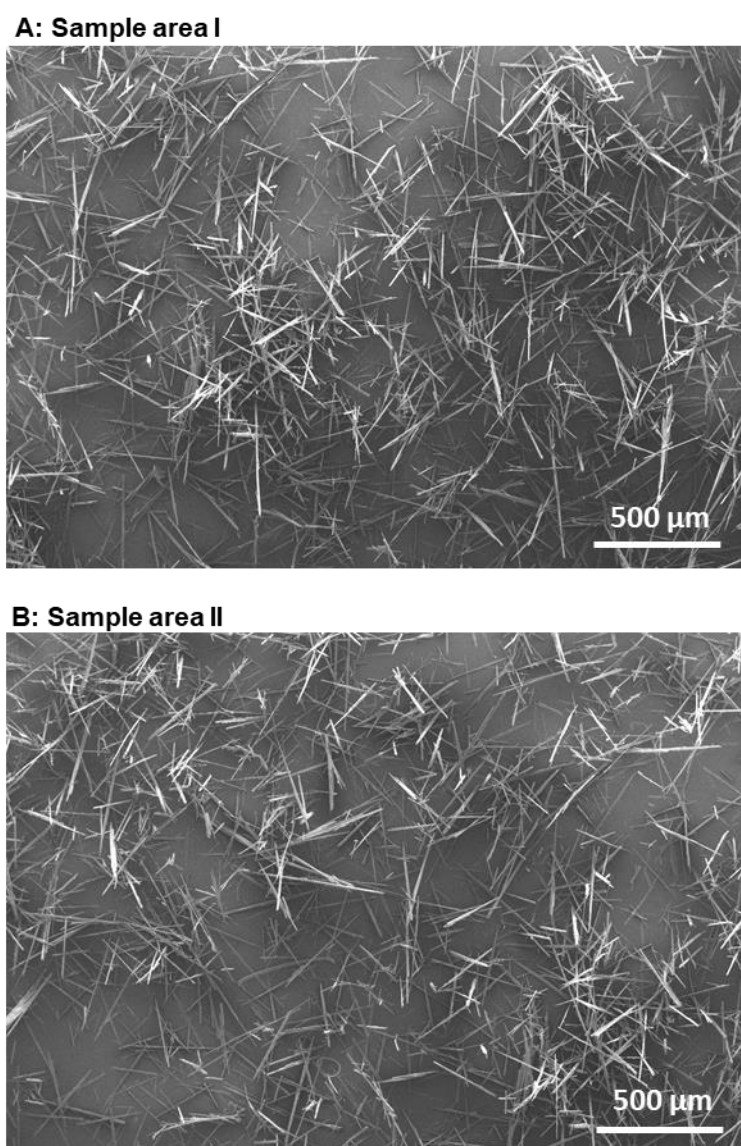


Figure 4-18. **Top view of scanning electron microscopy images of flocked neat BTA fibers.** BTA fibers were deposited on the electrode by the two-brush method. **A** and **B**: show two different sample areas.

4.4 Electrostatic flocking with optimized conditions

From previous experiments aiming for optimization in the flocking process for BTA fibers the following influences were determined and optimized:

- i.* Isolation process of BTA fibers after controlled self-assembly
- ii.* Sieving and fractionation process regarding BTA fiber length (size selection: fibers from the 100 μm net)
- iii.* Equipment with conductive-enhancing material with suitable concentration (1.0 g/L CTAC) for fiber charging and free-flowing properties
- iv.* Application method onto the electrode (two brush method)

The following chapter uses these optimized conditions to flock CTAC equipped BTA fibers and investigate the influence of the flocking time and evaluation of the flock density. The properties of the supramolecular flock are further evaluated with respect to their orientation and supramolecular fiber length.

4.4.1 Influence of the flocking time

In addition to dependencies on fiber length and free-flowing properties which have been optimized in the previous chapters, electrostatic flocking and the density of the resulting flock is dependent on the flocking time. Typically, the longer the flocking time the higher the fiber density. Thus, the flocking time was altered to investigate whether the density can be increased with increasing time. Therefore, the optimized BTA fibers – equipped with CTAC and fraction from 100 μm net - are used and the flocking time was raised from 10 s (A) to 20 s (B) and 30 s (C). The increasing coverage on the used SEM stub is optically visible with increasing flocking time as depicted in Figure 4-19. Most of the fibers show vertical alignments which is supported by the cross-section supplements the top view revealing that most of the fibers are vertically aligned and coverage increases with flocking time (see Figure 4-20).

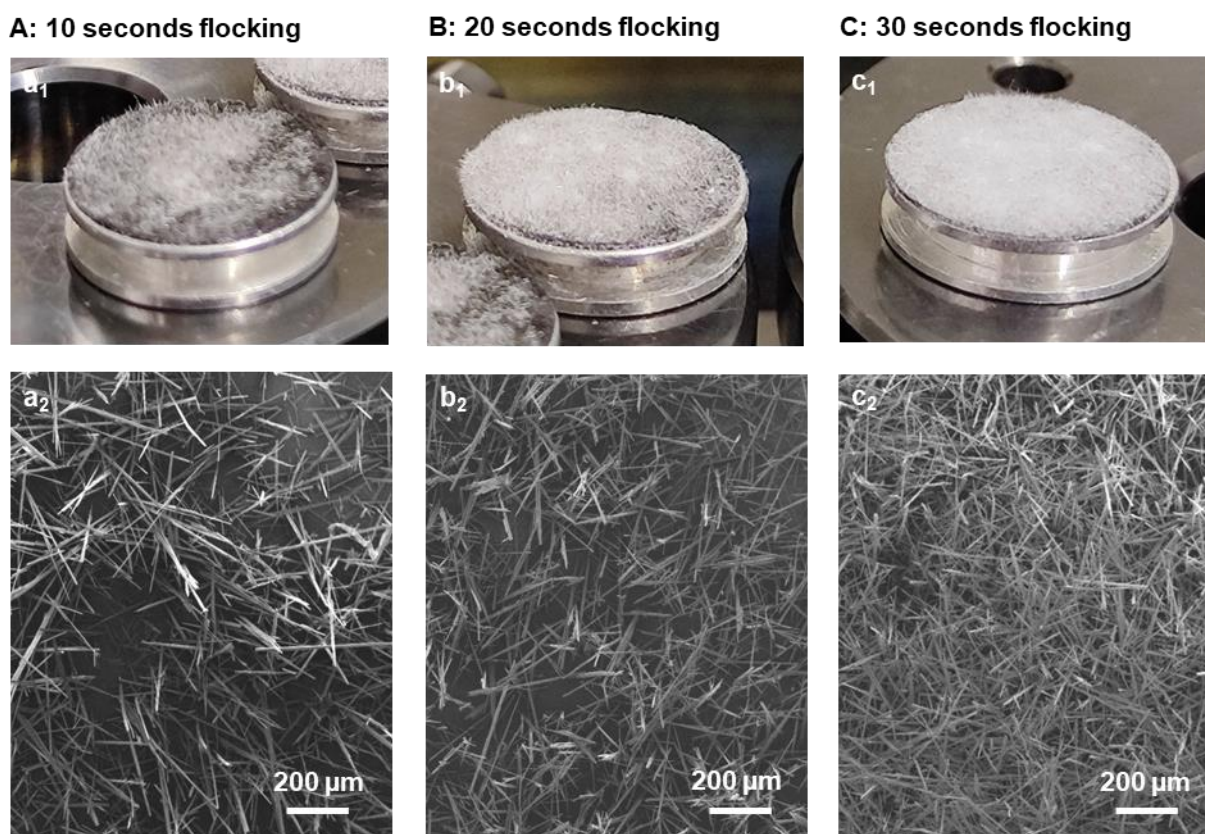
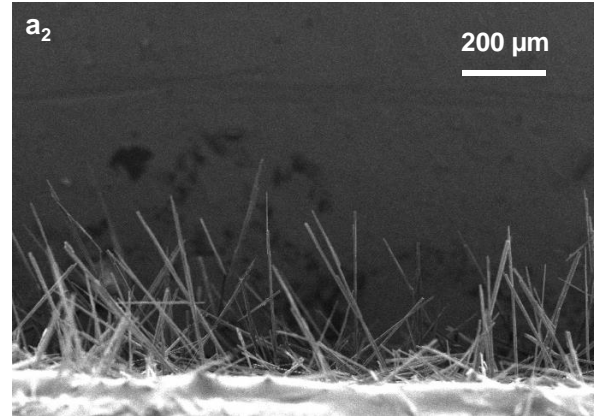
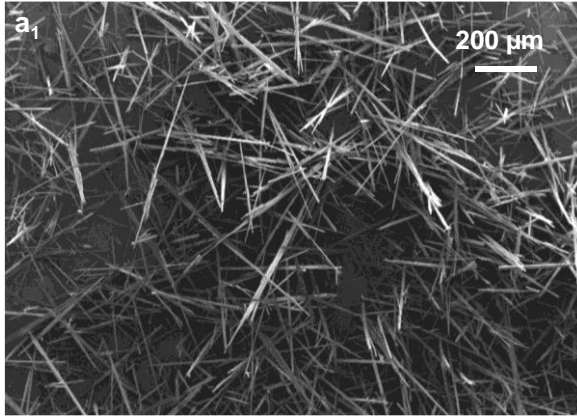
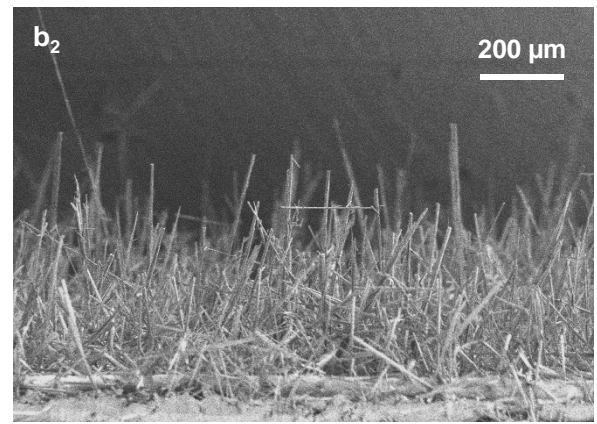
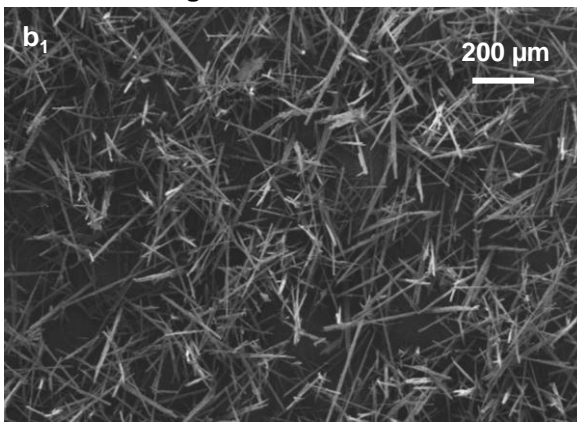


Figure 4-19. **Flocked BTA samples on SEM stubs prepared with different flocking times. A:** Flocking time of 10 seconds, **B:** 20 seconds and **C:** 30 seconds. **a₁-c₁:** SEM stub of the flocked samples. **a₂-c₂:** top view of corresponding scanning electron microcopy images of the flocked samples.

A: 10 s flocking time



B: 20 s flocking time



C: 30 s flocking time

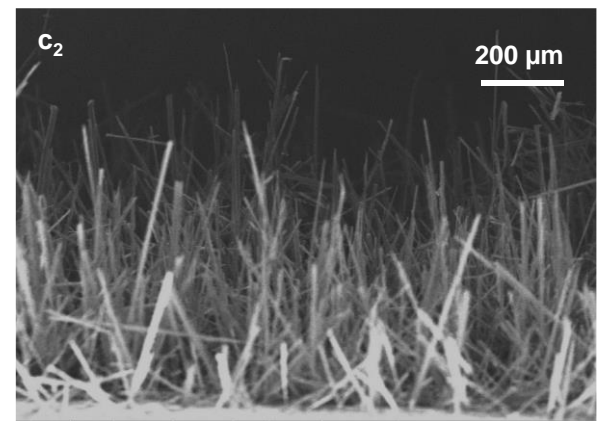
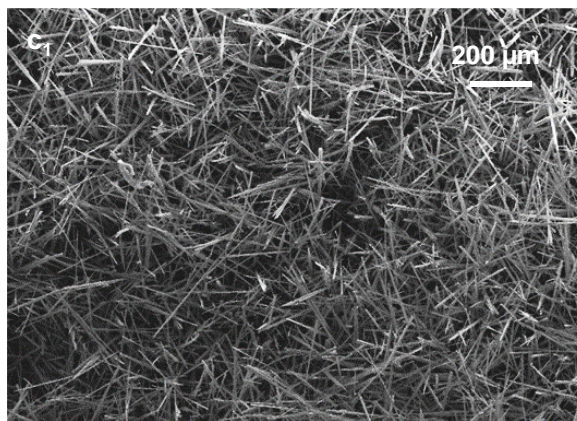


Figure 4-20. Scanning electron microcopy images of the top view and the corresponding cross-sections of BTA samples flocked with different flocking times. **A:** Flocking time of 10 seconds, **B:** 20 seconds and **C:** 30 seconds. **a₁-c₁:** Top view of the sample. **a₂-c₂:** cross-section of the sample.

4.4.2 Orientation of the supramolecular fibers

A further observation was made after analysing the morphology of the flocked sample. As a plate to point electrode set-up is used, the electric field lines will follow as described in Figure 4-21 A. This leads to a specific orientation of the BTA fibers at the edge of the SEM stub as schematically depicted. The corresponding SEM images are shown in Figure 4-21 B for the left side of the SEM stub (b_1) and right side of the SEM stub (b_2). This is a clear evidence that the BTA fibers are accelerated in the electric field and follow the field lines.

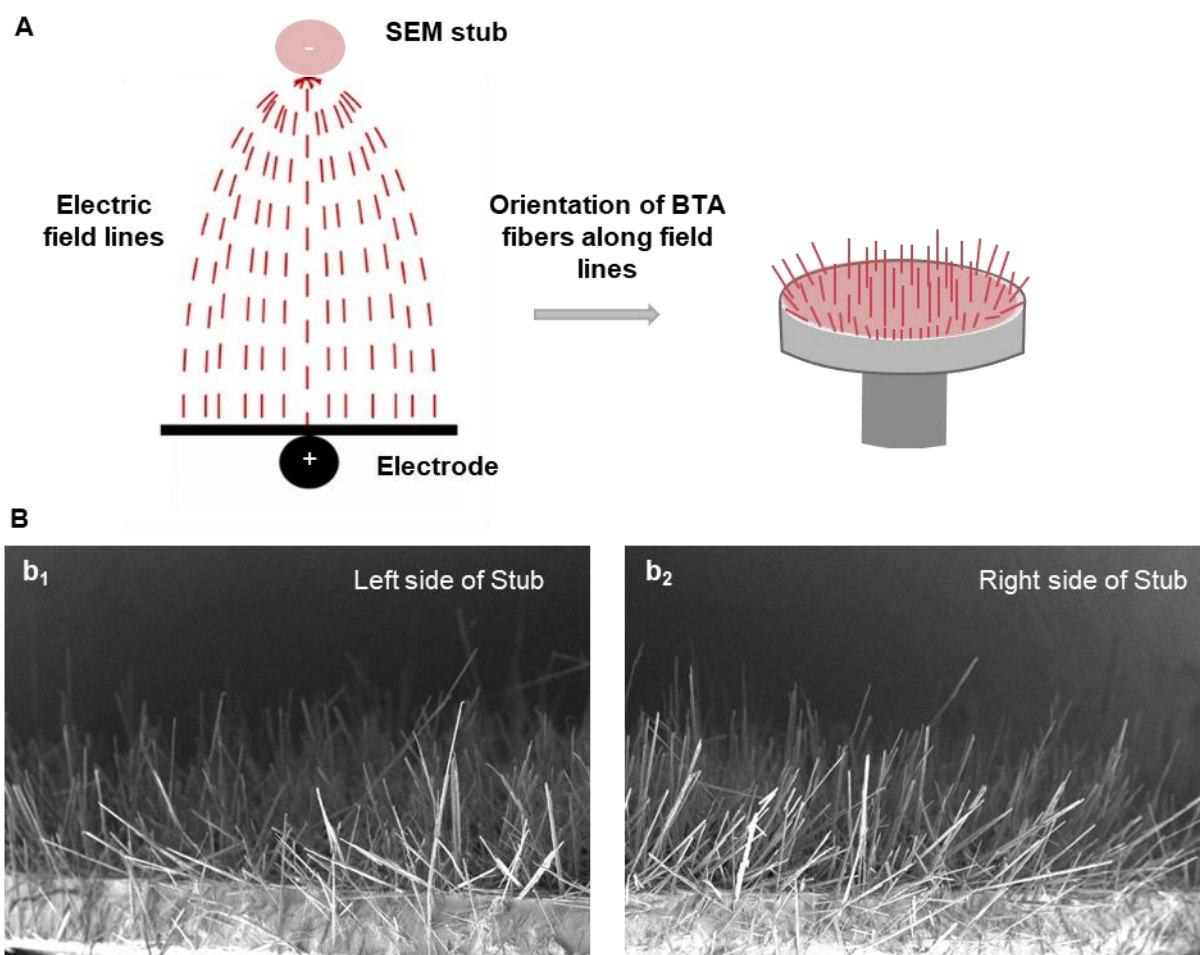


Figure 4-21. **Schematic presentation of the electric field lines and the orientation of the BTA fibers along the field lines.** **A:** Illustration of the plate to point electrode set-up and the corresponding electric field line generation with orientation of the BTA fibers. **B:** Resulting flocked BTA sample. **b_1 and b_2 :** Cross-section of the flocked sample revealing the orientation of the BTA fibers on the SEM stub, which initially followed the electric field lines.

4.4.3 Properties of the supramolecular flock

Finally, the samples were analyzed regarding the fiber length and orientation depending on the flocking time. The results are summarized in Table 4-3. Starting with the fiber length, which has been evaluated from the cross-section images from the corresponding flock samples. The fiber length is quite similar for all three flocking times with about 250 μm . This was expected as the same samples from the fractioning process of the 100 μm net are used with a mean length of $184 \pm 84 \mu\text{m}$. Interestingly, the larger fibers of the sample seem to be accelerated preferably leading to slight distribution shift towards $\sim 250 \mu\text{m}$.

The orientation for all samples is calculated from the cross-section images and defined as $0^\circ < \Theta < 180^\circ$; angles of zero and 180 degree refer to an orientation parallel to the substrate and the degree of 90 represent a perpendicular orientation. The perpendicular orientation thus represents a perfect aligned flock sample. The supramolecular flock samples show an orientation in the range of 70 degree for all flocking times. The angle with respect to the substrate below 90° can be explained by the small distance of the two electrodes to generate a sufficient electric field. If the distance between the two electrodes is too small, fibers may not rotate sufficiently, and their angle will be well below 90° . However, an average angle of 70° is representative for typical polymer flocks^[116] and thus a typical orientation of the supramolecular flock is achieved.

Table 4-3. Fiber length and orientation of the BTA flock in dependence on the applied flocking time.

Flocking time	Fiber length	Orientation
Sample 10 s	$235 \pm 98 \mu\text{m}$	$68 \pm 16^\circ$
Sample 20 s	$257 \pm 93 \mu\text{m}$	$70 \pm 17^\circ$
Sample 30 s	$250 \pm 90 \mu\text{m}$	$68 \pm 19^\circ$

In summary, electrostatic flocking of BTA fibers was achieved by using a controlled shape and dimension of the self-assembled fibers and optimization procedure with a conductivity enhancing material.

4.5 Conclusion to electrostatic flocking of supramolecular fibers

In this chapter the objective was to achieve *electrostatic flocking using supramolecular fibers* for the first time with the aim to fabricate densely packed and vertically aligned BTAs. Electrostatic flocking is an industrial technique that accelerates and aligns short cut polymer microfibers in an electric field ultimately promoting their perpendicular arrangement on substrates used for various applications. One key requirement for electrostatic flocking is a suitable aspect ratio and very defined dimensions, both are challenging to achieve for supramolecular fibers by self-assembly. Thus, specifically strongly rigid BTA fibers with a cyclohexyl periphery and narrowly distributed diameters and lengths from the first part of the thesis were selected as promising candidate. In particular, the defined fiber lengths with narrow distributions were successfully achieved by developing a straightforward non-destructive sieving process. Thus, BTA fibers with the dimensions of a mean diameter with $9 \pm 3 \mu\text{m}$ and $270 \pm 178 \mu\text{m}$ are prepared in a custom-made experimental set-up. A multi-step sieving process allows to isolate fibers with a narrower distribution of the mean length such as with $184 \mu\text{m} \pm 84 \mu\text{m}$. Interestingly it was shown that neat BTA fibers without additives can be successfully flocked. This supports the hypothesis that their intrinsic macrodipole moment facilitates fiber alignment within an electric field. However, further improvement regarding flockability and the final density of the BTA fibers was necessary. Thus, efforts were made to optimize the free-flowing properties of the BTA fibers to transport single fibers in the electric field. This was achieved by using a tenside which also features conductivity-enhancing properties. With this equipment of the BTA fibers, higher flocking densities and more vertical fiber alignment was realized. It was also shown that the density can be tailored by adjusting the flocking time. The longer the flocking time, the denser the BTA flock.

5 Self-assembly of supramolecular fibers within polymer flocks

Approach of self-assembly of supramolecular fibers within polymer flocks

BTAs are widely known to form supramolecular fibers from solution upon cooling or solvent evaporation. This process highly depends on the molecular structure, the solvent, the concentration and the starting temperature or thermal processing window. In this situation, it is expected that at a certain point during processing, (homo)nuclei are formed in solution, which continuously grows to fiber by consuming the dissolved molecular building blocks in the solution. The vessel walls are mainly expected to play no or a minor role for the nucleation process. Typically, this applies also if self-assembly proceeds in thin liquid films close to substrates such as glass slides. Using porous structures such as nets, woven fabrics or nonwovens allows for the self-assembly within these supports resulting in fiber-fiber composites. This is achieved by immersion of the support structure into a BTA solution, whereas the solution is soaked in by capillary forces. Upon removing the support, the solvent starts to evaporate resulting in an increase of the BTA concentration, which ultimately initiates the fiber formations. The highly porous micro or nanofiber-based support structure strongly increases the contact of the building blocks to the heterogeneous structure but do not necessarily initiate the self-assembly by the heterogeneous fibers. This was demonstrated by D. Weiss et al.^[135] or H. Misslitz et al.^[105], which showed that homogeneous supramolecular fibers are formed within conventional polyester/viscose nonwovens. The supramolecular fibers span over the pores of the nonwoven and wrap around the polymer microfibers. This fiber-fiber composite can be beneficially used as air filter media. This situation changes if the BTA seeds are deposited on electrospun fibers of a nonwoven as shown by M. Burgard et al.^[113] Differently, off-standing BTA fibers are observed, whose morphology resembles natural penguin-downy feathers which has been also used for air filtration applications. The same applies if nonwovens with suitable patchy micelles are decorated. However, in this case it is assumed that structural similar groups resulting in a concentration increase of the BTAs close to the patches, which ultimately leads to the initiation of the self-assembly of BTAs.^[54,114] In all of the cases above, with and without nucleation, the supramolecular fibers are formed randomly within the scaffold. Also, due to the different pore sizes and the fiber layers within a nonwoven, the drying process is rather complex.

In this chapter, the self-assembly process in a different porous support, i.e. polymer flocks, is presented. Differently to the nonwovens mentioned above, a polymer flock consists of vertically aligned polymer microfibers fabricated via electrostatic flocking. The array of the oriented microfibers features capillary effects, which are different to statistically deposited fiber layers in nonwovens. This feature of the polymer flocks opens completely new possibilities for self-assembly of BTAs from solution. To comprehensively study the self-assembly of BTAs within the polymer flock and the influencing parameters the following investigations are addressed:

- i)* Material selection of BTAs
- ii)* Solubility studies of the selected BTAs in polar solvents
- iii)* Self-assembly studies of the selected BTAs upon solvent evaporation
- iv)* Selection and preparation of a polymer flock substrate
- v)* Self-assembly studies of the BTAs within polymer flocks upon solvent evaporation

5.1 Material selection of BTAs

In general, BTAs form supramolecular fibers with a distinct morphology in solution depending on the set of conditions such as solvent, concentration and temperature profile. Changing towards other methods such as self-assembly upon solvent evaporation directly impacts the self-assembly behavior. Furthermore, prior research has demonstrated that the selection of a support can also have an impact on BTA self-assembly and the resulting morphology.^[54,105,113,135] In this work a polymer flock, i.e. vertically aligned polar polymer microfibers such as polyamides will be selected as support for the self-assembly of BTAs upon solvent evaporation. Thus, a critical process parameter is the solvent, because it must *i)* allow for the dissolution/self-assembly of the building blocks, *ii)* evaporable at mild conditions, *iii)* suitable to interact with the polymer flocks (and the respective capillary forces).

Therefore, BTAs with functional peripheral groups were selected, which are expected to meet these features. The polar peripheral groups make them soluble in polar organic solvents such as alcohols and thus suitable for the use upon solvent evaporation in the chosen polyamide flock. The selected BTAs as depicted in Figure 5-1 are two derivatives with sulfur-containing groups, BTA-3 (A) with a methionine methyl ester periphery and BTA-4 (B) featuring a 2-(methylthio)ethyl periphery. The third derivative exhibits peripheral groups with *N,N*-diisopropylaminoethyl functionality, namely BTA-5 (C).

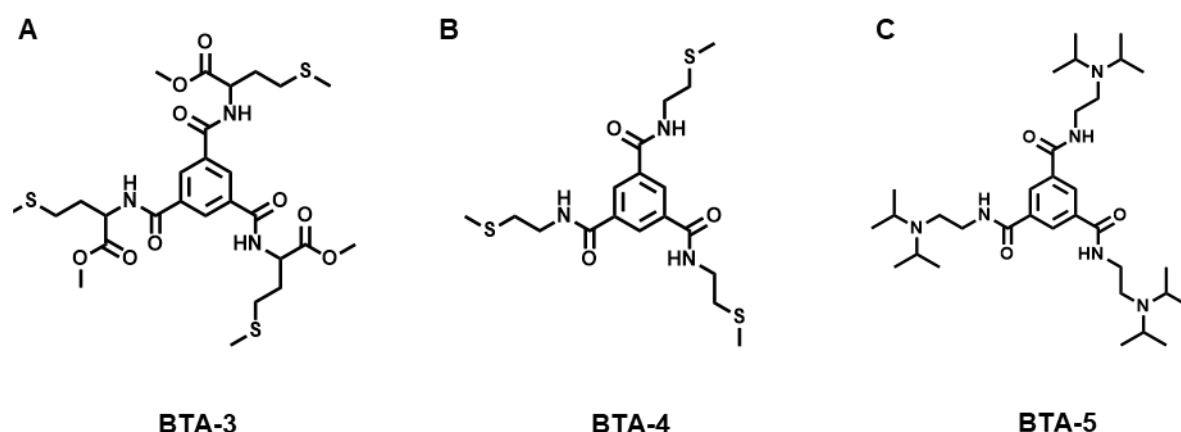


Figure 5-1. **Chemical structures of the selected BTA derivatives.** **A:** BTA-3 with a methionine methyl ester periphery. **B:** BTA-4 with a 2-(methylthio)ethyl periphery. **C:** BTA-5 with a *N,N*-diisopropylaminoethyl periphery.

5.2 Solubility and self-assembly studies of the selected BTAs

5.2.1 Solubility studies of the selected BTAs in polar solvents

The three BTAs are first investigated regarding their solubility and self-assembly behavior in 2-propanol at different temperatures. To get more detailed information of the self-assembly behavior at constant concentration, temperature-dependent turbidity measurements were performed to determine the cloud and clearing points. For all BTAs concentrations from 0.05 wt.% up to 4.25 wt.% in 2-propanol were prepared at room temperature. The samples were isothermal heated at 75 °C for 30 minutes at 600 rpm to ensure complete solubility of the BTA. Samples that showed no fully dissolved solution at these conditions were considered as “not completely soluble”. After the isothermal step and first dissolution, the temperature-dependent transmittance of each sample was recorded for three cycles upon heating and cooling with a rate of 0.10 °C min⁻¹ or 0.50 °C min⁻¹ in the range from 75 °C to 0 °C while stirring with 600 rpm. The change in transmittance upon cooling from 100 % to 0 % is defined as cloud point and indicates the self-assembly of BTAs into turbid solutions. In contrast, the change in transmittance upon heating from 0 % to 100 % is defined as clearing point since dissolution occurs resulting in a clear solution. Cloud and clearing points were determined at 50% of transmittance.

In the following, the three selected BTAs are described in the following order a) Methionine methyl ester substituted BTA (BTA-3), b) 2-(methylthio)ethyl substituted BTA (BTA-4) and c) *N,N*-diisopropylaminoethyl substituted BTA (BTA-5).

a) Self-assembly in solution of BTA-3

The first BTA derivative, which was investigated regarding its solubility was the methionine methyl ester substituted BTA (see Figure 5-2 A). For this, the temperature-dependent turbidity measurements were performed to determine the cloud and clearing points by means of transmittance. Based on all solubility measurements the concentration-dependent development of the cloud and clearing points of the BTA-3 in 2-propanol as mean values including the standard deviation from the applied three heating and cooling cycles were obtained. With this data a phase diagram of the BTA-3 in 2-propanol from 5 to 75 °C can be created as depicted in Figure 5-2 B. The phase diagram can be divided into three regions:

- **Region I:** *In this region, no self-assembly takes place.* Here, the BTA-3 is fully soluble in 2-propanol at low concentrations in the temperature range from 5 °C to 75 °C. This is valid for concentrations up to 0.05 wt.%.
- **Region II:** *In this region, controlled self-assembly takes place.* The BTA-3 self-assembles into fibers upon cooling and reversibly dissolves upon heating the sample. This is observed for concentrations of 0.05 wt.% - 2.50 wt.%. The cloud points increase from 9 °C (0.05 wt.%) to 70°C (2.50 wt.%) with increasing concentration of the BTA. Concentrations > 0.30 wt.% result in a fibrous gel structure of the BTA-3. The clearing points raising from 19 °C (0.05 wt.%) to 72 °C (2.50 wt.%). Above the clearing points, the BTA-3 is completely dissolved again. The high reproducibility of the self-assembly process is indicated by the small error bars of the mean values for the cloud and clearing points.
- **Region III:** *In this region, no controlled self-assembly takes place.* For concentrations larger than 2.50 wt.% in 2-propanol, BTA-3 is not completely soluble anymore even at elevated temperatures. Self-assembly occurs upon cooling the solution, because not dissolved BTAs are still present in the solution, acting as nuclei and trigger further growth. This results in a mixture of bulk material and supramolecular fibers.

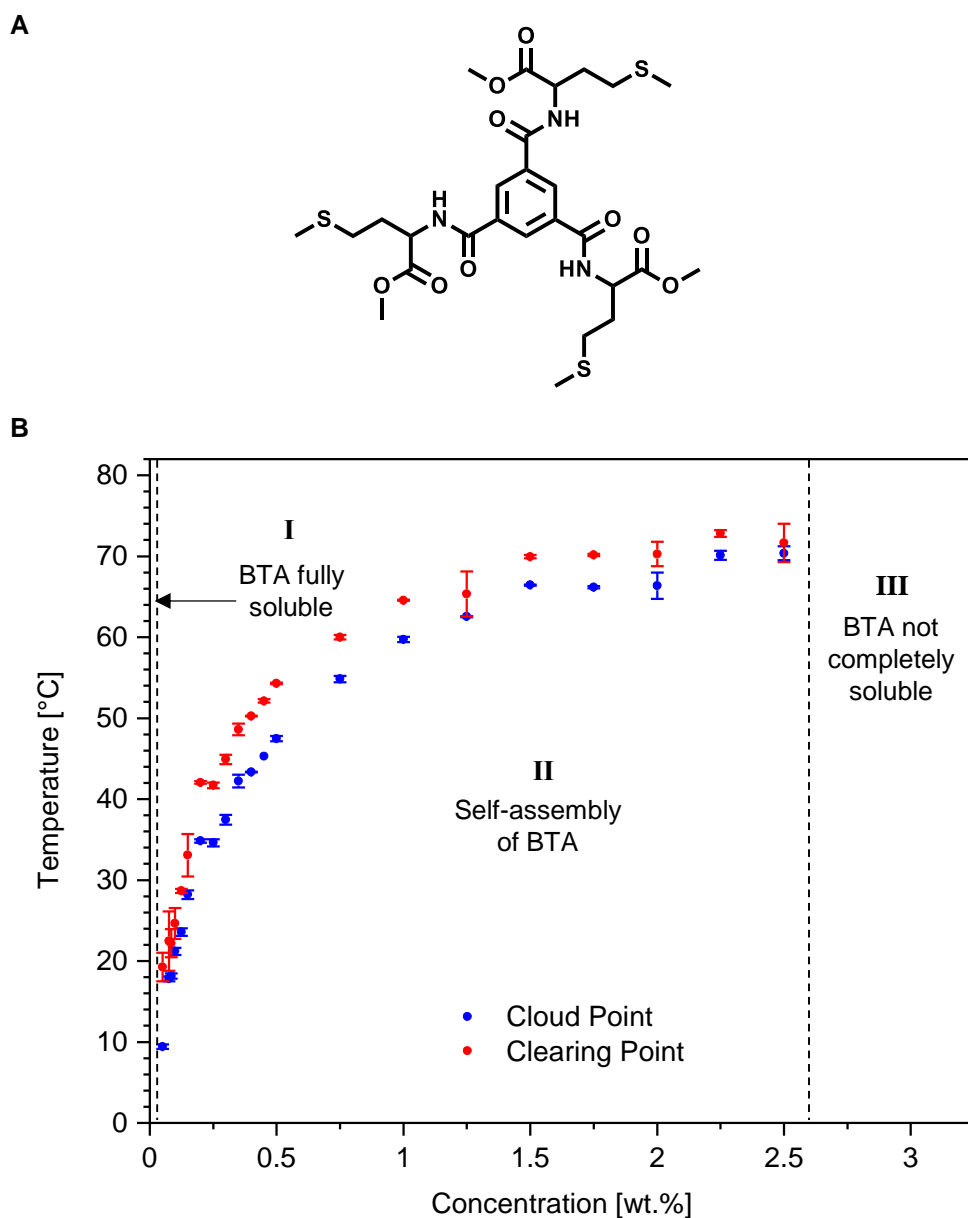


Figure 5-2. **Phase-diagram of methionine methyl ester substituted BTA (BTA-3) in 2-propanol.** **A:** Chemical structure of BTA-3. **B:** The concentration-dependent development of the cloud and clearing points of the BTA-3 in 2-propanol as mean values including the standard deviation from the applied three heating and cooling cycles with a scanning rate of $0.50\text{ }^{\circ}\text{C min}^{-1}$. Region I: No self-assembly takes place as the BTA-3 is fully soluble in 2-propanol at low concentrations up to 0.05 wt.% in the given temperature range. Region II: Controlled self-assembly of the BTA-3 self-assembly upon cooling and reversibly dissolution upon heating the sample for concentrations 0.05 wt.% - 2.50 wt.%. Region III: No controlled self-assembly takes place as the BTA-3 is not completely soluble anymore for concentrations > 2.50 wt.%.

b) Self-assembly in solution of BTA-4

The next BTA which is investigated regarding its solubility in 2-propanol is the 2-(methylthio)ethyl substituted BTA (see Figure 5-3 A). The phase diagram extracted from the turbidity measurements is depicted in Figure 5-3 B and shows the three typical regions:

- **Region I:** *In this region, no self-assembly takes place.* Here, the BTA-4 is fully soluble in 2-propanol at low concentrations in the temperature range from 5 °C to 75 °C. This is valid for concentrations up to 0.35 wt.%.
- **Region II:** *In this region, controlled self-assembly takes place.* The BTA-4 self-assembles into fibers upon cooling and reversibly dissolves upon heating the sample. This is observed for concentrations of 0.35 wt.% - 2.0 wt.%. The cloud points increase from 5 °C (0.35 wt.%) to 41 °C (2.0 wt.%) with increasing concentration of the BTA-4. The clearing points raising from 21 °C (0.35 wt.%) to 51 °C (2.0 wt.%). Above the clearing points, the BTA-4 is completely dissolved again. The high reproducibility of the self-assembly process is indicated by the small error bars of the mean values for the cloud and clearing points.
- **Region III:** *In this region, no controlled self-assembly takes place.* For concentrations larger than 2.0 wt.% in 2-propanol, BTA-4 is not completely soluble anymore even at elevated temperatures. Self-assembly occurs upon cooling the solution, because not dissolved BTAs are still present in the solution, acting as nuclei and trigger further growth. This results in a mixture of bulk material and supramolecular fibers.

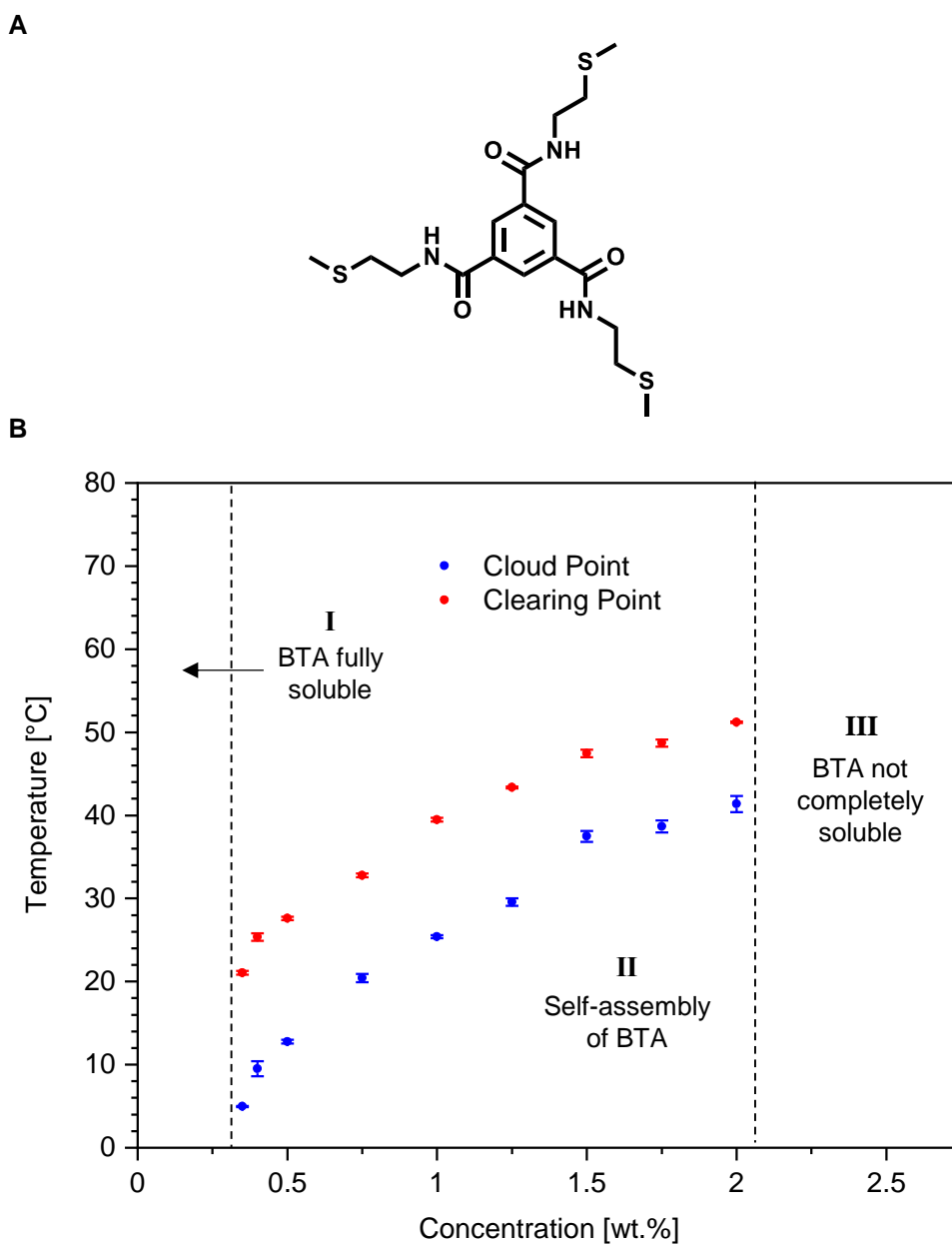


Figure 5-3. **Phase-diagram of 2-(methylthio)ethyl substituted BTA (BTA-4) in 2-propanol.** **A:** Chemical structure of BTA-4. **B:** The concentration-dependent development of the cloud and clearing points of the BTA-4 in 2-propanol as mean values including the standard deviation from the applied three heating and cooling cycles with a scanning rate of $0.50\text{ }^{\circ}\text{C min}^{-1}$. Region I: the BTA-4 is fully soluble in 2-propanol at low concentrations up to 0.35 wt.% in the given temperature range. Region II: BTA-4 self-assembly upon cooling and reversible dissolution upon heating the sample for concentrations of 0.35 wt.% - 2.0 wt.%. Region III: the BTA-4 is not completely soluble anymore for concentrations $> 2.0\text{ wt.}\%$.

c) Self-assembly in solution of BTA-5

Changing the molecular structure from the sulfur-containing peripheral groups towards the *N,N*-dialkylamine (Figure 5-4 A) influences the solubility in 2-propanol and thus the self-assembly behavior. The results of the temperature-dependent turbidity measurements were summarized in a phase diagram of BTA-5 in 2-propanol as depicted in Figure 5-4 B. Again, the three typical regions can be identified in the phase diagram:

- Region I: *In this region, no self-assembly takes place.* Here, the BTA-5 is fully soluble in 2-propanol at low concentrations in the temperature range of 5 °C to 75 °C. This is valid for concentrations up to 0.50 wt.%.
- Region II: *In this region, controlled self-assembly takes place.* The BTA-5 self-assembles into a fibrous gel upon cooling and reversibly dissolves upon heating the sample. This is observed for concentrations of 0.75 wt.% - 4.0 wt.%. The cloud points increase from 10 °C (0.75 wt.%) to 63 °C (4.0 wt.%) with increasing concentration of the BTA-5. The clearing points raising from 27 °C (0.75 wt.%) to 68 °C (4.0 wt.%). Above the clearing points, the BTA-5 is completely dissolved again. The high reproducibility of the self-assembly process is indicated by the small error bars of the mean values for the cloud and clearing points.
- Region III: *In this region, no controlled self-assembly takes place.* For concentrations larger than 4.0 wt.% in 2-propanol, BTA-5 is not completely soluble anymore even at elevated temperatures. Self-assembly occurs upon cooling the solution, because not dissolved BTAs are still present in the solution, acting as nuclei and trigger further growth. This results in a mixture of bulk material and supramolecular fibers.

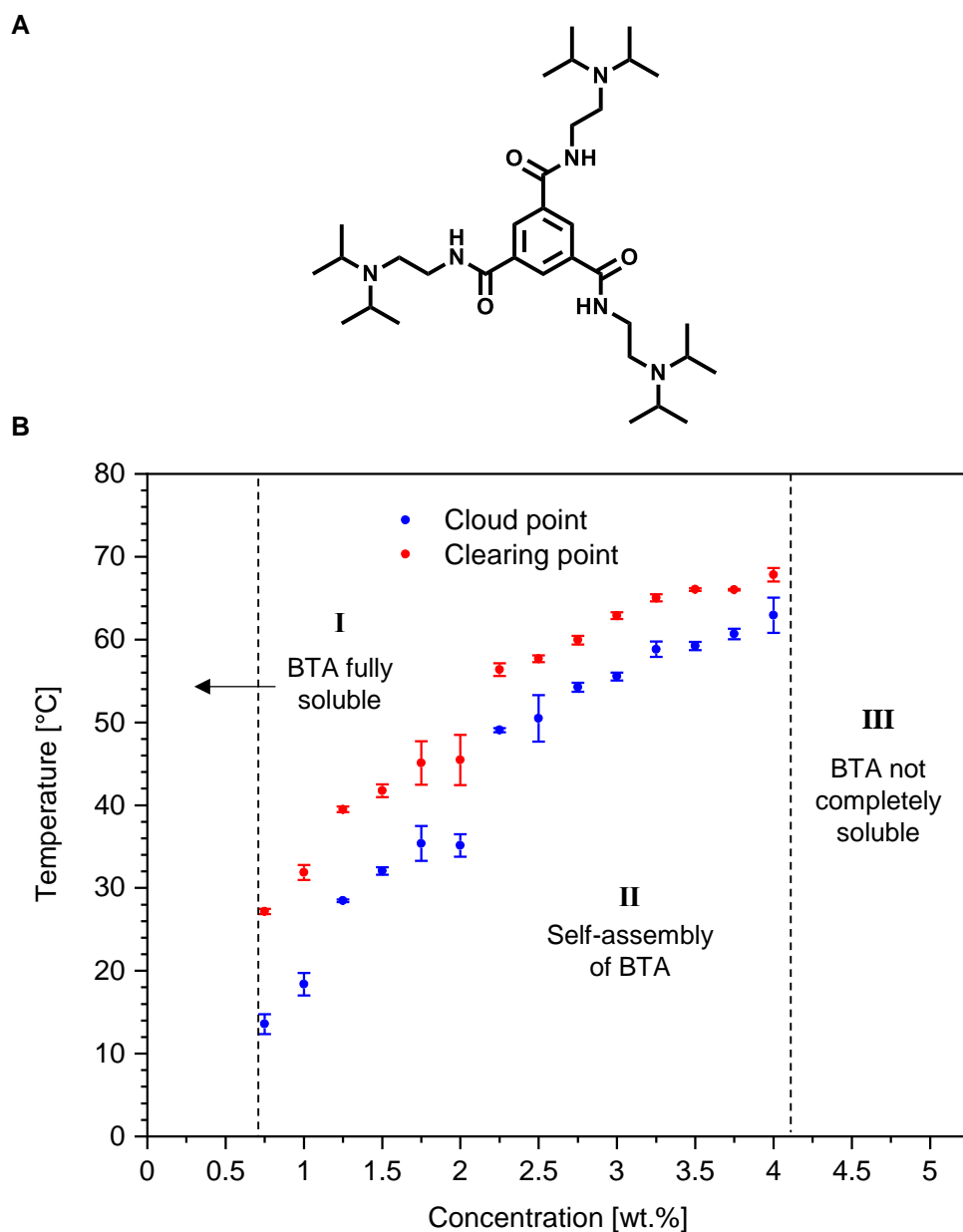


Figure 5-4. **Phase-diagram of *N,N*-diisopropylaminoethyl substituted BTA (BTA-5) in 2-propanol.** **A:** Chemical structure of BTA-5. **B:** The concentration-dependent development of the cloud and clearing points of BTA-5 in 2-propanol as mean values including the standard deviation from the applied three heating and cooling cycles with a scanning rate of $0.10\text{ }^{\circ}\text{C min}^{-1}$. Region I: No self-assembly takes place as the BTA-5 is fully soluble in 2-propanol at low concentrations in the temperature range. Region II: Controlled self-assembly of the BTA-5 self-assembles into fibrous gels upon cooling and reversibly dissolves upon heating the sample. Region III: No controlled self-assembly takes place as the BTA-5 is not completely soluble anymore at elevated temperatures in 2-propanol for concentrations $> 4.0\text{ wt.}\%$.

5.2.2 Self-assembly studies of the selected BTAs upon solvent evaporation

In the next step, self-assembly upon solvent evaporation is investigated with the purpose to reveal the morphology of the BTA assemblies of the different BTAs. The process routes towards fibers are depicted in Figure 5-5. Here, a concentration of 0.50 wt.% in 2-propanol is chosen for all BTA derivatives. The solutions were prepared and completely dissolved typically at elevated temperatures. BTA-4 and BTA-5 were treated by process route 1. A solution at room temperature (A) was given on aluminum foil (5 μ l drop) at ambient conditions and the solvent was allowed to evaporate (B-D). In contrast to that, BTA-3 was treated by process route 2 as the solution at this concentration already starts to self-assemble upon cooling. To prevent self-assembly prior solvent evaporation, the BTA solution was dropped hot (A) onto a substrate and cooling and solvent evaporation occurred simultaneously resulting in (B). All three samples resulted in supramolecular fibers (D) which is shown for each BTA derivatives separately in the upcoming chapters.

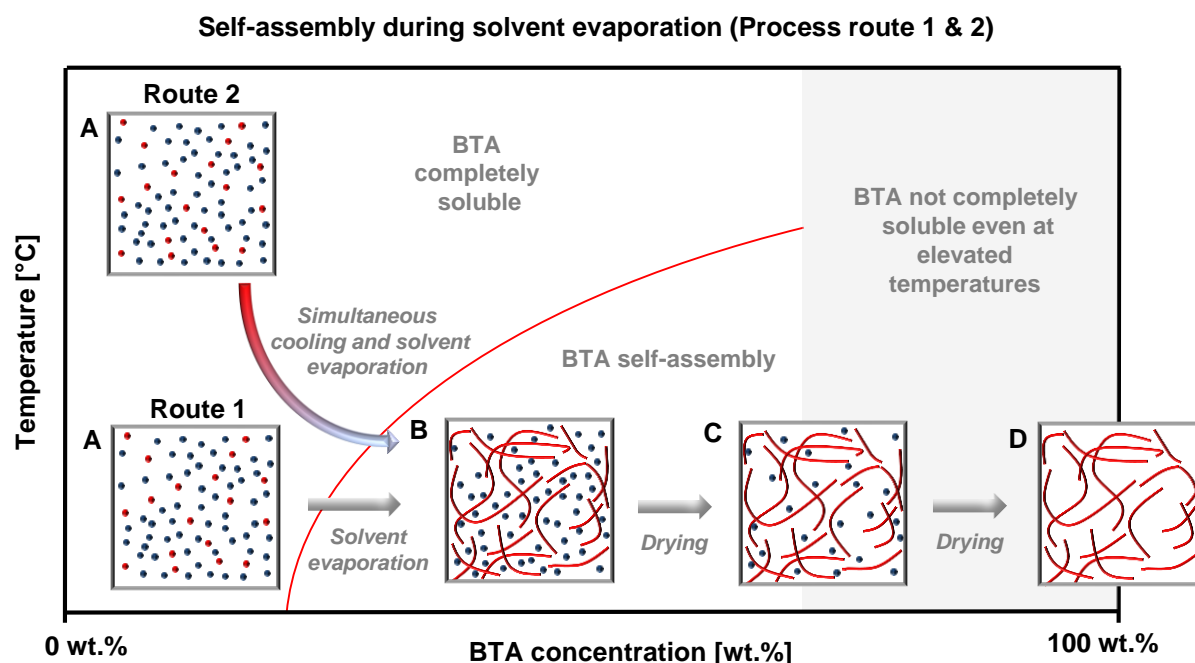


Figure 5-5. **Schematic representation of the self-assembly process routes of BTAs for solvent evaporation.** **A:** Complete molecularly dissolved BTA molecules (red dots) in a selective solvent (blue dots). **B:** Supramolecular fibers (red lines) coexisting with remaining solvent (blue dots). **C:** Further drying. **D:** Complete solvent evaporation results in dried supramolecular fibers. Two process routes are illustrated. Process route 1: Solvent evaporation from a molecularly dissolved solution. Process route 2: Simultaneous cooling and solvent evaporation from a molecularly dissolved solution at elevated temperatures. The phase diagram exhibit three regions: Region I: BTA completely soluble, Region II: BTA self-assembly and Region III: BTA not completely soluble even at elevated temperatures. Source: Macromolecular Chemistry I, University of Bayreuth.

a) Self-assembly upon solvent evaporation of BTA-3

Scanning electron microscopy images reveal the resulting morphology of the assemblies prepared via simultaneous cooling and solvent evaporation on aluminum foil in Figure 5-6 from a 0.50 wt.% BTA solution in 2-propanol. Fibrous assemblies are visible which exhibit a straight fiber morphology with a mean diameter of $363 \text{ nm} \pm 90 \text{ nm}$ and a mean length of $26 \pm 6 \text{ }\mu\text{m}$, respectively.

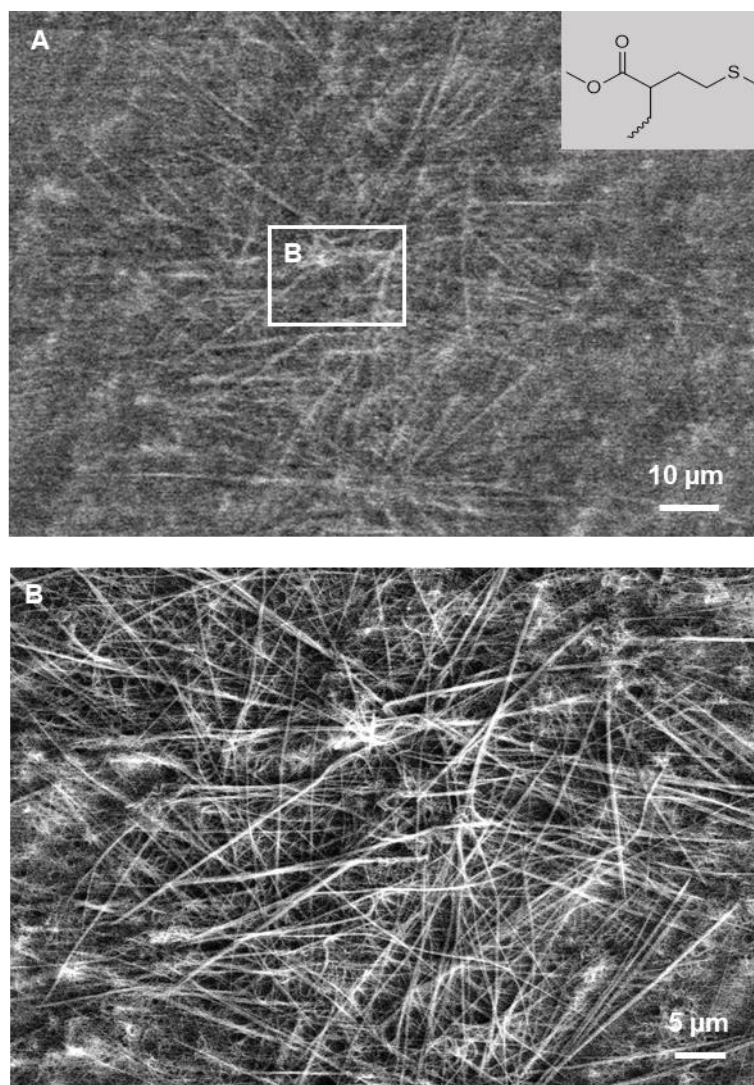


Figure 5-6. Scanning electron microscopy images of self-assembled methionine methyl ester substituted BTA (BTA-3) fibers upon solvent evaporation on aluminum foil. The BTA fibers were prepared from a hot 0.50 wt.% BTA solution in 2-propanol by simultaneous cooling and solvent evaporation at ambient conditions.

b) Self-assembly upon solvent evaporation of BTA-4

The results for the self-assembly upon solvent evaporation on aluminum foil for BTA-4 reveal a fibrous morphology as depicted in Figure 5-7. Here, the self-assembly process is triggered by solvent evaporation at ambient conditions from a 0.50 wt.% BTA solution from 2-propanol. The short fibers show a fan-like self-assembly behavior where one fiber sprouts into several new fibers thus mean diameter and length are not determined.

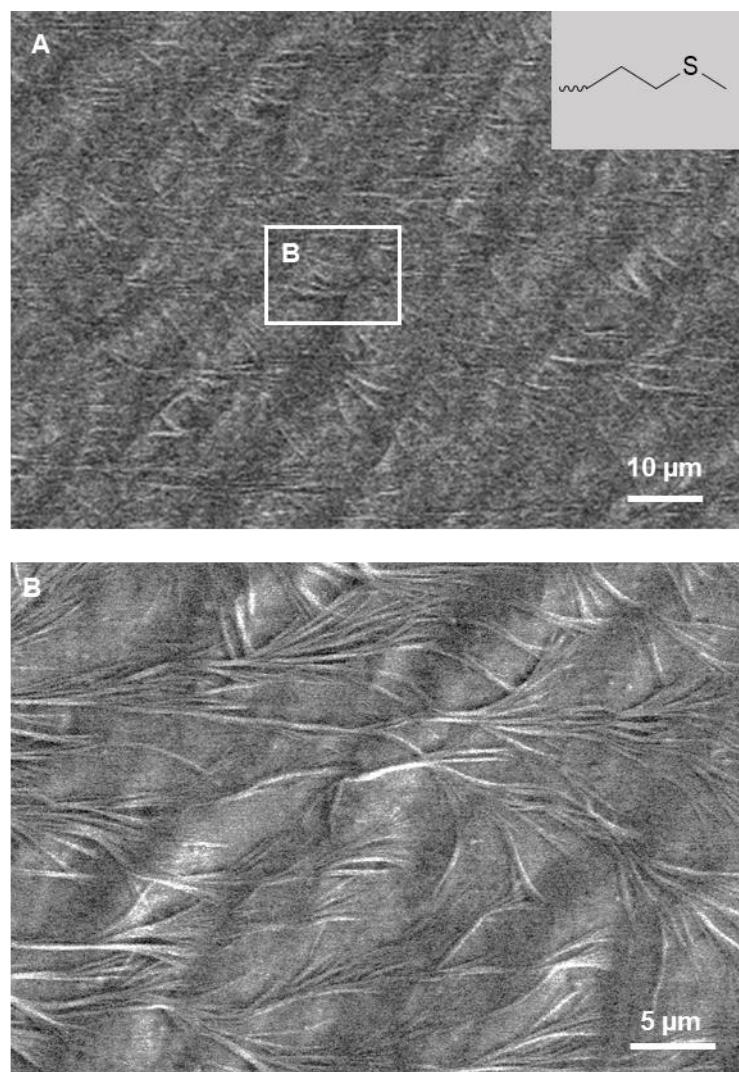


Figure 5-7. Scanning electron microscopy images of self-assembled 2-(methylthio)ethyl substituted BTA (BTA-4) fibers upon solvent evaporation on aluminum foil. The BTA fibers were prepared from a 0.50 wt.% BTA solution in 2-propanol by solvent evaporation at ambient conditions.

c) Self-assembly upon solvent evaporation of BTA-5

The self-assembly behavior upon solvent evaporation from a 0.50 wt.% in 2-propanol solution of BTA-5 results in self-assembled BTA fibers with diameters ranging from 150 nm – 400 nm as shown in Figure 5-8. Due to some entanglement and bending of the fibers, the length cannot be determined. Moreover, the resulting fibers are significantly longer than observed for the sulfur-containing derivatives from 2-propanol. At higher magnifications as shown in Figure 5-8 B, the surface of the BTA fibers shows a structuring. This is attributed to a hierarchical self-assembly, which means that starting from single columns further aggregation into fiber bundles occurs, which ultimately forms the structured fibrils.

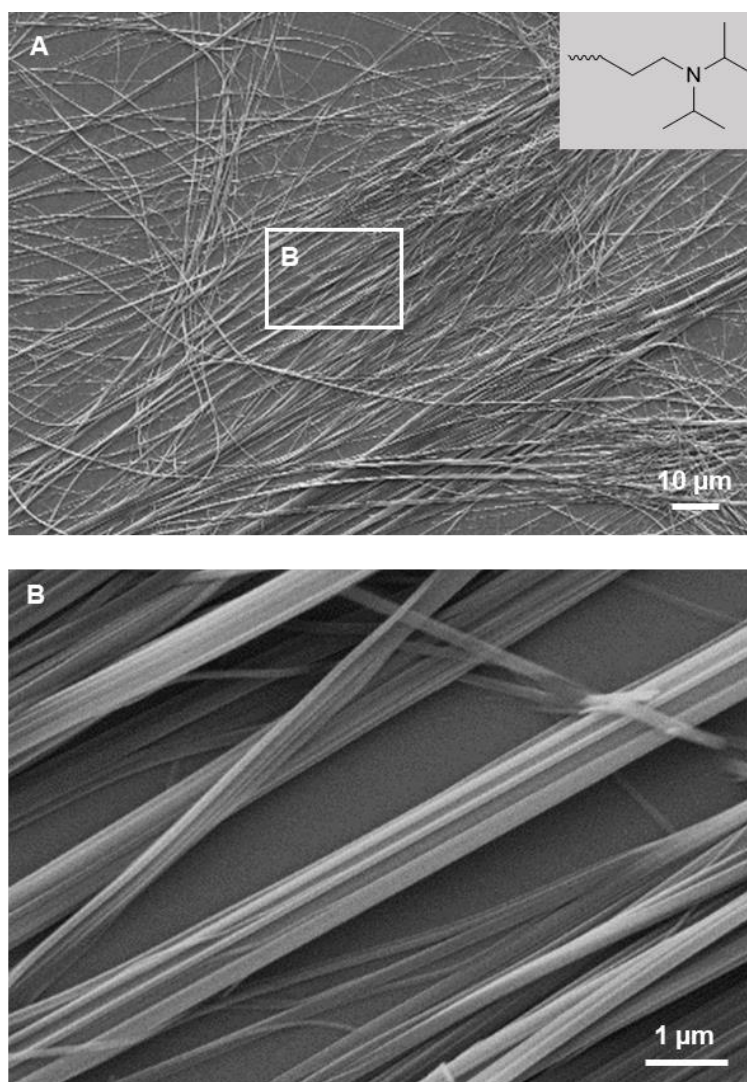


Figure 5-8. **Scanning electron microscopy images of self-assembled *N,N*-diisopropylaminoethyl substituted BTA (BTA-5) fibers upon solvent evaporation on aluminum foil.** The BTA fibers were prepared from a 0.50 wt.% BTA-5 solution in 2-propanol by solvent evaporation at ambient conditions. Figure adapted and reproduced with permission from Ref.^[136] Copyright © 2024 The Authors. *Advanced Materials Interfaces* published by Wiley-VCH GmbH.

5.3 Site-specific self-assembly in polymer flocks

5.3.1 Selection and preparation of a polymer flock substrate

A polymer flock is an interesting substrate comprising a porous structure. Due to the vertically aligned array of microfibers the substrate comprises anisotropy and thus may lead to unique morphologies and applications when combined with the self-assembly of BTAs, which will be explored in the following chapters. First, the preparation of the polymer flock is presented followed by the self-assembly of the BTAs in the polymer flock.

The preparation of a polyamide flock was carried out *via* electrostatic flocking as shown in Figure 5-9 by Felix Bretschneider (Macromolecular Chemistry II, University of Bayreuth). Polyamide (PA) was chosen as microfibers, since they represent a polar class of polymers and provide a significant stiffness which makes them promising as substrate for the solution-based BTA self-assembly. Upon processing, the polyamide microfibers are accelerated in the electrostatic field under applied voltage and vertically attached to an adhesive-coated polyethylene terephthalate (PET) mesh.

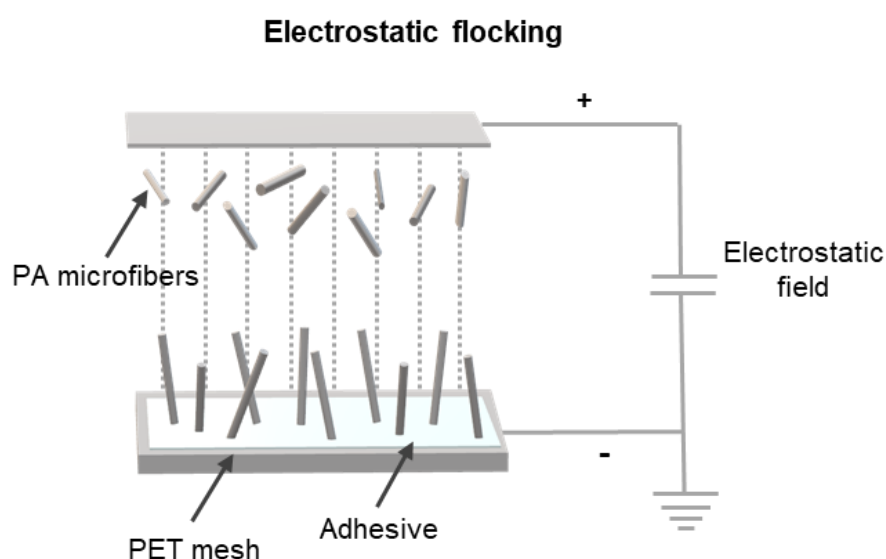


Figure 5-9. **Schematic illustration of the electrostatic flocking process and the resulting flocked microfibers on a PET mesh.** Under applied voltage of 2.3 kV cm^{-1} the polyamide (PA) microfibers are accelerated and aligned in the electrostatic field and adhered to a polyethylene terephthalate (PET) mesh (mesh size $100 \mu\text{m}$) with an adhesive. Figure adapted and reproduced with permission from Ref.^[136] Copyright © 2024 The Authors. Advanced Materials Interfaces published by Wiley-VCH GmbH.

A schematic representation of the PA flock with its dimensions and optical microscope images of the PA flock are depicted in Figure 5-10. The PA flock microfibers exhibit a length of $l = 500 \mu\text{m}$ with diameters of $d = 19$ resulting in an aspect ratio of $l/d \approx 26$. The flock can be overall characterized by two variables: the orientation of the microfibers relative to the substrate and the density of flock microfibers per area. The flocking yielded an overall microfiber orientation of 70 degree and a density of 3 mg cm^{-2} . Figure 5-10 shows the PA flock side view (B) and the view of the PET mesh from the bottom after flocking (C).

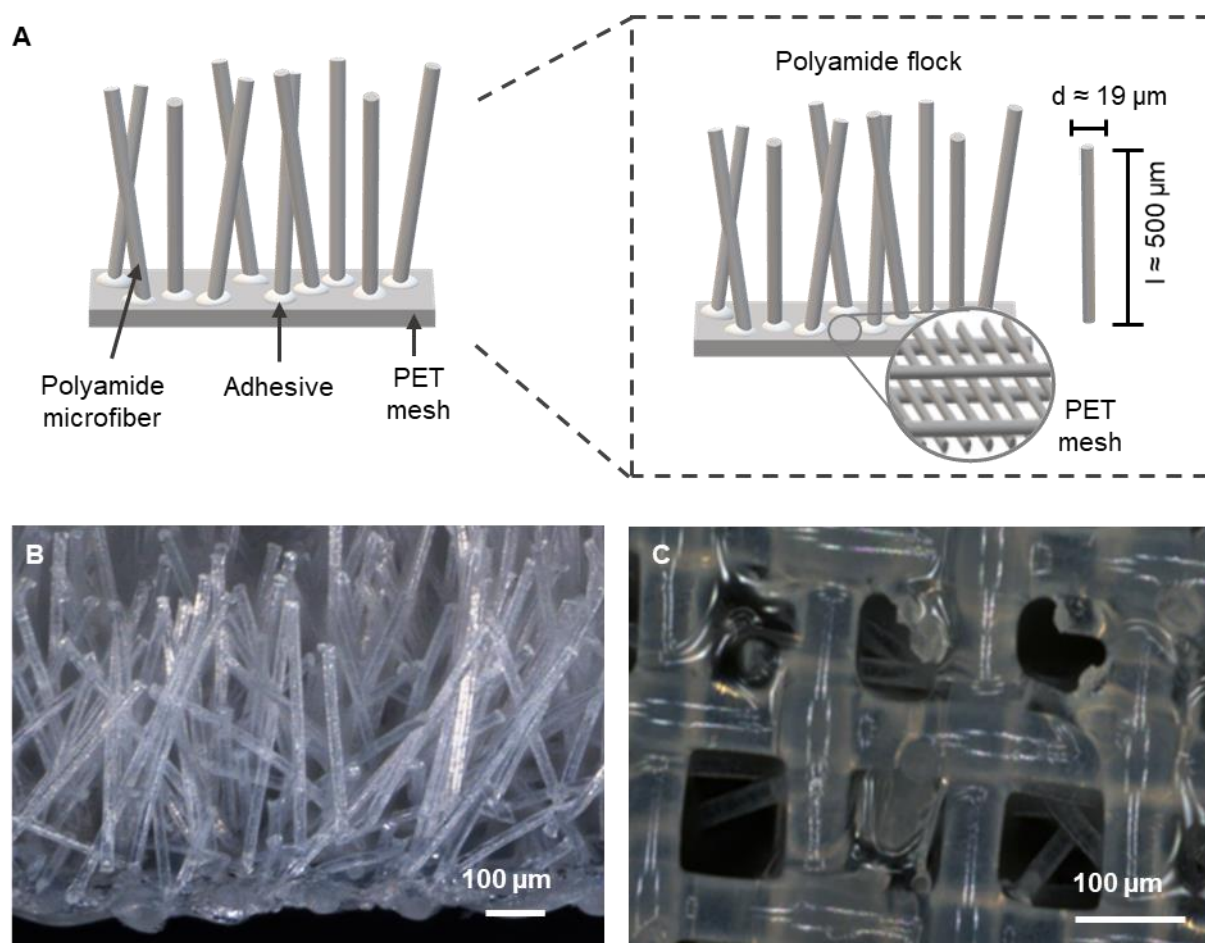


Figure 5-10. **Schematic representation of the polyamide flock with its dimensions and optical microscope images of the polyamide flock.** **A:** Schematic representation of the polyamide flock with the components and dimensions. **B:** polyamide flock side view and **C:** view of the PET mesh covered with adhesive from the bottom. Figure adapted and reproduced with permission from Ref.^[136] Copyright © 2024 The Authors. Advanced Materials Interfaces published by Wiley-VCH GmbH.

5.3.2 Self-assembly studies of the BTAs within polyamide flocks upon solvent evaporation

This chapter elaborates the self-assembly behavior of different BTAs within polymer flocks. Experimentally, the self-assembly of the selected BTAs within flocks upon solvent evaporation was realized using a PA flock as described in chapter *Selection and preparation of a polymer flock*. For the initial studies, 3 x 3 cm PA flock samples are used for the combination with the BTA solutions. The PA flock is immersed in 1 mL of the BTA solutions for 30 s, taken out and the soaked PA flock was placed on a petri dish on the bench. The solvent was allowed to evaporate at ambient conditions. After complete evaporation, the sample was placed on a SEM stub and investigated regarding the possible formation of BTA fibers within the flock. In the case of BTA-3, the PA flock is immersed in a hot solution for 30 s and self-assembly in solution already proceeds upon cooling, because no stable solution at 0.50 wt.% at room temperature can be achieved. The soaked PA flock was then placed on a petri dish on the bench and the solvent was allowed to evaporate simultaneously cooled during this process at ambient conditions.

a) Self-assembly within polyamide flocks with BTA-3 solution

The results after solvent evaporation and simultaneous cooling are depicted in Figure 5-11 for BTA-3. Under the applied conditions as described before, BTA 3 seems to self-assemble in a layer-like but inhomogenously distributed nets of fine BTA fibers between the PA flock microfibers. Some parts of the nets feature a dense packing of BTA fibers, whereas at other positions with the flock no BTA fibers were found. This situation changes if the concentration was reduced to 0.35 wt.% leading to more defined net structures and less dense parts. If a concentration of 0.10 wt.% for the processing is used, which is remains stable at room temperature, no network of BTA fibers between the PA flock microfibers is found and only small BTA fibers, which self-assembled on the top of the flock fibers are observed. This example demonstrates the importance of the set of conditions, which is required to achieve a site-specific self-assembly. These findings also suggest that comparable stable solutions have to be used if processed at ambient conditions. Since the useful concentration for BTA-3 is only at 0.10 wt.% and below resulting in tiny structures, this derivative is not considered for further experiments.

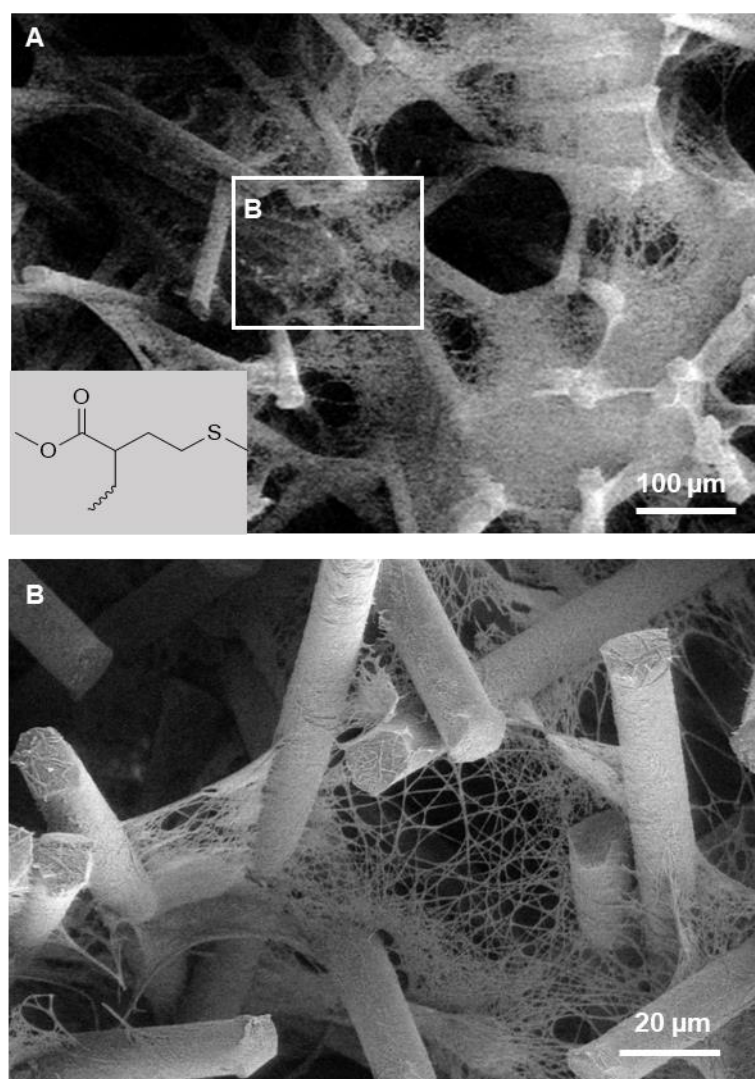


Figure 5-11. **Scanning electron microscopy images of a PA flock after immersion into a hot 0.50 wt.% BTA-3 solution in 2-propanol and subsequent drying at ambient conditions. A:** an overview of the PA flock with self-assembled BTA-3 and **B:** magnification of the white box showing the self-assembled BTA-3 onto the PA microfibers.

b) Self-assembly within polyamide flocks with BTA-4 solution

The results of the self-assembled BTA-4 in a PA flock after solvent evaporation are shown in Figure 5-12. Surprisingly, under the applied conditions as described before, the BTA-4 is mostly located at the top of the flock microfibers head. Only a few fibers entwining along the PA microfiber. Interestingly, here most of the BTA-4 fibers are not only located at the PA head but also spreading away in any direction from the PA flocks' heads. The location of the BTA-4 fibers at the PA heads is indicative for the effective capillary effects from the flock fibers during the drying process apparently leading to a directed solution transport. These results agree with the aforementioned experiments, requiring stable solutions of BTAs. If the solution is not stable, early self-assembly during cooling occurs leading to the structures observed for BTA-3 (net-structure within the polymer flock). However, for BTA-4 and the chosen set of conditions leads to a site-specific self-assembly at the top of the PA fibers, which was never demonstrated before. This new self-assembly approach is from now on called *site-specific self-assembly*.

Even more surprisingly, the self-assembled structures reveal a conical shape as shown in Figure 5-12 B. The conical assemblies have a length around 20 μm . Further experiments with higher concentrations of the BTA solution in 2-propanol did not result in a significant change of appearance. Same conical structures are observed from ethanol or butanol as solvent, always located at the PA flocks head.

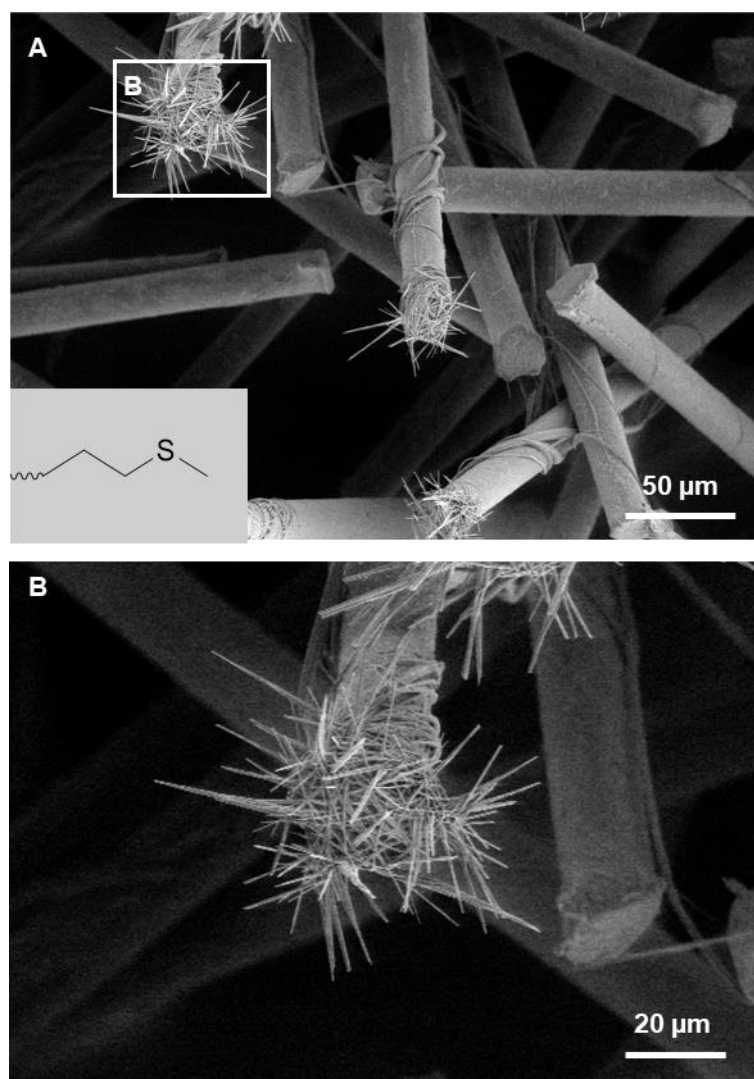


Figure 5-12. Scanning electron microscopy images of a PA flock after immersion into a 0.50 wt.% BTA-4 solution in 2-propanol and subsequent drying at ambient conditions. **A:** an overview of the self-assembled BTA-4 structures within the PA flocks and **B:** magnification of self-assembled BTA-4 structures onto the PA microfibrils head.

c) Self-assembly within polyamide flocks with BTA-5 solution

The combination of a stable 0.50 wt.% in 2-propanol solution of BTA-5 with the polymer flocks and subsequent solvent evaporation results in site specific self-assembly where BTA assemblies are mostly located at the head of the PA flock microfibers as depicted in Figure 5-13 A. The BTA assemblies show a conical shape and homogenously spread away from the head of the polymer flock into every direction (Figure 5-13 B). It can also be observed, that if a PA flocks head is equipped with BTA-5, the BTA fibers completely cover the whole PA flock head. In contrast to the conical structures from BTA-4, the conical structures of BTA-5 exhibits significantly more and longer spines with lengths exceeding 20 μm using the same concentration, solvent and drying procedure.

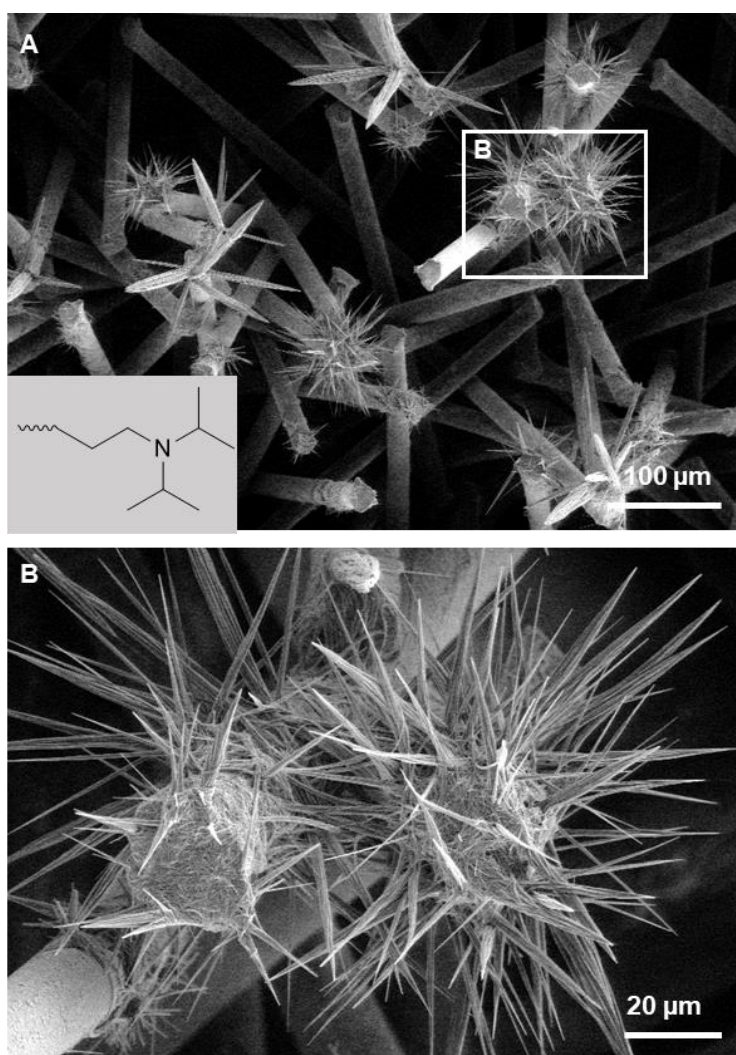


Figure 5-13. **Scanning electron microscopy images of a PA flock after immersion into a 0.50 wt.% BTA-5 solution in 2-propanol and subsequent drying at ambient conditions. A:** an overview of the self-assembled BTA-5 structures within the PA flocks and **B:** magnification of self-assembled BTA-5 structures onto the PA microfibers head. Figure adapted and reproduced with permission from Ref.^[136] Copyright © 2024 The Authors. *Advanced Materials Interfaces* published by Wiley-VCH GmbH.

5.3.3 Influencing parameter of the site-specific self-assembly

From the initial experiments of the selected BTAs within the PA flocks it become clear, that the process is complex and proper self-assembly conditions are required to achieve a site-specific self-assembly. Furthermore, the appearance of the BTA fibers seem to strongly depend on the self-assembly conditions, too.

Among the results of the experiments with the selected BTAs within the flock microfibers, the self-assembly into conical microstructures of the BTA-5 feature the most promising in morphology as well as usefulness. Hence, a more in-depth investigation of the self-assembly behavior of BTA-5 within the microfiber flock is conducted to improve the understanding of the site-specific self-assembly.

This involves investigations and optimizations regarding:

- i)* the application method onto the polymer flock
- ii)* the drying process
- iii)* the BTA concentration

as schematically depicted in Figure 5-14. The optimization includes A) the application of the BTA solution onto the polymer flock. Here the question arises whether the polymer flock need to be fully soaked for efficient site-specific self-assembly. B) Applying a defined drying protocol so that capillary forces come into effect and the solvent evaporation is achieved from the top of the flock fibers. C) Optimized site-specific supramolecular self-assembly if the proper processing conditions were found. Here, the concentration of the BTA-5 is taking into account. For this, the different settings of the processing window are adapted to implement a self-assembly protocol for the fabrication of the conical assemblies in a controlled and reproducible manner.

Site-specific self-assembly into conical assemblies

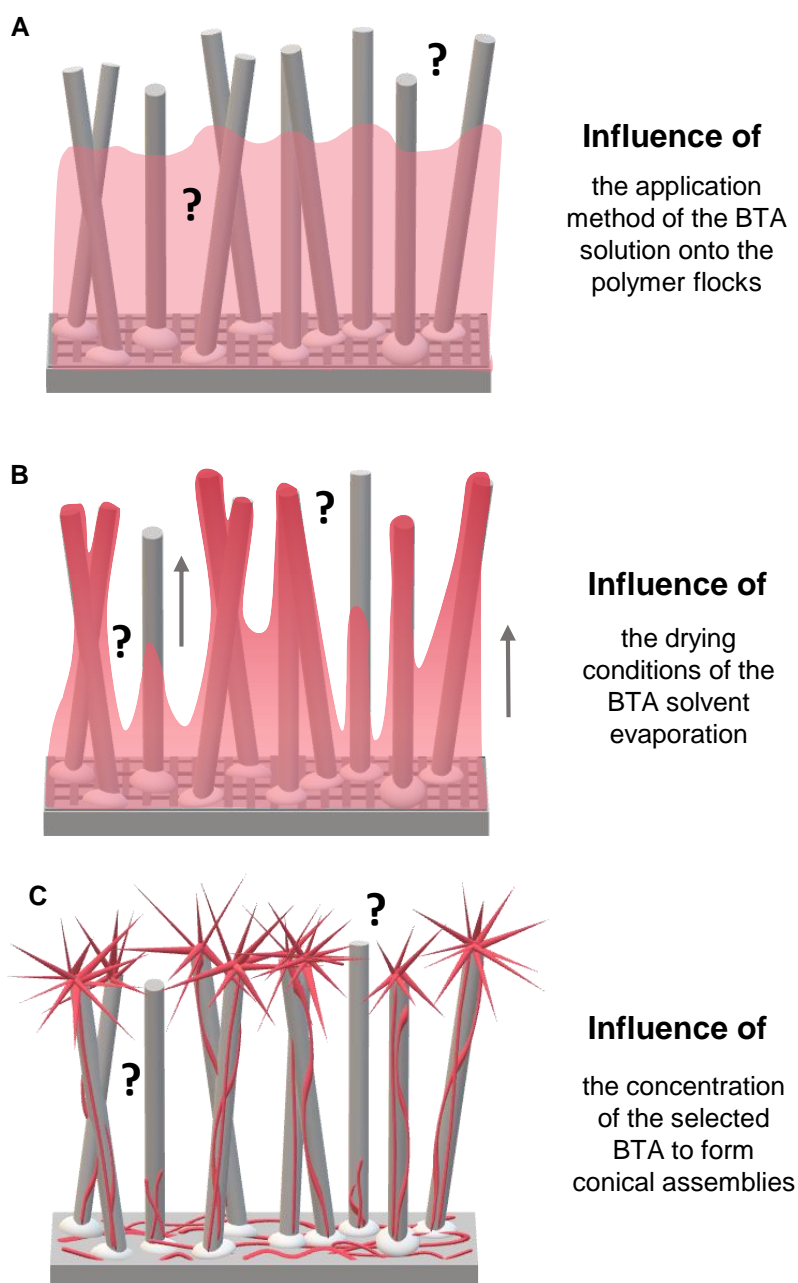


Figure 5-14. **Schematic illustration of the preparation of conical BTA assemblies on top of PA microfibers.** **A:** Application of the BTA solution onto the polymer floccs. **B:** Drying conditions to achieve site-specific self-assembly. **C:** Site-specific self-assembly into conical assemblies with proper self-assembly conditions such as the processing from A and B and BTA concentration and solvent. Figure adapted and reproduced with permission from Ref.^[136] Copyright © 2024 The Authors. *Advanced Materials Interfaces* published by Wiley-VCH GmbH.

a) Influence of the application method onto the polymer flock

This series of experiments explored different application methods of the BTA-5 solution onto the microfiber flock to determine which method yields the best conical morphologies. For this, the flock was treated with three different methods as schematically shown in Figure 5-15. In this set of experiments, the BTA-5 solution was either dropped, sprayed onto the flock or the flock was again immersed into the BTA-5 solution (see methods and scanning electron microscopy images of the results in *Appendix B* Figure 8-7).

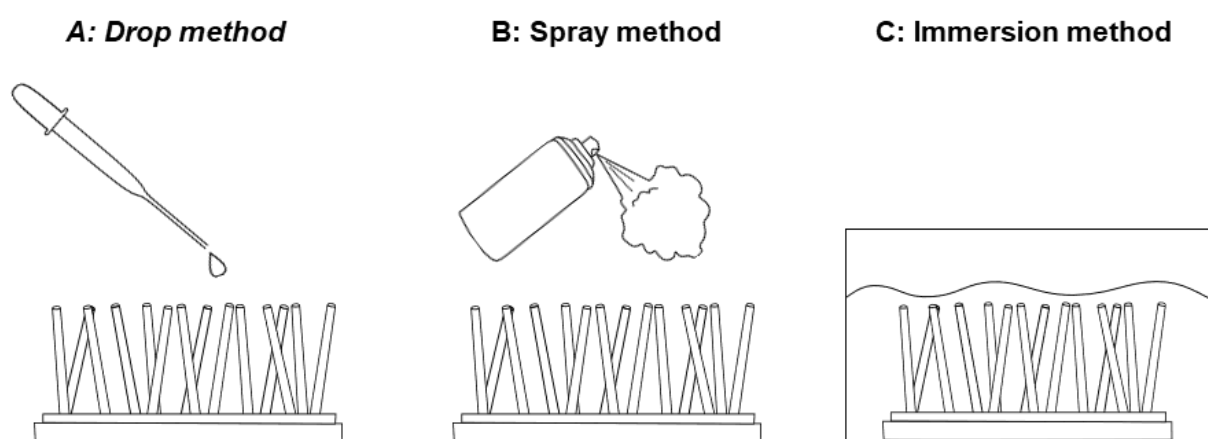


Figure 5-15. **Different application methods of BTA-5 solution onto the PA flock.** **A:** The BTA solution was dropped with a pipette onto the PA flock. **B:** The BTA solution was sprayed onto the PA flock. **C:** The PA flock was immersed into the BTA solution.

The results demonstrate conical BTA-5 fibers spreading away of the flock microfibers head for all three application methods. The only difference among the three application methods was the amount of BTA-5 assemblies as well as the length of the observed conical microstructures. The least visible amount was found for the spray method, followed by the drop method. The immersion method yielded the highest number of assemblies and the longest conical BTA-5 fibers, with lengths exceeding 20 μm . Thus, it is assumed, that the immersion method probably ensures a homogenous wetting of the whole flock, which may lead to the formation of the most promising BTA-5 conical fibers. It was also observed, that removing excess of the solution by a filter paper before the drying procedure results in more well-defined conical BTA spines. Thus, it is assumed that the polymer flock need to be fully soaked once achieved by immersion, however, for the capillary effects to come into action removing of the excess of the solution is necessary. Further experiments were conducted by using those optimizations.

b) Influence of the drying process

In this chapter the influence of the drying procedure is investigated representing the next optimization step. Instead of allowing the immersed sample to dry under ambient conditions, which results in the rapid evaporation of 2-propanol, the sample was now placed in a petri dish covered with a perforated aluminum foil. This procedure was kept identical for all experiments, to ensure the same evaporation conditions. With this method, the solvent, 2-propanol, was evaporated slowly at 30 °C under controlled conditions. Exemplary results of the samples treated using this method are shown in Figure 5-16 A-D. The BTA-5 fibers spreads into conical structures predominantly at the flock microfibers head. Beneficially, with this drying procedure, the conical microstructures exhibit lengths exceeding the 20 μm as it has been observed before. Here, the BTA-5 spines exhibit an average length of around 50 μm and a half apex angle of 6 degrees. Also, the number of spines per individual flock microfiber ranges from about 20 up to 80 and in exceptional cases, more than 100 spines. Some examples with noted numbers of spines per flock microfiber are summarized in *Appendix B* Figure 8-8.

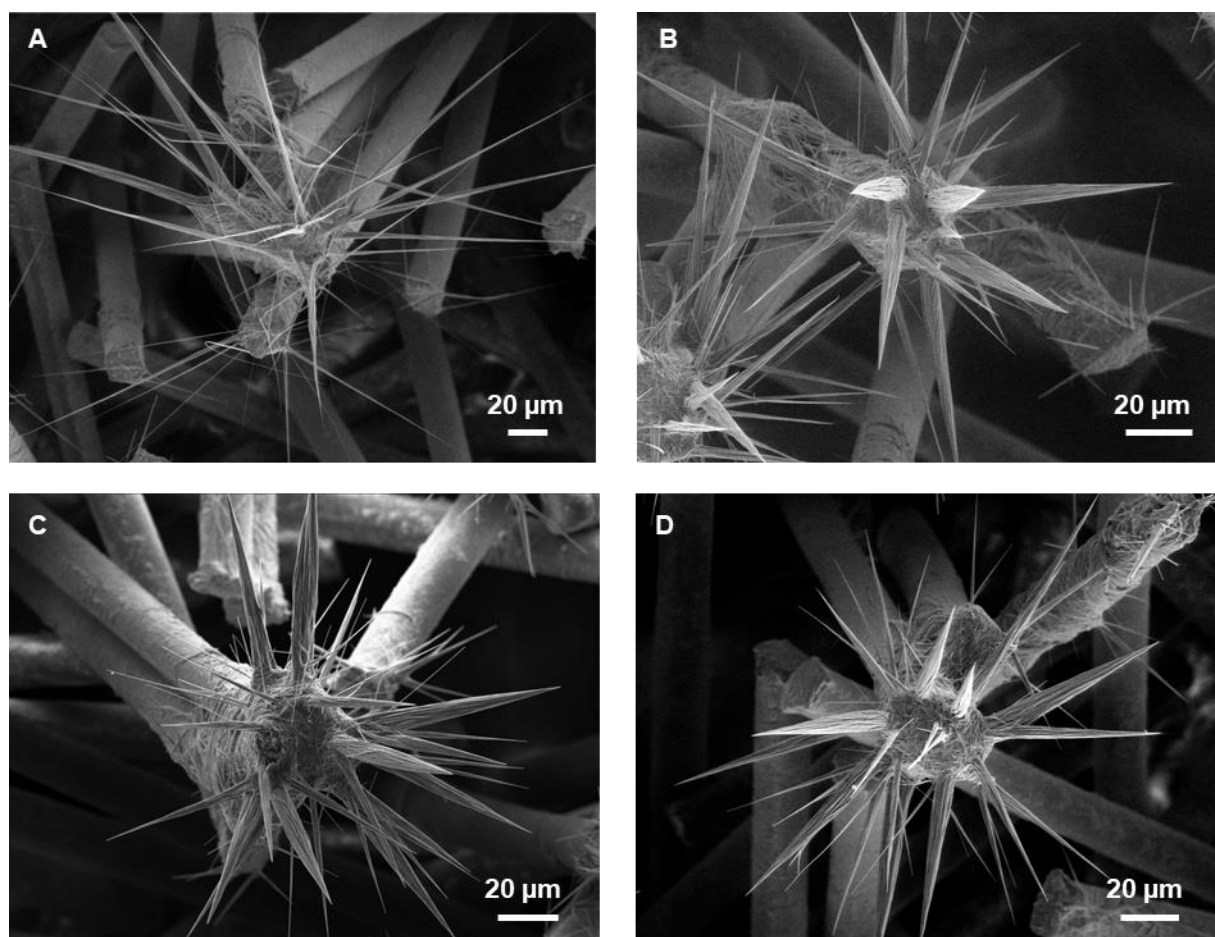
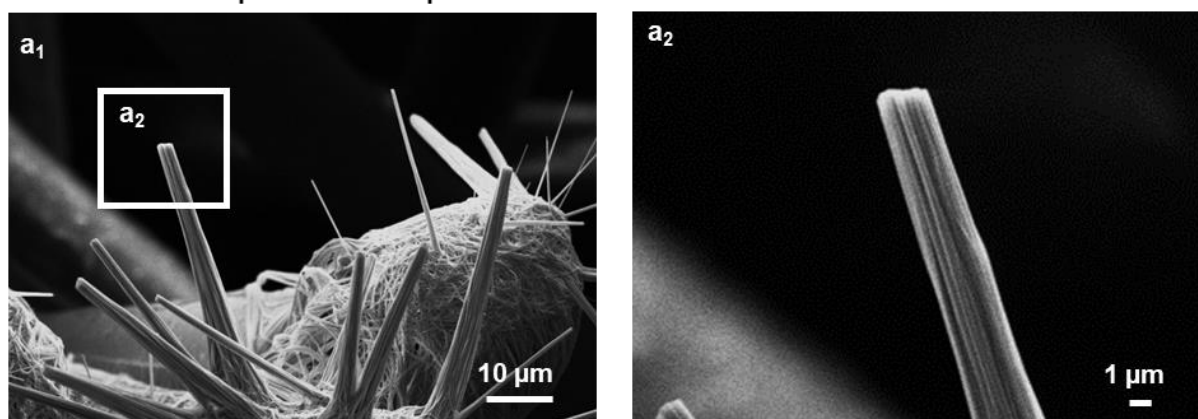


Figure 5-16. **Scanning electron microscopy images of a PA flock after immersion into a 0.50 wt.% BTA-5 solution in 2-propanol and subsequent drying under defined conditions at 30 °C. A-D:** Supramolecular spines spreading away from the PA microfibrils head. Different individual PA microfibrils are depicted. Figure adapted and reproduced with permission from Ref.^[136] Copyright © 2024 The Authors. *Advanced Materials Interfaces* published by Wiley-VCH GmbH.

Furthermore, another observation was made in which supramolecular spines are not fully developed. Figure 5-17 depicts two different positions at the same BTA decorated flock are (A and B). The microstructures in Figure 5-17 A are not fully evolved i.e. missing the supramolecular spines tip. However, the conical morphology of the spine can be clearly seen. This phenomenon is not fully understood and probably attributed to the complex drying process within the polymer flock. Figure 5-17 B shows a completely formed supramolecular spine with a hierarchical structure. When reviewing all the microstructures in a given flock sample, different scenarios become apparent. In certain instances, there are microstructures which are not fully developed at a specific flock microfiber and in some cases, no conical microstructures are formed at all.

This might be attributed to the situation when the microfibers are arranged in a manner that either prevents the existence of capillary effects or weakens them, leading to the absence of equipped flock microfibers or partially developed BTA microstructures. However, the preponderant majority of spines are completely formed with a well-defined tip. This proves that the BTA solution is effectively transported to the head the PA microfibers through capillary effects on most of the flock microfibers. However, it cannot be controlled which and how much PA microfibers are decorated with the BTA spines due to the dependence on the order and alignment of the PA flocks to each other.

A: Half-formed supramolecular spine



B: Completely formed supramolecular spine

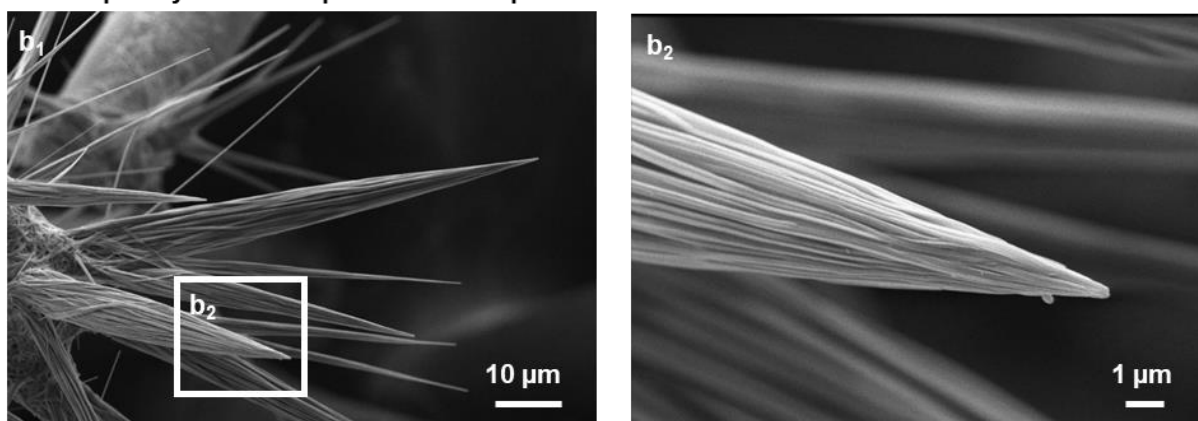


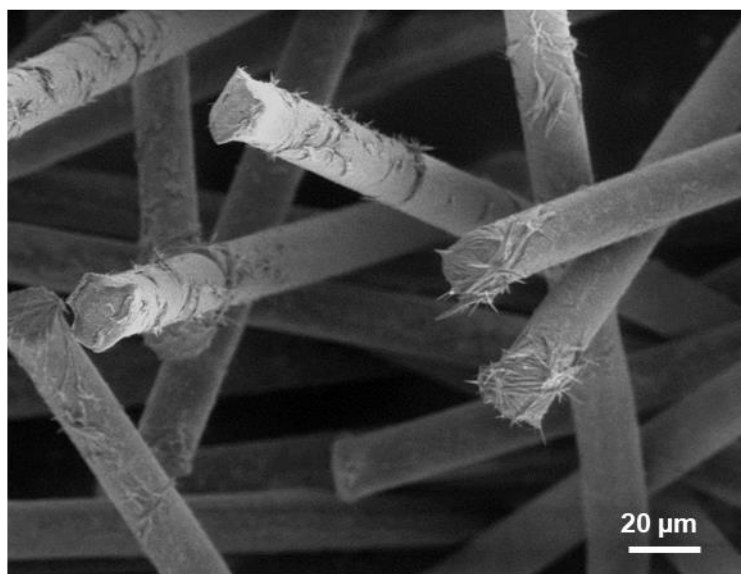
Figure 5-17. **Scanning electron microscopy images of half and completely formed BTA spines.** **A:** Supramolecular spine missing the tip with **a₁**: an overview of the sample and **a₂** as magnification. **B:** Completely formed BTA spines exhibiting a defined tip with **b₁**: an overview and **b₂**: as magnification.

c) Influence of the concentration

In view of reproducibility of the self-assembly protocol, stable solutions are assumed to be mandatory. Solutions above 0.50 wt.% were observed to self-assemble at room temperature, rendering them unsuitable for the intended process. Even though the concentration of 0.50 wt.% under the applied self-assembly conditions seem to yield defined conical assemblies, lower concentrations are tested to investigate the influence of the concentration. Thus, concentrations ranging from 0.05 wt.% to 0.50 wt.% were explored. Performing experiments at 0.05 wt.%, only BTA-5 fibers were formed along the PA microfibers, while at 0.10 wt.%, small fiber-like structures were observed on top of the PA fibers Figure 5-18 A. Concentrations of 0.25 wt.% resulted in only small spines being formed on top of the PA fibers Figure 5-18 B. Thus, the concentration of 0.50 wt.% is considered as ideal concentration for the formation of the supramolecular spines.

Furthermore, two other solvents ethanol and DMF were tested to investigate the influence of the solvent onto the conical assemblies. When immersing the flock into ethanol or DMF solutions of BTA with a concentration of 0.50 wt.% and applying the same self-assembly protocol, no well-defined spines are observed. The structures resulting from an ethanol solution which similarly evaporates as 2-propanol are predominantly located on top of the flock microfibers however only a few BTA fibers spreading away from the PA flock head. Higher concentration of the BTA in ethanol does not change the overall appearance or significant improvement. Compared to that DMF evaporates much slower, taking several days for complete solvent evaporation. Here, BTA fibers are formed but they rather agglomerate and no conical shape is observed.

A: BTA concentration of $c_{\text{BTA}} = 0.10$ wt.%



B: BTA concentration of $c_{\text{BTA}} = 0.25$ wt.%

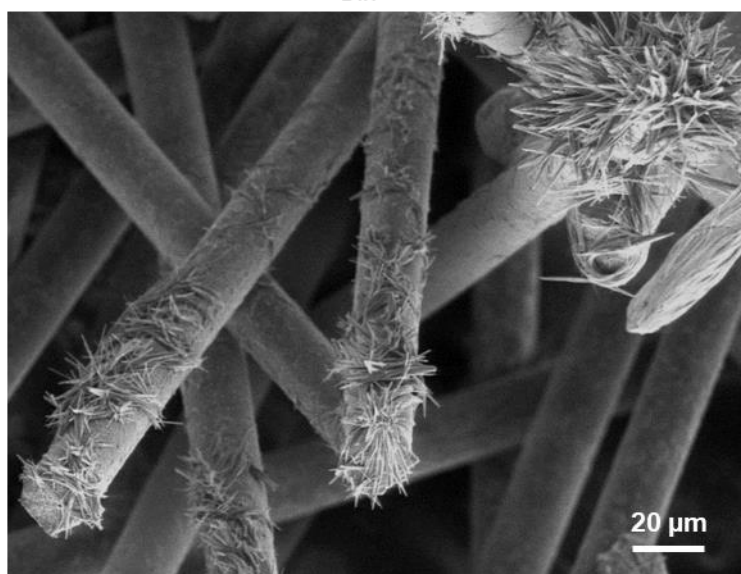


Figure 5-18. Scanning electron microscopy images of a PA flock after immersion into BTA solutions in 2-propanol and subsequent drying at ambient conditions. **A:** Self-assembled microstructures resulting from concentrations of the BTA solution of $c_{\text{BTA}} = 0.10$ wt.% and **B:** $c_{\text{BTA}} = 0.25$ wt.%.

5.4 Supramolecular spines

5.4.1 Proposed mechanism to site-specific supramolecular spine formation

From the different optimization steps and experiments, a set of conditions of the optimal processing window was determined that reproducibly fabricate the BTA spines in a controlled manner. The optimal parameters include the immersion of the PA flock into a 0.50 wt.% BTA solution in 2-propanol, applying a filter paper to remove excessive solution and subsequent controlled evaporation at 30 °C in a covered petri dish.

The proposed mechanism to site-specific supramolecular spine formation is schematically illustrated in Figure 5-19. The PA flock is immersed into a 0.50 wt.% BTA in 2-propanol solution (A) and subsequently placed on a filter paper for a to partially remove the BTA solution (B). Then, the capillary effect of the vertically aligned microfiber array takes place. The capillary forces of the flocks transport the BTA solution towards the top of the flock microfibers (C). Upon further evaporation of the 2-propanol, the concentration of the BTA increases locally at the top of the PA microfibers and seeds are formed. These seeds initiating the self-assembly which is site-specific at the top of the PA flock microfibers. The BTA spines starts to grow while the solvent is further evaporating. As evaporation proceeds, additional BTA building blocks are fed to the initially formed BTA structures. As a result, the flock microfibers are decorated with supramolecular spines (D). At the end of the evaporation process, the remaining BTA molecules form BTA fibers along the flock microfiber and at the bottom of the substrate. This process is highly reproduceable and BTA spines are found over the entire PA flock. The proposed formation is supported by observing the drying process by optical microscopy where the capillary effects as well as the formation of the conical spines can be observed.

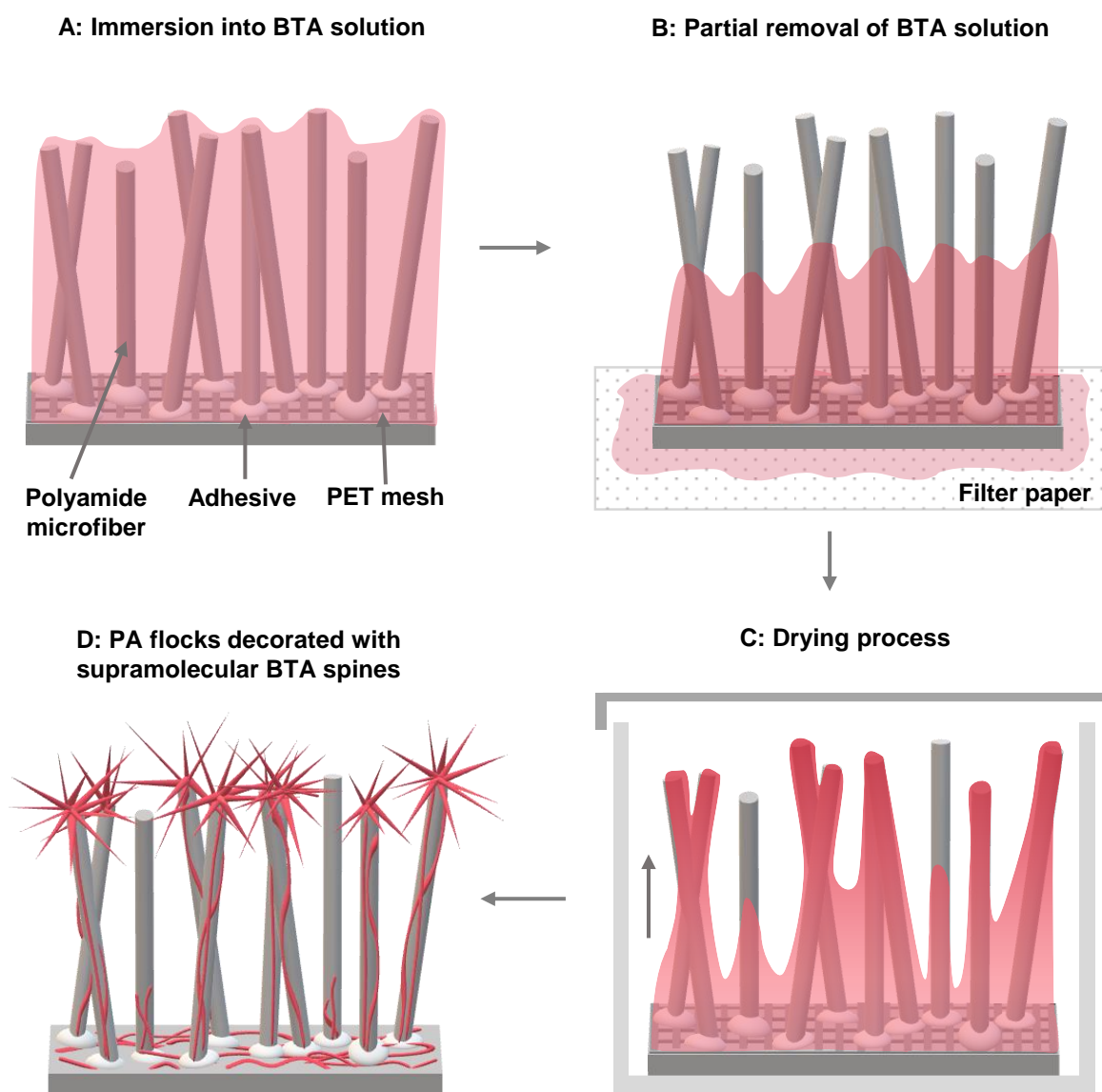


Figure 5-19. **Schematic illustration of the proposed mechanism to site-specific supramolecular spine formation.** **A:** The PA flock is immersed into an BTA solution. **B:** The soaked PA flock is then placed on a filter paper for a dedicated time to partially remove the BTA solution. **C:** During drying process in a covered petri dish capillary forces of the PA flocks transport the BTA solution towards the PA microfibers head and evaporation of the solvent occurs and self-assembly is initiated at the PA microfibers head. **D:** Individual PA microfibers decorated with BTA spines. Figure adapted and reproduced with permission from Ref.^[136] Copyright © 2024 The Authors. *Advanced Materials Interfaces* published by Wiley-VCH GmbH.

5.4.2 Hierarchical level of the supramolecular spines

The investigation with scanning electron microscopy of the supramolecular spines clearly shows a hierarchical structure in the images (see Figure 5-17 B). From the knowledge about BTA self-assembly in general, the hierarchy of the supramolecular spines can be derived as described in Figure 5-20. The hierarchy of the BTA spines comprise three hierarchical levels and span from the nano- to the microscopic scale:

- I. The molecular building blocks self-assemble into a *supramolecular column* by triple hydrogen bonding (A).
- II. These single columns further aggregate due to macrodipole interactions and form a *supramolecular fibril* (B).
- III. The supramolecular fibrils form the *artificial supramolecular spine* with a conical shape and microgrooves (C).

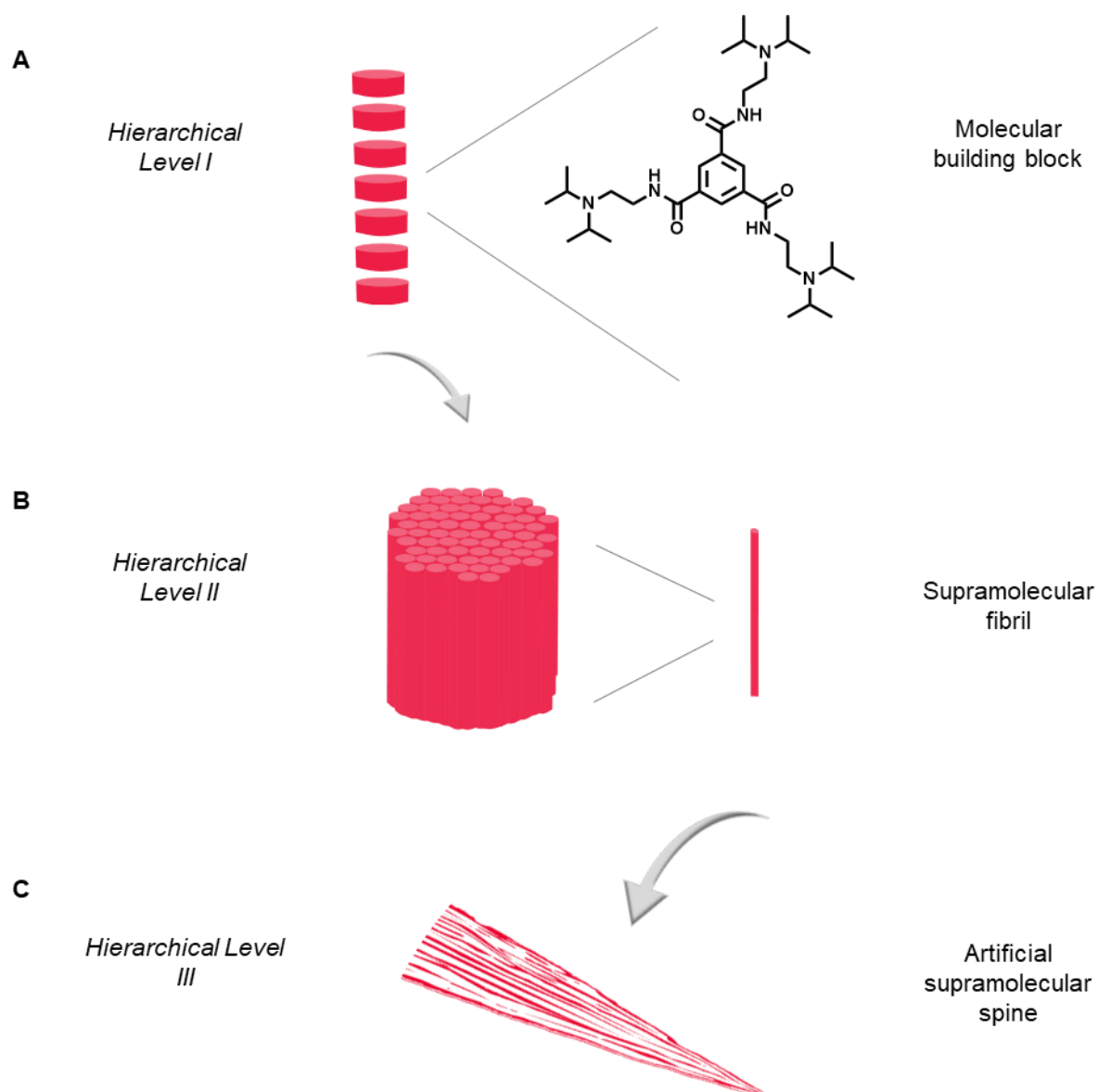


Figure 5-20. Schematic illustration of the self-assembly process towards a supramolecular spine featuring different hierarchical level. Molecular building blocks self-assemble into *supramolecular columns* (I) with further formation to *supramolecular fibrils* (II) resulting in the *artificial supramolecular spine* (III). Figure adapted and reproduced with permission from Ref.^[136] Copyright © 2024 The Authors. *Advanced Materials Interfaces* published by Wiley-VCH GmbH.

To investigate the hierarchy and composition of the supramolecular spines, a supramolecular spine was cut in half and the cross-section was investigated by means of scanning electron microscopy. The cross-section is depicted in *Appendix B* Figure 8-11. In this view, the fibrils and their alignment along a particular axis become distinctly evident. Further evidence for the high ordered columnar arrangement of the BTA molecules and thus, the orientation of the fibrils along the spines is provided by confocal polarized RAMAN measurements. The confocal polarized Raman measurements at an BTA spine in dependence of the angle of the polarizer is shown in Figure 5-21. When the BTA molecules self-assemble into a columnar arrangement, the benzene rings are stacked on top of each other. Here, the benzene rings of the stacked BTAs within the spine show strong dependence to the angle of the polarizer. Measuring with a parallel polarization along the columns causes a reduced signal of the benzene units, whereas a measurement with a perpendicular angle of the polarizer results in an increased signal intensity. This finding serves as evidence that individual supramolecular columns share the same orientation as the fibrils and, consequently, as the spines.

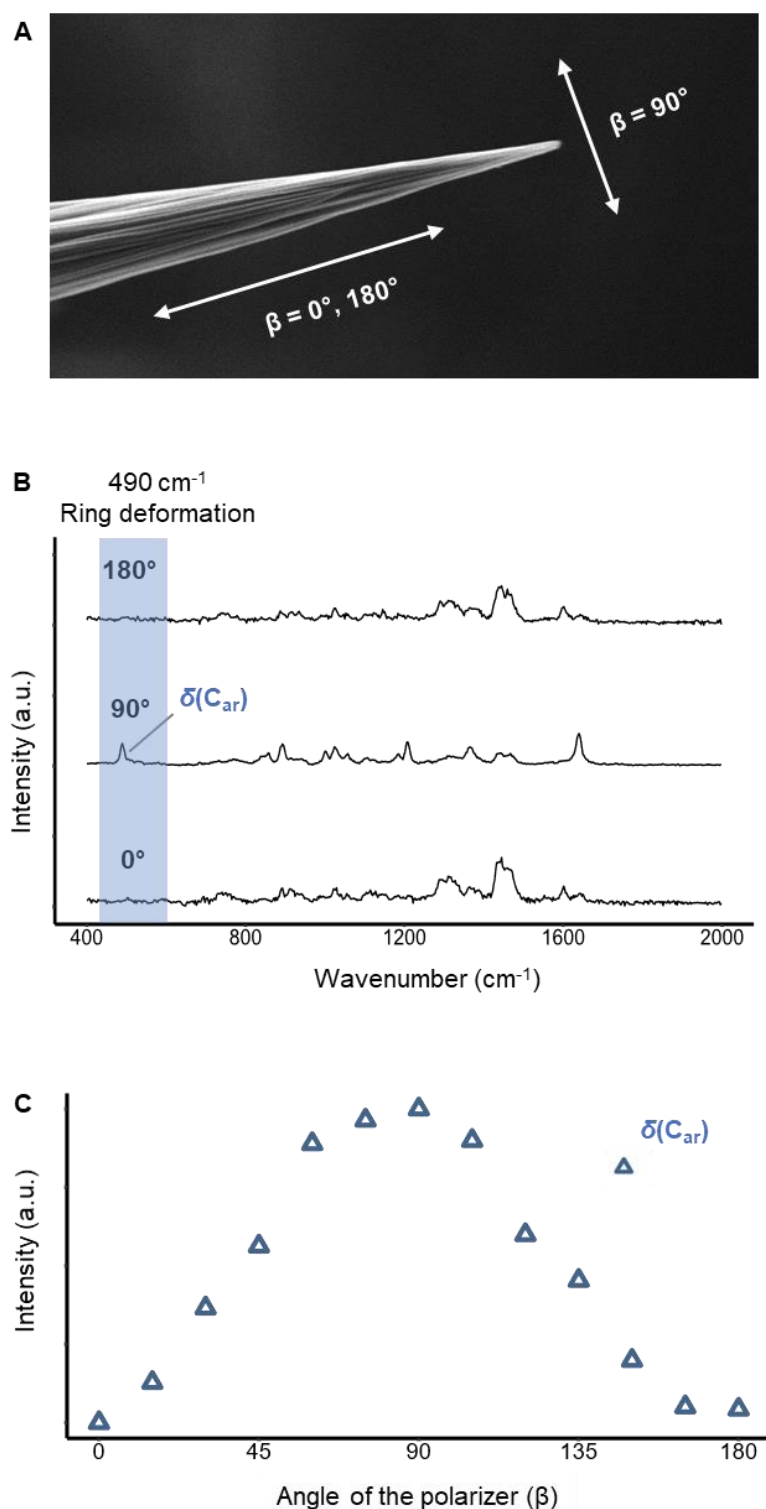


Figure 5-21. **Confocal polarized Raman measurements at the supramolecular spine in dependence of the angle of the polarizer.** **A:** Scanning electron microscopy image of a supramolecular spine with noted angle of the polarizer ($\beta = 0^\circ, 90^\circ$ and 180°) **B:** Confocal polarized Raman spectra of a supramolecular spine measured in dependence of the angle of the polarizer. The aromatic band of the ring deformation $\delta(\text{C}_{\text{ar}})$ at $\nu = 490 \text{ cm}^{-1}$ and of the BTA is present at $\beta = 90^\circ$ whereas the band vanishes at $\beta = 0^\circ$ and 180° **C:** Intensity of the aromatic band $\delta(\text{C}_{\text{ar}})$ plotted against the polarization angle measured from $\beta = 0^\circ$ to $\beta = 180^\circ$ in 15° steps with the maxima at 90° . Figure adapted and reproduced with permission from Ref.^[136] Copyright © 2024 The Authors. *Advanced Materials Interfaces* published by Wiley-VCH GmbH.

5.4.3 Morphology of the hierarchical structured supramolecular spines

The morphology of a single BTA spine can be seen in the scanning electron microscopy images in Figure 5-22 revealing the existence of BTA fibrils that built the conical BTA structure with a microgrooved surface. The Figure 5-22 A shows three boxes which reveal a magnification of the tip (a_1), the middle (a_2) and the base (a_3) of the spine, respectively. The spines tip features a smooth and defined shape with less than 400 nm in diameter as depicted in the Figure 5-22 a_1 . The fibrils converge at the end of the spine building the tip, which is attributed to the self-assembly process. This indicates that the tip is composed of finely structured fibrils featuring fibril diameter in a few hundred nanometer range. However, in the middle part of the spine (a_2) the fibril diameter raises to 500 nm – 1 μ m. The fibrils are arranged in an orientated way. As the fibrils emerge at some points, it is not possible to determine the exact fibril diameter. The organization of the fibrils forms intrinsic longitudinal aligned microgrooves (a_2). At the base (a_3), the BTA fibrils are more randomly oriented creating a microgrooved surface of the conical BTA due to the large fibril diameter up to 1 μ m. In summary, the supramolecular fibrils are aligned and densely packed with high degree of order at the tip whereas at the base of the BTA spine, the arrangement of the supramolecular fibrils deviates from the main orientation axis. As a result of these features, which is attributed to the self-assembly process, the supramolecular fibrils become significantly smaller in diameter from the base to the tip of the spine, resulting in a roughness gradient along the spine. Such fibrillar structure of the BTA is indicative for a highly hierarchical order and will be discussed in more detail in the following chapter.

The transition from the well-oriented supramolecular spines to the PA microfiber head is shown in *Appendix B* Figure 8-9. The fibrils exhibit a random orientation as they wrap around the head of the PA microfibers before extending into several highly oriented supramolecular spines. Furthermore, when BTA spines detach from the PA microfiber heads, they break at a specific point, which is the transition from the randomly oriented BTA fibers that wrap around the PA head to the highly organized and hierarchical BTA spine as depicted in *Appendix B* Figure 8-10. There has been no observation of an BTA spine breaking in the middle of the spine independently suggesting a high mechanical strength of the supramolecular fibers.

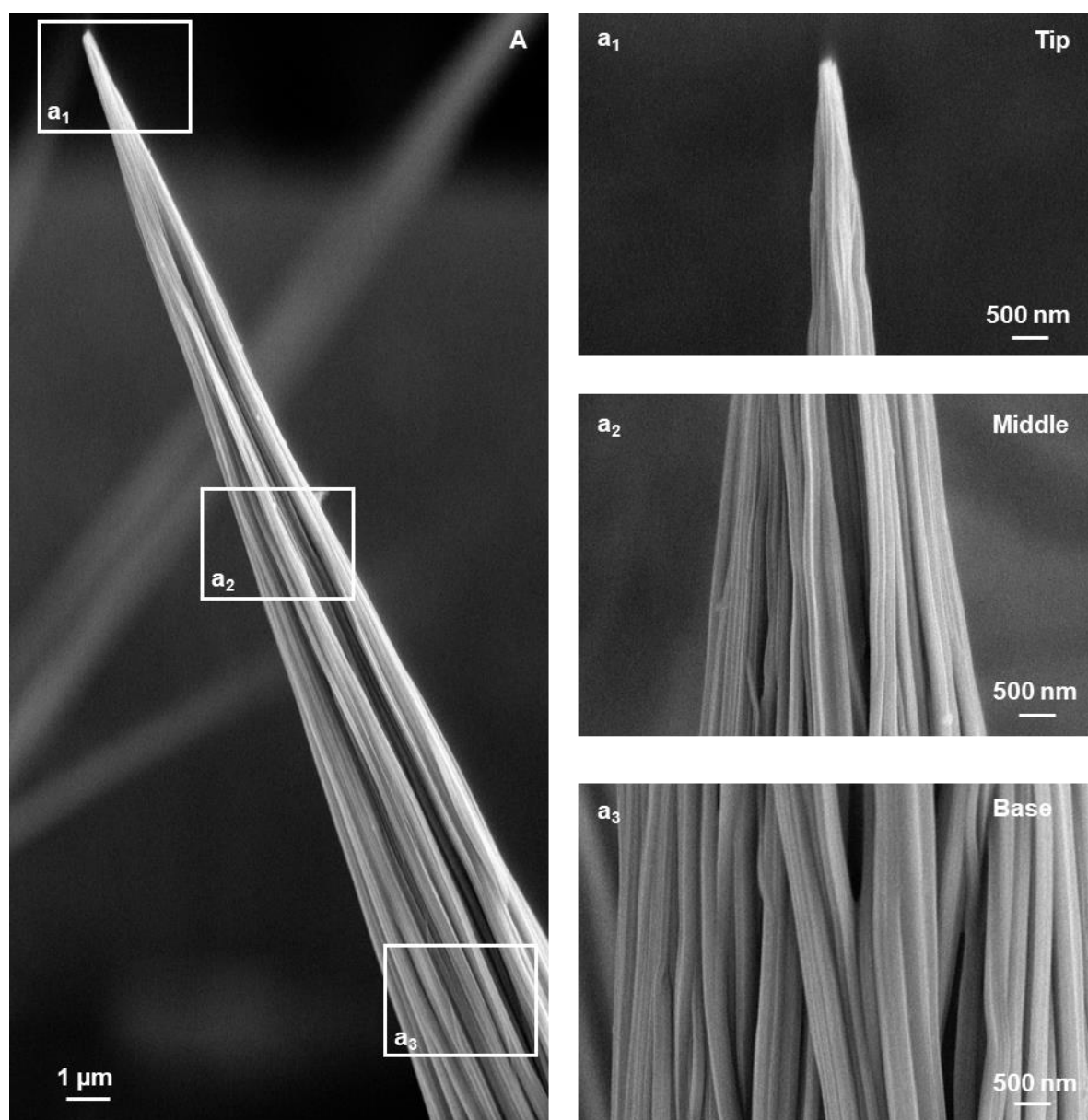


Figure 5-22. **Scanning electron microscopy images of a single conical BTA microstructure at different positions.** Single BTA microstructure with white boxes indicating the three zones of the conical microstructure: the tip, the middle and the base. **a₁**: depicts the tip of the BTA microstructure, **a₂**: the middle part of the microstructure and **a₃**: the base of the microstructure. Figure adapted and reproduced with permission from Ref.^[136] Copyright © 2024 The Authors. *Advanced Materials Interfaces* published by Wiley-VCH GmbH.

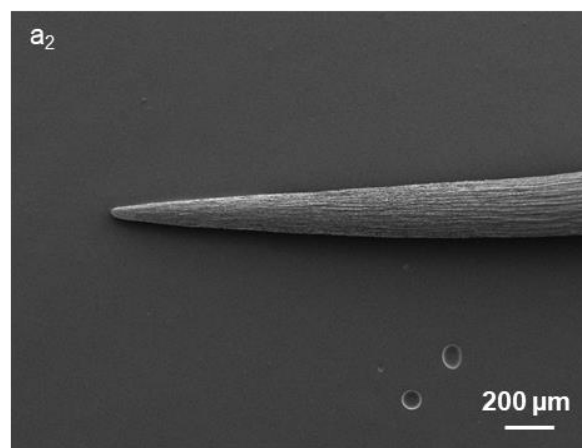
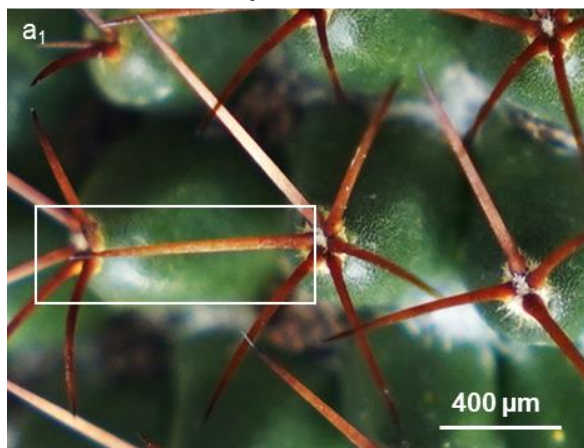
5.4.4 Similarities of supramolecular spines to natural cactus spines and biomimetic concept

Interestingly, so far, no conical BTA fibers have been published yet. Using the straightforward method of immersion, the PA flocks into a BTA solution and simple solvent evaporation lead to conical supramolecular structures of BTA-5 spreading into a multitude of spines at only one PA head. The conical structure of the BTA spines have strong similarities to natural cactus spines which spread away from a cactus body, in detail the so-called trichomes. Generally, natural cactus spines are formed from longitudinal fiber strands that assemble into straight fiber bundles – a similar feature was already shown before.^[137] Cactus spines can have many different dimensions depending on the cacti species. The cactus *mammillaria neocoronaria* as an example is depicted in Figure 5-23 A showing the cactus body and several natural spines spreading away (a₁). Some cactus spines are composed of fiber bundles. Due to these hierarchical levels of these fiber bundles along the cactus spine, certain cactus spines such as the *mammillaria neocoronaria* exhibits longitudinal microgrooves as visible in Figure 5-23 a₂.

The similarity of the natural cactus spines with the supramolecular conical structures of BTA-5 in this work is evident as shown in Figure 5-23 (compare A and B). As the natural spines spread away from the trunk of the cactus body, the artificial BTA spines spread away from the PA microfibers head (compare a₁ and b₁). Furthermore, the supramolecular conical structures of BTA-5 exhibit similar longitudinal microgrooves as observed for the natural cactus spines as depicted in Figure 5-23 b₂ (compare a₂ and b₂).

The feature of microgrooves combined with the conical structure of natural spines are mainly responsible for the ability of the spines to nucleate and collect atmospheric water in form of fog and dew in arid regions. Due to this unique water harvesting potential, cactus plants can survive in these harsh conditions of deserts.^[138] Due to the conical structure of the supramolecular spines and the microgrooved surface, these artificial spines have the potential to nucleate, collect, and transport atmospheric water as well and thus mimick the cacti spines in form and function.

A: Natural cactus spine



B: Artificial supramolecular spine

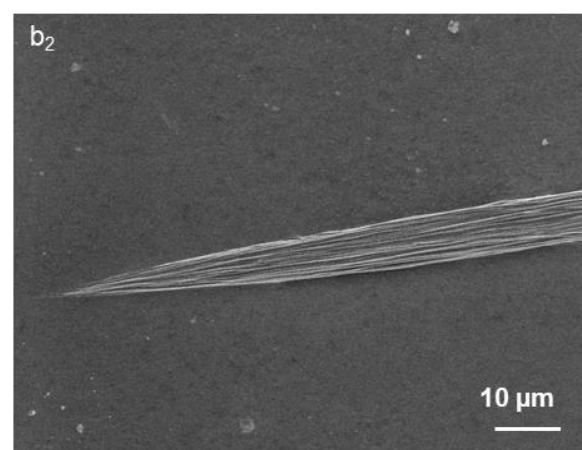
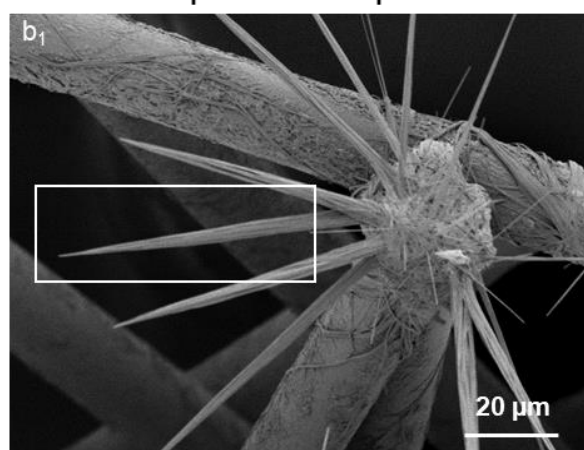


Figure 5-23. **Comparison of natural cactus spines and artificial supramolecular spines.** **A:** Natural cactus spine with **a₁**: an optical image of the natural cactus *mammillaria neocoronaria* and **a₂**: scanning electron microscopy image of a single natural spine from this plant. **B:** Artificial supramolecular spine with SEM images of **b₁**: an overview of a PA flock fiber with several artificial supramolecular BTA spines and of **b₂**: a single BTA spine. Figure adapted and reproduced with permission from Ref.^[136] Copyright © 2024 The Authors. *Advanced Materials Interfaces* published by Wiley-VCH GmbH.

Thus, in the following a closer look on the water harvesting features of natural cacti spines, the structural considerations and physical connections are made.

5.5 Background to natural cactus spines and their water interaction

Structural features and morphology of natural cactus spines

Nature developed intriguing approaches to harvest atmospheric water in arid regions without rainfall ensuring the water demand of several species.^[139] The effective interception, transport and collection of atmospheric water is achieved by an interplay of form, surface structure and chemistry. A variety of plants have adapted mechanisms to survive in arid regions such as grasses, wildflowers or cacti.^[139] For example, distinct cacti species are known to capture fog or nucleate dew and unidirectionally transport the water along their spines.^[138,140,141] An outstanding feature is that the nucleated or captured water is directionally transported towards the spine's base even against gravity owing to their conical morphology, surface structure and wettability.^[138] Reaching the spine's base, the droplet is absorbed by the cactus leaf and stored in the tissue. For example, Ju et al.^[138] demonstrated that the cactus *O. microdasys* with orientated barbs at the tip and aligned microgrooves along the spine as depicted in Figure 5-24 can efficiently collect fog with a water transport velocity of $\sim 12 \mu\text{m s}^{-1}$.^[142,143]

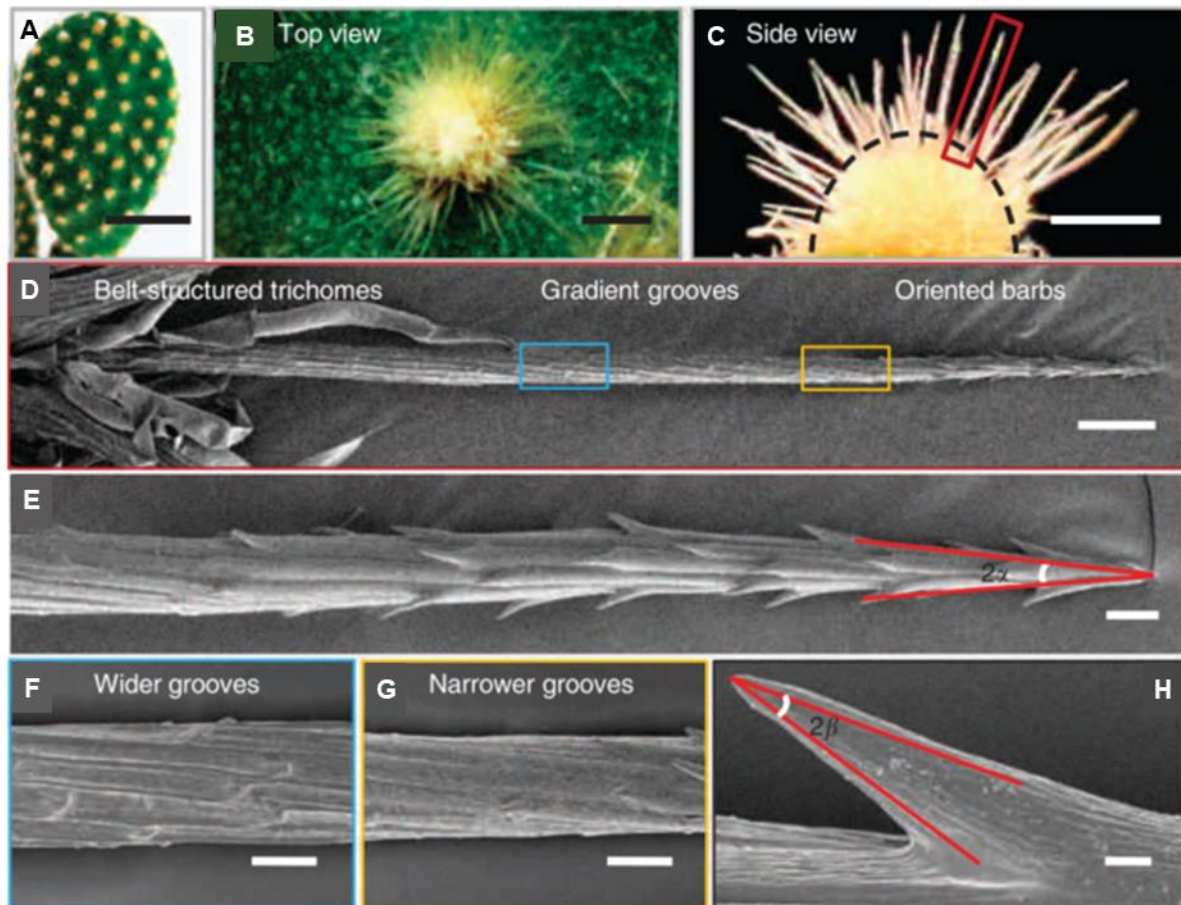


Figure 5-24. **Characteristics and surface features of the cactus *O. microdasys*.** **A:** Optical image of a segment of the cactus *O. microdasys* covered with evenly clusters of spines and trichomes. **B and C:** Close-up optical images show an individual cluster with spines growing from the trichomes, illustrating both top (**B**) and side (**C**) perspectives. **D:** Scanning electron microscopy image of a single spine with its three distinct regions: **E:** the tip features an apex angle (2α) with oriented barbs, while **F and G:** the middle exhibits gradient grooves. The base of the spine is adorned with belt-structured trichomes. Further magnified images (**F and G**) focus on regions near the base and tip of the cactus spine, highlighting differences in the width and density of microgrooves near the base and tip. **H:** Magnification of a single barb with an apex angle (2β) that covers the spine's tip (**E**). Scale bars are 5 cm (**A**), 500 mm (**B and C**), 100 mm (**D**), 20 mm (**E-G**) and 2 mm (**H**). Figure adapted and reproduced with permission from Ref.^[138] Copyright © 2012 Macmillan Publishers Limited. All rights reserved.

In general several driving forces can lead to a directional droplet movement mostly caused by gradients such as a chemical gradient,^[144] a thermal gradient^[145] or a shape gradient.^[138,146] Furthermore, the directional liquid transport has been reported for many living organisms (e.g. peristome of pitcher plants,^[147] spider silk^[148] and cactus plants^[138]) that use their structural features and the named driving forces often as combination to achieve the liquid movement. The water transport on cacti spines for example is caused by a shape gradient in combination with a microstructured surface and a resulting wettability gradient along the spine. These three features are described in more detail in the following:

D) *Conical structure*

The conical structure of the spine results in a shape gradient along the spine axis and thus induces a forced droplet movement.^[138,149] The curvature of the spine leads to a LAPLACE pressure difference on the opposite sides of the captured water droplet as shown in Figure 5-25. If a droplet interacts with a conical surface of the spine, it will adapt to the geometry of the surface resulting in a higher LAPLACE pressure at the side of the droplet with the smaller radius (R_1) and larger LAPLACE pressure at the side of the bigger radius (R_2). This causes the water droplet to move towards the spine's base.

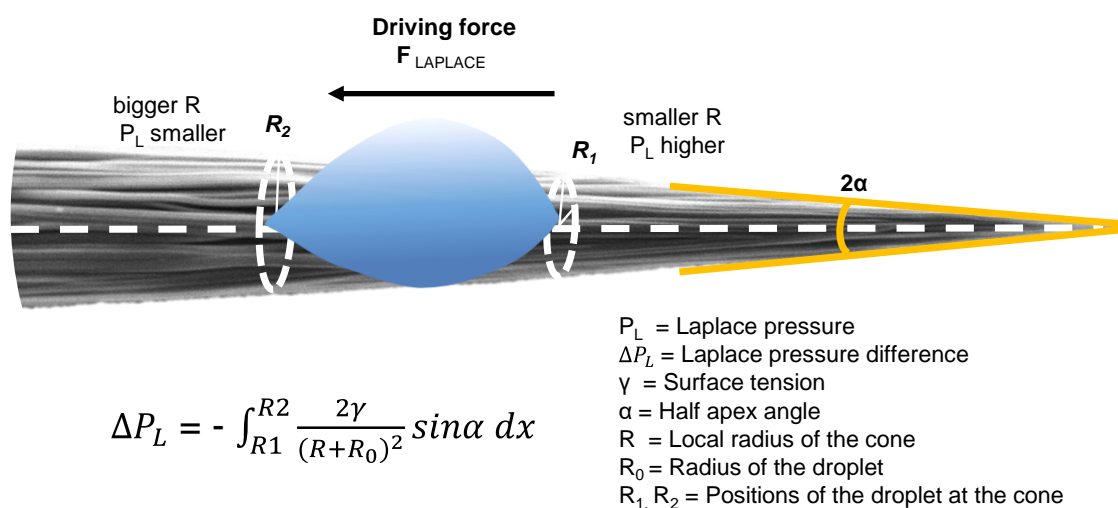


Figure 5-25. Schematic and mathematical presentation of the LAPLACE pressure difference at a water droplet on a spine featuring a conical morphology.

II) *Microgrooves*

The natural cactus spines feature a microgrooved surface. These microgrooves vary in frequency and are able to channel the water along the spine.^[138,150] Figure 5-26 depicts the work of Gurera et al.^[150] which systematically investigated the influence of the water droplet movement on cylinder and cones with ungrooved and grooved surface, respectively. Their investigations show that cylinders collect water droplets at their tip which subsequently grow and fall off. Thus, grooves have no influence on a cylinder. The water droplets are not transported due to the missing LAPLACE pressure difference. In contrast to that, cones transport the water unidirectionally with and without grooves. However, the cones with a grooved surface collect more water (in respect to the weight) as it is channeled along the cone.

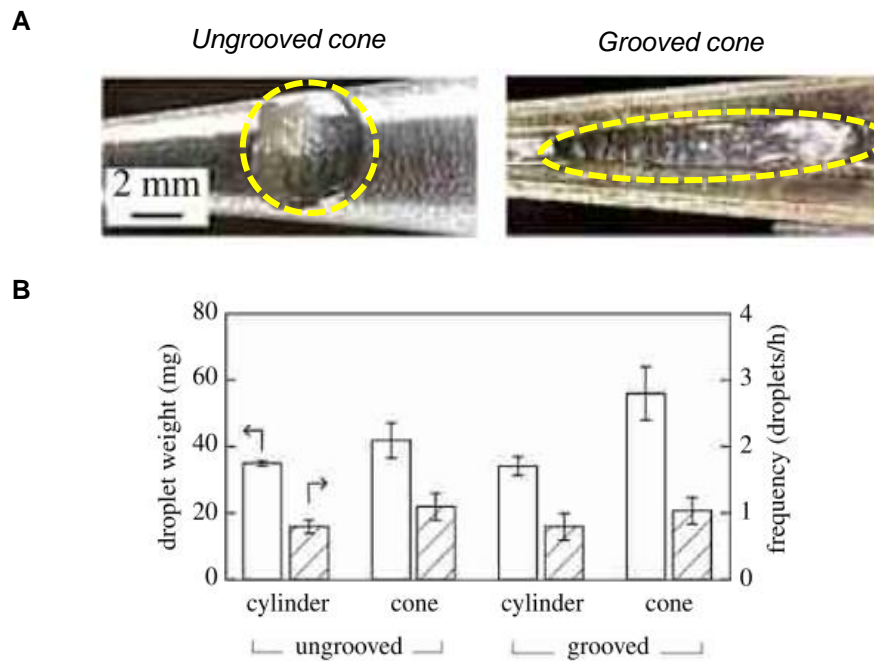


Figure 5-26. **Water interaction on ungrooved/grooved cylinder and cones.** **A:** optical images of a water droplet located on an ungrooved cone and a grooved cone. The yellow circles indicate the droplet shape. Here, the grooves causing the droplet to elongate. **B:** comparison of the droplet weight and frequency collection at the base. Figure adapted reproduced with permission from Ref.^[150] Copyright © 2018 The Author(s) Published by the Royal Society.

III) *Wettability and roughness gradient*

In contrast to fog harvesting, Malik et al.^[140,141] observed that dew harvesting is only possible for cacti that exhibit spines with a hydrophilic surface and microgrooves, whereas a cactus with a hydrophobic surface and microstructuring in form of barbs is not able to nucleate water and thus no collection of dew occurs. This relationship corresponds with the work of Gurera and Bhushan^[150] who proved that the superhydrophilicity of the spine's surface is more efficient in transporting the water from the tip to the base due to spreading of the droplet. A highly hydrophilic surface favors the water droplet nucleation, thus resulting in higher nucleation rates as the free energy barrier is lowered.^[151,152] This can be explained in detail by the wettability of surfaces described as the parameter "contact angle" (CA).^[153] When a droplet is in contact with a solid surface, it tends to be in the lowest-energy state. The contact angle represents the definite angle between the solid and the vapor surrounded. This static state can be described with the classical Young equation^[154] (Equation 1) as example for ideal smooth surfaces.

$$\cos \theta = \frac{(\gamma_{SV} + \gamma_{SL})}{\gamma_{LV}} \quad (1)$$

where the contact angle value is represented by θ and the surface tension of the solid-vapor, solid-liquid and liquid-vapor by γ_{SV} , γ_{SL} and γ_{LV} , respectively.

If the CA value is $90^\circ < \theta < 150^\circ$ the surface is considered as hydrophobic. If the CA value exceeds the 150° it is classified as superhydrophobic whereas CA lower than 90° are classified as hydrophilic and CA close to zero as superhydrophilic.^[155] Considering the non-ideal case such as a rough surface, different models have been established to describe the effect of roughness on the CA of droplets, namely the Wenzel and the Cassie-Baxter model. Roughness can be defined by the roughness factor r which is the ratio of the actual surface and the geometric surface.^[156] For any realistic solid exhibiting surface roughness, the actual surface (rough) deviates from the geometric surface (smooth) being significantly greater ($r > 1$). Wenzel propose a fully wetting model, where the water droplet is in full contact with the rough surface.^[156] In contrast to that, the Cassie-Baxter model assumes that the droplet is only in contact with the grooves and the voids below are filled with air.^[157] In real systems, a coexistence of both states and models can be present. In conclusion, for the static state of a droplet on a solid surface, its roughness and chemical properties play an important role to predict the wetting behavior. Besides the static state of droplets on solid surfaces, there exist several dynamic states that a droplet can experience which are mostly driven by the topographical or chemical composition. The resulting wettability gradient causes an asymmetrical spreading behavior of the droplet which is directional as observed and described for the conical spines of cacti plants.

Preparation of artificial cactus spines

Research dedicates significant effort to made use of these natural approaches or to mimick. This research is driven because access to fresh water has become a serious issue today as supply and demands are significant.^[158] To address the increasing water shortage, atmospheric water in form of fog and dew is therefore considered as a promising supplementary fresh water source.^[159–161] Fog is a meteorological phenomenon that occurs when warm, moist air encounters colder conditions, causing water vapor to condense into tiny droplets suspended in the air, creating a visible aerosol.^[139] The diameter of such fog droplets are around 10-50 μm and can achieve speed wind of 1-5 cm s^{-1} up to 1-10 m s^{-1} .^[162] In contrast to that, dew is a surface phenomenon where the water collection takes place on a surface through condensation. In detail, nanodroplets will nucleate on the surface which then merge and eventually grow during the proceeding condensation process. This happens when the surface temperature of the object is below the dew point temperature.^[163] In arid regions, temperature drops drastically at night which can be lower than the dew point and thus give the possibility to water condensation.

The fabrication of artificial spines designed for the specific purpose of unidirectionally water transport have been in focus in recent years. Some examples of artificial spines fabricated by different approaches are shown in Figure 5-27. For example, Bai et al.^[164] prepared artificial spines via a combination of electrospinning with a sacrificial template method (A). In detail, they used a silver needle which was covered by polystyrene/ poly(amic acid) composite fibers in an electrospinning set-up. Afterwards they conducted thermal imidization resulting in a polyimide fiber. These polyimide based artificial spines exhibit a grooved surface structure as depicted in Figure 5-27 a₁-a₃.

Other approaches are based on gradient electrochemical corrosion (Figure 5-27 B),^[165] electrochemical etching,^[166] a vapor-phase approach,^[167] magnetic particle-assisted molding (Figure 5-27 C),^[168] magnetorheological drawing lithography (Figure 5-27 D),^[169] an integrative electrochemical corrosion and hydrothermal method (Figure 5-27 E),^[170] or 3-D-printing^[171,172] (Figure 5-27 F)^[173] to generate artificial spines for fog harvesting. Here, the main concept of all methods focused on the conical shape of the resulting material. Some artificial spines show a wettability gradient created via chemical gradients.^[174] Moreover, it's worth noting that most of these spines were designed for fog harvesting, and their polarity was not considered, thereby omitting the potential for dew nucleation.

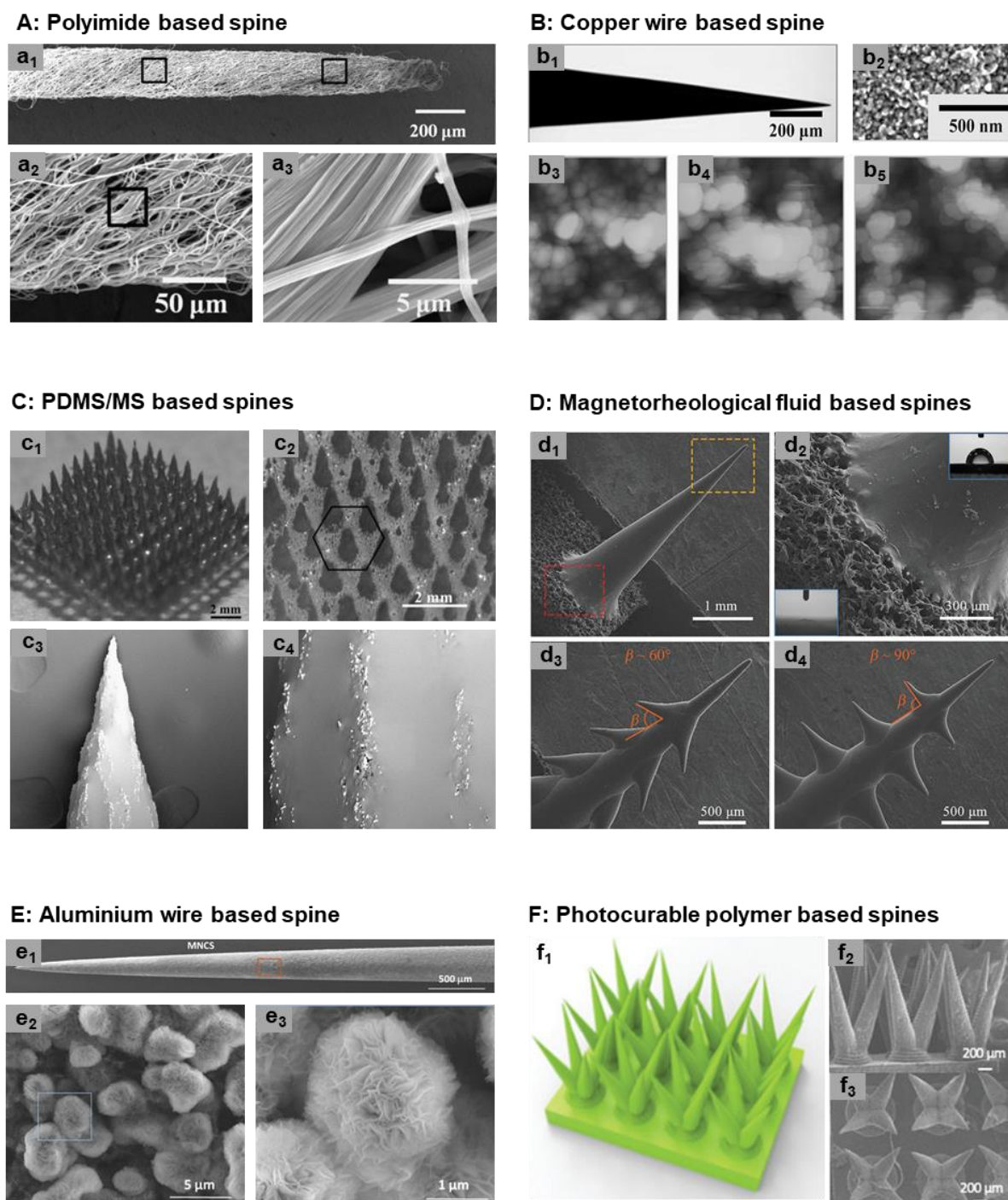


Figure 5-27. **Artificial spines reported in literature.** **A:** Polyimide based spine prepared via a combination of electrospinning with a sacrificial template method.^[164] **B:** Copper wire based spines prepared gradient electrochemical corrosion.^[165] **C:** polydimethylsiloxane and cobalt magnetic particles (PDMS/MS) based spines prepared via magnetic particle-assisted molding.^[168] **D:** Magnetorheological fluid based spines prepared via magnetorheological drawing lithography.^[169] **E:** Aluminum wire based spine prepared via an integrative electrochemical corrosion and hydrothermal method.^[170] **F:** Photocurable polymer based spines prepared via 3-D printing.^[173] Figures adapted and reproduced with permission from Refs. Copyright © 2015 The Authors. Published by WILEY-VCH Verlag GmbH & Co. KGaA, Weinheim, © 2013 WILEY-VCH Verlag GmbH & Co. KGaA, Weinheim, © 2014 WILEY-VCH Verlag GmbH & Co. KGaA, Weinheim, © 2019 WILEY-VCH Verlag GmbH & Co. KGaA, Weinheim, © 2018 WILEY-VCH Verlag GmbH & Co. KGaA, Weinheim and © 2019 WILEY-VCH Verlag GmbH & Co. KGaA, Weinheim.

5.6 Water interaction studies on supramolecular spines

For the upcoming experiments, the BTA derivative BTA-5 is selected. Even though BTA-4 with the sulfur containing periphery shows similar self-assembly into conical structures at the PA flocks head, the BTA-4 is not water-stable which would be inconvenient for the investigations with water. Furthermore, the microstructuring of the surface was not as pronounced as found for BTA-5. Thus, BTA-5 was identified as the best candidate for further experiments to biomimick natural cactus spines, as it exhibits high water stability and pronounced microstructuring on the surface of the conical spines.

5.6.1 Water condensation on supramolecular spines

The unidirectional water transport from the tip to the base, observed on natural cactus spines, is primarily attributed to three factors: a Laplace pressure difference due to the conical shape, longitudinal microgrooves, and a roughness gradient as described in detail in the background chapter.^[138,149,175] Whereas in literature typically a conical shape is used, combining these structural characteristics in artificial spines clearly enhances directional water transport. The fabricated supramolecular spines exhibit all of these features, including a conical shape, longitudinal microgrooves due to the alignment of the supramolecular fibrils and a roughness gradient that increases from the tip to the base since the supramolecular fibrils become thinner towards the tip during the self-assembly process. To investigate the wettability of the BTA spines environmental scanning electron microscopy (ESEM) on a single supramolecular spine was conducted. For this, a single spine was mechanically removed from the PA flock fiber and placed on a sample holder. The sample chamber in the ESEM is designed to control the surrounding environment, in particular temperature, humidity and pressure. This allows the investigation of samples in environmentally controlled states and furthermore how materials interact with moisture in real time. To comprehend how water behaves under varying temperature and pressure conditions in the ESEM and how pressure affects phase transitions, a pressure-temperature phase diagram of water is a valuable tool (Figure 5-28).

This diagram provides insight into the changes in water's physical state under different combinations of temperature and pressure. The phase transition can be induced by either changing the temperature at a given pressure or vice versa. As shown in Figure 5-28, by maintaining a constant pressure of 720 Pa and gradually lowering the temperature, the water molecules first are in the gaseous phase at 3.9 °C (1) and then pass the line at 2 °C (2+3) corresponding to the dew point. Passing the dew point ultimately leads to the condensation of water molecules on the sample's surface.

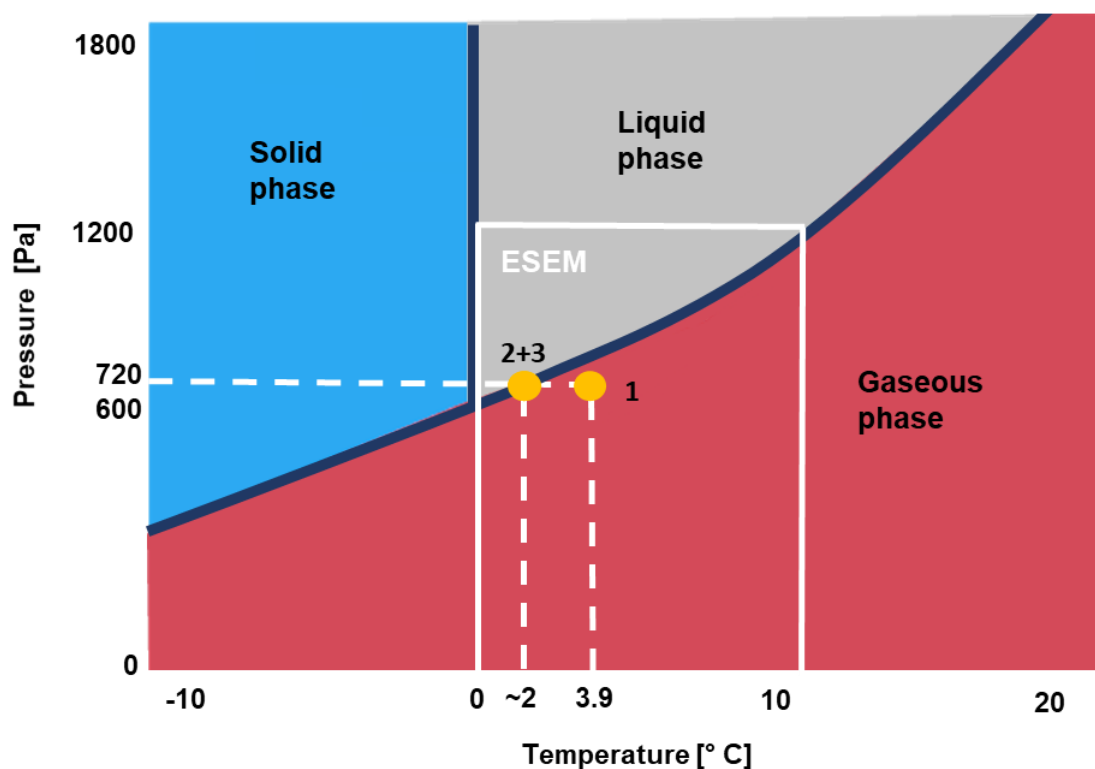


Figure 5-28. **Pressure-temperature phase diagram of water for environmental scanning electron microscopy and dew condensation.** Pressure-temperature phase diagram of water with the indicated gaseous, liquid and solid phase, respectively. Holding the pressure constant at 720 Pa and cooling down subsequently the water molecules are in the gaseous phase at 3.9 °C (1) and crossing the line at 2 °C (2+3) resulting in condensation of the water molecules. Figure adapted and reproduced from Ref.^[176] Copyright © 2019 Springer Nature Switzerland AG.

For the ESEM measurement, a single isolated BTA spine was used as this SEM method has its limitations with respect to sample origins and geometries. In this case, the polymer flock acts as an isolator hampering a proper and defined cooling of the entire sample. This results in a defined cooling of the flock bottom but an insufficient cooling of the spines. This issue is solved by studying isolated BTA spines. For this, the BTA spines are extracted from the polymer flock and placed onto the cooling stage of the ESEM. The measurements were conducted at a constant water vapor pressure of 720 Pa as depicted in Figure 5-29 A. During the ESEM measurements, the stage and subsequently the spines were cooled from 3.9 °C to 1.9 °C at a cooling rate of 1.0 °C min⁻¹, reaching the dew point at 2.0 °C under these conditions. The initial state prior water condensation on the BTA spines is displayed in Figure 5-29 a₁. The arrow indicates the microstructured surface of the spine. As the temperature drops and reaches the dew point at approximately 2.0 °C, water nucleation occurs at the surface of the spine, resulting in a significant wetting and filling of the grooves indicated by the arrow (see Figure 5-29 a₂). With further cooling to 1.9 °C, water condensation continues, and simultaneously, directional water transport from the tip towards the base of the spine occurs. This is indicated by the formation of a droplet reservoir at the base of the spine Figure 5-29 a₃. The extensive spreading of water over the BTA spine suggests a superhydrophilic surface behavior.^[177] This process is reversible. Heating the stage again above the dew point, the water evaporates and the filling of the grooves vanishes.

The experiments were repeated with the same conditions for neat polyamide microfibers, i.e. not decorated with BTA fibers (Figure 5-29 B). Again, individual microfibers are measured instead of the flock as the same issue occurs for the neat flock, where only the bottom is cooled sufficiently to induce water condensation. The initial state prior water condensation on the neat polyamide microfibers is displayed in Figure 5-29 b₁. As the temperature on the stage and thus of the microfibers reaches the dew point at approximately 2.0 °C, water nucleation at the surface is visible. In strong contrast to the observation of the water nucleation on the BTA spines, the neat PA microfibers only shows random droplet formation on the microfiber surface as depicted in Figure 5-29 b₂. The arrow shows such a water droplet. Proceeding cooling leads to further droplet formation and enlargement of some droplets (Figure 5-29 b₃). However, no spreading of the water on the polyamide surface is observed. A more likely observation is the coalescence of individual drops in certain areas. Such a droplet formation is indicative for a more hydrophobic surface compared to the BTA spines.

The surface of the polyamide microfiber without a conical shape or any grooves and microstructuring show only droplet formation and no movement of the water droplets in any direction. This is in line with the work of Gurera et al.^[150] who investigated that cones with a microgrooved surface efficiently collect water as it is channeled along the cone. They further proved that the superhydrophilicity of the spine's surface is more efficient in transporting the water from the tip to the base due to spreading of the droplet. This renders the of the supramolecular spines interesting candidates to study unidirectional water transport, which will be investigated in the next chapter.

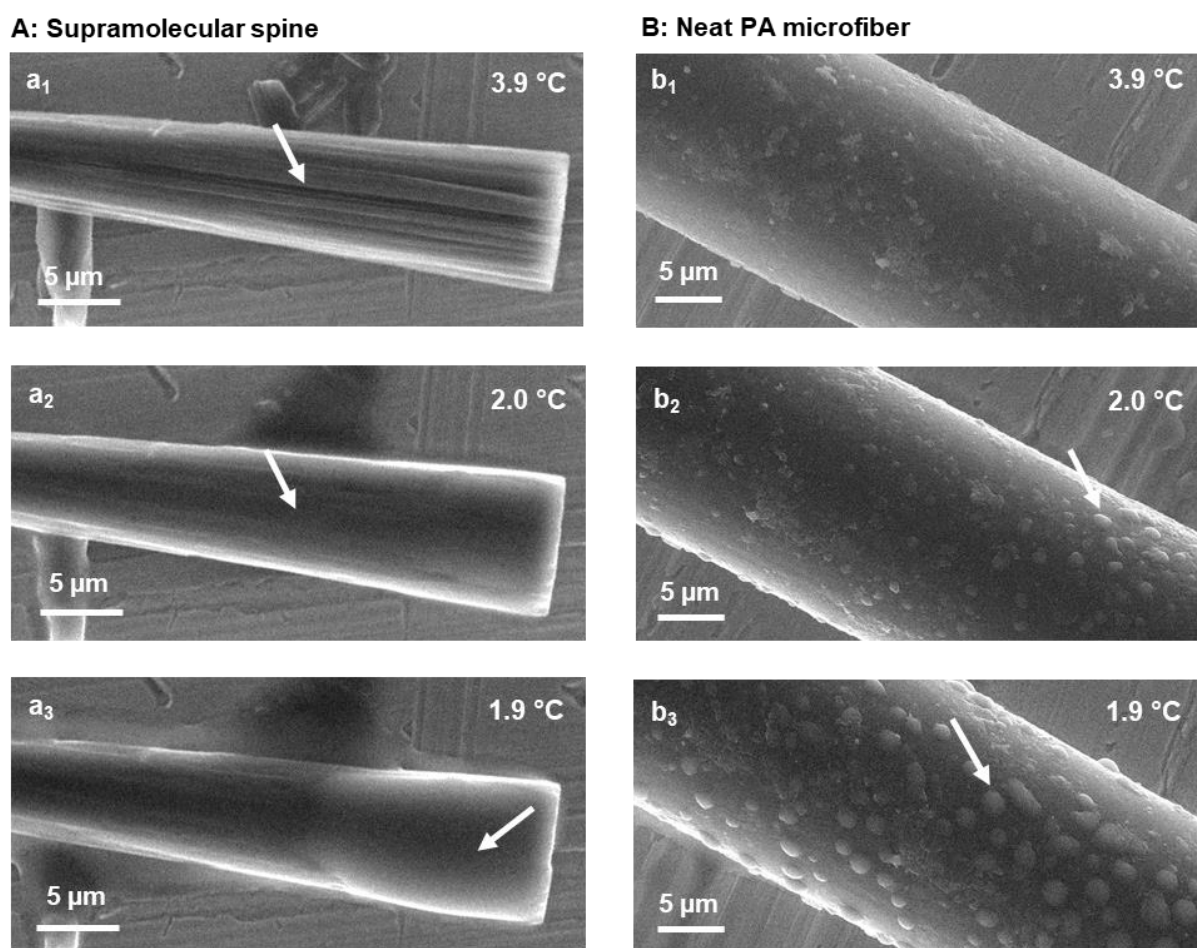


Figure 5-29. **Environmental scanning electron microscope (ESEM) measurements of an BTA spine (A) and a neat PA microfiber (B).** The measurements were conducted an at constant water vapor pressure of 720 Pa and different temperatures between 3.9 °C and 1.9 °C. The state prior water condensation is shown in **a₁**: for the BTA spine and **b₁**: for the neat PA microfiber. **a₂** and **b₂**: Upon cooling at around 2.0 °C the dew point is reached at both samples. Water condensation occurs resulting in a complete wetting and filling of the grooves for the BTA spine (**a₂**) and droplet formation on the neat PA microfiber (**b₂**). **a₃** and **b₃**: Further cooling to 1.9 °C leads to a water transport towards the base of the spine (**a₃**) and further grow of droplets on the neat microfibers (**b₃**). Figure adapted and reproduced with permission from Ref^[136] Copyright © 2024 The Authors. *Advanced Materials Interfaces* published by Wiley-VCH GmbH.

5.6.2 Unidirectional water transport on supramolecular spines

To investigate the BTA spines' capability for unidirectional water transport, artificially generated fog was steamed onto the spine. Therefore, the fog was created artificially by an ultrasonic humidifier. The sample is placed under an optical microscope and the flock decorated with BTA spines is irrigated with fog. This allows an in-situ observation of the water interaction with the BTA spines. The observations are captured in a video, which can be found in the Supplementary Information of Reference. ^[136] Images of the video are shown exemplarily in Figure 5-30. The left row (A, C and D) depicts a top view of a flock microfiber decorated with BTA spines spreading away from the microfibers head and fog irrigation. The right row (B, D and F) shows a magnification of the captured water droplets on an BTA spine (white boxes). The respective time interval is noted in the top right corner. The fog droplets are collected at the BTA spines tip and then unidirectionally transported to the base of the spine as shown in Figure 5-30 B, D and F. These experiments were repeated and documented at different days and samples showing always the same reproducible unidirectional water transport from the BTA spines tip to the base. On the basis of the in-situ fog irrigation experiments the droplet velocity was determined to be $150 \mu\text{m s}^{-1}$. Compared to the well-investigated model cactus *Opuntia microdasys* where water droplet transportation occurs at a rate of around $\sim 12 \mu\text{m s}^{-1}$, ^[138,142,143] the water transport facilitated by BTA spines is notably faster, exceeding this rate by a factor of more than 10.

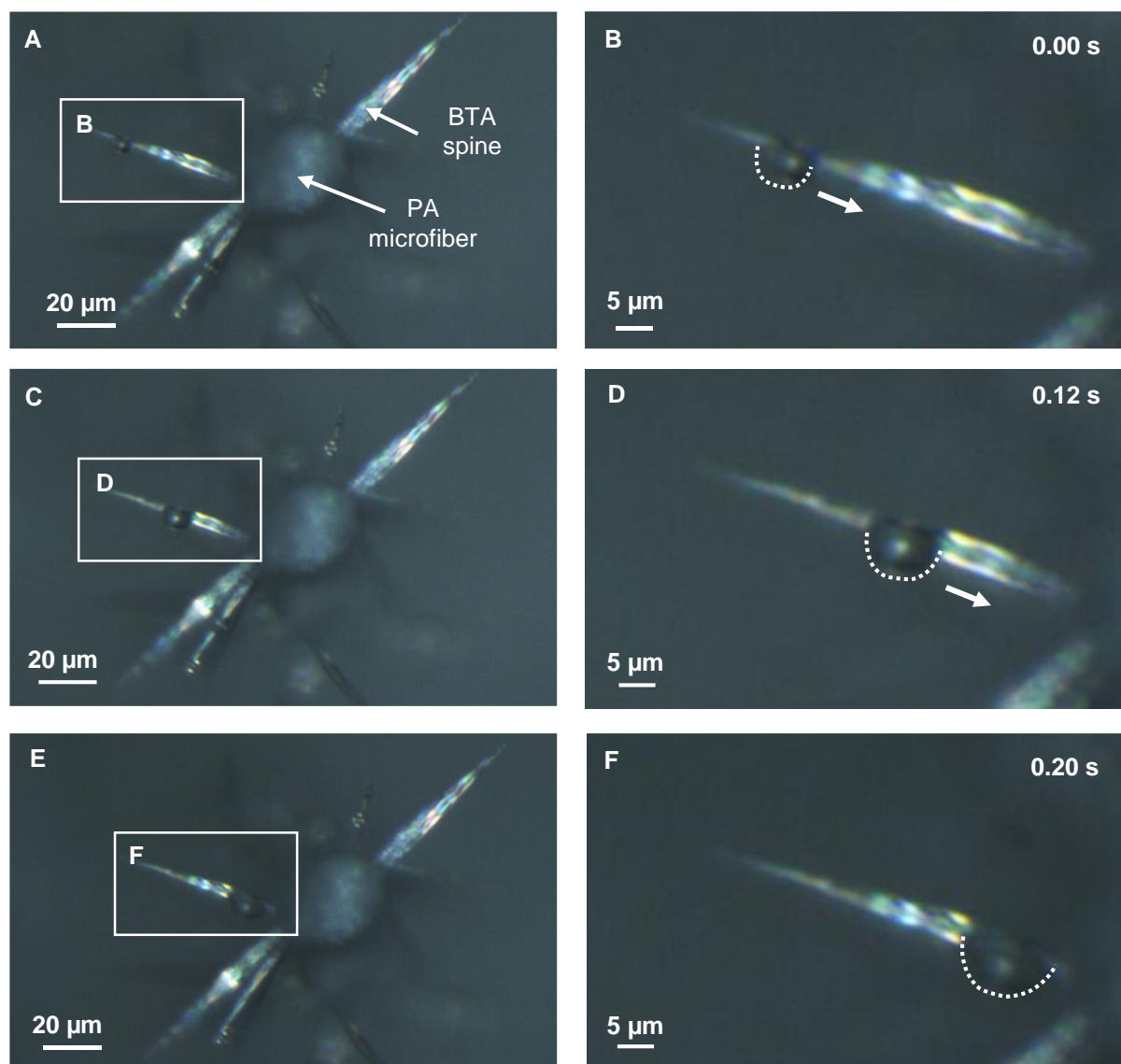


Figure 5-30. **Optical microscope images of the unidirectional water transport on a BTA spine.** **A, C and D:** Overview of a PA microfiber decorated with BTA spines and irrigation with fog. **B, D and F:** Magnification of an of an individual BTA spine showing the droplet movement of captured water from the tip towards the base at different times. Figure adapted and reproduced with permission from Ref.^[136] Copyright © 2024 The Authors. *Advanced Materials Interfaces* published by Wiley-VCH GmbH.

In addition to the water droplet transport of the artificial fog another observation is noted: the initial water collection and transport process of droplets proceed in the above described manner until a homogeneous water film is formed due to the superhydrophilic character of the spines. Once the spine is thoroughly wetted from previously transported droplets, the subsequent droplets start to spread, resulting in the formation of a water film along the BTA spine. This is consistent with the findings from ESEM: the BTA spine gets wetted due to its hydrophilicity, and as a result, the microgrooves are filled with water. The presence of the water film causes an acceleration of water droplets along the spine and thus enhances the water transport. This water transport is too fast to be observed with the used setup. This phenomenon has been already

reported in literature for water transport on spines and is referred to as "lubrication effect".^[149,174,178] Additionally, the spreading of the water droplet contributes to a higher LAPLACE pressure difference. The increase in the radii R_1 (R'_1) and R_2 (R'_2) at opposite sides of the droplet results in an overall higher-pressure difference, which, in turn, produces a greater driving force ($F'_{LAPLACE}$) and consequently faster water transport.^[174] The initially water droplet transport and the followed water collection process with schematically shown influence on the radii is depicted in Figure 5-31. The water droplet transport shown in Figure 5-31 A owing to the driving force $F_{LAPLACE}$. A water film (blue marked spine, filled grooves) in Figure 5-31 B causes a further spreading of a large droplet as schematically depicted. The increasing radii difference of the droplet results in a higher driving force $F'_{LAPLACE}$. Thus, it can be stated that the transport velocity of the droplets, accelerated by the lubrication effect, is significantly faster than the initial droplet transport and surpasses the transport velocities of the natural cactus *O. microdasys* by a much larger factor as it can be determined.

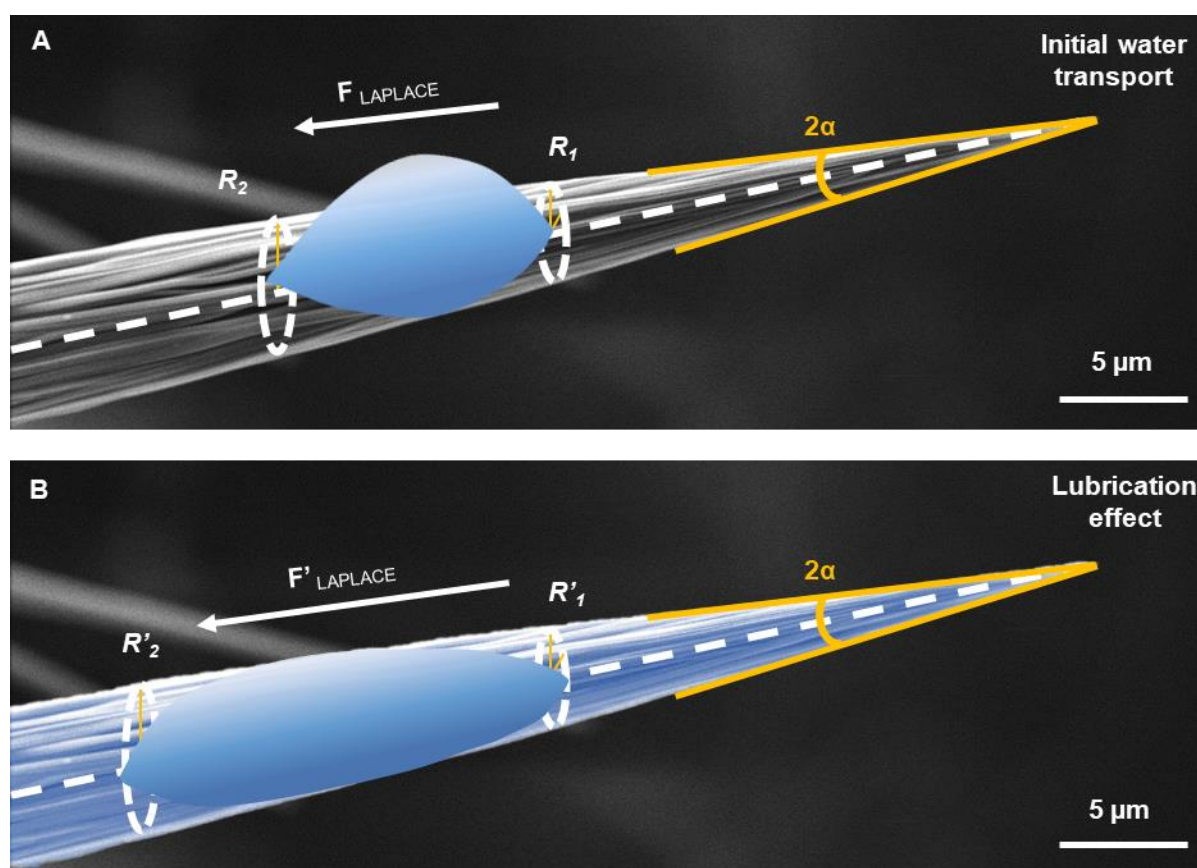


Figure 5-31. **Schematic representation of the initial water droplet transport and the lubrication effect.** **A:** Initial water transport of droplets on an BTA spine generating the driving force $F_{LAPLACE}$ from the radii difference (R_1 , R_2) at the opposite sides of the droplet. **B:** A wetted spine (blue false colored) results in a lubrication effect and spreading of the droplet. This generates a higher driving force $F'_{LAPLACE}$ due to increased radii difference (R'_1 , R'_2) at the opposite sides of the droplet. The apex angle is described by 2α . Figure adapted and reproduced with permission from Ref.^[136] Copyright © 2024 The Authors. *Advanced Materials Interfaces* published by Wiley-VCH GmbH.

5.7 Conclusion to self-assembly of supramolecular fibers within polymer flocks

This chapter made use of polymer flocks with the aim to explore the self-assembly of supramolecular fibers within polymer flocks as a novel self-assembly approach. This work was performed in collaboration with Felix Bretschneider (Macromolecular Chemistry II, Prof. Dr. Greiner). The primary objective here was to explore how capillary forces within aligned polymer flocks act as structure-directing substrate by driving the transport of the solution to the top of the flock. For this, a polyamide (PA) flock was prepared and exposed to solutions of three selected BTAs. It was found, that for distinct BTAs and proper processing conditions the polyamide flock indeed serves as structure-directing substrate comprising capillary effects along the vertically aligned microfibers and transporting the solutions towards the polyamide heads, which eventually led novel selectively formed supramolecular fiber morphologies. This process led mostly to supramolecular fibers on top of the PA fibers, if sufficient capillary forces are present. More surprisingly, the BTA fibers feature a unique conical shape with microstructured surfaces. In depth investigations of the new BTA fibers morphology reveal that beside the conical shape, the spines exhibit several hierarchical levels and are composed of supramolecular fibrils which are responsible for the microstructured surface. Furthermore, by optimizing the self-assembly conditions within the polymer flock by adjusting the solvent and drying conditions, reproducible supramolecular spines are obtained spreading away of the polyamide's heads. The BTA spines feature length around 50 μm and the amount of BTA spines per PA microfibers vary from less than 20 to 80 and occasionally over 100 spines are observed.

The conical shape with its structural features such as microgrooves and structural gradients mimics that of natural cactus spines in form and function enabling the nucleation and directional transport of water towards the spine's base. Environmental scanning electron microscopy reveal that these artificial BTA spines feature a superhydrophilic surface, which potentially further improves the water transport. Here, a water droplet velocity of 150 $\mu\text{m s}^{-1}$ was found, exceeding those of the natural cactus *O. microdasys* by more than a factor of ten.

6 Thermal diffusivity of supramolecular fibers

6.1 Background to lock-in thermography

Infrared (IR) thermography, as a thermal imaging technique, determines the surface temperature distribution of an object in a contactless non-destructive manner over considerable distances of several 100s of μm .^[179] IR thermography relies on the heat transfer mode of thermal radiation, that is the emission of electromagnetic radiation in the infrared spectral range.^[179] This method allows for the investigation of dynamic temperature changes, thus evaluating the time-dependence of temperature distributions in an object, referred to as thermal diffusivity (α).^[180] One prominent example for “active or dynamic thermography” is the so-called lock-in thermography. In this method, the object is periodically excited by a heat source with a certain lock-in frequency ($f_{lock-in}$). Thus, the heat is introduced in an oscillating manner and the sample experience subsequent heating and cooling. The temperature will oscillate with the same frequency as the applied lock-in frequency. The amplitude and phase of the oscillating temperature are position dependent and detected with an IR camera and typically calculated by a software.^[179]

The experimental set-up of the lock-in thermography measurement is schematically depicted in Figure 6-1 A and B. The heat is introduced into the sample via a modulated laser and the detection of the resulting temperature distribution occurs via an IR camera. The acquired signal is then converted to amplitude and phase data by a computer applying a Fourier transformation.^[181] Here, a 1-D fiber is fixated onto a 3-D-printed sample holder and thermally excited by the laser at the center (Figure 6-1 C).^[182] The sample is placed inside a vacuum chamber to minimize heat losses. If heat losses from the sample to the surrounding are negligible, the so-called *slope method* can be applied to obtain the thermal diffusivity.^[183,184] For this, the natural logarithm of the amplitude and the phase is plotted against the distance to the laser spot for each pixel. In the linear region at sufficient distance from the excitation spot, the amplitude and phase slope are ideally identical with respect to the relative distance to the laser beam and only depend on the lock-in frequency and the thermal diffusivity. As a consequence, the slopes can be used to determine the thermal diffusivity of the material as exemplarily shown in Figure 6-1 D and E.

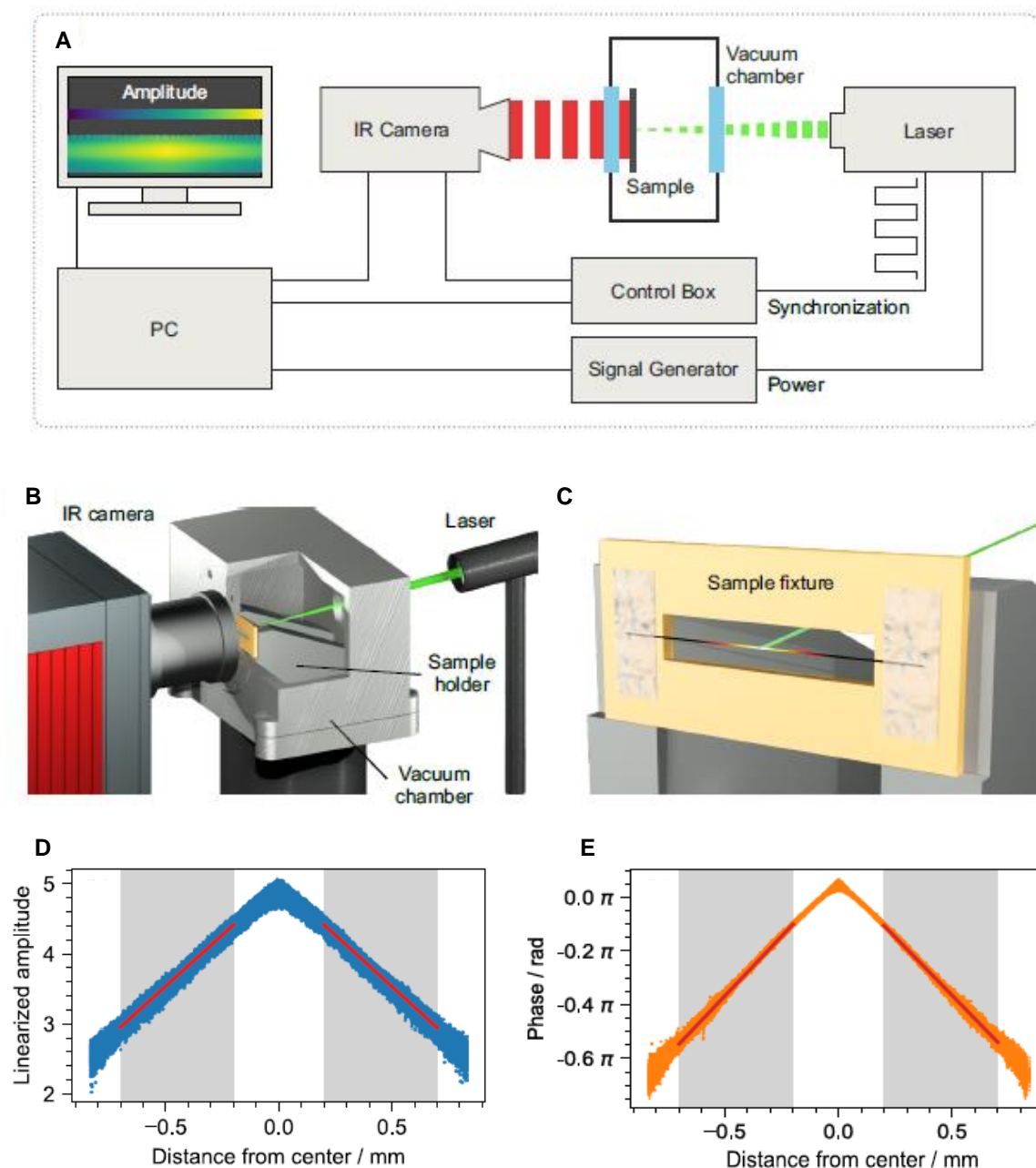


Figure 6-1. **Measurement set-up and resulting amplitude and phase plots.** **A:** Schematic presentation of the measurement set-up. A modulated laser is responsible for the heat introduction of the sample and the resulting temperature distribution is detected by an IR camera. The acquired signal is then converted to amplitude and phase data by a computer. **B:** Schematic presentation of the vacuum chamber with the sample holder, IR camera and laser. The sample is placed inside a vacuum chamber. **C:** Schematic presentation of the sample holder for thermal excitation by the laser. **D and E:** The natural logarithm of the amplitude and phase are plotted against the distance to the laser spot for each pixel, respectively. The linear slope (red line) is calculated within the gray area in both plots. Figure adapted and reproduced with permission from Ref.^[182] Copyright © 2022, American Chemical Society.

To obtain reliable and reproducible data, several requirements and influences on the lock-in thermography measurements need to be considered:

i) Sample Coating

As the detection principle relies on thermal radiation rather than temperature itself, it's essential to note that the sample's emissivity influences the measurement result. The sample need to exhibit adequate absorption/emission characteristics in both the visible and infrared ranges. Absorption in the visible range is essential for the laser excitation, while emission in the IR range is necessary for detection with the IR camera. The low absorptivity/emissivity of samples can be enhanced by coating thin layers of a high-emissivity material, such as carbon.^[182,184]

ii) Sample size

The sample size is a critical factor. Initially, the sample must have a specific length to prevent thermal waves from reaching the edges, as this could deform the amplitude and phase profiles and lead to an overestimation of thermal diffusivities. Additionally, the samples must possess sufficient thickness to ensure mechanical stability and withstand vacuum application. Fibers with diameters of 10 μm have been reported to be measurable.^[183] For 1-D samples, the length must be much larger than the thermal decay length. The thermal decay length depends on the lock-in frequency, so it is advisable to investigate unknown samples at different frequencies. Ideally, evaluating the resulting data will reveal a plateau region, indicating the validity of the data evaluation.^[184]

iii) Diffraction Effects

Diffraction effects can occur at high frequencies induced by the microscope lens. As a consequence, the thermal diffusivities are overestimated.^[185] Hence, frequency sweeps are useful to evaluate the optimal lock-in frequency by choosing a frequency in the plateau region and generally low frequencies at < 10 Hz avoid the issue.^[186]

iv) *Heat losses*

The sample in lock-in thermography measurements is heated in an oscillating manner, which means heated and cooled periodically. However, the sample is not cooled actively. The cooling occurs due to heat conduction to the rest of the sample and surrounding. As a consequence, after a specific measurement duration, the average temperature of the sample will stabilize at a higher level than initially reaching the so called “quasi-steady-state”. This is schematically depicted in Figure 6-2 where the surface temperature of the sample is shown as a function of the measurement duration. Within each complete lock-in period, the heat introduced during each heating cycle equals the heat loss to the surrounding environment resulting in the quasi-equilibrium state.

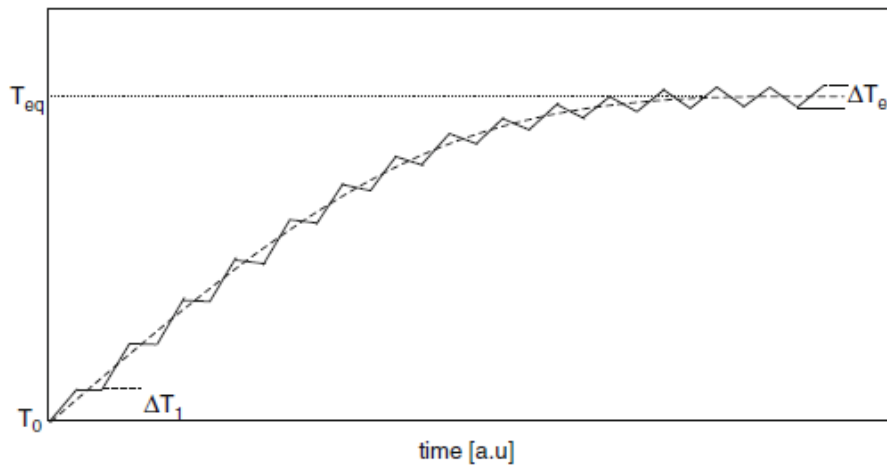


Figure 6-2. **Illustration of a qualitative temperature profile at the initiation of a lock-in thermography experiment.** Figure adapted and reproduced with from Ref.^[179] Copyright © 2018.

Too low frequencies will eventually lead to higher heat losses and thus the thermal diffusivity does not fit the actual value.^[184] To obtain reliable values, heat losses can be compensated by using the product of the diffusivities obtained from the amplitude and from the phase data.

v) *Laser Power*

Power dependencies are found for materials that exhibit lower thermal diffusivities such as polymers, shown by Tran et al.^[182] for the polyether ether ketone as a result of temperature effects. Lower laser powers will excite the fiber to a lesser extent and thus the fiber is less heated per period leading to high temperature fluctuations of the fiber. This is even more pronounced for thinner fibers. Thus, a good signal-to-noise ratio need to be achieved to obtain reliable data. Power sweeps at a suitable frequency can help to evaluate adequate power values for the measurements.

Approach in this thesis for thermal diffusivity measurements of supramolecular fibers

Until to date, no work has been published using lock-in thermography to investigate the thermal diffusivity at BTA fibers, which held together by hydrogen bonding. Literature reports different measurements on 1-D fibers regarding their thermal diffusivity such as spider silk fibers ($\alpha = 0.2 \text{ mm}^2 \text{ s}^{-1}$),^[187] silica fiber bundles ($\alpha = 0.2 \text{ mm}^2 \text{ s}^{-1}$),^[188] quartz fibers ($\alpha = 0.68\text{-}0.8 \text{ mm}^2 \text{ s}^{-1}$)^[189,190] or polyether ether ketone fibers ($\alpha = 0.5 \text{ mm}^2 \text{ s}^{-1}$).^[184]

In this chapter of the thesis, the thermal diffusivity of BTA fibers should be determined by means of the lock-in thermography method in a collaboration work with Ina Klein (Physical chemistry I, Prof. Dr. Retsch). Since BTA fibers have not yet been measured by the lock-in thermography method, this chapter aims for the evaluation of the parameter settings to determine the thermal diffusivity of BTA fibers in a reproduceable manner. Prior that, a suitable self-assembly method need to be elaborated to prepare fibers with distinct dimensions as well as anisotropy and columnar arrangement. For this several aspects are addressed:

- i)* Material selection and preparation of BTA fibers with dedicated shape and dimensions being sufficiently long (up to 1 centimeter) and rigid with suitable diameter (μm -range) via slow solvent evaporation
- ii)* Investigation of the prepared fibers regarding their anisotropy and columnar arrangement via polarized optical microscopy and IR spectroscopy
- iii)* Frequency sweeps to elaborate the optimal frequency for BTA fibers in the lock-in thermography measurements
- iv)* Power sweeps to determine power dependencies and the optimal power for BTA fibers in the lock-in thermography measurements
- v)* Variation of the BTA fiber diameter and elaboration of the influence on the measurements
- vi)* Lock-in thermography measurements for various BTAs to investigate whether there is an influence of the structural variety on the thermal diffusivity.

6.2 Preparation of supramolecular fibers for lock-in thermography measurements

To obtain reliable and reproducible thermal diffusivities from lock-in thermography measurements on 1-D fibers, several requirements need to be considered. One important part are the dimensions of the fibers to be measurable via lock-in thermography and to fit into the custom-made sample holder. The sample holder was manufactured by 3-D printing of PLA and the geometry is shown in Figure 6-3. This sample holder allows for the deposition of four fibers which are fixated at both ends onto an adhesive tape. With this method most of the whole fiber is freestanding (white background of fibers 1-4) and in no contact to the sample holder and thus ensure reliable measurements. For this, the fibers need to exhibit at least 0.50 cm – 1.0 cm in length to fit onto the sample holder. Furthermore, they should show stability against the vacuum to not be removed from the sample holder. Vacuum will be applied for the carbon vapor deposition onto the fibers as well as during the measurements.

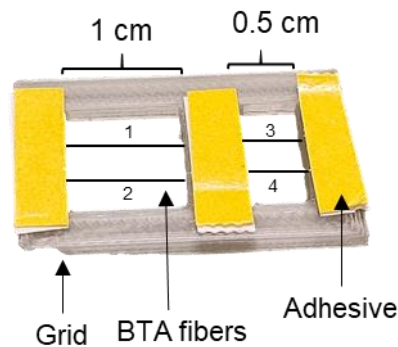


Figure 6-3. **Sample holder for lock-in measurements of fibers.** The sample holder consists of a 3-D printed PLA grid with 1 cm and 0.5 cm place for four BTA fibers (1-4). Adhesive tape holds the BTA fibers in place.

6.2.1 Preparation of suitable supramolecular fibers

To achieve fibers with the required dimensions on the micro and macroscale from BTAs to fit into the sample holder, slow solvent evaporation is the most promising method as depicted in Figure 6-4. First, the BTA is dissolved in the selected solvent typically at elevated temperatures. Upon cooling, the solution stays stable and no self-assembly occurs at the chosen concentration (A). The solution is then transferred into a covered container in which slow solvent evaporation can take place and self-assembly starts (B). Further slow and controlled solvent evaporation results in self-assembly of the BTA molecules into long fibers (C) and is finished when all solvent is evaporated (D). Here, a solvent is chosen that have low vapor pressure to ensure slow evaporation rates. The solvent selected, which shows the necessary characteristics, was DMF.

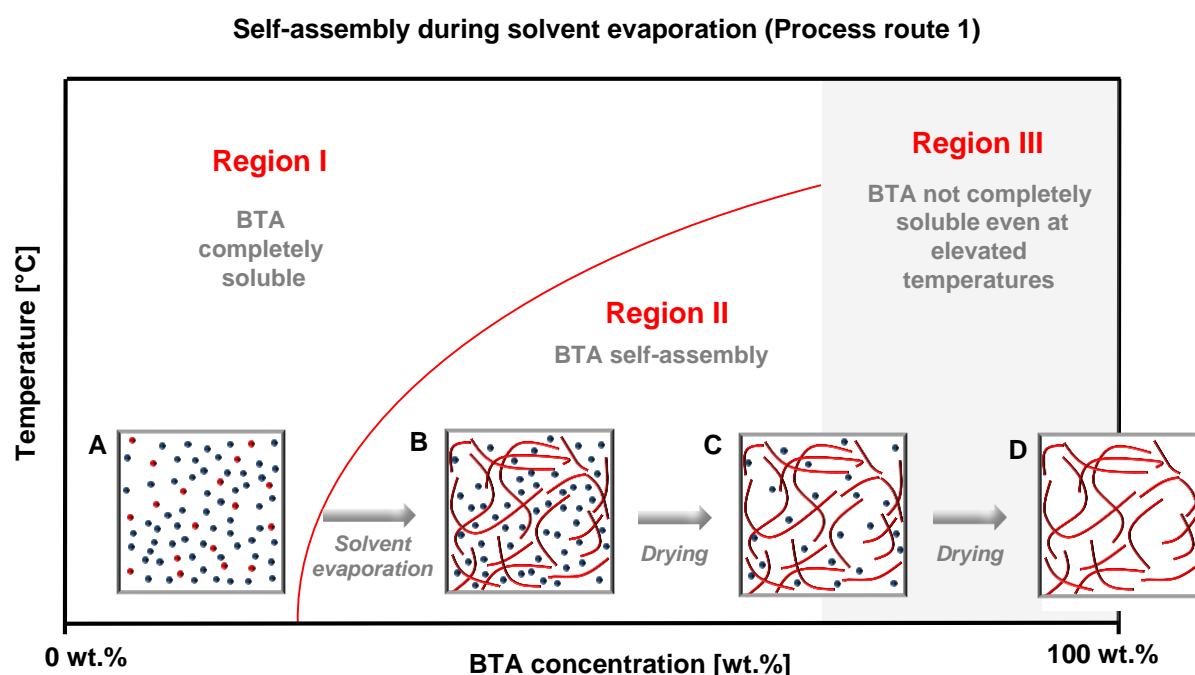


Figure 6-4. **Schematic representation of the self-assembly process of BTAs for solvent evaporation.** **A:** Complete molecularly dissolved BTA molecules (red dots) in a selective solvent (blue dots) **B:** Supramolecular fibers (red lines) coexisting with remaining solvent (blue dots). **C:** Further drying. **D:** Complete solvent evaporation results in dried supramolecular fibers. Region I -BTA completely soluble, Region II – BTA self-assembly and Region III – BTA not completely soluble even at elevated temperatures.

The slow evaporation method was used as follows: The BTA solutions in DMF were given in a petri dish which was laid out with aluminum foil and covered with a crystallization dish as schematically depicted in Figure 6-5. The solvent was allowed to evaporate slowly (1 week) resulting in self-assembled BTA structures.

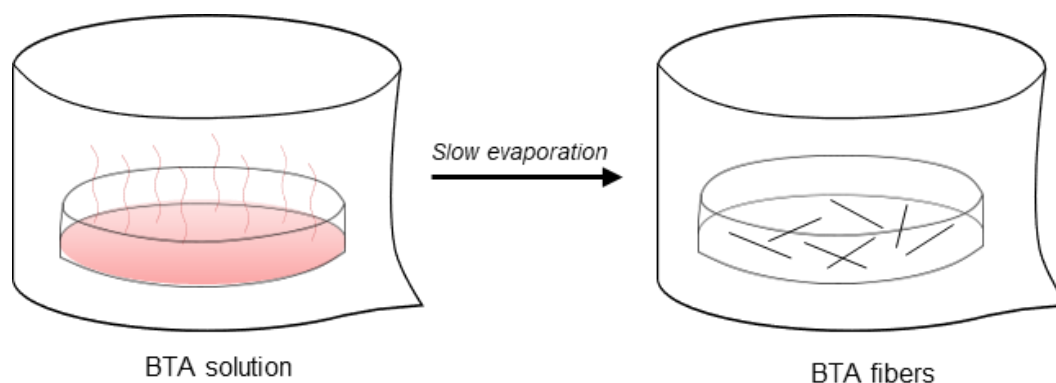


Figure 6-5. **Schematic presentation of the preparation of supramolecular BTA fibers via slow evaporation of the solvent.** The BTA solution is given in a petri dish which is laid out with aluminum foil. After a week of solvent evaporation, BTA structures are formed.

6.2.2 Material selection for thermal diffusivity measurements

The aim here was to identify BTAs that self-assemble from DMF via slow solvent evaporation into sufficient long and rigid fibers to be measured by lock-in thermography. A complete list of all tested BTAs is summarized in Appendix C. For this, 20 candidates were selected from a large pool of substances encompassing structural variations in their amide connectivity and peripheral groups. The BTA candidates are categorized into four groups regarding their peripheries and the amide connectivity (A-D). *Category A* covers BTA derivatives with cyclohexyl side groups but different amide connectivity, *Category B* includes BTA derivatives with tert. butyl side groups but different amide connectivity, *Category C* consists of BTA derivatives with different branched aliphatic side groups and *Category D* has derivatives with additional functional heteroatoms in the periphery. The BTAs were tested regarding their solubility and self-assembly behavior in DMF towards fibers. The solubility tests of the selected BTAs in DMF were performed with concentrations from 0.10 – 0.50 wt.%. To summarize the solubility and self-assembly experiments, the self-assembly was divided regarding the different outcomes:

- i)* the selected BTA is soluble in DMF and fiber formation was obtained (**fibers ✓**) (Figure 6-6 and Appendix C)
- ii)* the selected BTA is soluble in DMF and fiber formation was obtained, however fibers do not exhibit the required dimensions (**fibers ~**) (Appendix C)
- iii)* the BTA is soluble in DMF; however, no fiber formation upon solvent evaporation (**fibers ✗**) was observed (Appendix C)
- iv)* the BTA is not soluble in DMF and thus no further experiments were conducted (**fibers ✗ not soluble**) (Appendix C)

The derivatives which were successful in fiber formation are summarized in Figure 6-6. The nomenclature arises from counting of the used BTA derivatives throughout the thesis. BTA-1 and BTA-4 have been used in the other chapters of this work, thus the same nomenclature is used. The derivatives featuring a benzene core, cyclohexyl side groups and different amide connectivity from *Category A*, show good solubility at 80 °C in DMF with 0.50 wt.% and stable solutions at rt for all four tested derivatives. However, fibers suitable for the thermal measurements were obtained for only two derivatives (BTA-1 and BTA-6) upon slow solvent evaporation. In the *Category B* of BTA derivatives with a benzene core, tert. butyl side groups and varying amide connectivity three out of four derivatives were found to be soluble in DMF and self-assemble into suitable fibers (BTA-7, BTA-8 and BTA-9). BTAs with (linear and branched) aliphatic side groups ($n = 8$) in the periphery (*Category C*) feature sufficient solubility of all seven tested derivatives. However, only two derivatives self-assembled into fibers with suitable dimensions being measurable with lock-in thermography (BTA-10 and BTA-11). The last *Category D* include BTA derivatives that have heteroatoms in their peripheral side chains. All five derivatives were found to be soluble in DMF. Nevertheless, only one BTA derivative was successfully assembled into supramolecular fibers (BTA-4). In total, 20 BTA derivatives were tried to be self-assembled from DMF into suitable fibers whereby eight BTA derivatives were found to exhibit suitable fiber shape and dimensions.

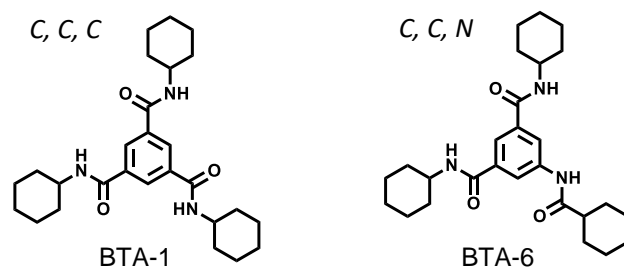
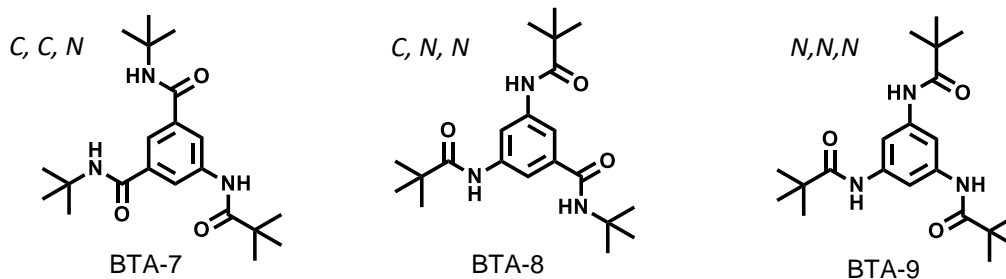
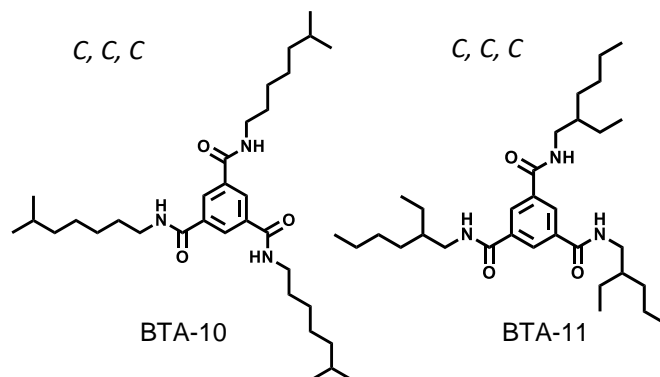
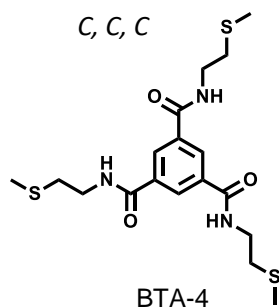
Category A: BTA derivatives with cyclohexyl side groups**Category B: BTA derivatives with tert-butyl side groups****Category C: BTA derivatives with different branched aliphatic side groups****Category D: BTA derivatives with additional functional heteroatoms in the periphery**

Figure 6-6. **Four categories (A-D) of BTA derivatives that were successful in fiber formation upon solvent evaporation.** Chemical structures with corresponding indication of the amide connectivity (C for C-centered and N for N-centered at the benzene core). **Category A:** BTA-1 and BTA-6 with cyclohexyl side groups, **Category B:** BTA-7, BTA-8 and BTA-9 with tert-butyl side groups, **Category C:** BTA-10 and BTA-11 with different branched aliphatic side groups and **Category D:** BTA-4 with additional functional heteroatoms in the periphery.

6.2.3 Sample preparation for lock-in thermography measurements

An example of such self-assembled fibers prepared via slow solvent evaporation is shown in Figure 6-7 for the derivative BTA-1. The fibers can be easily handled with tweezers and exhibit fiber lengths of several centimeters as required for the upcoming experiments.

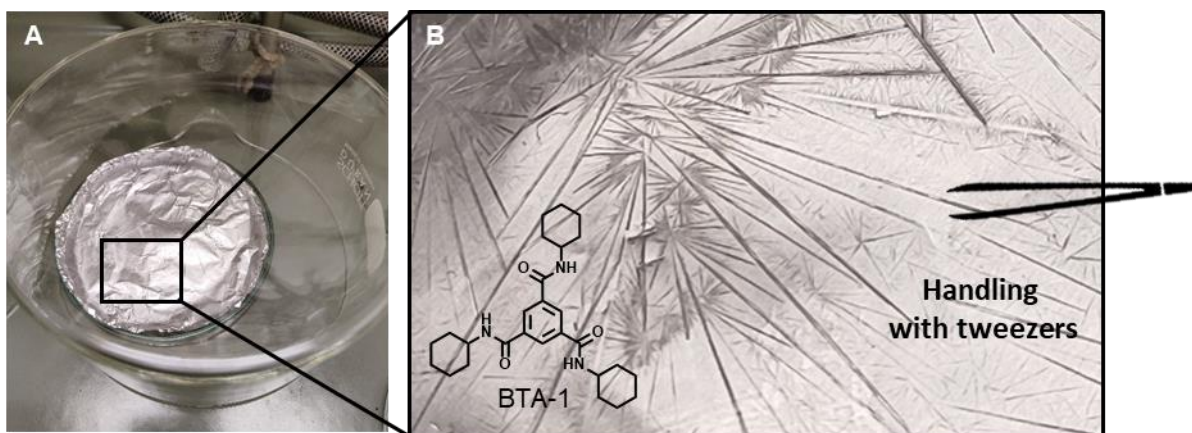


Figure 6-7. **Self-assembled fibers from BTA-1 via slow solvent evaporation from DMF.** **A:** Petri dish with aluminum foil and self-assembled BTA-1 fibers. **B:** Magnification showing the self-assembled fibers on the aluminum foil and the structural formula of BTA-1.

An example for the sample preparation on the custom-made sample holder for the lock-in thermography measurements is shown in Figure 6-8. Three BTA-1 fibers were taken with tweezers from the aluminum foil and fixated onto the 3-D printed grid with the help of adhesive tape (A). The fibers on the grid were then analyzed with a polarized optical microscope before the measurements to ensure the desired fiber morphology of an anisotropic fiber and measurements of the fiber diameter (B). Afterwards, the fibers on the grid were coated with a carbon layer (C).

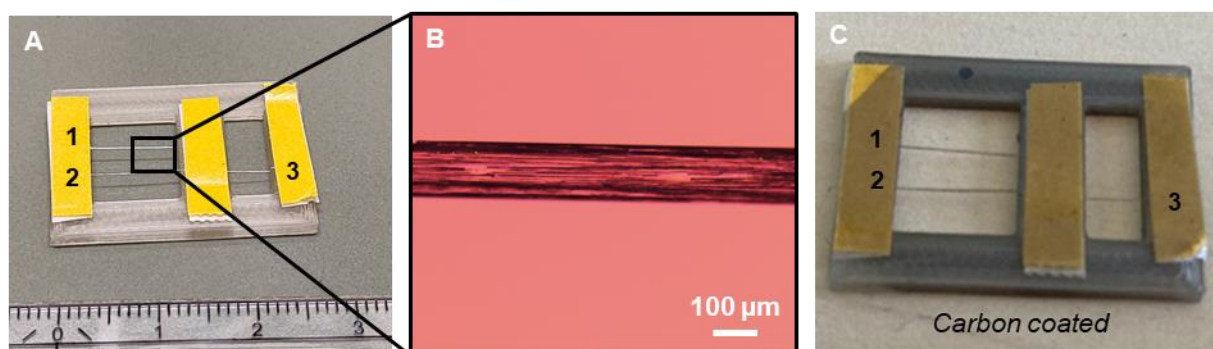


Figure 6-8. **Sample preparation of BTAs for lock-in thermography measurements.** **A:** Sample holder with three fixated BTA fibers, noted with 1-3. **B:** Section of a polarized optical microscope image of the corresponding BTA fiber from image A. **C:** Sample holder with the three fixated BTA fibers after carbon coating.

6.3 Properties of selected self-assembled BTAs

The selected BTA fibers were investigated with a polarized optical microscope regarding their dimensions and shape. Furthermore, IR was conducted to detect relevant IR signals of the amide groups demonstrating the intramolecular hydrogen-bonding and columnar helical arrangement of the BTAs in the solid state. The polarized optical microscope image of the BTA-1 with notation of a representative diameter and the corresponding chemical structure and IR spectrum is exemplarily shown in Figure 6-9. The data of the polarized optical microscope images and the full IR spectra for the other BTAs are shown in *Appendix C* Figure 8-16 – Figure 8-22 and summarized in Table 6-1.

Here, the diameter of this specific BTA-1 fiber was found to be $191 \pm 5 \mu\text{m}$ obtained from a 0.50 wt.% solution after solvent evaporation. By varying the concentration from 0.10 wt% to 0.50 wt.% a large variety of fiber diameters were obtained for BTA-1 ranging from $37 \mu\text{m}$ to $239 \mu\text{m}$ as it is typically expected. However, compared to the other BTAs, BTA-1 showed a pronounced dependency on the concentration and thus fiber diameter variation. Also compared to the other self-assembled fibers, BTA-1 was the only fiber which self-assembled into highly rigid fibers. This makes the BTA-1 derivative the most promising for the upcoming experiments regarding lock-in thermography. The birefringence of the BTA-1 fiber appears bright under crossed polarizers (Figure 6-9 A) and vanishes if the polarization is changed in way that the polarizer and analyzer are parallel to each other. This indicates that the BTA-1 fiber is highly ordered and anisotropic.

To investigate whether the fiber additionally exhibits a columnar order, IR spectroscopy was applied by using the self-assembled state (fibers) of each BTA. The IR spectrum of BTA-1 is shown in Figure 6-9 B with the marked vibrations. In general, threefold, α -helical-type intermolecular hydrogen-bonding between adjacent molecules and thus *columnar* arrangement are attributed to the vibrations observed for the: ^[37,45,46,77]

- i) N-H stretch at $\sim 3240 \text{ cm}^{-1}$ (Amide A, $\nu(\text{N-H})$),
- ii) the C=O stretch at $\sim 1640 \text{ cm}^{-1}$ (Amide I, $\nu(\text{C=O})$),
- iii) the amide II band at $\sim 1560 \text{ cm}^{-1}$ (Amide II, $\nu(\text{amide II})$, superposition of N-H bend and C-N stretch vibrations).

Note that these vibrations correspond for BTA derivatives with *CCC*-connectivity.

Investigations from our group and Stals et al.^[46] showed, that *non-columnar* BTAs still feature the C=O stretch at around 1640 cm^{-1} and either:

- iv) missing the NH stretch vibration at 3240 cm^{-1} and amide II band at 1560 cm^{-1} and shifting of the bands towards higher wavenumbers $> 3300\text{ cm}^{-1}$ and lower wavenumbers at around 1530 cm^{-1} ,
- v) or show the NH stretch vibration at 3240 cm^{-1} **and** a band at wavenumbers $> 3300\text{ cm}^{-1}$ and coupled with a shift of the amide II band towards lower wavenumber at around 1530 cm^{-1} .

Note, that these observations are known for BTA derivatives with *CCC*-connectivity.

The BTA-1 shows a $\nu(\text{N-H})$ vibration at 3218 cm^{-1} , the C=O stretch at 1628 cm^{-1} and the $\nu(\text{amide II})$ band at 1557 cm^{-1} . Even though the $\nu(\text{N-H})$ is at slightly smaller wavenumbers as typically observed at 3240 cm^{-1} for columnar arrangement, the $\nu(\text{amide II})$ vibration can be identified in the corresponding range for columnar arrangement. Thus, the structures from BTA-1 self-assembled from DMF into fibers are considered as columnar structures which has been previously confirmed by the crystallographic analysis from Kristiansen et al. for this BTA derivative.^[42]

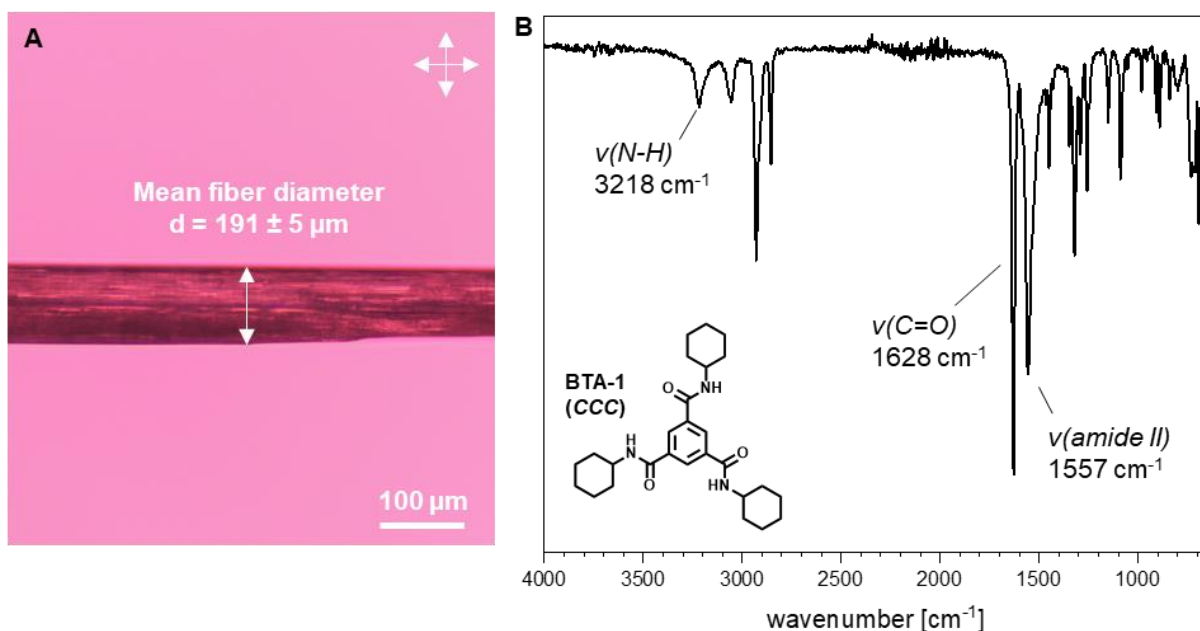


Figure 6-9. **Polarized optical microscope image and corresponding IR spectrum of BTA-1 fibers.** **A:** Fibers of BTA-1 with indication of the mean fiber diameter and **B:** IR spectrum of self-assembled BTA-1 fibers with indications of the NH stretch $\nu(\text{N-H})$, the C=O stretch $\nu(\text{C=O})$ and the amide II band $\nu(\text{amide II})$.

An example of typical IR spectra of BTA derivatives featuring a *CCC*-, *NNN*- and *CCN*-connectivity is shown in Figure 6-10 with BTA-10 (*CCC*), BTA-9 (*NNN*) and BTA-7 (*CCN*). Here, a cut-out is made from 1700 cm^{-1} – 3000 cm^{-1} to concentrate on the relevant bands for the investigation regarding the columnar arrangement. The complete IR spectra of each BTA is shown in *Appendix C*, respectively.

The BTA-10 as representative for *CCC*-connected BTA derivatives show the three typical bands at $\nu(\text{N-H}) = 3241 \text{ cm}^{-1}$, $\nu(\text{C=O}) = 1634 \text{ cm}^{-1}$ and the $\nu(\text{amide II}) = 1557 \text{ cm}^{-1}$. As known from reported literature this indicates a columnar arrangement due to threefold, α -helical-type intermolecular hydrogen-bonding.

The BTA-9 (*NNN*, tert butyl side groups) has been previously confirmed to be helical due to intermolecular hydrogen bonding using a combined approach based on X-ray powder diffraction and solid-state NMR spectroscopy.^[43] IR data and corresponding regimes for the typical bands as reported for *CCC*-connected BTA derivatives are not given in the literature. However, referring to the X-ray powder diffraction and solid-state NMR spectroscopy from the literature as well as previous work in our group, columnar arrangement of the BTA-9 derivative is anticipated. IR results show that the $\nu(\text{N-H})$ and $\nu(\text{C=O})$ bands are shifted to slightly higher values at 3296 cm^{-1} and 1656 cm^{-1} , however the $\nu(\text{amide II})$ band is shifted to lower wavenumbers at 1530 cm^{-1} compared to the *CCC*-derivatives. This IR data is considered to show the typical bands for columnar arrangement of *NNN*-connected BTA derivatives.

In contrast to that, the *CCN*-connected BTA derivative BTA-7 shows a mixture of the bands from *CCC*- and *NNN*-connected BTA derivatives. One significant $\nu(\text{N-H})$ band is observed at 3232 cm^{-1} and a shoulder is visible around 3291 cm^{-1} . Two clear bands are visible for the $\nu(\text{C=O})$ stretch and the $\nu(\text{amide II})$. The bands for the $\nu(\text{C=O})$ are located at 1659 cm^{-1} and 1634 cm^{-1} . The $\nu(\text{amide II})$ bands are observed at 1557 cm^{-1} and 1525 cm^{-1} . The two bands for each vibration correspond to the wavenumbers observed for the *CCC*- and *NNN*-connected BTA derivatives.

The spectra with the relevant vibrations ($\nu(\text{N-H})$, $\nu(\text{C=O})$ and the $\nu(\text{amide II})$) for all self-assembled fibers are shown in *Appendix C* Figure 8-23 and Figure 8-24.

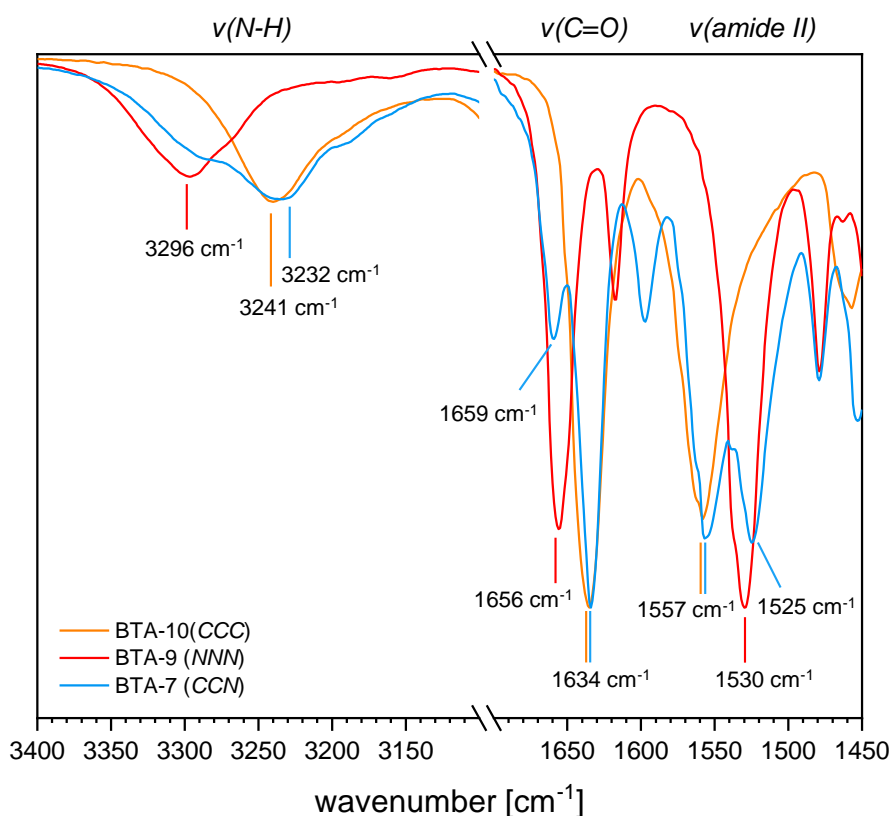


Figure 6-10. IR spectra of self-assembled BTA-10, BTA-9 and BTA-7 representing BTA derivatives with CCC-, NNN-, and CCN-connectivity. Indications of the NH stretch $\nu(\text{N-H})$, the C=O stretch $\nu(\text{C=O})$ and the amide II band $\nu(\text{amide II})$ is given for each BTA-derivative, BTA-10 (orange), BTA-9 (red), BTA-7 (light blue).

The exact wavenumbers for each BTA for the relevant vibrations are summarized in Table 6-1. The evaluation of the main $\nu(\text{N-H})$ stretch vibrations of all BTAs shows that the bands are located at wavenumbers clearly less than 3300 cm^{-1} , thus not exceeding wavenumbers where non-columnar arrangement is typically observed. All BTAs featuring a CCC amide connectivity (BTA-1, BTA-4, BTA-10 and BTA-11) are located close to the reference value at 3240 cm^{-1} which is also observed for BTA-7 (CCN). Within the group of CCC-connected BTA derivatives the following tendencies are observed for the wavenumbers of the $\nu(\text{N-H})$ bands:

BTA-11 and BTA-10 (CCC, long branched aliphatic side group) > BTA-4 (CCC, functional heteroatom) > BTA-1 (CCC, cyclohexyl side groups).

Furthermore, a tendency is observed, where the N-H stretch vibration is shifted towards higher wavenumbers with higher number of inverted groups:

NNN (BTA-9) > CNN (BTA-8) > CCN (BTA-6) > CCN (BTA-7)
 3296 cm^{-1} > 3290 cm^{-1} > 3264 cm^{-1} > 3232 cm^{-1}

Evaluating the $\nu(\text{C}=\text{O})$ bands for all BTAs show that each band is located in the region for the typical $\nu(\text{C}=\text{O})$ vibrations.^[191,192] All *CCC*-connected BTA derivatives are found around 1634 cm^{-1} and the *NNN*-connected BTA derivative at 1656 cm^{-1} . All other BTA derivatives with inverted connectivity have two bands representing the values for the *CCC*- and *NNN*-connected BTA derivatives. This is also valid for the $\nu(\text{amide II})$ vibrations with only one band in the range of the reference values around 1557 cm^{-1} for the *CCC*-connected BTAs and 1530 cm^{-1} for the *NNN*-connected BTA. Two bands are observed for the BTA derivatives with inverted connectivity. However, the *CNN*-connected BTA shows only one band at lower wavenumbers of 1530 cm^{-1} as seen for the *NNN*-connected BTA.

Table 6-1. BTAs from the four different categories (A-D) with the relevant IR vibrations ($\nu(\text{N-H})$, $\nu(\text{C}=\text{O})$ and the $\nu(\text{amide II})$).

Category	Sample (amide connectivity)	$\nu(\text{N-H})$ [cm^{-1}]	$\nu(\text{C}=\text{O})$ [cm^{-1}]	$\nu(\text{amide II})$ [cm^{-1}]
A (cyclohexyl side groups)	BTA-1 (<i>CCC</i>)	3218	1628	1557
	BTA-6 (<i>CCN</i>)	3264	1630/1679	1548/1525
B (tert-butyl side groups)	BTA-7 (<i>CCN</i>)	3232	1634/1659	1557/1525
	BTA-8 (<i>CNN</i>)	3290	1635/1658	1525
	BTA-9 (<i>NNN</i>)	3296	1656	1530
C (branched and aliphatic side groups)	BTA-10 (<i>CCC</i>)	3241	1634	1557
	BTA-11 (<i>CCC</i>)	3241	1635	1558
D (with functional heteroatoms)	BTA-4 (<i>CCC</i>)	3245	1634	1552

Taking all specific bands into considerations it is indicative that all investigated BTA derivatives have a columnar arrangement due to threefold, α -helical-type intermolecular hydrogen-bonding.

6.4 Thermal diffusivity measurements of selected BTAs

After the successful preparation of suitable BTA fibers with macroscopic dimensions and their fixation onto the sample holder, the fibers were coated with a carbon layer as high-emissivity material to enhance the absorptivity/emissivity of the BTA fibers. This is important as the sample's emissivity influences the measurement result. The sample needs to exhibit adequate absorption/emission characteristics in both the visible and infrared ranges. Absorption in the visible range is essential for the laser excitation, while emission in the IR range is necessary for detection with the IR camera. After successful coating of the fibers on the sample holder, lock-in thermography measurements were conducted by Ina Klein (Physical chemistry department I, Prof. Dr. Retsch).

For the initial experiments, BTA-1 was chosen due to its ability to self-assemble into the longest fibers. Additionally, the thickness of the fibers could be adjusted by using different concentrations, providing a BTA suitable for validating lock-in thermography measurements on BTAs. The upcoming experiments represent the first-time measurements of BTAs using the experimental set-up as described in chapter 6.1 (see also Figure 6-1). Critical parameters, which need to be carefully considered to achieve reliable and meaningful results, are the lock-in frequency and the laser power. To determine the optimal measurement window and to check dependencies, frequency sweeps and power sweeps need to be conducted. Identifying the optimal frequency and power of the laser during the measurements ensures the generation of the most reliable and reproducible data, enabling the determination of the thermal diffusivity of the BTA fibers.

6.4.1 Frequency sweep

The frequency sweep measurements for BTA-1 fibers with a mean diameter of $d = 113 \pm 8 \mu\text{m}$ is depicted in Figure 6-11. The sample is measured with different lock-in frequencies from 0.02 to 5 Hz at a constant laser power of $\sim 54 \mu\text{W}$. The resulting thermal diffusivities from the phase (orange dots) and amplitude (blue squares) slopes are plotted against the different lock-in frequencies. The product (green route, diamond shape) of the phase and amplitude slope results in the final value for the thermal diffusivity of the fiber. Two data points are shown, corresponding to the measurements taken on the left and right sides of the fiber from the point where the laser impacts. A plateau is visible for moderate frequencies where the phase, the amplitude and the product of both are in a similar range. At higher frequencies, all values increase to a certain extent which has been reported as diffraction effects of the microscope lens for poor conductors.^[185,193] In contrast to that, at low frequencies the phase show significantly higher values of thermal diffusivities whereas the values for the amplitude decrease and thus the product values stay the same. This can be attributed to heat losses which has been previously reported by Mendioroz et al.^[184] From this data, a frequency can be chosen from the plateau region which is then used for further measurements. Here, a frequency should be used within the plateau and where the data of phase and amplitude still exhibits linear slopes. In this case, a frequency of 0.27 Hz is chosen which covers both requirements.

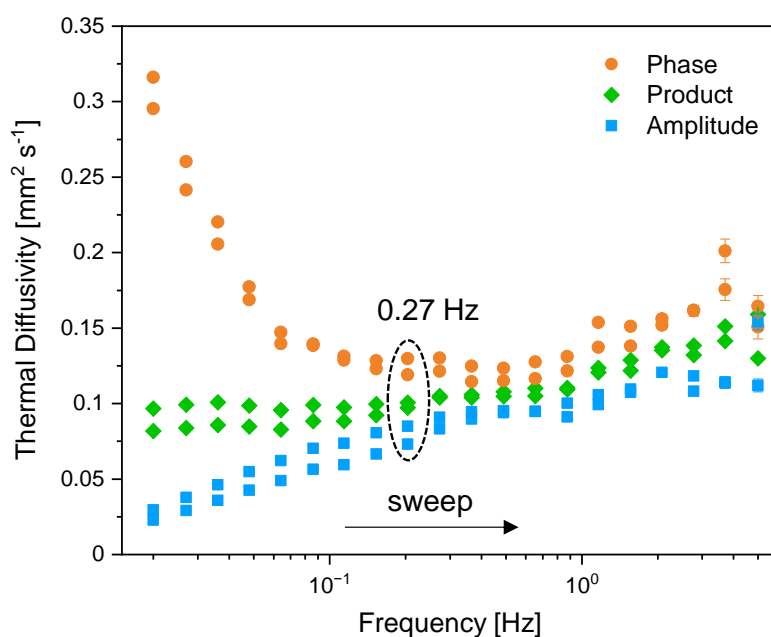


Figure 6-11. **Frequency sweep data for a BTA-1 fiber ($d = 113 \pm 8 \mu\text{m}$).** The resulting thermal diffusivities from the phase (orange dots) and amplitude (blue squares) slopes are plotted against the different lock-in frequencies. The product (green route, diamond shape) of the phase and amplitude slope results in the final value for the thermal diffusivity of the fiber. The arrow indicates the sweep direction.

6.4.2 Power Sweep

The optimal lock-in frequency was determined to be 0.27 Hz, thus power sweeps are conducted with this parameter. For the power sweep, a BTA-1 fiber with a diameter of $d = 75 \pm 11 \mu\text{m}$ is used. The laser power is varied from high to lower power values, applying voltages from 600 mV to 50 mV in steps of 25 mV resulting in powers of ~ 225 to $18 \mu\text{W}$, respectively. The resulting thermal diffusivities from the phase (orange dots) and amplitude (blue squares) slopes are plotted against the different laser power applied. The product (green route, diamond shape) of the phase and amplitude slope results in the final value for the thermal diffusivity of the fiber. Two data points are shown which correspond to the measured data point of the left and right side of the fiber. Here, at a power $> 72 \mu\text{W}$ the values of phase, amplitude and resulting product decrease. This small decrease stands for a power dependency which is however not pronounced for this fiber diameter. Thin fibers will have more heat fluctuations and can be heated easily. Using a high laser power will eventually heat up the fiber more drastically, resulting in a downward trend as the thermal diffusivity decreases with increasing temperature.^[194] Thus, a compromise is chosen for the laser power for further measurements. A low but well evaluable power of $\sim 54 \mu\text{W}$ is selected and used for further measurements. Both, phase and amplitude show a linear slope in the selected power region. This is valid for the tested BTA fiber with a diameter of $d = 75 \pm 11 \mu\text{m}$.

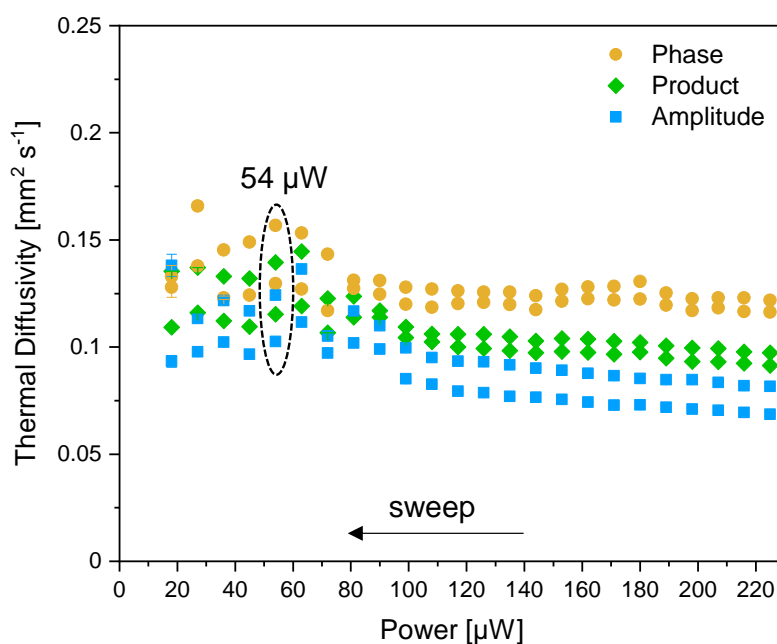


Figure 6-12. **Power sweep data for a BTA-1 fiber ($d = 75 \pm 11 \mu\text{m}$).** The resulting thermal diffusivities from the phase (orange dots) and amplitude (blue squares) slopes are plotted against the different laser power used in the measurements. The product (green route, diamond shape) of the phase and amplitude slope results in the final value for the thermal diffusivity of the fiber. The sweep is done from high to low power values. The arrow indicates the sweep direction.

6.4.3 Dependency on BTA fiber diameter

As the diameters vary among different BTA derivatives, it is crucial to assess whether the diameter has an impact on lock-in thermography measurements. Typically, thin fibers will have more heat fluctuations and can be heated easily by choosing the wrong laser power which leads to an underestimation of the thermal diffusivities. To investigate whether the BTA fiber diameter has an influence on the measurements and to assess the optimal laser power, BTA fibers of one BTA derivative with different diameters are required. For this, BTA-1 was self-assembled from a concentration of 0.50 wt.% via slow solvent evaporation resulting in different fiber diameters. Here, BTA-1 fibers ranging from 37 μm – 239 μm are chosen as exemplarily samples for the determination of the diameter influence on the lock-in thermography measurements. The chosen supramolecular fibers exhibit diameters of 37 μm , 56 μm , 79 μm , 95 μm , 127 μm , 150 μm , 172 μm , 180 μm and 239 μm . This diameter variation provides a suitable range for the lock-in thermography measurements. The resulting mean thermal diffusivities from the power sweeps are summarized in Table 6-2.

Table 6-2. Thermal diffusivities for BTA 1 fibers prepared from different concentrations with specification of the resulting diameter.

Diameter	Thermal diffusivity
37 μm	$\alpha = 0.083 \pm 0.007 \text{ mm}^2 \text{ s}^{-1}$
56 μm	$\alpha = 0.094 \pm 0.046 \text{ mm}^2 \text{ s}^{-1}$
79 μm	$\alpha = 0.106 \pm 0.010 \text{ mm}^2 \text{ s}^{-1}$
95 μm	$\alpha = 0.103 \pm 0.068 \text{ mm}^2 \text{ s}^{-1}$
127 μm	$\alpha = 0.116 \pm 0.073 \text{ mm}^2 \text{ s}^{-1}$
150 μm	$\alpha = 0.128 \pm 0.039 \text{ mm}^2 \text{ s}^{-1}$
172 μm	$\alpha = 0.132 \pm 0.059 \text{ mm}^2 \text{ s}^{-1}$
180 μm	$\alpha = 0.118 \pm 0.018 \text{ mm}^2 \text{ s}^{-1}$
239 μm	$\alpha = 0.165 \pm 0.073 \text{ mm}^2 \text{ s}^{-1}$

The data of these experiments show that the values of the thermal diffusivities raise with increasing diameter. The power sweep data for a BTA-1 fiber with a diameter of 37 μm shows slightly decreasing thermal diffusivities with increasing laser power (see Figure 6-13). This power dependency is a sign of temperature effects, i.e. temperature fluctuations in the thin fiber. This effect seems to get less pronounced with increasing diameter of the BTA fibers. However, the thickest fiber with 239 μm diameter shows increased values for laser powers below 20 μW . The values for the thermal diffusivity increase from around 0.15 $\text{mm}^2 \text{s}^{-1}$ ($> 30 \mu\text{W}$) up to 0.45 $\text{mm}^2 \text{s}^{-1}$ ($< 20 \mu\text{W}$). Below the 20 μW laser power, the evaluation of the phase and amplitude slope is difficult, thus reliable data of BTA fibers with larger diameter is obtained with laser powers $> 30 \mu\text{W}$.

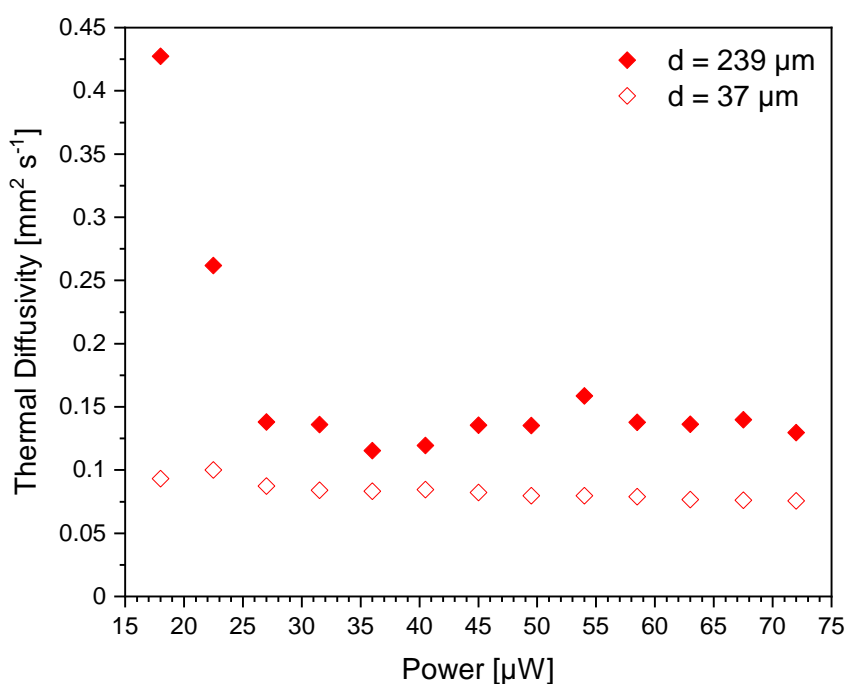


Figure 6-13. **Power sweep data for BTA-1 fibers with varying diameter (d = 37 μm and 239 μm).** The resulting thermal diffusivities from the product are plotted against the different laser power used in the measurements. Here, a mean value for the thermal diffusivity is depicted from the two data points obtained from the measurements, corresponding to the left and right side data points of the fiber.

With this knowledge, further experiments were conducted by using different laser powers in the beforementioned critical transition region and the varying diameter of the BTA-1 fibers between the 37 μm and 239 μm . The chosen laser powers were $\sim 22.4 \mu\text{W}$ and $\sim 36 \mu\text{W}$. The results are shown in Figure 6-14. The data for the laser power of $\sim 22.4 \mu\text{W}$ shows that diameters below 100 μm have a downward trend in the thermal diffusivity values whereas the thermal diffusivity stays constant for diameters greater than 100 μm at around 0.10 $\text{mm}^2 \text{s}^{-1}$. However, the downward trend is not pronounced showing a reduction of around 0.02 $\text{mm}^2 \text{s}^{-1}$, thus values

around $0.08 \text{ mm}^2 \text{ s}^{-1}$. In contrast to that, the results using a laser power of $\sim 36 \mu\text{W}$ show a similar downward trend for diameters below $100 \mu\text{m}$ with $0.10 \text{ mm}^2 \text{ s}^{-1}$ and a significant upward trend of thermal diffusivities for fiber diameters greater than $125 \mu\text{m}$. Here the upward trend is very pronounced and results in a raise of the thermal diffusivity of $0.15 \text{ mm}^2 \text{ s}^{-1}$ and thus values of $0.25 \text{ mm}^2 \text{ s}^{-1}$ for the thickest BTA-1 fiber of $239 \mu\text{m}$. For BTA-1, fibers with diameters of below $100 \mu\text{m}$ seem to be similarly affected by the different powers, whereas fibers with diameters $\geq 150 \mu\text{m}$ show different thermal diffusivities with different laser powers.

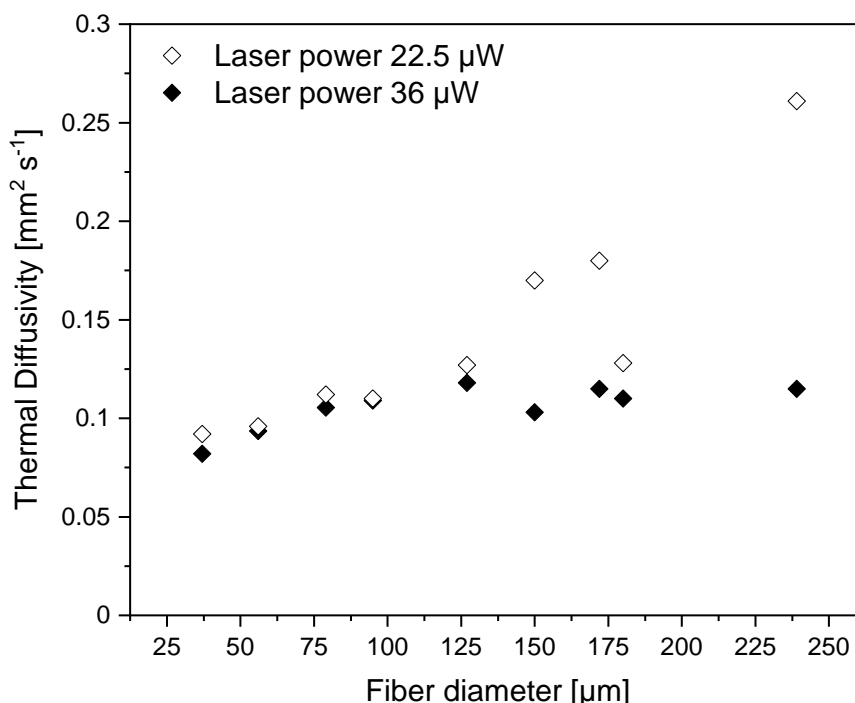


Figure 6-14. **Thermal diffusivities for varying BTA-1 fiber diameter in dependency of two different laser powers (22.5 μW und 36 μW).** The product of the phase and amplitude slope results in the final value for the thermal diffusivity of the fiber. Here, a mean value for the thermal diffusivity is depicted from the two data points obtained from the measurements, corresponding to the left and right side data points of the fiber.

In summary, the diameter of the BTA fibers play a significant role and power dependency is visible. From the data can be concluded that low laser powers need to be chosen for thin fibers and higher laser powers for thick fibers. To analyse the data correctly, a constant amplitude maximum should be obtained instead of using a constant power for all BTA fibers to be able to compare different BTA fibers with varying fiber diameter. Furthermore, it should be checked if the phase decrease for thin fibers or increase for thick fibers as an indicator of a false power use.

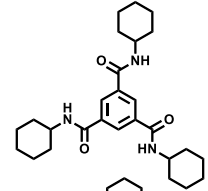
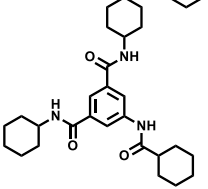
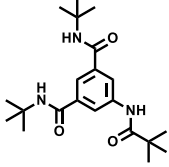
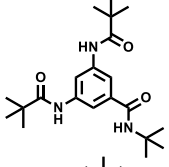
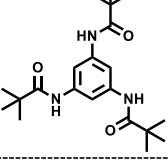
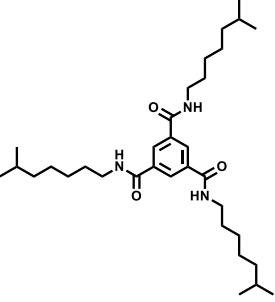
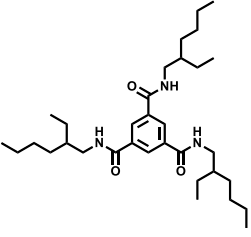
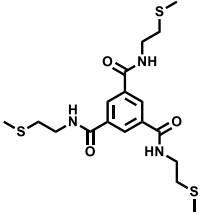
6.4.4 Lock-in thermography measurements on supramolecular fibers

After the elaboration of a suitable lock-in frequency and the power dependency, the other self-assembled BTA fibers were measured by lock-in thermography. Therefore, for each BTA three suitable fibers were measured with a constant lock-in frequency of $f_{\text{lock-in}} = 0.27$ Hz and a chosen power where the amplitude maximum stays constant. The results of the thermal diffusivities as a mean value of all data of each BTA are summarized in Table 6-3. Comparison will be made in each category with the same structural peripheries but different amide connectivity as well as between the categories with correlations of the amide connectivity.

In category A, the two BTA derivatives feature cyclohexyl side groups. Here, the *CCC* derivative shows a higher thermal diffusivity than the *CCN* derivative. In category B, the three BTA derivatives feature tert. butyl side groups. Here, the thermal diffusivity decreases with increasing inversion of the amide groups. Thus, the *NNN* derivative (BTA-9) exhibits a lower thermal diffusivity. Interestingly, the BTA derivatives (BTA-10 and BTA-11) from category C with *CCC* connectivity, however different branching of the alkyl side groups (both $n = 8$) show the lowest thermal diffusivity. The BTA derivative in category D, BTA-4 (*CCC*) with sulfur as heteroatom in the side groups is the only candidate in this group, however shows the highest thermal diffusivity values of all tests BTA derivatives.

When comparing the different BTA derivatives from the categories with each other it can be said that BTA-4 has the highest thermal diffusivity with $\alpha = 0.114 \text{ mm}^2 \text{ s}^{-1}$ being *CCC*-connected and the only BTA derivative with a heteroatom (sulfur) in the periphery. From the IR data can be derived that this derivative should have strong intramolecular hydrogen bonding as the $\nu(\text{N-H})$ and $\nu(\text{C=O})$ are shifted to slightly lower wavenumbers. In contrast to that, lower thermal diffusivity is observed for the *NNN*-connected BTA-9 derivative with $\alpha = 0.085 \text{ mm}^2 \text{ s}^{-1}$. This might be explained by the fact, that the hydrogen bonding of the BTA-9 derivative might be weaker because the N-H and C=O bonds are stronger (indicated by the shift towards higher wavenumbers of N-H and C=O vibrations) compared to the BTA derivatives with *CCN* or *CCC* connectivity. However, all the measured thermal diffusivities are rather low when compared to other materials such as spider silk fibers ($\alpha = 0.2 \text{ mm}^2 \text{ s}^{-1}$),^[187] silica fiber bundles ($\alpha = 0.2 \text{ mm}^2 \text{ s}^{-1}$),^[188] quartz fibers ($\alpha = 0.68 - 0.8 \text{ mm}^2 \text{ s}^{-1}$)^[189,190] or polyether ether ketone fibers ($\alpha = 0.5 \text{ mm}^2 \text{ s}^{-1}$).^[184] Typically, thermal diffusivities in the range of $\alpha = 0.1 - 0.3 \text{ mm}^2 \text{ s}^{-1}$ are observed for biomaterials and considered as thermal insulators whereas good thermal conductors are in the range of $300 \text{ mm}^2 \text{ s}^{-1}$.^[187,195]

Table 6-3. Thermal diffusivities of all measured BTAs with indication of their category, chemical structure, nomenclature and amide connectivity.

Category	Nomenclature	Thermal diffusivity
A	 BTA-1 (CCC)	$\alpha = 0.105 \pm 0.009 \text{ mm}^2 \text{ s}^{-1}$
	 BTA-6 (CCN)	$\alpha = 0.101 \pm 0.006 \text{ mm}^2 \text{ s}^{-1}$
B	 BTA-7 (CCN)	$\alpha = 0.095 \pm 0.012 \text{ mm}^2 \text{ s}^{-1}$
	 BTA-8 (CNN)	$\alpha = 0.087 \pm 0.007 \text{ mm}^2 \text{ s}^{-1}$
	 BTA-9 (NNN)	$\alpha = 0.085 \pm 0.009 \text{ mm}^2 \text{ s}^{-1}$
C	 BTA-10 (CCC)	$\alpha = 0.081 \pm 0.004 \text{ mm}^2 \text{ s}^{-1}$
	 BTA-11 (CCC)	$\alpha = 0.080 \pm 0.004 \text{ mm}^2 \text{ s}^{-1}$
D	 BTA-4 (CCC)	$\alpha = 0.114 \pm 0.009 \text{ mm}^2 \text{ s}^{-1}$

6.5 Conclusion to thermal diffusivity of supramolecular fibers

The final part of this thesis aimed at the preparation of highly ordered, columnar and anisotropic BTA microfibers, which was used to investigate the time-dependence of the temperature distribution, i.e., thermal diffusivity of supramolecular fibers for the first time. This work was performed in collaboration with Ina Klein (Physical Chemistry I, Prof. Dr. Retsch). The thermal diffusivity was determined with the lock-in thermography method by introducing heat into the sample via a modulated laser and following detection of the resulting temperature distribution via an IR camera. For this method high aspect ratio BTA fibers with suitable diameter in the μm -range and length exceeding centimeters while the order and columnar arrangement is maintained, were required. Consequently, fibers of eight structurally different BTAs were successfully prepared for a comparative study. This was achieved by slow solvent evaporation from DMF. This self-assembly method consistently produced supramolecular fibers with large dimensions for BTA fibers with lengths up to centimeters and diameters ranging from about $40\ \mu\text{m}$ up to $240\ \mu\text{m}$. The prepared BTA fibers were investigated regarding their anisotropy and columnar arrangement with polarized optical microscopy and IR spectroscopy suggesting that a threefold, α -helical-type of intermolecular hydrogen-bonding between adjacent molecules is present. Thus, all eight investigated BTA derivatives feature a columnar arrangement of the building blocks. Subsequently, a comprehensive study of the required parameter set (lock-in frequency and laser power) to achieve reliable and reproducible lock-in thermography measurements were performed. The measured thermal diffusivities of these microfibers were found to be in the range of 0.080 to $0.114\ \text{mm}^2\ \text{s}^{-1}$ and is similar to that of thermal insulators. The findings indicate that the thermal characteristics improve with increasing strength of the hydrogen bonds and order in the fibers.

7 Experimental Part

7.1 Methods

¹H-NMR spectroscopy

¹H-NMR spectra were recorded on a BRUKER Avance AC 300 spectrometer at a frequency of 300 MHz at room temperature. If not otherwise noted, all chemical shifts are reported in ppm (δ) and referenced to the chemical shifts of the solvents (DMSO- d_6 = 2.50 ppm or CDCl₃ = 7.26 ppm).

Fourier-transform infrared (FT-IR) spectroscopy

FT-IR spectra were recorded with a Perkin-Elmer Spectrum 100 FT-IR spectrometer equipped with a universal ATR accessory at a resolution of 4 cm⁻¹ in the range of 4000 cm⁻¹ to 650 cm⁻¹. If not otherwise noted, peaks with % T \geq 30 % are reported in the corresponding characterization data.

Mass spectrometry (MS)

Mass spectra were recorded on a Finnigan MAT 8500 spectrometer (Thermo Fisher Scientific) (EI, 70 eV) using direct injection mode. Only molecule peak (M⁺) and peaks with relative intensities \geq 30 % are reported in the corresponding characterization data.

Maldi-ToF:

Matrix-assisted laser desorption/ionization time-of-flight mass spectroscopy (MALDI-ToF MS) measurements were performed using a Bruker AutoFlex Max mass spectrometer equipped with a Smartbeam II laser. The analyte was embedded in the matrix material trans-2-[3-(4-tert-butylphenyl)-2-methyl-2-propenylidene]malononitrile (DCTB) in a matrix:analyte mass ratio of 10:1.

Scanning electron microscopy (SEM)

SEM samples were first sputtered with 2 nm platinum using a Cressington 208HR with planetary stage and QCM crystal. The sputtered samples were measured with a FEI Quanta FEG 250 (Thermo Fisher Scientific). High vacuum mode: SEM micrographs were recorded with an acceleration voltage of 1-5 kV in high vacuum mode and an everhart-thornley detector. Low vacuum mode: SEM micrographs were recorded with a water pressure around 50-70 Pa using an acceleration voltage of 3-5 kV and a large-field (gaseous secondary electron) detector.

Environmental scanning electron microscopy with water vapor pressure (ESEM)

The condensation behavior and wettability of the samples were investigated by FEI Quanta FEG 250 (Thermo Fisher Scientific) in the ESEM mode. The samples were investigated without prior sputtering with a conductive layer. ESEM measurements were conducted using 9 kV acceleration using a gaseous secondary electron detector. To realize temperature-dependent measurements, the instrument was equipped with a Peltier cooling stage (ThermoFisher). The chamber pressure was adjusted to 720 Pa and the temperature set to 4.0 °C, which was then cooled to 1.9 °C with a cooling rate of 1 K min⁻¹ and held at the condensation temperature until condensation and wetting was observed at the sample. The sample was then heated back to 4.0 °C and evaporation of the condensed water occurs.

Optical microscopy

Flock samples and in-situ water transport were investigated by a digital optical microscope (Zeiss, Smartzoom5) with a 4.2 megapixel sensor. The objective (Zeiss PlanApo D5x/0.3FWD 30 mm, 101x-1010x magnification) was illuminated with a coaxial brightfield and ring light.

Polarized optical microscopy

Samples were prepared on a glass slide (Menzel-Gläser). Images were taken between crossed polarizers, some in the presence of a $\lambda/4$ plate, using a Nikon Diaphot 300 microscope (10x, 20x or 40x magnification).

Polarized Raman spectroscopy

A WITec Alpha RA+ imaging system, featuring a UHTS 300 spectrometer and a back-illuminated Andor Newton 970 EMCCD camera, was utilized for confocal Raman imaging. The measurements were carried out with an excitation wavelength of $\lambda = 532$ nm, employing a laser power of 5 mW and an integration time of 1 s. Baseline correction routines were applied to all spectra.

Solubility tests using the crystallization platform Crystal16

Temperature-dependent turbidity measurements of BTA solutions were determined optically at a wavelength of $\lambda = 645$ nm using the crystallization system Crystal16® (Technobis™ Crystallization Systems). The device consists of four chambers, each with four slots. Each chamber can be used independently. The BTA dispersions or solutions were prepared at room temperature and placed into the slots and heated to close below the boiling points of the corresponding solvents and stirred for 30 min up to 1 h with a bottom stirrer for dissolution. The transmittance at $\lambda = 645$ nm of each sample was recorded for three cycles in the range of 5 to 90 °C, depending of the boiling points of the solvents. Each cycle consists of a heating and cooling step with a scanning rate of 0.1 - 0.5 °C min⁻¹ and an isothermal hold at the corresponding end temperature while stirring the whole time with 400 – 600 rpm. The change in transmittance upon cooling from 100 % to 0 % indicates clouding of the sample and thus the self-assembly of BTAs into self-assembled fibers. In contrast, the change in transmittance upon heating from 0 % to 100 % indicates dissolution of the self-assembled fibers resulting in a clear solution. The cloud and clearing points were determined at a transmittance of 50% upon cooling and heating, respectively. From this data, concentration-dependent development of the cloud and clearing points as mean values including the standard deviation from the applied three heating and cooling cycles can be obtained and a phase diagram of the selected BTA is obtained. Concentrations of samples which did not dissolve were claimed as not soluble.

7.2 Experimental procedure

7.2.1 Controlled preparation of supramolecular fibers

Solubility tests

Prior to the supramolecular fiber preparation, solubility tests are conducted with the crystallization system Crystal16® (Technobis™ Crystallization Systems) as described in 7.1 Methods.

Custom-made experimental set-up

The custom-made experimental set-up used for the fabrication of defined BTA fibers is made of a screw-mountable 1 L vessel (laboratory glass bottle DURAN GLS 80) filled with a dispersion of a BTA in a selected solvent. The cap of the vessel is modified to insert a mechanical stirrer (Heidolph, Hei-TORQUE 400) and an immersion sensor as well as to prevent evaporation. The immersion sensor measures the temperature in the vessel and is linked to the digital precision thermometer, GHM Greisinger 3210, to record and save the time-dependent temperature profiles the software, EBS 20M. The vessel is placed in a water bath of a cryostat (Huber CC 80w), that is able to heat and cool with a defined linear chosen heating and cooling rate, respectively. Furthermore, a camcorder (SONY FDRAX43) is set in a way, that it records the experiment to obtain the self-assembly point upon cooling the solutions.

Self-assembly in the custom-made experimental set-up

BTA-1 (N¹,N³,N⁵-tricyclohexylbenzene-1,3,5-tricarboxamide):

In general, the solvent and the BTA-1 was weight in the vessel which was then sealed and placed into the set-up. At this point, the BTA-1 is dispersed in the solvent. The mixture was heated up to 75 °C and isothermally hold for about 30 minutes until all BTA-1 was molecularly dissolved. A cooling profile was then applied and the BTA-1 solution was cooled down to 15°C with a chosen linear cooling rate of 0.50 °C min⁻¹ and 0.25 °C min⁻¹. A non-linear cooling rate was established by removing the vessel from the water bath after complete dissolution of the BTA-1 at 75°C in the selected solvent and placed on the bench to cool down to room temperature. To investigate the influence of stirring, the stirring rates are varied with the following values: no stirring (0 rpm), 25 rpm, 100 rpm and 200 rpm. To investigate the influence of concentration, the cooling rate of 0.50 °C min⁻¹ is used and the concentration of 0.175 wt.%, 0.20 wt.% and 0.25 wt.% are chosen. Reproducibility measurements (n = 10) are conducted at a parameter set of: 25 rpm stirring rate, concentration of 0.175 wt.% and 0.50 °C min⁻¹ as cooling rate.

BTA-2 (N¹,N³,N⁵-tris(2,4,4-trimethylpentan-2-yl)benzene-1,3,5-tricarboxamide):

As described before, the mixture of BTA-2 and solvent was heated up to 75 °C and isothermally hold for about 30 minutes until all BTA-2 was molecularly dissolved. The cooling profile was then started and the BTA-2 solution was cooled down to 15°C with a chosen linear cooling rate of 0.50 °C min⁻¹ or non-linear cooling rate. To investigate the influence of stirring, the stirring rates are varied with the following values: no stirring (0 rpm), 25 rpm or 100 rpm. The concentration was kept constant at 0.150 wt.% in 2-propanol.

BTA-3 (Trimethyl 2,2',2''-(benzenetricarbonyltris(azanediyl))tris(4-(methylthio)-butanoate)):

The mixture of BTA-3 and solvent was then heated up to 75 °C and isothermally hold for about 30 minutes until all BTA-3 was molecularly dissolved. The cooling profile was then started and the BTA solution was cooled down to 15°C with a chosen linear cooling rate of 0.50 °C min⁻¹ or non-linear cooling rate. To investigate the influence of stirring, the stirring rates are varied with the following values: no stirring (0 rpm), 25 rpm or 100 rpm. The concentration was kept constant at 0.30 wt.% in 1-propanol.

General sample preparation method for scanning electron microscopy measurements

The self-assembled fibers are isolated by a glass pipette and deposited on a PET mesh with mesh-size of 50 µm. The deposited BTA fibers are then washed with water to get rid of the remaining BTA in solution and prevent further self-assembly upon solvent evaporation. After the BTA fibers are dried, they are fixed on a sample holder, so called SEM stub, which is equipped with a conductive adhesive layer. The fixation is achieved by stamping.

7.2.2 Electrostatic flocking of supramolecular fibers

Controlled self-assembly in solution towards supramolecular fibers

The self-assembled fibers were prepared in the custom-made set-up according to the procedure described in the section *Experimental procedure of controlled preparation of supramolecular fibers: Custom-made experimental set-up*. Shortly, the BTA-1 (N^1, N^3, N^5 -tricyclohexylbenzene-1,3,5-tricarboxamide) was weight in the vessel with MEK with a concentration of 0.20 wt.%. The vessel was then sealed and placed into the custom-made set-up. At this point, the BTA-1 is dispersed in the solvent. The mixture was heated up to 75 °C and isothermally hold for about 30 minutes until all BTA-1 was molecularly dissolved. A cooling profile from 75 °C to 15 °C with a linear cooling rate of 0.50 °C min⁻¹ was then applied with constant stirring of 25 rpm.

Isolation and sieving of the supramolecular fibers from solution

After the successful preparation of the self-assembled fibers, the dispersion of the BTA fibers is then given through a PET net with varying mesh sizes from 50 μm – 400 μm to filter off the self-assembled fibers. The fibers are subsequently washed with water to remove the remaining solvent with residual dissolved BTA and dried in an oven at 80 °C overnight.

Surface decoration of BTA fibers with salt and tenside

To manipulate the surface conductivity of the BTA fibers to improve the flocking procedure in an electric field, the BTA fibers were dispersed in a solution containing the salt ammonium sulfate ((NH₄)₂SO₄). Furthermore, the tenside N,N,N -Trimethyl-1-hexadecan-aminiiumchloride (CTAC) is added to improve the dispersibility of the BTA in the aqueous solution. One gram of isolated and dried BTA fibers are given into the (NH₄)₂SO₄ /CTAC mixture of various concentrations. In the next step, the fibers are given through a PET net construction with three different PET nets varying in mesh size which are assembled on top of each other with magnetic 3-D-printed PP holder. The PET net on top features a mesh size of 400 μm, the second PET net in the middle has a mesh size of 100 μm and the third on the bottom features a mesh size of 50 μm. With this method, the BTA fibers are selected in size due to the different mesh-sizes of the assembled nets. Furthermore, less BTA fibers are at each net and thus reducing agglomeration. The nets with the BTA fibers are dried in an oven at 80 °C overnight. The dried BTA fibers are then used for the flocking experiments.

Electrostatic flocking of supramolecular fibers

The BTA fibers are applied onto the electrode of the electrostatic flocking machine (WWS pro grass box - 67474271). The power is switched on and a SEM stub covered with a conductive adhesive layer and connected to the ground cable is held over the electrode at distance of 1-3 cm with the deposited BTA fibers. When the flocking process is finished, the flocked SEM stub is tapped several times to remove BTA fibers which are not adhered into the adhesive layer.

7.2.3 Self-assembly of supramolecular fibers within polymer flocks

Preliminary self-assembly experiments upon solvent evaporation on aluminum foil

A solution containing 0.50 wt.% of the corresponding BTA-4 (N^1, N^3, N^5 -tris[2-(methylthio)-ethyl]-1,3,5-benzenetricarboxamide) or BTA-5 (N^1, N^3, N^5 -tris[2-(diisopropylamino)-ethyl]-1,3,5-benzenetricarboxamide) in 2-propanol were prepared at ambient conditions. Then, 5 μL of this solution was dropped on aluminum foil and the solvent was allowed to evaporate. In case of BTA-3 (Trimethyl 2,2',2''-(benzenetricarbonyltris(azanediyl))tris(4-(methylthio)-butanoate)) the solution was prepared at elevated temperatures. 5 μL of the hot solution was dropped on aluminum foil and cooling and solvent evaporation at ambient conditions took place simultaneously.

Electrostatic flocking of polyamide flocks

Electrostatic flocking was performed with a semiautomatic flocking device (RF 500, Borchert+Moller). In preparation of the PET-substrate, an adhesive and hardener (tubicoll 1510A, L5515) were mixed in a 1:1 wt.-ratio for approximately 15 min. After allowing a 5-min settling period, the PET meshes were dip-coated with a thin adhesive layer and then transferred to a paper towel. Excess adhesive was removed by squeegeeing with a glass rod. The adhesive-coated PET mesh was placed on an aluminum foil as an electrode and positioned beneath the flocking chamber. An electric field of 2.3 kV cm^{-1} was applied for 60 s. After a 10 s delay, the flock feed was activated for 30 s. Subsequently, the PET mesh with vertically aligned polyamide microfibers ($d \sim 19 \mu\text{m}$, $l \sim 500 \mu\text{m}$, reinweiß) was placed on a steel tray and moved into a convection oven to crosslink the adhesive at $120 \text{ }^\circ\text{C}$ for 20 min. Following this, the flocked material was stored for 24 h at rt to complete the adhesive curing process. The samples were then cleaned with pressured air to remove loose microfibers, washed with H_2O , ethanol, 2-propanol, acetone, and dried in a vacuum at $50 \text{ }^\circ\text{C}$ for 12 h

Self-assembly experiments within polymer flocks

First experiments were conducted by varying the concentrations (0.050 - 0.50 wt.%), solvents (2-propanol, EtOH, DMF), application methods (drop, spray or immersion), immersion times and the drying procedures. For this, the stable BTA solutions with varying concentrations were combined with the polyamide flocks in different ways and dried under ambient conditions or covered in a petri dish stored at 30°C.

Self-assembly into supramolecular spines

The optimized procedure to obtain supramolecular spines on top of the PA flocks requires the PA flock to be immersed into a BTA-5 solution of 0.50 wt.% in 2-propanol for 30 s and placed 10 s on a filtration paper. The sample was then covered in a petri dish and stored at 30 °C for complete solvent evaporation. After complete evaporation, the sample was placed on a SEM stub and investigated regarding the possible formation of BTA fibers within the flock.

In-situ observation of water collection

Artificial fog was created by an ultrasonic humidifier (Beurer LB 88). The sample is placed under the optical microscope (Zeiss, Smartzoom5) and the flock decorated with BTA spines is irrigated with the artificial fog whereby the water collection and transport along the BTA spines were recorded as a video simultaneously with the camera of the optical microscope.

7.2.4 Thermal diffusivity of supramolecular fibers

Self-assembly upon solvent evaporation

For the preparation of BTA fibers suitable for lock-in thermography measurements, self-assembly upon solvent evaporation at ambient conditions is conducted. First, the BTA is dissolved in DMF at elevated temperatures. The solution was then given in a petri dish laid out with aluminum foil. When it was cooled down to room temperature and covered with a crystallization dish. The solvent was allowed to evaporate slowly for 1 week.

Fixation on Grid

The BTA fibers were taken with tweezers from the aluminum foil and fixated onto the 3-D printed grid with the help of an adhesive tape. Typically, two fibers exceeding 1 cm in length were fixated on the longer half and two fibers exceeding 0.5 cm on the other side as schematically shown in Figure 7-1.

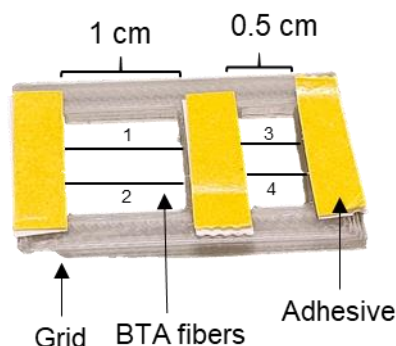


Figure 7-1. **Sample holder for lock-in measurements of fibers.** The sample holder consists of a 3-D printed PLA grid with 1 cm and 0.5 cm place for the BTA fibers. Adhesive tape holds the BTA fibers in place. The four BTA fibers on the grid are indicated by the numbers.

Carbon vapor deposition

Vapor deposition of a 10-20 nm layer of carbon onto of the sample holder with the BTA fibers was conducted using the Leica EM ACE600 machine.

Lock-in thermography measurements

To measure the thermal diffusivity of BTA fibers, the sample on the sample holder is situated within an aluminum vacuum chamber (pressure $< 10^{-2}$ mbar). The vacuum chamber, mounted on a three-axis translation stage and a tip-tilt rotation stage, facilitates the focusing and alignment of the fiber. A point laser (51nano-N-520-0.9-O05-P-12-4-28-0-150, Schäfter+Kirchhoff GmbH) enters the vacuum chamber through an optically transparent N-BK7 glass window at an angle of approximately 5° . The camera lens is coated to prevent the laser from reaching the detector. Utilizing an angled point laser prevents the reflection of the laser at the camera lens from creating a secondary heating spot on the fiber. A signal generator (DG1022A, RIGOL Technologies Co., Ltd.) regulates the laser's maximum power by applying a direct current (DC) voltage. The power is modulated periodically by a control interface (BreakOut-Box, Infratec GmbH). The control interface is synchronized with an IR camera (Image IR 9430, InfraTec GmbH) located at the front of the vacuum chamber and the computer. The InfraTec's IRBISactiveonline software manages the synchronization.

Measurements and data acquisition were performed and provided by Ina Klein (Physical department I, Prof. Dr. Retsch).

7.3 Synthesis and characterization of 1,3,5-benzenetrisamides

N^1,N^3,N^5 -tricyclohexylbenzene-1,3,5-tricarboxamide (BTA-1)

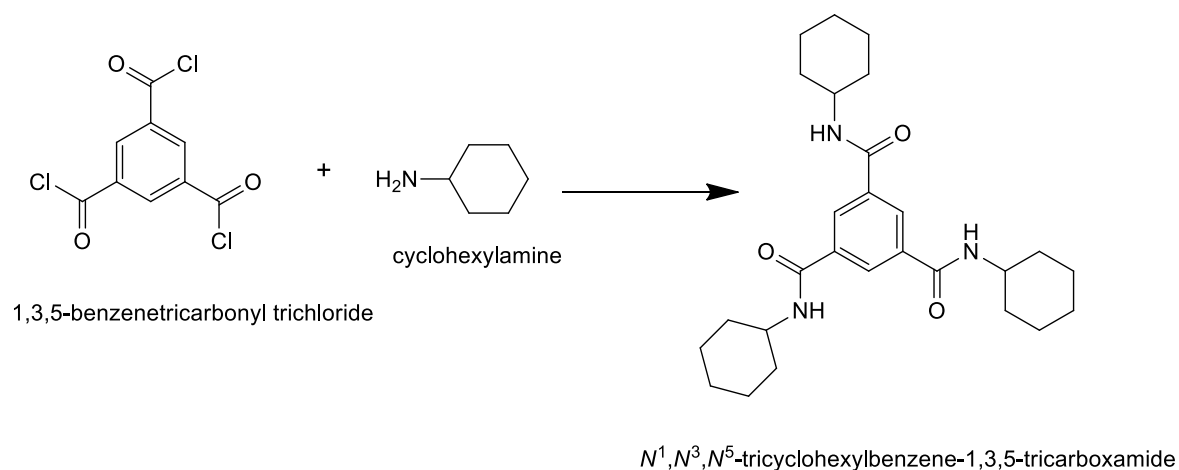


Figure 7-2. Synthetic scheme to N^1,N^3,N^5 -tricyclohexylbenzene-1,3,5-tricarboxamide.

Synthesis:

100 g (0.38 mol) of 1,3,5-benzenetricarbonyl trichloride

123.2 g (1.2 mol) of cyclohexylamine

98.3 g (1.2 mol) of pyridine

300 mL THF

Cyclohexylamine, THF and pyridine were mixed together. 1,3,5-benzenetricarbonyl trichloride were dissolved in 300 mL THF and was slowly added under an argon atmosphere at 5°C to the mixture. The reaction mixture was stirred at room temperature for 12 h. Subsequently, the mixture was concentrated in a rotary evaporator to 1 L, precipitated in 3 L water and stirred for 12 h. The solid was filtered off and washed with water. The crude product was heated to 120 °C in 3 L DMF for 10 minutes and filtered off and then again solved under heating in 1 L acetone, filtered off and dried under high vacuum at 80°C.

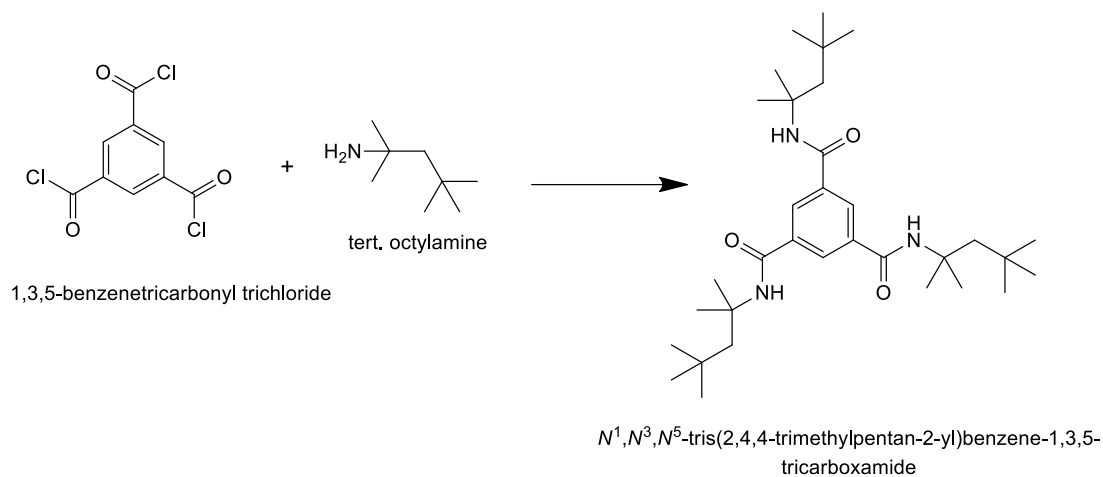
Characterization:

Yield: 122.8 g (70 %)

$^1\text{H-NMR}$: δ (ppm) in DMSO- d_6 : 1.11 - 1.13 (m, 15H), 1.28-1.73 (m, 15H), 3.75 (s, 3H), 8.29 (s, 3H), 8.46 (d, 3H).

MS: m/z : 453 (M^+), 372, 355, 290, 208, 98.

IR: $\tilde{\nu}$ (cm^{-1}): 3214, 3053, 2928, 2854, 1629, 1556, 1321, 692.

***N*¹,*N*³,*N*⁵-tris(2,4,4-trimethylpentan-2-yl)benzene-1,3,5-tricarboxamide (BTA-2)**Figure 7-3. Synthetic scheme to *N*¹,*N*³,*N*⁵-tris(2,4,4-trimethylpentan-2-yl)benzene-1,3,5-tricarboxamide.**Synthesis:**

100 g (0.38 mol) of 1,3,5-benzenetricarbonyl trichloride

1000 g (7.7 mol) of tert. octylamine

1 L H₂O

The amine was given into a 2 L flask and cooled to 5°C under argon. The 1,3,5-benzenetricarbonyl trichloride is slowly added under an argon atmosphere and ice cooling. A white precipitate was observed. The reaction was stirred at room temperature for 12 h. 1 L of water was added until a turbid slurry was obtained. The suspension was filtered off. The crude product was recrystallized in 4 L DMF and dried under high vacuum at 80°C.

Characterization:

Yield: 146.9 g (71 %)

¹H-NMR: δ (ppm) in CDCl₃: 1.03 (s, 27H), 1.59 (s, 18H), 1.96 (s, 6H), 8.52 (s, 3H)MS: m/z: 472 (M⁺), 415, 360, 303, 191.IR: $\tilde{\nu}$ (cm⁻¹): 3223, 3058, 2954, 2891, 1633, 1556, 1365, 1299, 685.

**Trimethyl 2,2',2''-(benzenetricarbonyltris(azanediyl))tris(4-(methylthio)-butanoate)
(BTA-3)**

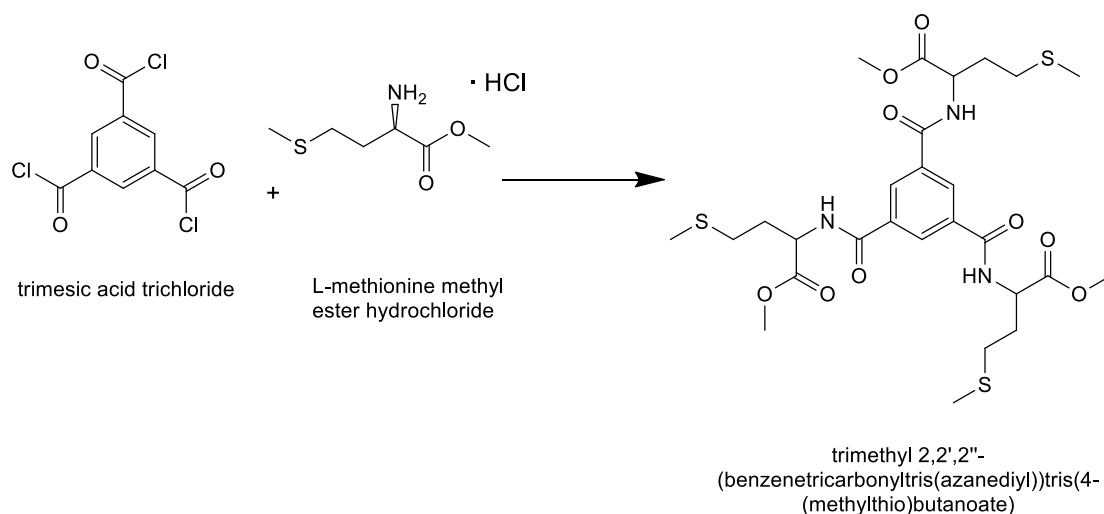


Figure 7-4. Synthetic scheme to trimethyl 2,2',2''-(benzenetricarbonyltris(azanediyl))tris(4-(methylthio)butanoate)

Synthesis:

10.0 g (38 mmol) of trimesic acid trichloride

24.8 g (120 mmol) of L-methionine methyl ester hydrochloride

33.6 mL triethylamine

220 mL THF

LiCl

To a mixture of L-methionine methyl ester hydrochloride, triethylamine and LiCl in THF, the trimesic acid trichloride (dissolved in a small amount of THF) were slowly added under argon atmosphere at 5°C. A white precipitate is observed. The mixture was stirred at room temperature for 3 h. The reaction mixture was precipitated in 2 L water and filtrated. The crude product was recrystallized in 250 mL MeOH. The solvent was removed under high vacuum yielding a white powder.

Characterization:

Yield: 22 g (90 %)

$^1\text{H-NMR}$: δ (ppm) in DMSO- d_6 : 2.09 (m, 5H), 2.62 (m, 2H), 3.67 (s, 3H), 4.61 (m, 1H), 8.50 (s, 1H), 9.16 (d, 1H)

MS: m/z: 645 (M $^+$), 571, 536, 483, 435, 376, 332, 217, 164, 75

IR: $\tilde{\nu}$ (cm^{-1}): 3222, 3056, 2951, 1744, 1635, 1547, 1435, 1302, 1207, 1167.

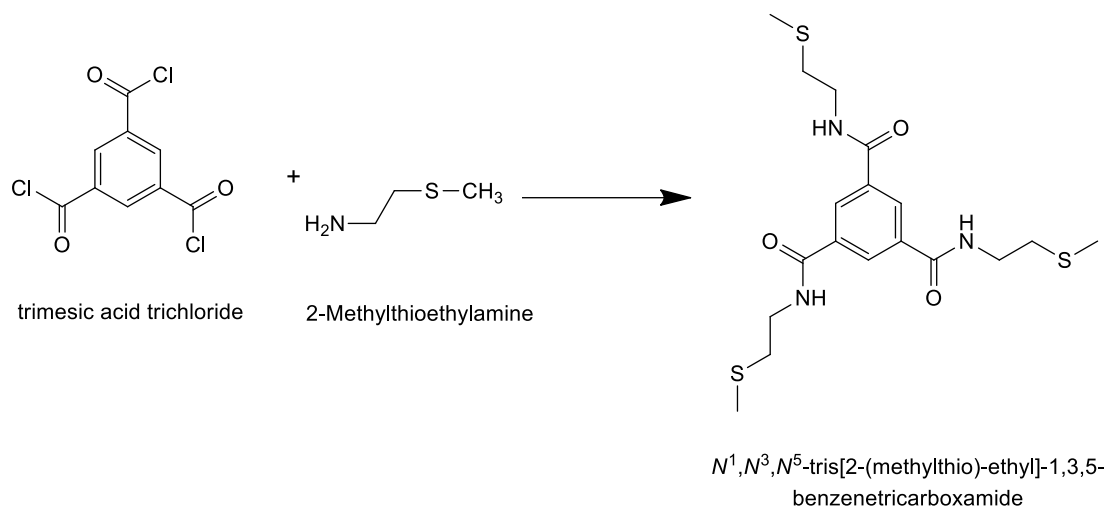
***N*¹,*N*³,*N*⁵-tris[2-(methylthio)-ethyl]-1,3,5-benzenetricarboxamide (BTA-4)**

Figure 7-5. Synthetic scheme to *N*¹,*N*³,*N*⁵-tris[2-(methylthio)-ethyl]-1,3,5-benzenetricarboxamide.

Synthesis:

4.4 g (17 mmol) of trimesic acid trichloride

5.0 g (55 mmol) of 2-methylthioethylamine

15 mL triethylamine

150 mL THF

To a mixture of 2-methylthioethylamine, THF and triethylamine, trimesic acid trichloride (dissolved in a small amount of THF) were slowly added under argon atmosphere and ice cooling. A white precipitate was observed. The mixture was stirred at room temperature for 12 h and the THF was removed afterwards. The obtained material was stirred in 500 mL water for 12 h, filtrated and recrystallized in 300 mL MeOH. The product was filtered off and dried under vacuum yielding a white powder.

Characterization:

Yield: 4 g (57 %)

¹H-NMR: δ (ppm) in DMSO-d₆: 2.11 (s, 9H), 2.65 (m, 6H), 3.47 (m, 6H), 8.42 (s, 3H), 8.87 (t, 3H)

MS: m/z: 429 (M⁺), 355, 339, 281, 265, 208, 103, 74

IR: $\tilde{\nu}$ (cm⁻¹): 3228, 3052, 2911, 1631, 1552, 1428, 1300, 1229, 716, 689.

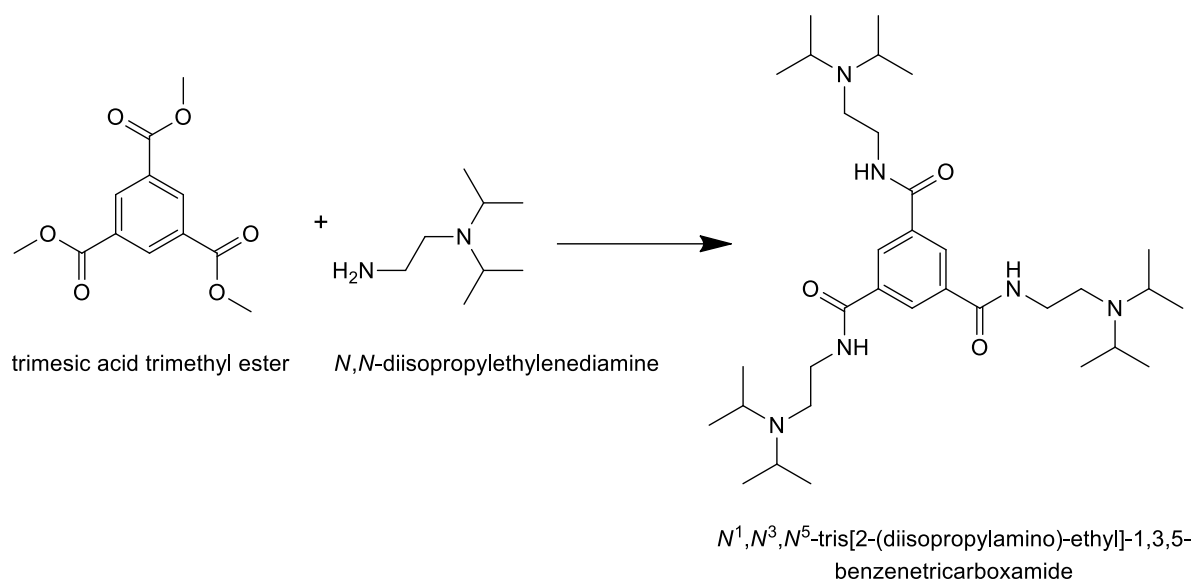
***N*¹,*N*³,*N*⁵-tris[2-(diisopropylamino)-ethyl]-1,3,5-benzenetricarboxamide (BTA-5)**

Figure 7-6. Synthetic scheme to *N*¹,*N*³,*N*⁵-tris[2-(diisopropylamino)-ethyl]-1,3,5-benzenetricarboxamide.

Synthesis:

7.17 g (28 mmol) of trimesic acid trimethyl ester

25 mL (140 mmol) of *N,N*-diisopropylethylenediamine

Trimesic acid trimethyl ester was dispersed in *N,N*-diisopropylethylenediamine under an nitrogen atmosphere. The mixture was stirred at 125 °C for 20 h and was then allowed to cool down to room temperature. The mixture was two times dispersed in 400 mL acetic acid ethyl ester, boiled and the solid was filtered off. The product was dried in high vacuum yielding a white powder.

Characterization:

Yield: 12.2 g (72 %)

¹H-NMR: δ (ppm) in CDCl₃: 1.06 (d, 36H), 2.71 (t, 6H), 3.07 (m, 6H), 3.45 (quartet, 6H), 7.23 (t(br), 3H), 8.41 (s, 3H)

MS: m/z: 588 (M⁺), 115, 114, 72, 43.

Maldi-ToF: m/z 589 (M⁺+H)⁺

IR: $\tilde{\nu}$ (cm⁻¹): 3238, 2964, 2872, 1637, 1554, 1286, 1181, 729, 691.

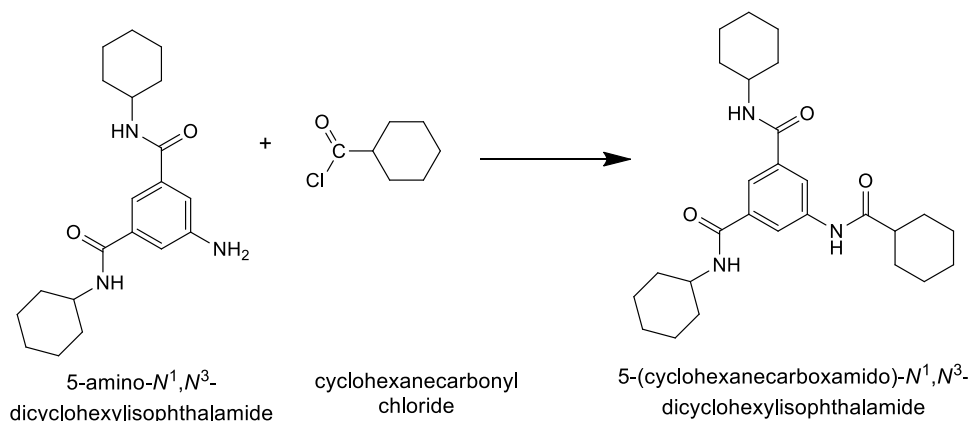
5-(cyclohexanecarboxamido)-*N*¹,*N*³-dicyclohexylisophthalamide (BTA-6)

Figure 7-7. Synthetic scheme to 5-(cyclohexanecarboxamido)-*N*¹,*N*³-dicyclohexylisophthalamide.

Synthesis:

4 g (12 mmol) of 5-amino-*N*¹, *N*³-dicyclohexylisophthalamide

1.74 mL (13 mmol) of cyclohexanecarbonyl chloride

1.03 mL (13 mmol) of pyridine

1.26 g (12 mmol) trimethylchlorosilane

200 mL NMP

The 5-amino-*N*¹, *N*³-dicyclohexylisophthalamide, pyridine, NMP, and trimethylchlorosilane were mixed together. The cyclohexanecarbonyl chloride was slowly added under an argon atmosphere and ice cooling. The reaction was stirred at room temperature for 2 h. The mixture was precipitated in 2 L of ice water and filtrated. The product was dried under vacuum yielding a white powder.

Characterization:

Yield: 4.87 g (92%)

¹H-NMR: δ (ppm) in DMSO-d₆: 1.07 - 1.47 (m, 15H), 1.57-1.73 (m, 15H), 2.32 (m, 1H), 3.71 – 3.78 (m, 2H), 7.80 (s, 1 H), 8.10 (s, 2H), 8.25-8.28 (m, 2H), 10.04 (s, 1H).

MS: m/z: 453 (M⁺), 372, 434, 328, 273, 179, 98, 83, 55.

IR: $\tilde{\nu}$ (cm⁻¹): 3258, 2928, 2850, 1705, 1630, 1551, 1440, 1326, 1256, 1171, 889, 697.

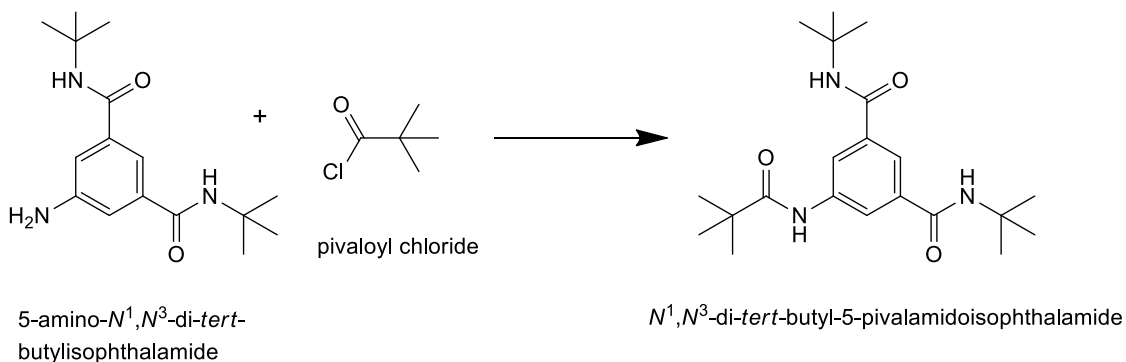
***N*¹,*N*³-di-*tert*-butyl-5-pivalamidoisophthalamide (BTA-7)**

Figure 7-8. Synthetic scheme to *N*¹,*N*³-di-*tert*-butyl-5-pivalamidoisophthalamide.

Synthesis:

6.8 g (24 mmol) of 5-amino-*N*¹,*N*³-di-*tert*-butylisophthalamide

3.2 mL (26 mmol) of pivaloyl chloride

2.1 mL pyridine

200 mL THF

To a mixture of 5-amino-*N*¹,*N*³-di-*tert*-butylisophthalamide, THF and pyridine, pivaloyl chloride was slowly added under argon atmosphere and ice cooling. The mixture was stirred at room temperature for 2 h. The reaction mixture was precipitated in 2 L ice cooled water and filtrated. The crude product was recrystallized in 500 mL MeOH. The product was dried under vacuum yielding a white powder.

Characterization:

Yield: 7.68 g (87 %)

¹H-NMR: δ (ppm) in DMSO-*d*₆: 2.23 (s, 9H), 1.38 (s, 18H), 7.72 (s, 1H), 7.86 (s, 2H), 8.08 (s, 2H), 9.44 (s, 1H)

MS: *m/z*: 375 (M⁺), 303, 247, 179, 57

IR: $\tilde{\nu}$ (cm⁻¹): 3232, 2964, 1634, 1557, 1525, 1454, 1365, 1311, 1225, 707, 681.

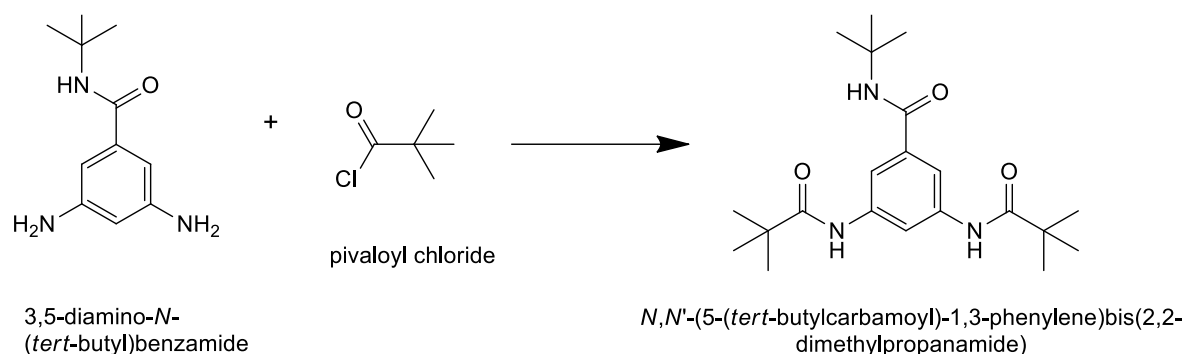
***N,N'*-(5-(*tert*-butylcarbamoyl)-1,3-phenylene)bis(2,2-dimethylpropanamide) (BTA-8)**

Figure 7-9. Synthetic scheme to *N,N'*-(5-(*tert*-butylcarbamoyl)-1,3-phenylene)bis(2,2-dimethylpropanamide).

Synthesis:

9.84 g (47 mmol) of 3,5-diamino-*N*-(*tert*-butyl)benzamide

13.63 mL (110 mmol) of pivaloyl chloride

400 mL NMP

80 mL pyridine

LiCl

The 3,5-diamino-*N*-(*tert*-butyl)benzamide, NMP, pyridine and LiCl were given in a flask. The mixture was stirred under argon atmosphere in an ice bath for 15 minutes. Then, the pivaloyl chloride was slowly added under argon atmosphere and ice cooling. The mixture was stirred at 80 °C for 2.5 h. The reaction mixture was precipitated in ice cooled water and filtrated. A Soxhlet with 500 mL EtOH was used to purify the product.

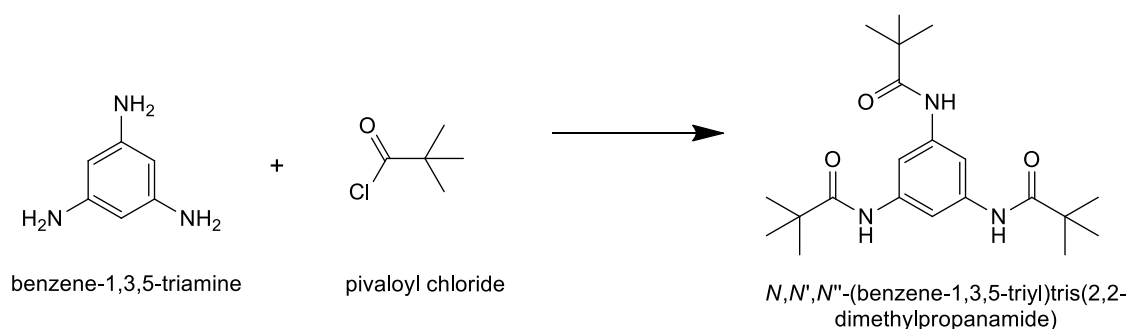
Characterization:

Yield: 15.40 g (87 %)

¹H-NMR: δ (ppm) in DMSO-*d*₆: 1.22 (s, 18H), 1.36 (s, 9H), 7.76 (s, 2H), 7.58 (s, 1H), 8.18 (s, 1H), 9.32 (s, 2H)

MS: *m/z*: 375 (M⁺)

IR: $\tilde{\nu}$ (cm⁻¹): 2963, 1657, 1527, 1420, 1365, 1213, 923, 866, 766, 669.

***N,N',N''*-(benzene-1,3,5-triyl)tris(2,2-dimethylpropanamide) (BTA-9)**Figure 7-10. Synthetic scheme to *N,N',N''*-(benzene-1,3,5-triyl)tris(2,2-dimethylpropanamide).**Synthesis:**

1 g (0.81 mmol) of benzene-1,3,5-triamine

3.23 g (27 mmol) of pivaloyl chloride

50 mL NMP

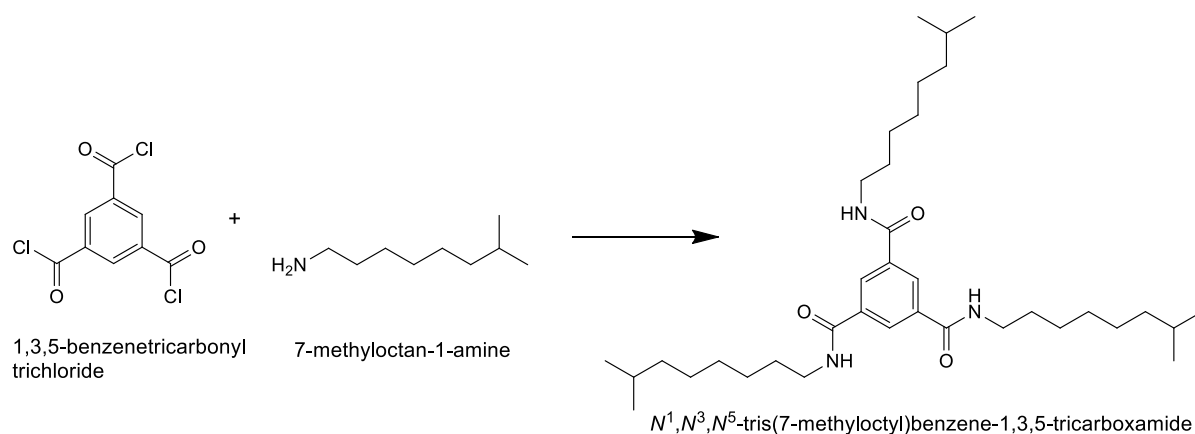
2.2 mL (27 mmol) pyridine

The amine, NMP and pyridine were given in a flask. The mixture was stirred under argon atmosphere. Then, the pivaloyl chloride was slowly added under argon atmosphere. The mixture was stirred at rt for 2h. The reaction mixture was precipitated in 1 L ice cooled water and filtrated.

Characterization:

Yield: 0.64 g (40 %)

¹H-NMR: δ (ppm) in DMSO-d₆: 1.19 (s, 27H), 7.61 (s, 3H), 9.17 (s, 3H)MS: m/z: 375 (M⁺), 291, 207, 57.IR: $\tilde{\nu}$ (cm⁻¹): 3300, 2968, 1658, 1534, 1438, 1367, 1216, 922, 851, 668.

***N*¹,*N*³,*N*⁵-tris(7-methyloctyl)benzene-1,3,5-tricarboxamide (BTA-10)**Figure 7-11. Synthetic scheme to *N*¹,*N*³,*N*⁵-tris(7-methyloctyl)benzene-1,3,5-tricarboxamide.**Synthesis:**

3.1 g (12 mmol) of 1,3,5-benzenetricarbonyl trichloride

5 g (40 mmol) of 7-methyloctan-1-amine

100 mL NMP

20 mL pyridine

LiCl

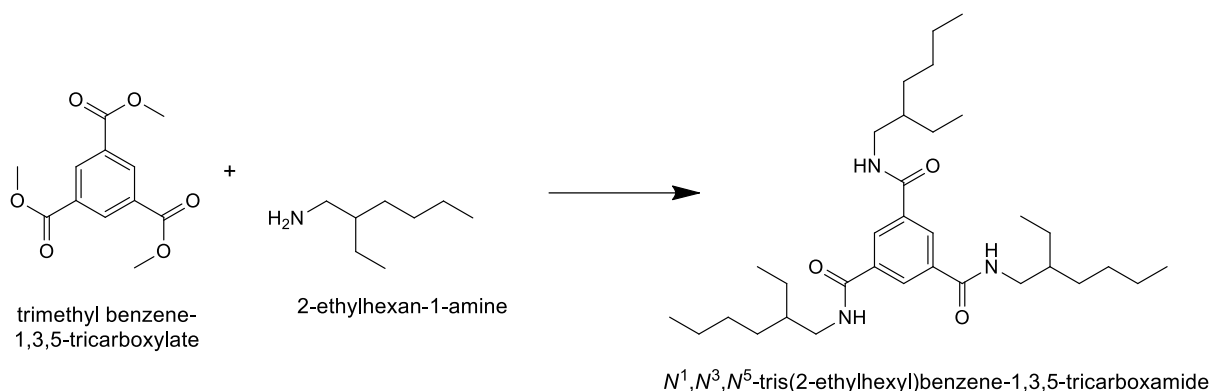
The amine, pyridine and LiCl were given in a flask. The mixture was stirred under nitrogen atmosphere in an ice bath. Then, the 1,3,5-benzenetricarbonyl trichloride was slowly added. The mixture was stirred at 60 °C overnight. The reaction mixture was precipitated in ice cooled water and filtrated. The crude product was recrystallized in 500 mL of MeOH.

Characterization:

¹H-NMR: δ (ppm) in DMSO-d₆: 0.89 (t, 18H), 1.38 (m, 24H), 3.19 (t, 6H), 8.35 (s, 3H), 8.60 (t, 3H).

MS: m/z: 544 (M⁺)

IR: $\tilde{\nu}$ (cm⁻¹): 3239, 3075, 2925, 1635, 1558, 1457, 1293, 726, 691.

N*¹,*N*³,*N*⁵-tris(2-ethylhexyl)benzene-1,3,5-tricarboxamide (BTA-11)**Figure 7-12. Synthetic scheme to *N*¹,*N*³,*N*⁵-tris(2-ethylhexyl)benzene-1,3,5-tricarboxamide.Synthesis:***

30.7 g (122 mmol) of trimethyl benzene-1,3,5-tricarboxylate

100 mL (609 mmol) of 2-ethylhexan-1-amine

The trimethyl benzene-1,3,5-tricarboxylate and amine were given in a flask and the mixture was stirred at 135 °C overnight. The reaction mixture was precipitated 300 ml acetone and filtrated. The crude product was stirred in 3 L acetone to purify the product. The product was dried at 50°C under vacuum overnight.

Characterization:

Yield: 36 g (54 %)

¹H-NMR: δ (ppm) in CDCl₃: 0.95 (m, 18H), 1.36 (m, 24H), 1.41 (m, 3H) 3.44 (m, 6H), 6.55 (t, 3H), 8.34 (s, 3H).MS: m/z: 543 (M⁺), 514, 486, 445, 415, 332, 57.IR: $\tilde{\nu}$ (cm⁻¹): 3240, 3077, 2925, 1635, 1557, 1456, 1293, 727, 691.

8 Appendix

Appendix A

Fiber diameter histograms prepared from of 0.175 wt.% BTA-1 in MEK at a cooling rate of 0.25 C min^{-1} (various stirring rates)

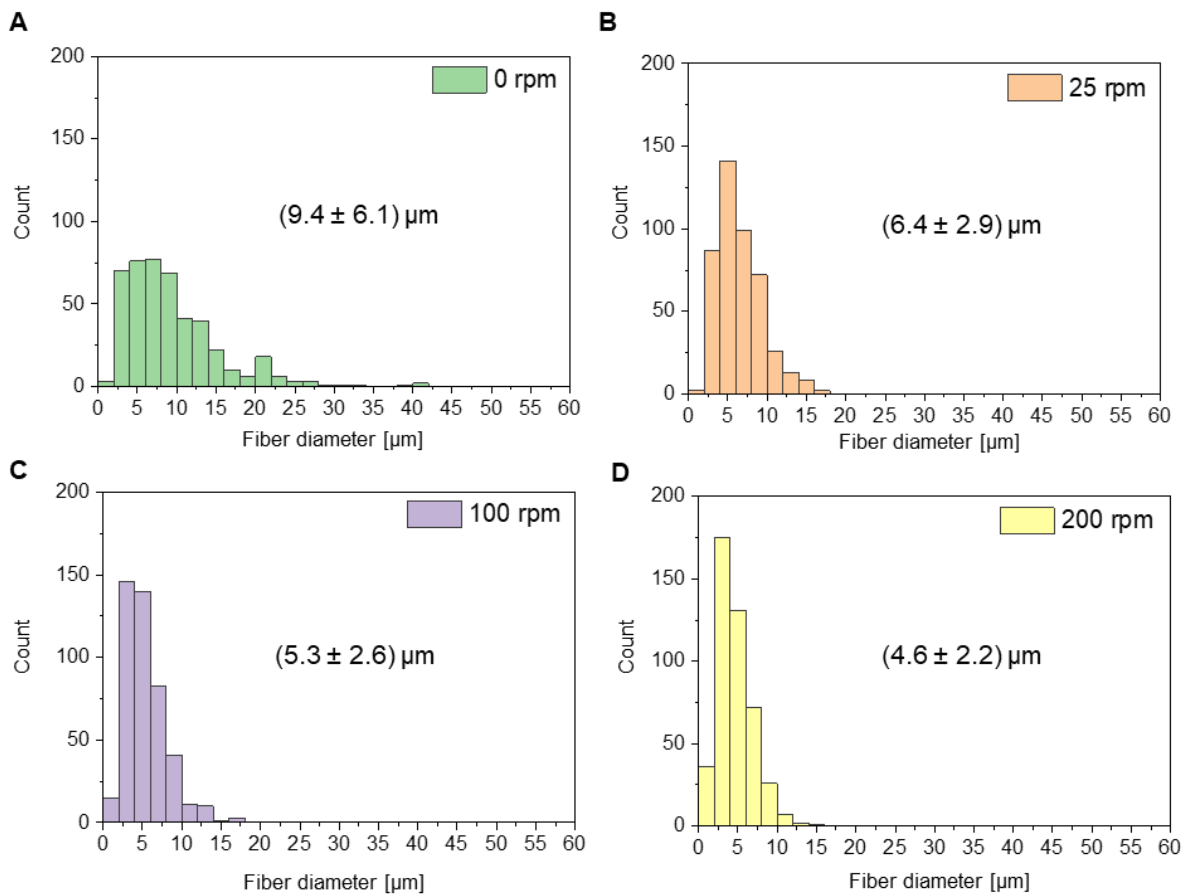


Figure 8-1. **Fiber diameter histograms of BTA-1 fibers** fabricated from a 0.175 wt.% solution in MEK at a constant cooling rate of 0.25 C min^{-1} and different stirring rates of 0 rpm, 25 rpm, 100 rpm and 200 rpm. The histograms of the fiber diameter are based on 450 fibers.

Fiber length histograms prepared from of 0.175 wt.% BTA-1 in MEK at a cooling rate of $0.25\text{ }^{\circ}\text{C min}^{-1}$ (various stirring rates)

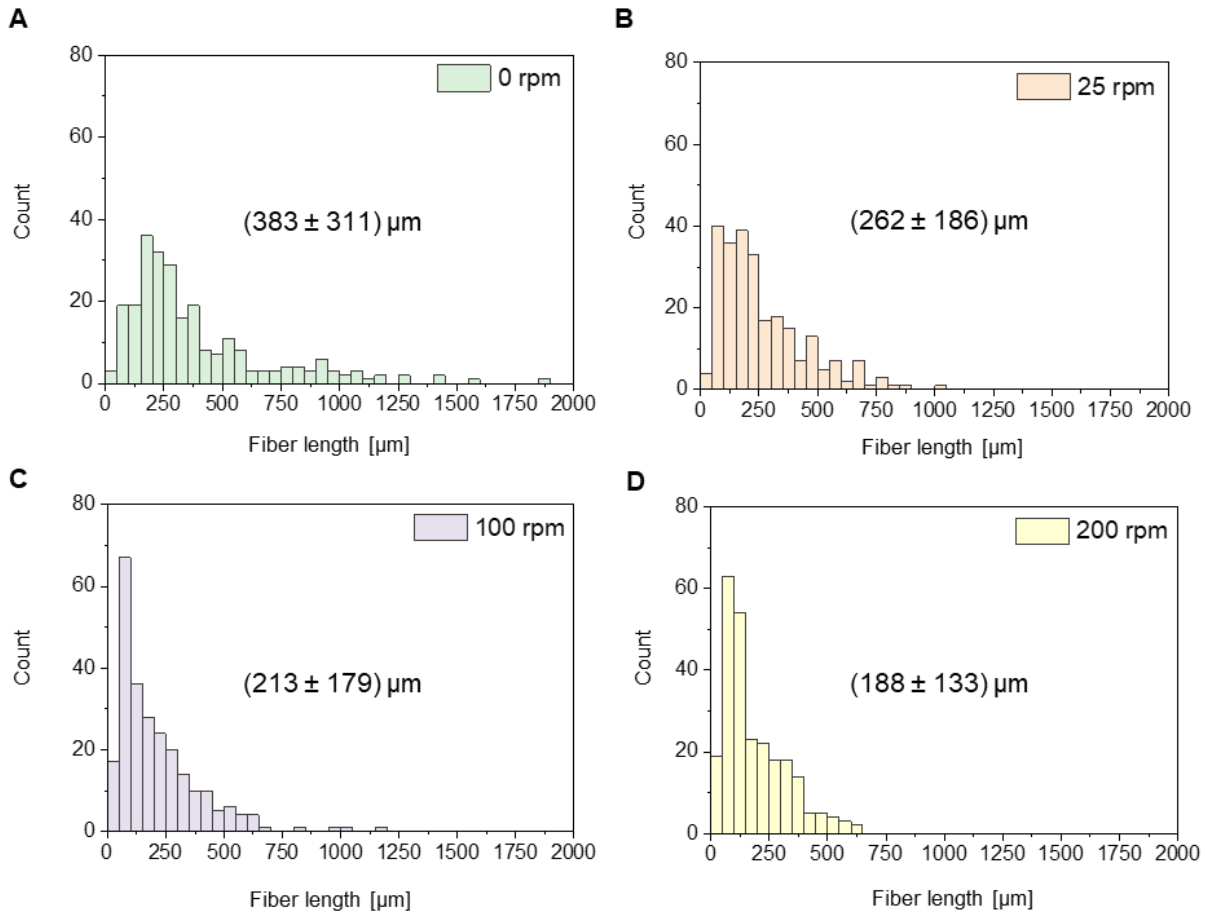


Figure 8-2. **Fiber length histograms of BTA-1 fibers** fabricated from a 0.175 wt.% solution in MEK, constant cooling rate of $0.25\text{ }^{\circ}\text{C min}^{-1}$ and different stirring rates of 0 rpm, 25 rpm, 100 rpm and 200 rpm. The histograms of the fiber length are based on 250 fibers.

Fiber diameter histograms prepared from of 0.20 wt.% BTA-1 in MEK at a cooling rate of 0.50 °C min⁻¹ (various stirring rates)

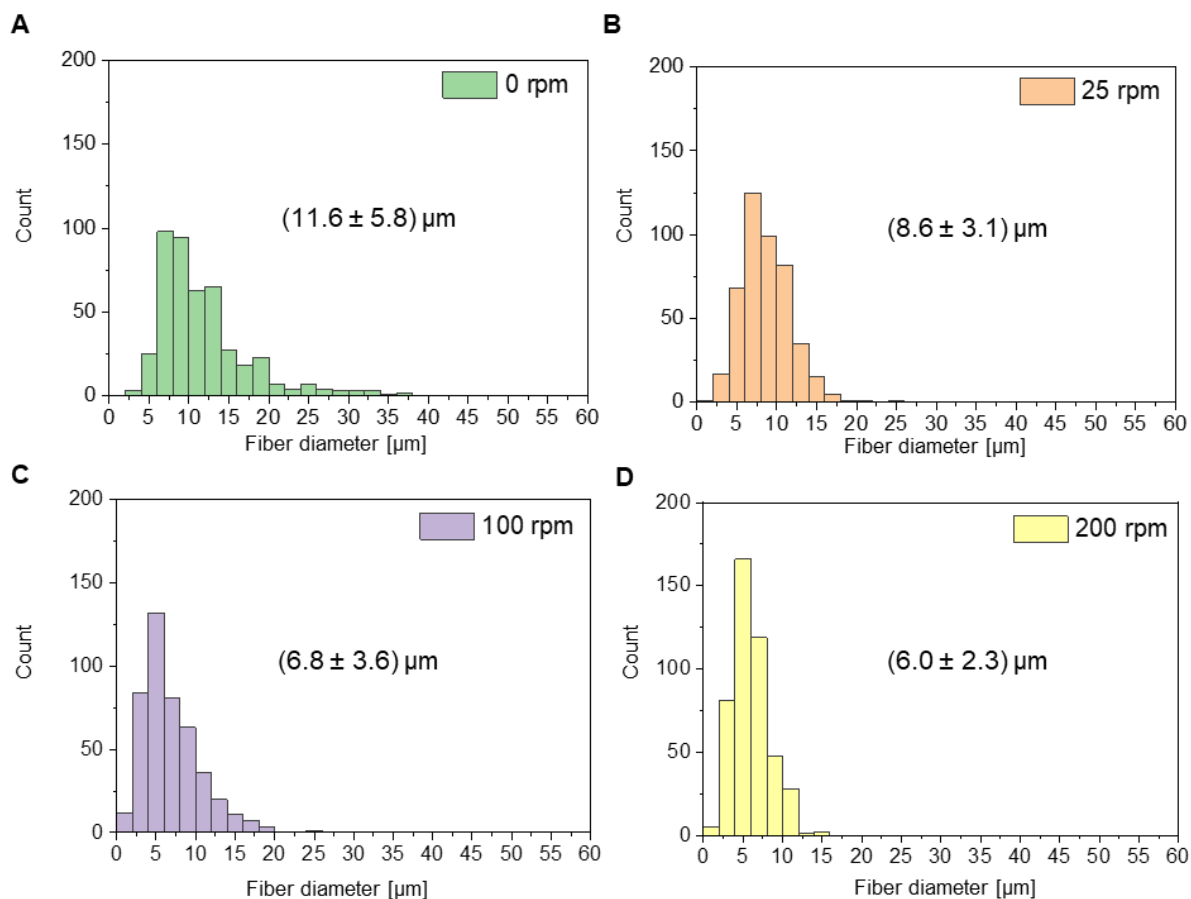


Figure 8-3. Fiber diameter histograms of BTA fibers fabricated from a 0.20 wt.% solution in MEK, constant cooling rate of 0.50 °C min⁻¹ and different stirring rates of 0 rpm, 25 rpm, 100 rpm and 200 rpm. The histograms of the fiber diameter are based on 450 fibers.

Fiber length histograms prepared from of 0.20 wt.% BTA-1 in MEK at a cooling rate of $0.50\text{ }^{\circ}\text{C min}^{-1}$ (various stirring rates)

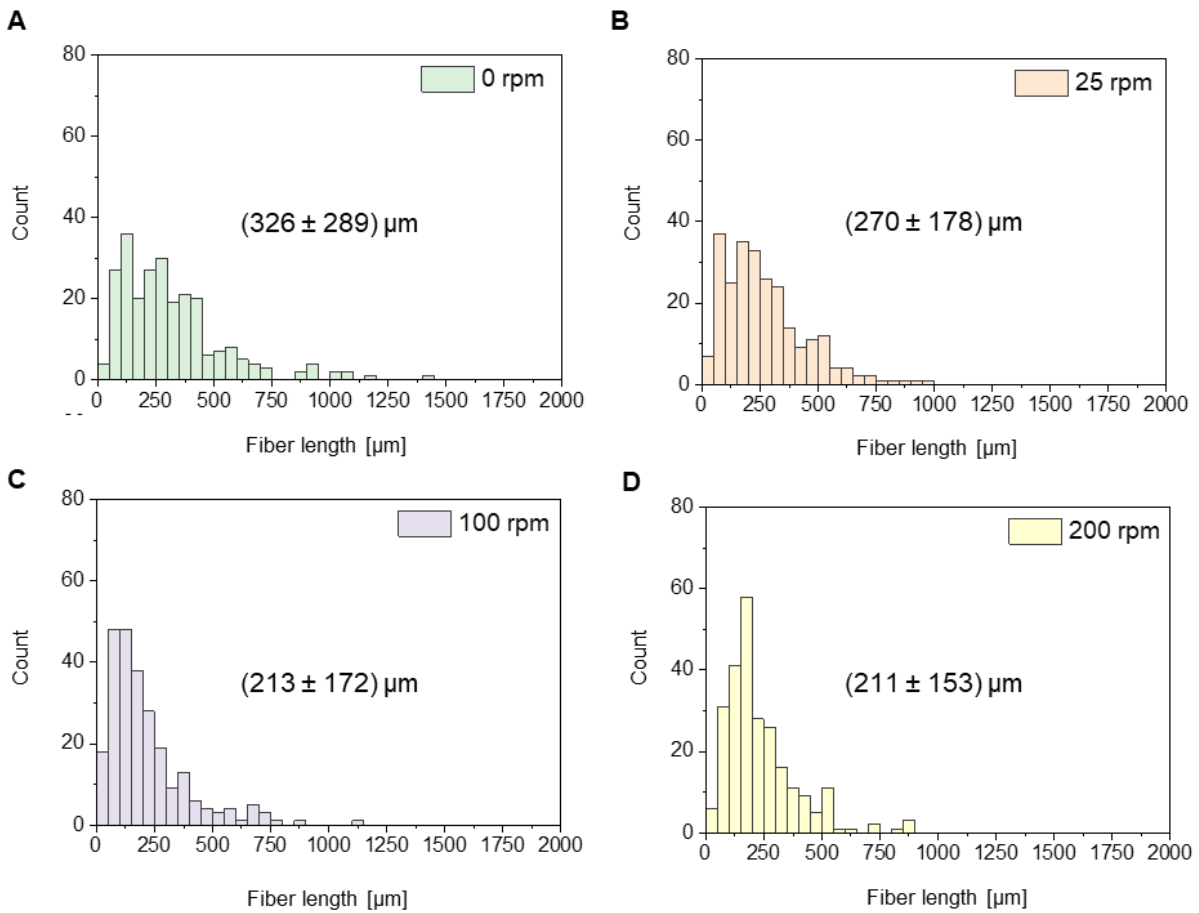


Figure 8-4. **Fiber length histograms of BTA-1 fibers** fabricated from a 0.20 wt.% solution in MEK, constant cooling rate of $0.50\text{ }^{\circ}\text{C min}^{-1}$ and different stirring rates of 0 rpm, 25 rpm, 100 rpm and 200 rpm. The histograms of the fiber length are based on 250 fibers.

Fiber diameter histograms prepared from of 0.25 wt.% BTA-1 in MEK at a cooling rate of $0.50\text{ }^{\circ}\text{C min}^{-1}$ (various stirring rates)

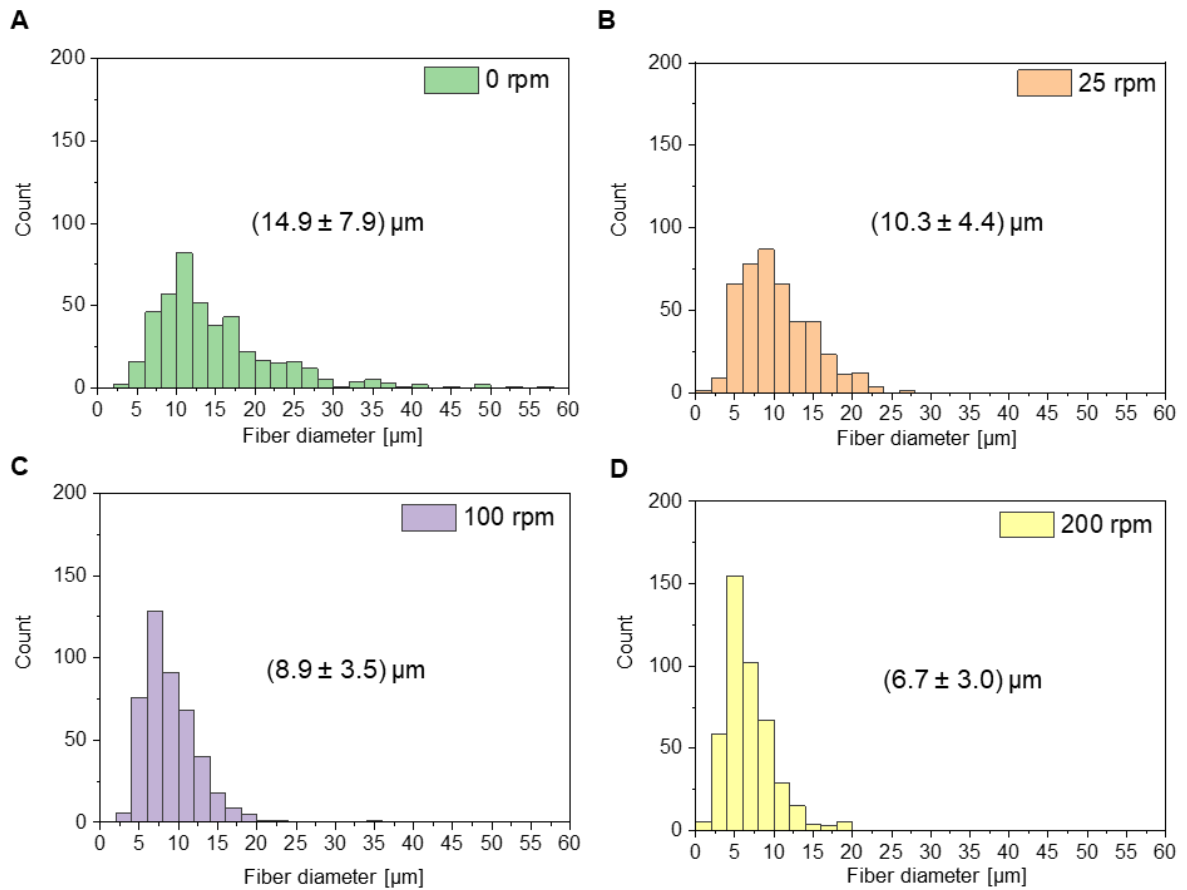


Figure 8-5. Fiber diameter histograms of BTA fibers fabricated from a 0.25 wt.% solution in MEK, constant cooling rate of $0.50\text{ }^{\circ}\text{C min}^{-1}$ and different stirring rates of 0 rpm, 25 rpm, 100 rpm and 200 rpm. The histograms of the fiber diameter are based on 450 fibers.

Fiber Length histograms prepared from of 0.25 wt.% BTA-1 in MEK at a cooling rate of $0.50\text{ }^{\circ}\text{C min}^{-1}$ (various stirring rates)

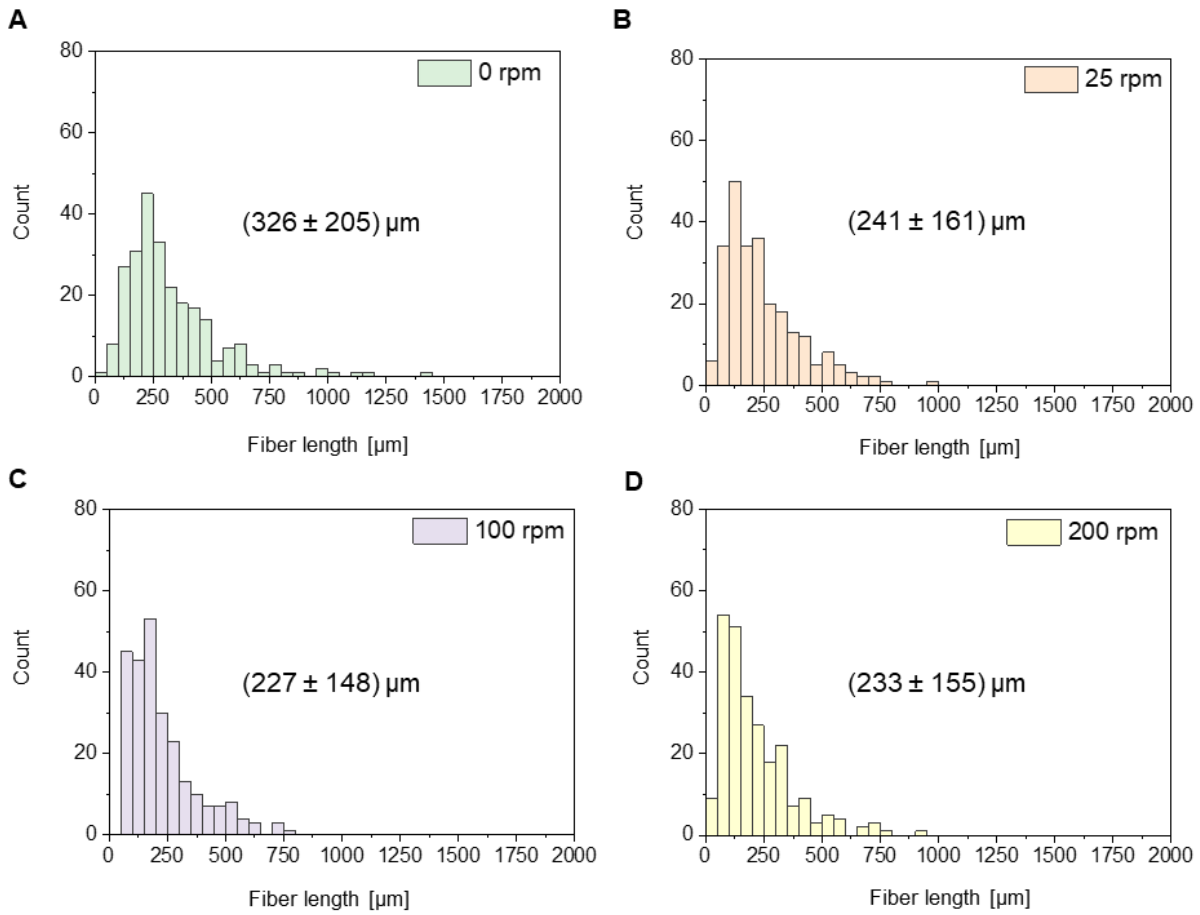


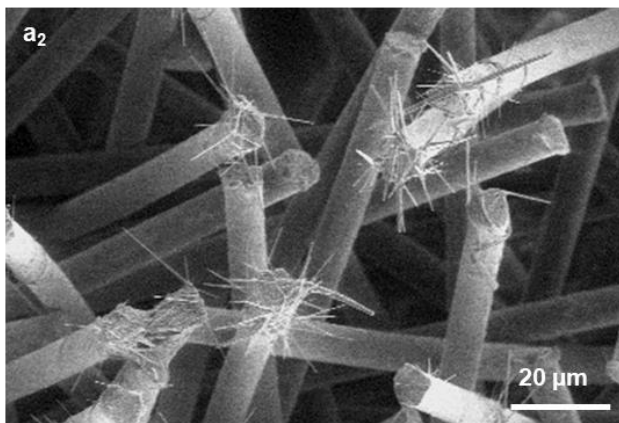
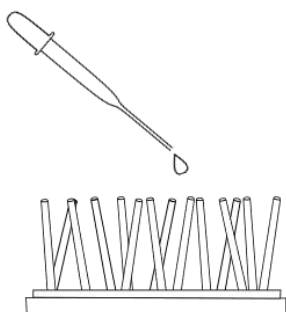
Figure 8-6. **Fiber length histograms of BTA-1 fibers** fabricated from a 0.25 wt.% solution in MEK, constant cooling rate of $0.50\text{ }^{\circ}\text{C min}^{-1}$ and different stirring rates of 0 rpm, 25 rpm, 100 rpm and 200 rpm. The histograms of the fiber length are based on 250 fibers.

Appendix B

Different investigated preparation methods to achieve supramolecular microstructures in polymer flocks

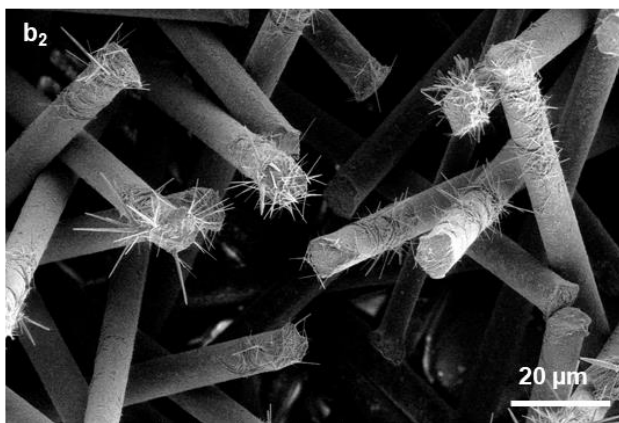
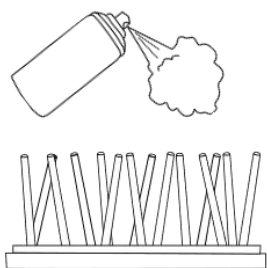
A: Drop method

a₁



B: Spray method

b₁



C: Immersion method

c₁

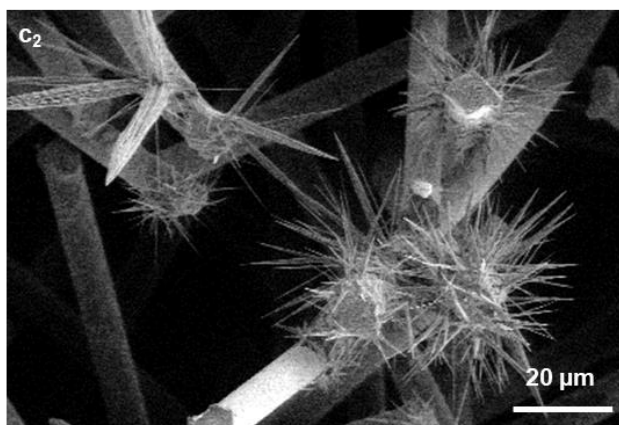
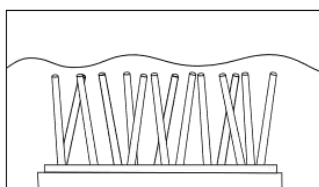


Figure 8-7. **Different preparation methods (a₁-c₁) and corresponding scanning electron microscopy images of supramolecular microstructures on PA flocks (a₂-c₂).** **A:** The BTA solution was dropped with a pipette onto the PA flock. **B:** The BTA solution was sprayed onto the PA flock. **C:** The PA flock was immersed into the BTA solution. Set of conditions: BTA solutions in 2-propanol with a concentration of 0.50 wt.% and subsequent solvent evaporation at ambient conditions.

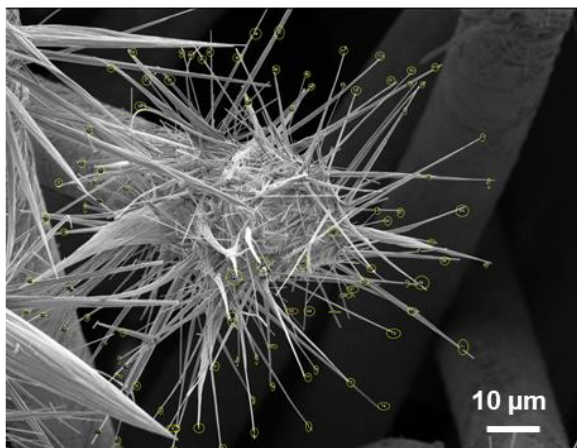
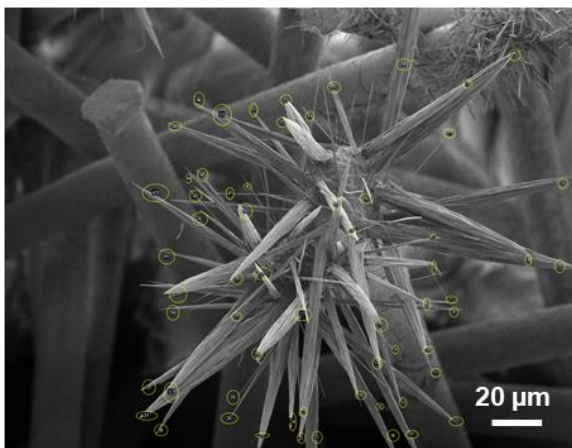
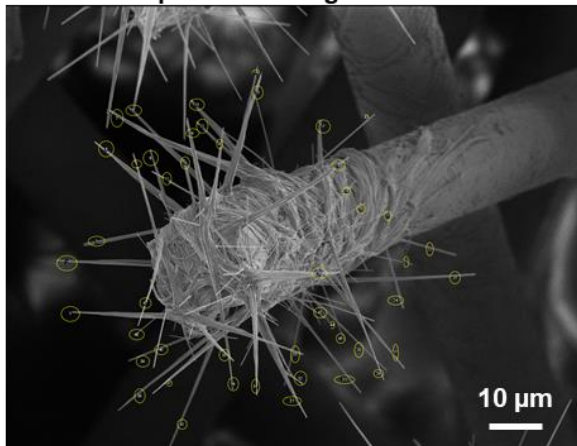
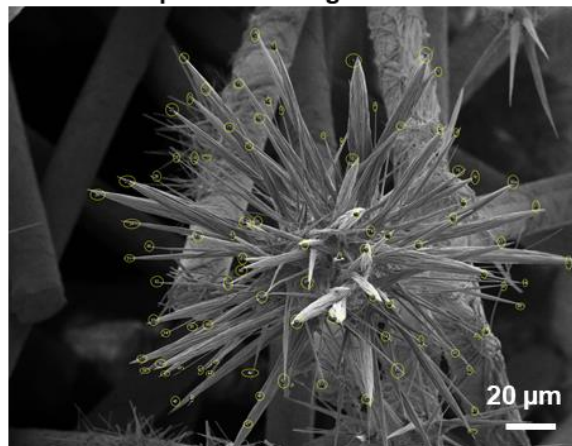
Determining the number of spines at various PA microfiber heads**A: 97 BTA spines at a single PA microfiber****B: 61 BTA spines at a single PA microfiber****C: 47 BTA spines at a single PA microfiber****D: 93 BTA spines at a single PA microfiber**

Figure 8-8. **Scanning electron microscopy images of four different PA microfibers covered with supramolecular spines. (A-D):** the individual spines were counted with the help of the software ImageJ resulting in 97 (A), 61 (B), 47 (C) and 93 (D) BTA spines at a single PA microfiber, respectively. Set of conditions: immersion into a 0.50 wt.% BTA solution in 2-propanol and subsequent drying under defined conditions (30°C in a closed chamber). Figure adapted and reproduced with permission from Ref.^[136] Copyright © 2024 The Authors. Advanced Materials Interfaces published by Wiley-VCH GmbH.

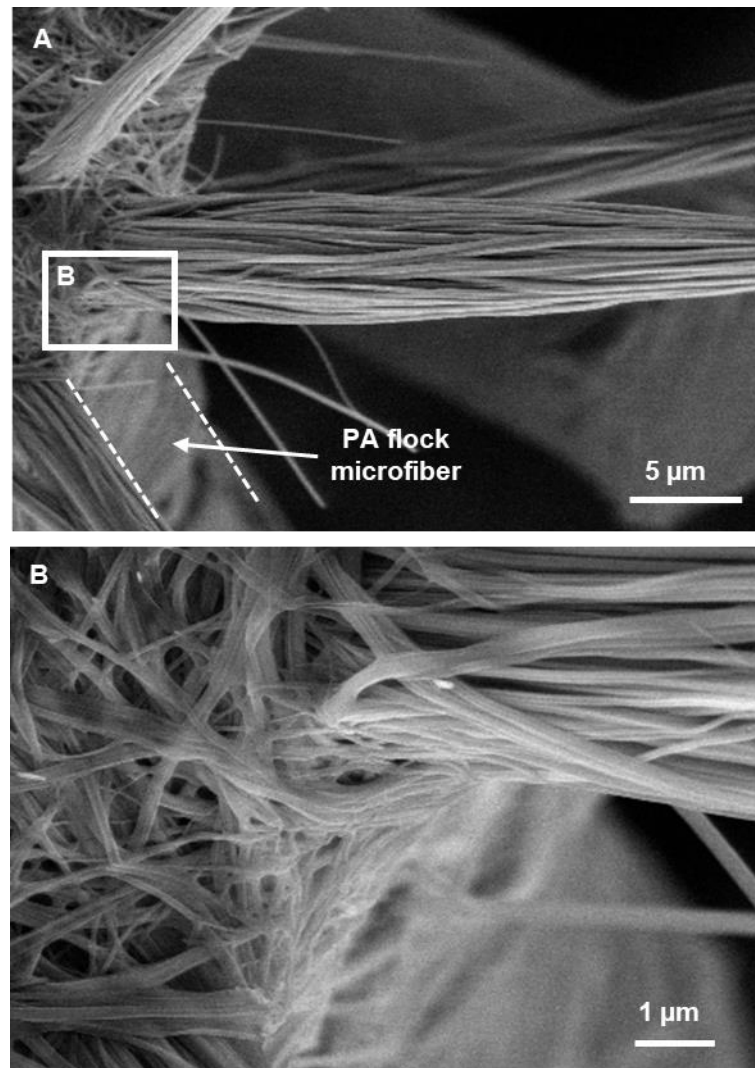
Magnification of the transition between supramolecular spines and a PA microfiber head

Figure 8-9. Scanning electron microscopy images at different magnifications of the transition between the highly orientated supramolecular spines and a PA microfiber head. A and B: At the transition, the fibrils are randomly orientated and wrapped around the PA microfiber head and then spread into several high orientated supramolecular spines. Figure adapted and reproduced with permission from Ref.^[136] Copyright © 2024 The Authors. Advanced Materials Interfaces published by Wiley-VCH GmbH.

Breaking points of supramolecular spines from the PA flocks

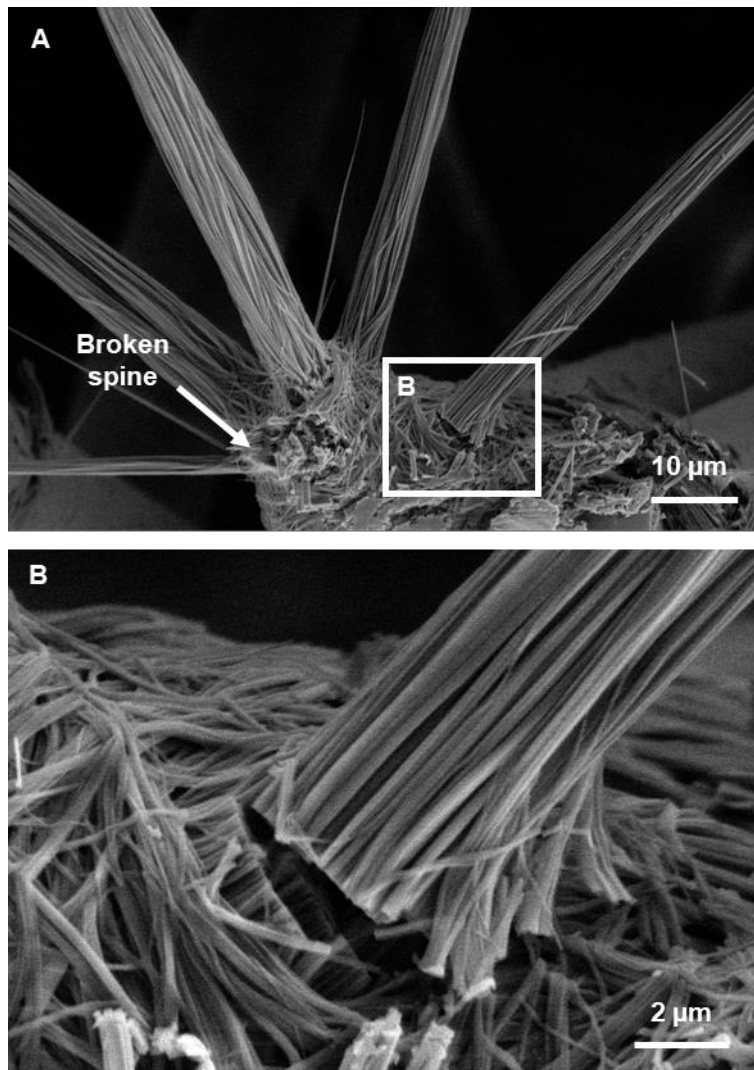


Figure 8-10. **Scanning electron microscopy images of PA microfibers head with broken or partially broken BTA spines.** The location where a spine used to be is indicated by the arrow. **A:** overview of the sample and **B:** magnification of the partially broken spine.

Cross-section of a close to the base detached supramolecular spine

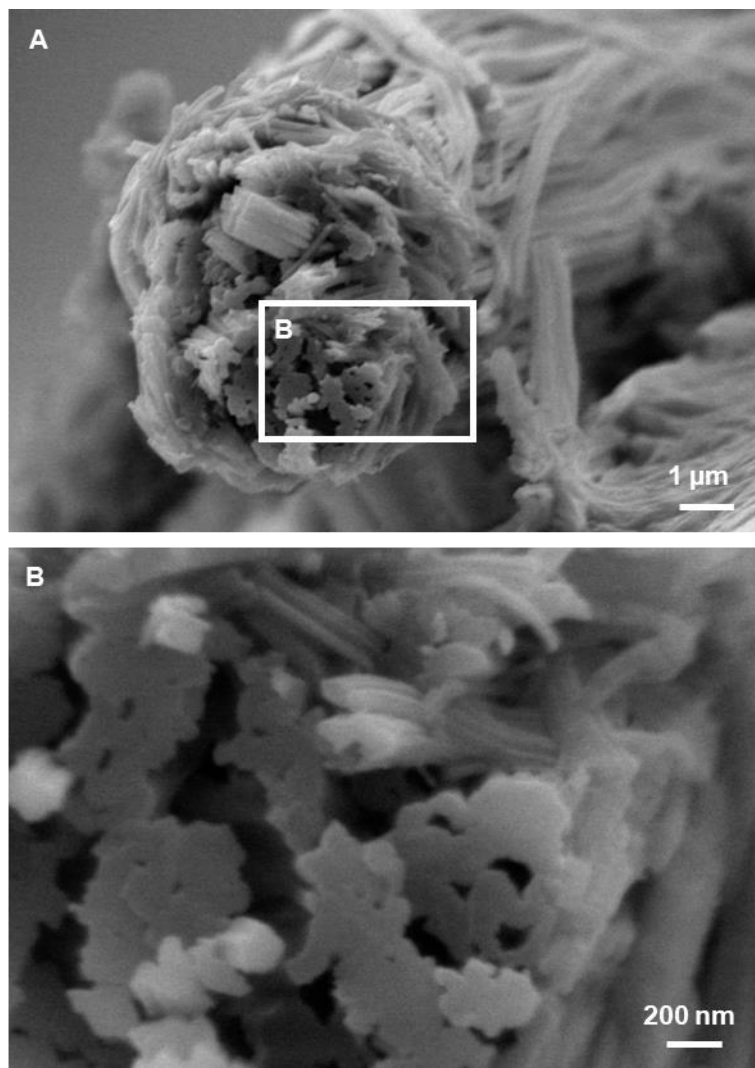


Figure 8-11. **Scanning electron microscopy images of a cross-section from an BTA spine. A:** The cross-section shows the fibrillar self-assembly and orientated alignment of the supramolecular fibrils. **B:** magnification of the white box.

Appendix C

Category A: BTA derivatives with cyclohexyl side groups

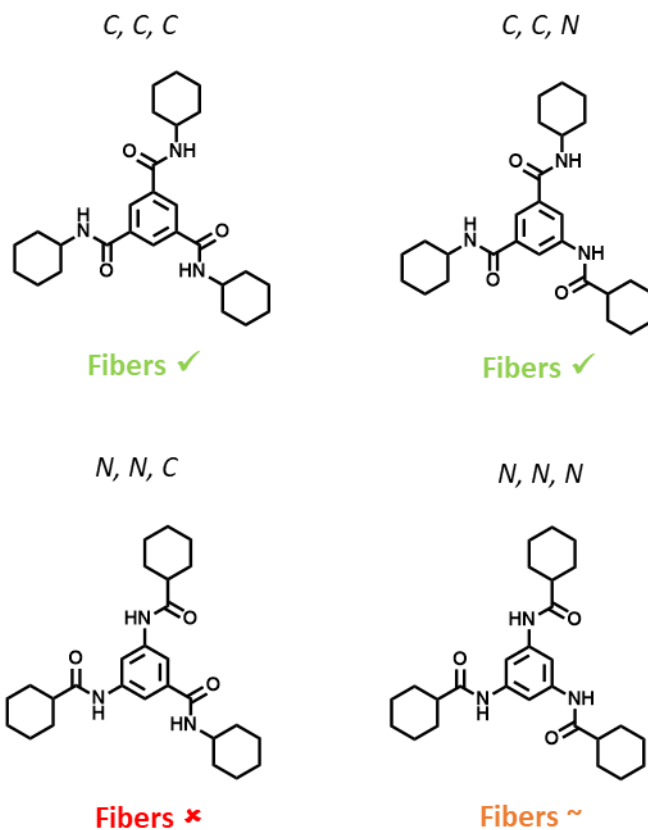


Figure 8-12. **Category A: Selected BTA derivatives with cyclohexyl BTA side groups that were investigated for fiber formation upon solvent evaporation from DMF.** Chemical structures with corresponding indication of the amide connectivity (C for C-centered and N for N-centered at the benzene core). Further declaration: fiber formation was obtained (**Fibers ✓**), the BTA is soluble in DMF, however, no fiber formation upon solvent evaporation was found (**Fibers ✗**) and the selected BTA is soluble in DMF and fiber formation was obtained, however, fibers do not exhibit the required dimensions (**Fibers ~**).

Category B: BTA derivatives with tert-butyl side groups

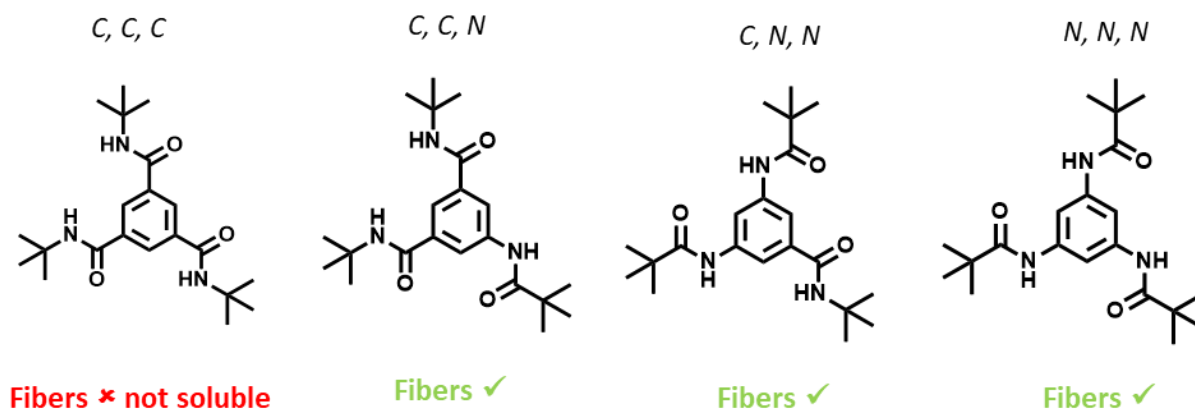


Figure 8-13. **Category B: Selected BTA derivatives with tert-butyl side groups that were investigated for fiber formation upon solvent evaporation from DMF.** Chemical structures with corresponding indication of the amide connectivity (C for C-centered and N for N-centered at the benzene core). Further declaration: BTA is not soluble in DMF (**Fibers ✗ not soluble**) and fiber formation was obtained (**Fibers ✓**).

Category C: BTA derivatives with different (branched and linear) aliphatic side groups

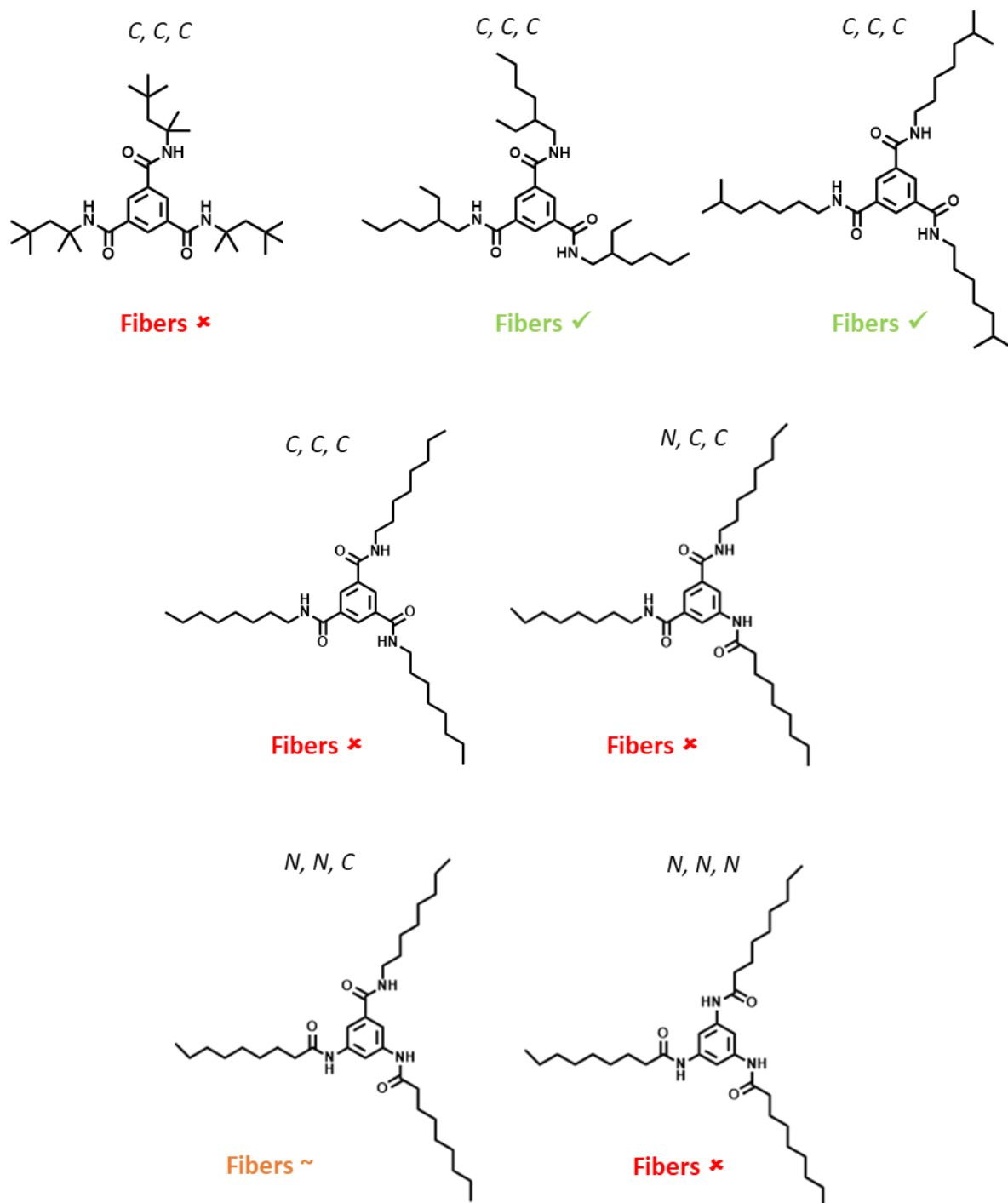


Figure 8-14. **Category C: Selected BTA derivatives with different aliphatic (branched and linear) side groups that were investigated for fiber formation upon solvent evaporation from DMF.** Chemical structures with corresponding indication of the amide connectivity (C for C-centered and N for N-centered at the benzene core). Further declaration: BTA is soluble in DMF, however, no fiber formation upon solvent evaporation was found (**Fibers ✘**), fiber formation was obtained (**Fibers ✓**) and the selected BTA is soluble in DMF and fiber formation was obtained, however, fibers do not exhibit the required dimensions (**Fibers ~**).

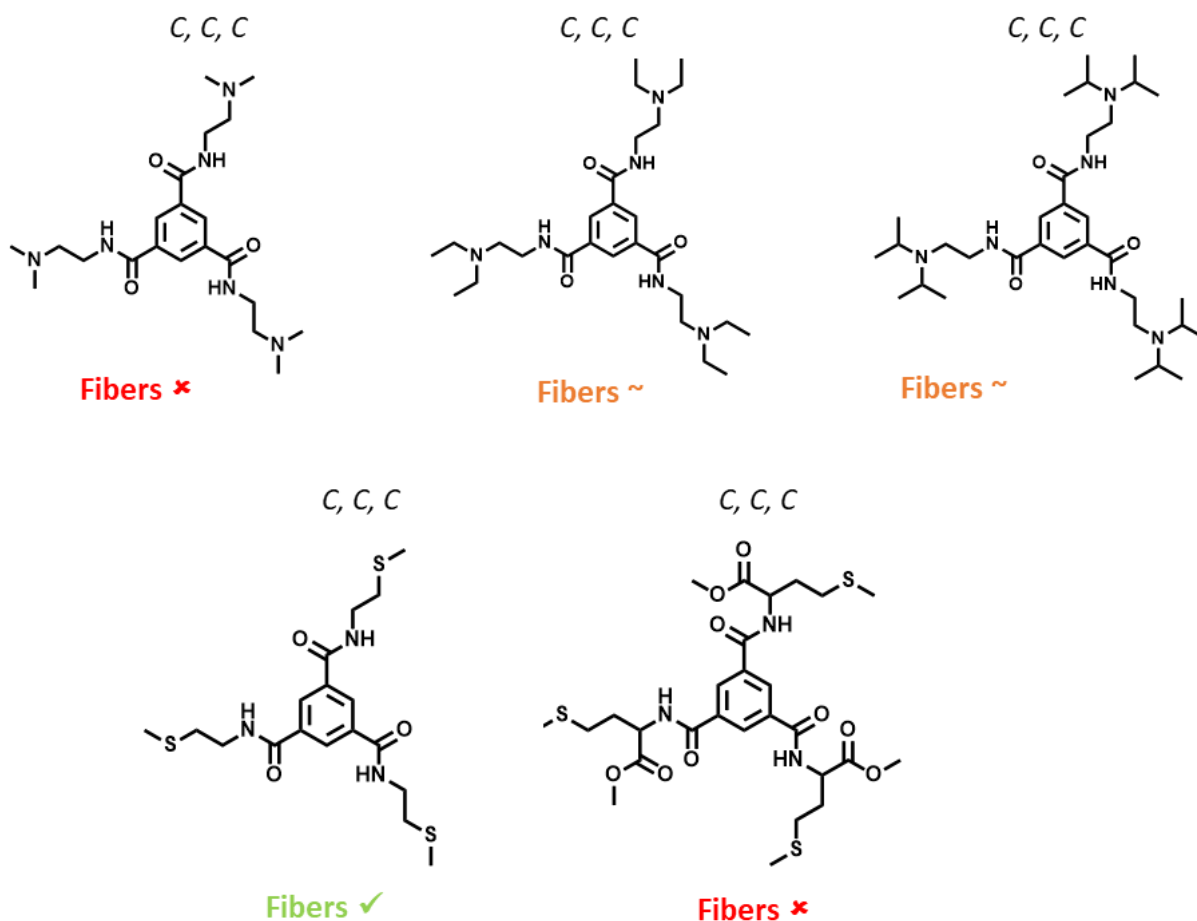
Category D: BTA derivatives with additional functional heteroatoms in the periphery


Figure 8-15. **Category D: Selected BTA derivatives with additional functional heteroatoms in the periphery were investigated for fiber formation upon solvent evaporation from DMF.** Chemical structures with corresponding indication of the amide connectivity (C for C-centered and N for N-centered at the benzene core). Further declaration: BTA is soluble in DMF, however, no fiber formation upon solvent evaporation was found (**Fibers ✘**), the selected BTA is soluble in DMF and fiber formation was obtained, however, fibers do not exhibit the required dimensions or stability (**Fibers ~**) and fiber formation was obtained (**Fibers ✓**).

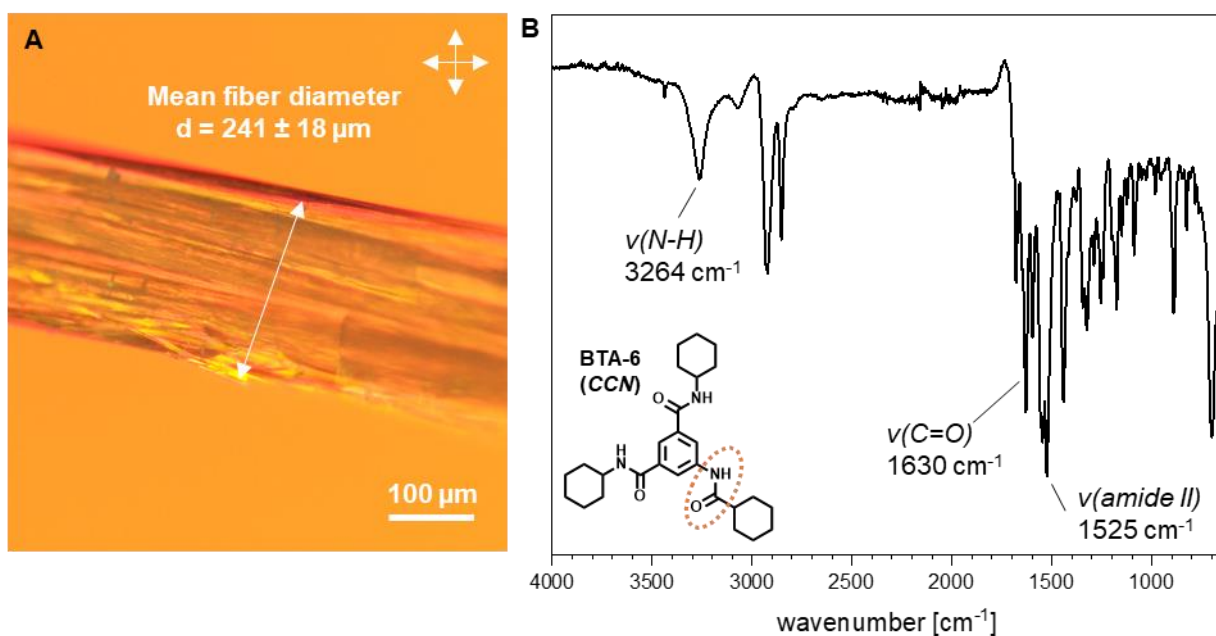
Polarized optical microscope images and corresponding IR spectra

Figure 8-16. **Polarized optical microscope image and corresponding IR spectrum of BTA-6 fibers.** **A:** Fibers of BTA-6 with indication of the mean fiber diameter and **B:** IR spectrum of self-assembled BTA-6 fibers with indications of the NH stretch $\nu(\text{N-H})$, the C=O stretch $\nu(\text{C=O})$ and the amide II band $\nu(\text{amide II})$.

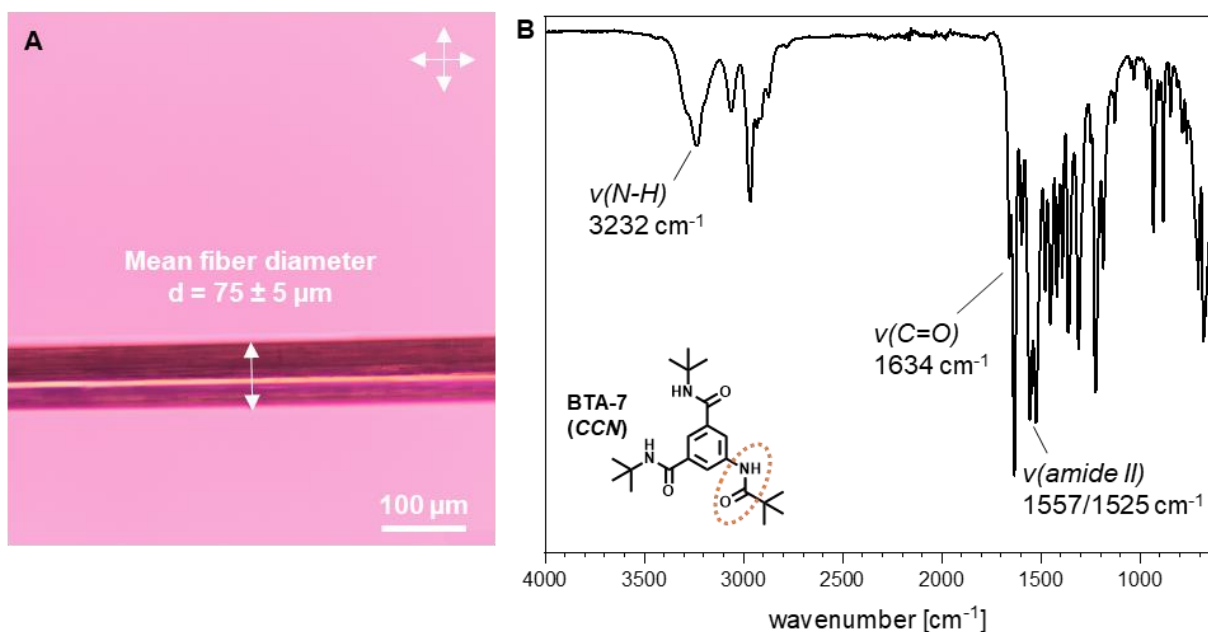


Figure 8-17. **Polarized optical microscope image and corresponding IR spectrum of BTA-7 fibers.** **A:** Fibers of BTA-7 with indication of the mean fiber diameter and **B:** IR spectrum of self-assembled BTA-7 fibers with indications of the NH stretch $\nu(\text{N-H})$, the C=O stretch $\nu(\text{C=O})$ and the amide II band $\nu(\text{amide II})$.

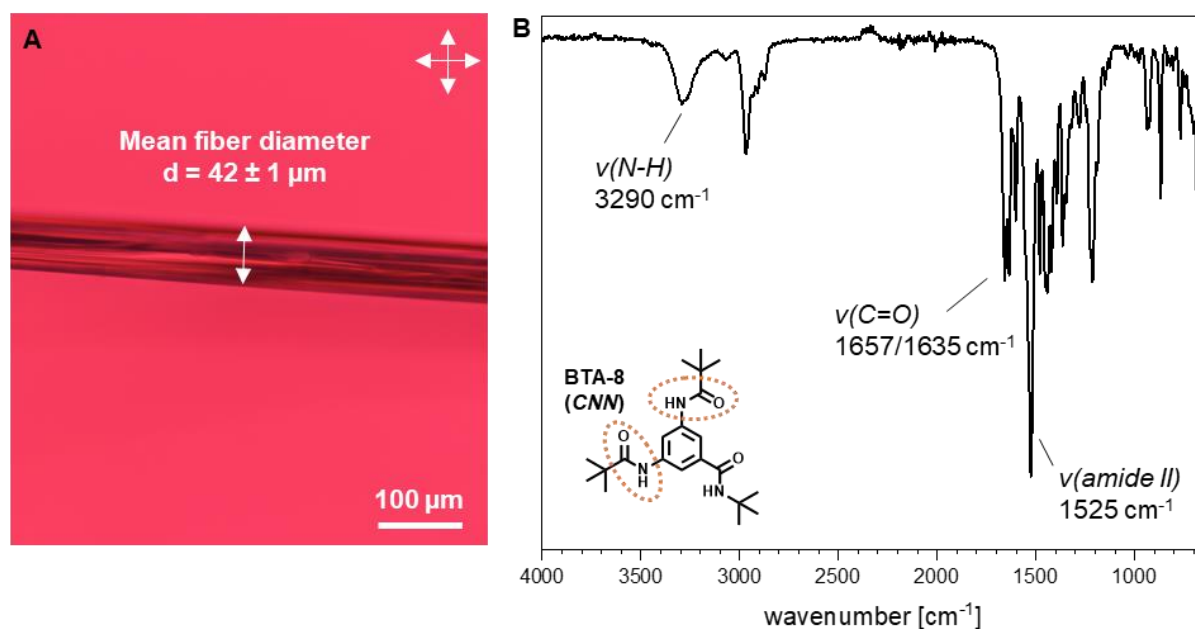


Figure 8-18. **Polarized optical microscope image and corresponding IR spectrum of BTA-8 fibers.** **A:** Fibers of BTA-8 with indication of the mean fiber diameter and **B:** IR spectrum of self-assembled BTA-8 fibers with indications of the NH stretch $\nu(\text{N-H})$, the C=O stretch $\nu(\text{C=O})$ and the amide II band $\nu(\text{amide II})$.

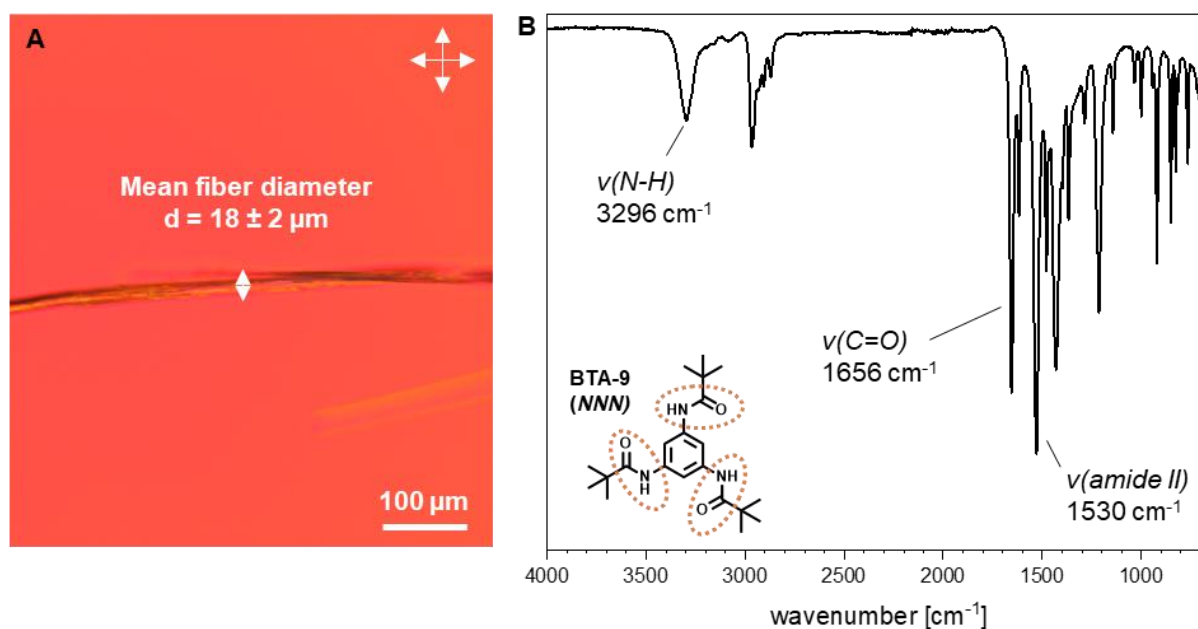


Figure 8-19. **Polarized optical microscope image and corresponding IR spectrum of BTA-9 fibers.** **A:** Fibers of BTA-9 with indication of the mean fiber diameter and **B:** IR spectrum of self-assembled BTA-9 fibers with indications of the NH stretch $\nu(\text{N-H})$, the C=O stretch $\nu(\text{C=O})$ and the amide II band $\nu(\text{amide II})$.

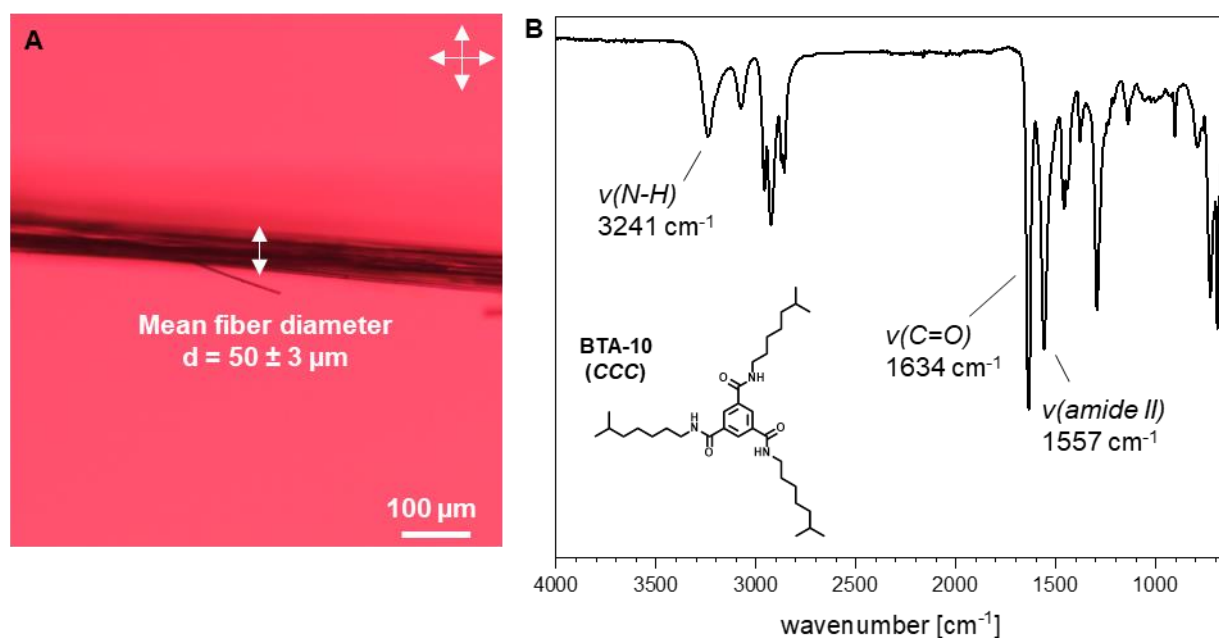


Figure 8-20. **Polarized optical microscope image and corresponding IR spectrum of BTA-10 fibers.** **A:** Fibers of BTA-10 with indication of the mean fiber diameter and **B:** IR spectrum of self-assembled BTA-10 fibers with indications of the NH stretch $\nu(\text{N-H})$, the C=O stretch $\nu(\text{C=O})$ and the amide II band $\nu(\text{amide II})$.

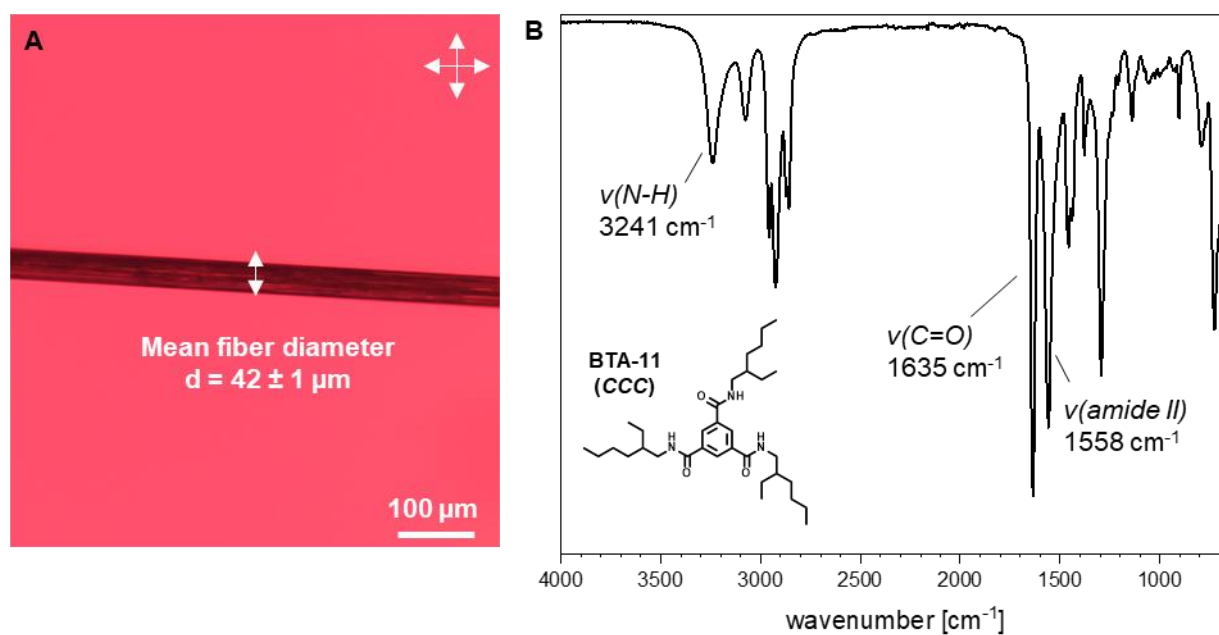


Figure 8-21. **Polarized optical microscope image and corresponding IR spectrum of BTA-11 fibers.** **A:** Fibers of BTA-11 with indication of the mean fiber diameter and **B:** IR spectrum of self-assembled BTA-11 fibers with indications of the NH stretch $\nu(\text{N-H})$, the C=O stretch $\nu(\text{C=O})$ and the amide II band $\nu(\text{amide II})$.

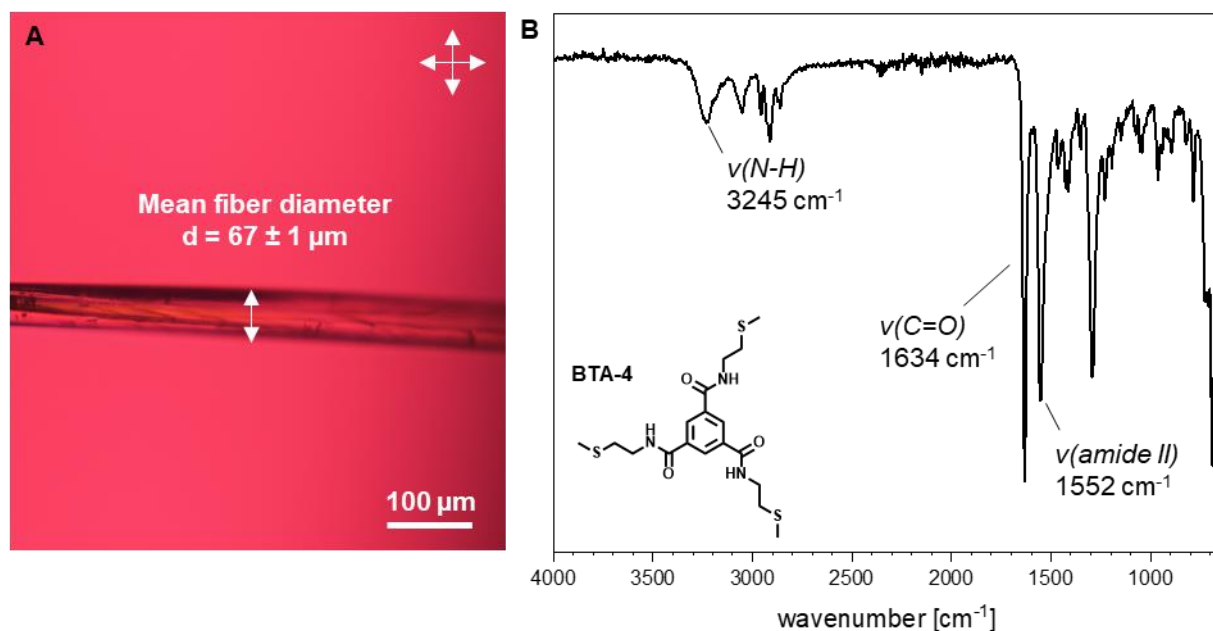


Figure 8-22. **Polarized optical microscope image and corresponding IR spectrum of BTA-4 fibers.** **A:** Fibers of BTA-4 with indication of the mean fiber diameter and **B:** IR spectrum of self-assembled BTA-4 fibers with indications of the NH stretch $\nu(\text{N-H})$, the C=O stretch $\nu(\text{C=O})$ and the amide II band $\nu(\text{amide II})$.

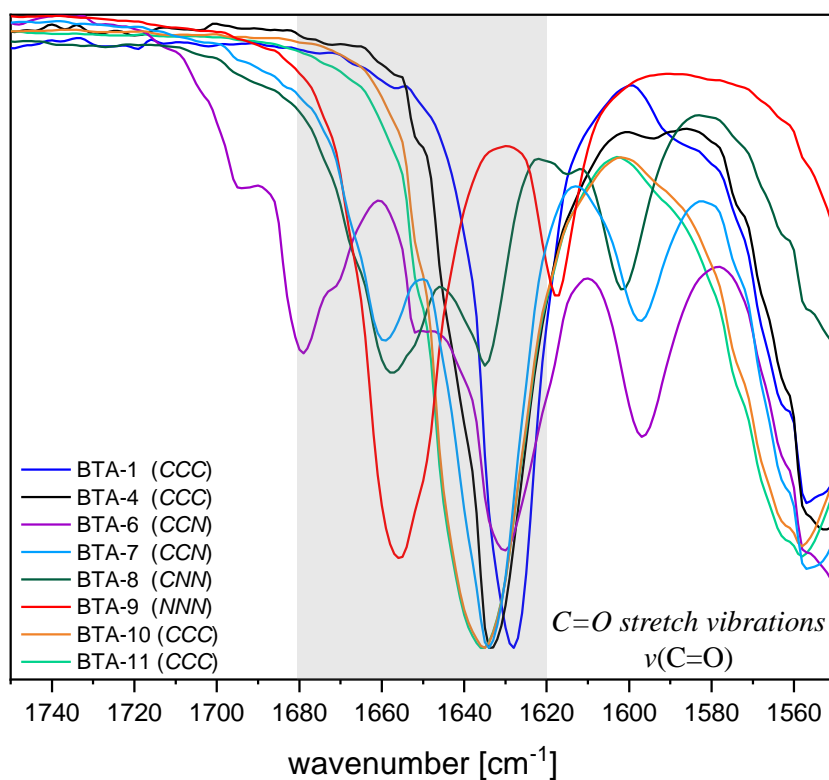


Figure 8-23. **IR-spectra section of the C=O stretch vibrations $\nu(\text{C=O})$ for the self-assembled BTAs from DMF.** The grey area (here $1680 - 1620 \text{ cm}^{-1}$)^[191,192] indicates the region for the typical $\nu(\text{C=O})$ vibrations.

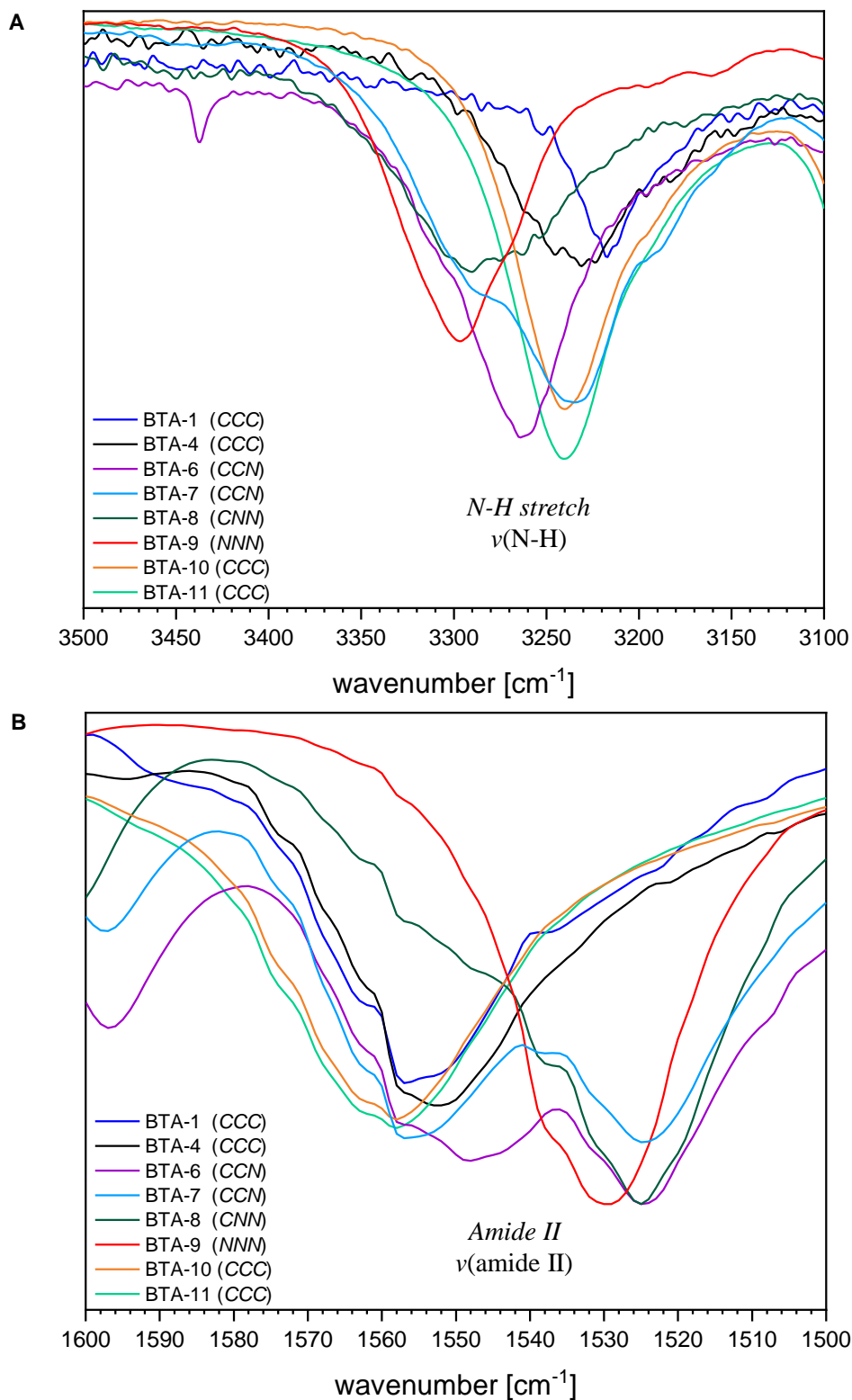


Figure 8-24. IR-spectra sections $\nu(\text{N-H})$ and $\nu(\text{amide II})$ for the self-assembled BTAs from DMF. **A:** Section of the N-H stretch vibrations $\nu(\text{N-H})$. **B:** Section of the amide II vibrations $\nu(\text{amide II})$.

9 References

- [1] J.-M. Lehn. Supramolecular Chemistry—Scope and Perspectives Molecules, Supermolecules, and Molecular Devices (Nobel Lecture), *Angew. Chem. Int. Ed. Engl.* **1988**, 27, 89.
- [2] J.-M. Lehn. Toward Self-Organization and Complex Matter, *Science* **2002**, 295, 2400.
- [3] J.-M. Lehn, *Supramolecular Chemistry: Concepts and Perspectives*, VCH Verlagsgesellschaft mbH, Weinheim **1995**.
- [4] A. C. Mendes, E. T. Baran, R. L. Reis and H. S. Azevedo. Self-assembly in nature: using the principles of nature to create complex nanobiomaterials, *WIREs Nanomed. Nanobiotechnol.* **2013**, 5, 582.
- [5] A. J. Savyasachi, O. Kotova, S. Shanmugaraju, S. J. Bradberry, G. M. Ó'Máille, T. Gunnlaugsson. Supramolecular Chemistry: A Toolkit for Soft Functional Materials and Organic Particles, *Chem.* **2017**, 3, 764.
- [6] J. W. Steed, J. L. Atwood, *Supramolecular chemistry*, John Wiley & Sons, Ltd., Chichester **2009**.
- [7] E. Krieg, H. Weissman, E. Shirman, E. Shimoni, B. Rybtchinski. A recyclable supramolecular membrane for size-selective separation of nanoparticles, *Nat. Nanotechnol.* **2011**, 6, 141.
- [8] S. Sengupta, D. Ebeling, S. Patwardhan, X. Zhang, H. von Berlepsch, C. Böttcher, V. Stepanenko, S. Uemura, C. Hentschel, H. Fuchs, F. C. Grozema, L. D. A. Siebbeles, A. R. Holzwarth, L. Chi and F. Würthner. Biosupramolecular Nanowires from Chlorophyll Dyes with Exceptional Charge-Transport Properties, *Angew. Chem. Int. Ed.* **2012**, 51, 6378.
- [9] K. Liu Y. Kang Z. Wang and X. Zhang. 25th Anniversary Article: Reversible and Adaptive Functional Supramolecular Materials: “Noncovalent Interaction” Matters, *Adv. Mater.* **2013**.
- [10] M. Blomenhofer, S. Ganzleben, D. Hanft, H.-W. Schmidt, M. Kristiansen, P. Smith, K. Stoll, D. Mäder, K. Hoffmann. “Designer” Nucleating Agents for Polypropylene, *Macromolecules* **2005**, 38, 3688.
- [11] C. Wang, Z. Wang, X. Zhang. Amphiphilic Building Blocks for Self-Assembly: From Amphiphiles to Supra-amphiphiles, *Acc. Chem. Res.* **2012**, 45, 608.
- [12] J. D. Watson and F. H. C. Crick. A structure for deoxyribose nucleic acid, *Nature* **1953**, 171, 737.

- [13] L. A. Pray. Discovery of DNA Structure and Function: Watson and Crick, *Nature Education* **2008**, *1*, 100.
- [14] F. J. Martin-Martinez, K. Jin, D. López Barreiro, M. J. Buehler. The Rise of Hierarchical Nanostructured Materials from Renewable Sources: Learning from Nature, *ACS nano* **2018**, *12*, 7425.
- [15] P. Fratzl and R. Weinkamer. Nature's hierarchical materials, *Prog. Mater. Sci* **2007**, *52*, 1263.
- [16] K. A. DeRocher, P. J. M. Smeets, B. H. Goodge, M. J. Zachman, P. V. Balachandran, L. Stegbauer, M. J. Cohen, L. M. Lyle, J. M. Rondinelli, L. F. Kourkoutis, D. Joester. Chemical gradients in human enamel crystallites, *Nature* **2020**, 583, 66.
- [17] A. Gautieri, S. Vesentini, A. Redaelli, M. J. Buehler. Hierarchical Structure and Nanomechanics of Collagen Microfibrils from the Atomistic Scale Up, *Nano Lett.* **2011**, *11*, 757.
- [18] A. Gautieri, S. Vesentini, A. Redaelli, M. J. Buehler. Hierarchical nanomechanics of collagen microfibrils, *Nat. Prec.* **2010**.
- [19] P. J. Russell, *iGenetics: A Molecular Approach*, Pearson Education Limited, Edinburgh Gate, Harlow **2014**.
- [20] C. Yuan, W. Ji, R. Xing, J. Li, E. Gazit, X. Yan. Hierarchically oriented organization in supramolecular peptide crystals, *Nat. Rev. Chem.* **2019**, *3*, 567.
- [21] R. V. Ulijn, A. M. Smith. Designing peptide based nanomaterials, *Chem. Soc. Rev.* **2008**, *37*, 664.
- [22] P. Zhu, X. Yan, Y. Su, A. Yang, J. Li. Solvent-Induced Structural Transition of Self-Assembled Dipeptide: From Organogels to Microcrystals, *Chem. Eur. J.* **2010**, *16*, 3176.
- [23] E. G. M. Reches. Casting Metal Nanowires Within Discrete Self-Assembled Peptide Nanotubes, *Science* **2003**, *300*, 625.
- [24] Q. Li, Y. Jia, L. Dai, Y. Yang, J. Li. Controlled Rod Nanostructured Assembly of Diphenylalanine and Their Optical Waveguide Properties, *ACS nano* **2015**, *9*, 2689.
- [25] J. Kim, T. H. Han, Y. Kim, J. S. Park, J. Choi, D. G. Churchill, S. O. Kim, H. Ihee. Role of Water in Directing Diphenylalanine Assembly into Nanotubes and Nanowires, *Adv. Mater* **2010**, *22*, 583.
- [26] X. Yan J. Li H. Möhwald. Self-Assembly of Hexagonal Peptide Microtubes and Their Optical Waveguiding, *Adv. Mater.* **2011**, *23*, 2796.
- [27] N. K. Kildahl. Bond Energy Data Summarized, *J. Chem. Educ.* **1995**, *72*, 423.

- [28] D. B. Varshey, J. R. G. Sander, T. Friščić, L.R. MacGillivray, *Supramolecular Interactions published in Supramolecular Chemistry: From Molecules to Nanomaterials*, John Wiley & Sons, Ltd **2012**.
- [29] J. Wei, F. Pan, H. Ping, K. Yang, Y. Wang, Q. Wang, Z. Fu. Bioinspired Additive Manufacturing of Hierarchical Materials: From Biostructures to Functions, *Research* **2023**, *6*, 0164.
- [30] X. Zhou, Q. Jin, L. Zhang, Z. Shen, L. Jiang, M. Liu. Self-Assembly of Hierarchical Chiral Nanostructures Based on Metal-Benzimidazole Interactions: Chiral Nanofibers, Nanotubes, and Microtubular Flowers, *Small* **2016**, *12*, 4743.
- [31] S. Li, R. Liu, D. Bekana, Y. Lai, J. Liu. Self-assembly of supramolecular nanotubes/microtubes from 3,5-dimethyl-4-iodopyrazole for plasmonic nanoparticle organization, *Nanoscale* **2018**, *10*, 20804.
- [32] K. Kong, S. Zhang, Y. Chu, Y. Hu, F. Yu, H. Ye, H. Ding, J. Hua. A self-assembled perylene diimide nanobelt for efficient visible-light-driven photocatalytic H₂ evolution, *Chem. Commun.* **2019**, *55*, 8090.
- [33] J. J. van Gorp, J. A. J. M. Vekemans, E. W. Meijer. C₃-Symmetrical Supramolecular Architectures: Fibers and Organic Gels from Discotic Trisamides and Trisureas, *J. Am. Chem. Soc.* **2002**, *124*, 14759.
- [34] Y. Harada, Y. Matsunaga. New Mesomorphic Compounds: N, N', N''-Trialkanoyl-2,4,6-trimethyl-1,3,5-benzenetriamines, *Bull. Chem. Soc. Jpn* **1988**, *61*, 2739.
- [35] Matthew P. Lightfoot, Francis S. Mair, Robin G. Pritchard and John E. Warren. New supramolecular packing motifs: p-stacked rods encased in triply-helical hydrogen bonded amide strands, *Chem. Commun.* **1999**.
- [36] L. Brunsveld, B. J. Folmer, E. W. Meijer, R. P. Sijbesma. Supramolecular polymers, *Chem. Rev.* **2001**, *101*, 4071.
- [37] S. Cantekin, T. F. A. de Greef, A. R. A. Palman. Benzene-1,3,5-tricarboxamide: a versatile ordering moiety for supramolecular, *Chem. Soc. Rev.* **2012**, *41*, 6125–6137.
- [38] A. Timme, R. Kress, R. Q. Albuquerque, H-W. Schmidt. Phase behavior and mesophase structures of 1,3,5-benzene- and 1,3,5-cyclohexanetricarboxamides: towards an understanding of the losing order at the transition into the isotropic phase, *Chemistry* **2012**, *18*, 8329.
- [39] R. Q. Albuquerque, A. Timme, R. Kress, J. Senker, H.-W. Schmidt. Theoretical investigation of macrodipoles in supramolecular columnar stackings, *Chem. Eur. J.* **2013**, *19*, 1647.

- [40] A. Sakamoto, D. Ogata, T. Shikata, O. Urakawa, K. Hanabusa. Large macro-dipoles generated in a supramolecular polymer of *N,N',N''*-tris(3,7-dimethyloctyl)benzene-1,3,5-tricarboxamide in n-decane, *Polymer* **2006**, *47*, 956.
- [41] M. P. Lightfoot, F. S. Mair, R. G. Pritchard, J. E. Warren. New supramolecular packing motifs: π -stacked rods encased in triply-helical hydrogen bonded amide strands, *Chem. Commun.* **1999**, 1945.
- [42] M. Kristiansen, P. Smith, H. Chanzy, C. Baerlocher, V. Gramlich, L. McCusker, T. Weber, P. Pattison, M. Blomenhofer, H.-W. Schmidt. Structural Aspects of 1,3,5-Benzenetrisamides—A New Family of Nucleating Agents, *Cryst. Growth Des.* **2009**, *9*, 2556.
- [43] M. Schmidt, J. J. Wittmann, R. Kress, D. Schneider, S. Steuernagel, H.-W. Schmidt, J. Senker. Crystal Structure of a Highly Efficient Clarifying Agent for Isotactic Polypropylene, *Cryst. Growth Des.* **2012**, *12*, 2543.
- [44] E. Fan, J. Yang, S. J. Geib, T. C. Stoner, M. D. Hopkins, A. D. Hamilton. Hydrogen-bonding Control of Molecular Aggregation: Self-complementary Subunits lead to Rod-shaped Structures in the Solid State, *J. Chem. Soc., Chem. Commun.* **1995**, 1251.
- [45] L. Brunsveld, A. P. H. J. Schenning, M. A. C. Broeren, H. M. Janssen, J. A. J. M. Vekemans, E. W. Meijer. Chiral Amplification in Columns of Self-Assembled *N,N',N''*-Tris((S)-3,7-dimethyloctyl)benzene-1,3,5-tricarboxamide in Dilute Solution, *Chem. Lett.* **2000**, *29*, 292.
- [46] P. J. M. Stals, M. M. J. Smulders, R. Martin-Rapfun, A. R. A. Palmans, E. W. Meijer. Asymmetrically Substituted Benzene-1,3,5-tricarboxamides: Self-Assembly and Odd–Even Effects in the Solid State and in Dilute Solution, *Chem. Eur. J.* **2009**, *15*, 2071.
- [47] D. Kluge, F. Abraham, S. Schmidt, H.-W. Schmidt, A. Fery. Nanomechanical properties of supramolecular self-assembled whiskers determined by AFM force mapping, *Langmuir* **2010**, *26*, 3020.
- [48] P. Besenius, K. P. van den Hout, H. M. H. G. Albers, T. F. A. de Greef, L. L. C. Olijve, T. M. Hermans, B. F. M. de Waal, P. H. H. Bomans, N. A. J. M. Sommerdijk, G. Portale, A. R. A. Palmans, M. H. P. van Genderen, J. A. J. M. Vekemans, and E. W. Meijer. Controlled supramolecular oligomerization of C₃-symmetrical molecules in water: the impact of hydrophobic shielding, *Chemistry* **2011**, *17*, 5193.
- [49] K. K. Bejagam, G. Fiorin, M. L. Klein, Michael, S. Balasubramanian. Supramolecular polymerization of benzene-1,3,5-tricarboxamide: a molecular dynamics simulation study, *J. Phys. Chem. B* **2014**, *118*, 5218.

- [50] C. S. Zehe, J. A. Hill, N. P. Funnell, Nicholas, K. Kreger, K. P. van der Zwan, A. L. Goodwin, H.-W. Schmidt, J. Senker. Mesoscale Polarization by Geometric Frustration in Columnar Supramolecular Crystals, *Angew. Chem. Int. Ed.* **2017**, *56*, 4432.
- [51] S. Anderson, M. O'Keeffe. Rod packings and crystal chemistry, *Acta Cryst. A* **1977**, *33*, 914.
- [52] A. Bernet, R. Q. Albuquerque, M. Behr, S. T. Hoffmann, H-W. Schmidt. Formation of a supramolecular chromophore: a spectroscopic and theoretical study, *Soft Matter* **2012**, *8*, 66.
- [53] M. Drummer, C. Liang, K. Kreger, S. Rosenfeldt, A. Greiner, H-W. Schmidt. Stable Mesoscale Nonwovens of Electrospun Polyacrylonitrile and Interpenetrating Supramolecular 1,3,5-Benzenetrisamide Fibers as Efficient Carriers for Gold Nanoparticles, *ACS Appl. Mater. Interfaces* **2021**, *13*, 34818.
- [54] A. Frank, M. Weber, C. Hils, U. Mansfeld, K. Kreger, H. Schmalz, H.-W. Schmidt. Functional Mesostructured Electrospun Polymer Nonwovens with Supramolecular Nanofibers, *Macromol. Rapid Commun.* **2022**, *43*, e2200052.
- [55] A. Jamadar, A. Das. A pH-responsive graftable supramolecular polymer with tailorable surface functionality by orthogonal halogen bonding and hydrogen bonding, *Polym. Chem.* **2020**, *11*, 385.
- [56] N. Helfricht, A. Mark, M. Behr, A. Bernet, H-W. Schmidt, G. Papastavrou. Writing with Fluid: Structuring Hydrogels with Micrometer Precision by AFM in Combination with Nanofluidics, *Small* **2017**, *13*, 1700962.
- [57] N. Raßmann, M. Weber, R. E. J. Glaß, K. Kreger, N. Helfricht, H-W. Schmidt, G. Papastavrou. Electrogelation: Controlled Fast Formation of Micrometer-Thick Films from Low-Molecular Weight Hydrogelators, *Langmuir* **2023**, *39*, 17190.
- [58] R. C. T. Howe, A. P. Smalley, A. P. M. Guttenplan, M. W. R. Doggett, M. D. Eddleston, J. C. Tan, G. O. Lloyd. A family of simple benzene 1,3,5-tricarboxamide (BTA) aromatic carboxylic acid hydrogels[†], *Chem. Commun.* **2013**, *49*, 4268-4270.
- [59] S. Lee, J.-S. Lee, C. H. Lee, Y.-S. Jung, J.-M. Kim. Nonpolymeric Thermosensitive Benzenetricarboxamides, *Langmuir* **5011**, *27*, 1560.
- [60] A. Frank, A. Bernet, K. Kreger, H.-W. Schmidt. Supramolecular microtubes based on 1,3,5-benzenetricarboxamides prepared by self-assembly upon heating, *Soft Matter* **2020**, *16*, 4564.

- [61] Y.-W. Hao, H.-Y. Wang, Y.-J. Huang, B.-R. Gao, Q.-D. Chen, L.-B. Li, H.-B. Su. Evidence of concerted inversion for the photon-induced molecular switching of azobenzene using rotation-free azobenzene derivatives, *J. Mater. Chem. C* **2013**, *1*, 5244.
- [62] Y. Matsunaga, N. Miyajima, Y. Nakayasu, S. Sakai, M. Yonenaga. Design of Novel Mesomorphic Compounds: *N,N',N''*-Trialkyl-1,3,5-benzenetricarboxamides, *Bull. Chem. Soc. Jpn* **1988**, *61*, 207.
- [63] J. Y. Chang, J. H. Baik, C. B. Lee, M. J. Han, S.-K. Hong. Liquid Crystals Obtained from Dislike Mesogenic Diacetylenes and Their Polymerization, *J. Am. Chem. Soc.* **1997**, *119*, 3197.
- [64] V. Nagarajan, V. R. Pedireddi. Gelation and Structural Transformation Study of Some 1,3,5- Benzenetricarboxamide Derivatives, *Cryst. Growth Des.* **2014**, *14*, 1895.
- [65] A. R. A. Palmans, J. A. J. M. Vekemans, H. Kooijman, A. L. Spek, E. W. Meije. Hydrogen-bonded porous solid derived from trimesic amide, *Chem. Commun* **1997**.
- [66] I. Paraschiv, M. Giesbers, B. van Lagen, F. C. Grozema, R. D. Abellon, L. D. A. Siebbeles, A. T. M. Marcelis, H. Zuilhof, E. J. R. Sudhölter. H-Bond-Stabilized Triphenylene-Based Columnar Discotic Liquid Crystals, *Chem. Mater.* **2006**, *18*, 968.
- [67] P. P. Bose, M. G. B. Drew, A. K. Das, A. Banerjee. Formation of triple helical nanofibers using self-assembling chiral benzene-1,3,5-tricarboxamides and reversal of the nanostructure's handedness using mirror image building blocks, *Chem. Commun.* **2006**.
- [68] B. Gong, C. Zheng, Y. Yan. Structure of *N,N',N''*-tris(carboxymethyl)-1,3,5-benzenetricarboxamide trihydrate, *J. Chem. Cryst.* **1999**, *29*, 649.
- [69] P. Besenius, G. Portale, P. H. H. Bomans, H. M. Janssen, A. R. A. Palmans, and E. W. Meijer. Controlling the growth and shape of chiral supramolecular polymers in water, *PNAS* **2010**, *107*, 17888.
- [70] A. Paikar, A. Pramanik, D. Haldar. Influence of side-chain interactions on the self-assembly of discotic tricarboxyamides: a crystallographic insight, *RSC Adv.* **2015**, *5*, 31845.
- [71] K. P. van den Hout, R. Martín-Rapún, J. A. J. M. Vekemans, E. W. Meijer. Tuning the stacking properties of C₃-symmetrical molecules by modifying a dipeptide motif, *Chemistry* **2007**, *13*, 8111.
- [72] M. A. VandenBerg, J. K. Sahoo, L. Zou, W. McCarthy, M. J. Webber. Divergent Self-Assembly Pathways to Hierarchically Organized Networks of Isopeptide-Modified Discotics under Kinetic Control, *ACS nano* **2020**, *14*, 5491.

- [73] H. Cao, P. Duan, X. Zhu, J. Jiang, M. Liu. Self-assembled organic nanotubes through instant gelation and universal capacity for guest molecule encapsulation, *Chem. Eur. J.* **2012**, *18*, 5546.
- [74] F. Abraham, H.-W. Schmidt. 1,3,5-Benzenetrisamide based nucleating agents for poly(vinylidene fluoride), *Polymer* **2010**, *51*, 913.
- [75] S. Varela-Aramburu, G. Morgese, L. Su, S. M. C. Schoenmakers, M. Perrone, L. Leanza, C. Perego, G. M. Pavan, A. R. A. Palmans, E. W. Meijer. Exploring the Potential of Benzene-1,3,5-tricarboxamide Supramolecular Polymers as Biomaterials, *Biomacromolecules* **2020**, *21*, 4105.
- [76] C. Kulkarni, E. W. Meijer, A. R. A. Palmans. Cooperativity Scale: A Structure-Mechanism Correlation in the Self-Assembly of Benzene-1,3,5-tricarboxamides, *Acc. Chem. Res.* **2017**, *50*, 1928.
- [77] K. Hanabusa, C. Koto, M. Kimura, H. Shirai and A. Kakehi. Remarkable Viscoelasticity of Organic Solvents Containing Trialkyl-1,3,5-benzenetricarboxamides and Their Intermolecular Hydrogen Bonding, *Chem. Lett.* **1997**.
- [78] C. A. Jiménez, J. B. Belmar, L. Ortíz, P. Hidalgo, O. Fabelo, J. Pasán, C. Ruiz-Pérez. Influence of the Aliphatic Wrapping in the Crystal Structure of Benzene Tricarboxamide Supramolecular Polymers, *Cryst. Growth Des.* **2009**, *9*, 4987.
- [79] Y. Matsunaga, Y. Nakayasu, S. Sakai, M Yonenaga. Liquid Crystal Phases Exhibited by *N,N,N'*-Trialkyl-1,3,5-Benzenetricarboxamides, *Mol. Cryst. Liq. Cryst.* **1986**, *141*, 327.
- [80] X. Wu, D. Wang, M. Chen, C. Wei, S. Wei, N. Huang, L. Li, G. Zhang. Robust Ordered Bundles of Porous Helical Nanotubes Assembled from Fully Rigid Ionic Benzene-1,3,5-tricarboxamides, *Chem. Eur. J.* **2015**, *21*, 15388.
- [81] D. Krishna Kumar, D. Amiln Jose, P. Dastidar, A. Das. Nonpolymeric Hydrogelators Derived from Trimesic Amides, *Chem. Mater.* **2004**, *16*, 2332.
- [82] N. Shi, G. Yin, M. Han, Z. X. Anions bonded on the supramolecular hydrogel surface as the growth center of biominerals, *Colloids Surf. B* **2008**, *66*, 84.
- [83] N. Shi, G. Yin, H. Li, M. Han, Z. Xu. Uncommon hexagonal microtubule based gel from a simple trimesic amide, *New J. Chem.* **2008**, *22*, 2011.
- [84] Y. Ishioka, N. Minakuchi, M. Mizuhata, T. Maruyama. Supramolecular gelators based on benzenetricarboxamides for ionic liquids, *Soft Matter* **2014**, *10*, 965.
- [85] S. Kumar, S. Bera, S. K. Nandi, D. Haldar. The effect of amide bond orientation and symmetry on the self-assembly and gelation of discotic tripeptides, *Soft Matter* **2021**, *17*, 113.

- [86] Y. Yasuda, E. Iishi, H. Inada, Y. Shirota. Novel Low-molecular-weight Organic Gels N, N', N'' - Tristearyltrimesamide/Organic Solvent System, *Chem. Lett.* **1996**.
- [87] D. Kluge, J. C. Singer, J. W. Neubauer, F. Abraham, H.-W. Schmidt, A. Fery. Influence of the molecular structure and morphology of self-assembled 1,3,5-benzenetrisamide nanofibers on their mechanical properties, *Small* **2012**, 8, 2563.
- [88] J. Li, N. Huang, D. Wang, L. Xu, Y. Huang, M. Chen, J. Tao, G. Pan, Z. Wu, and L. Li. Highly ordered, ultra long nanofibrils via the hierarchical self-assembly of ionic aromatic oligoamides, *Soft Matter* **2013**, 9, 4642.
- [89] D. Kluge, J. C. Singer, B. R. Neugirg, J. W. Neubauer, H.-W. Schmidt, A. Fery. Top-down meets bottom-up: A comparison of the mechanical properties of melt electrospun and self-assembled 1,3,5-benzenetrisamide fibers, *Polymer* **2012**, 53, 5754.
- [90] D. Weiss, K. Kreger, H.-W. Schmidt. Self-Assembly of Alkoxy-Substituted 1,3,5-Benzenetrisamides Under Controlled Conditions, *Macromol. Mater. Eng.* **2017**, 302, 16000390.
- [91] C. Steinlein, K. Kreger, H.-W. Schmidt. Controlling the Aspect Ratio of Supramolecular Fibers by Ultrasonication, *Macromol. Mater. Eng.* **2019**, 304, 1900258.
- [92] Y. Huang, D. Wang, L. Xu, Y. Cong, J. Li, L. Li. Multiscale fibers via supramolecular self-assembly of a fully rigid, discotic aromatic aramid molecule, *Eur. Polym. J.* **2013**, 49, 1682.
- [93] C. M. A. Leenders, L. Albertazzi, T. Mes, M. M. E. Koenigs, A. R. A. Palmans, E. W. Meijer. Supramolecular polymerization in water harnessing both hydrophobic effects and hydrogen bond formation, *Chem. Commun.* **2013**, 49, 1963-1965.
- [94] D. Weiss, *Controlled Assembly of Supramolecular Nanofibers and Their Applications*, Dissertationsschrift, Bayreuth **2015**.
- [95] P. A. Korevaar, C. Schaefer, T. F. A. de Greef, E. W. Meijer. Controlling Chemical Self-Assembly by Solvent-Dependent Dynamics, *J. Am. Chem. Soc.* **2012**, 134, 13482.
- [96] Z. Li, H. Qu, Y. Zhai, L. Liu. Phase-selective gelators based on benzene 1,3,5-tricarboxamide for aromatic solvents recovery and dye removal, *Soft Mater.* **2021**, 19, 148.
- [97] A. Ghosh, P. Das, R. Kaushik, K. K. Damodaran, D. Amilan Jose. Anion responsive and morphology tunable tripodal gelators, *RSC Adv.* **2016**, 6, 83303.
- [98] S. M. C. Schoenmakers, B. W. L. van den Bersselaar, S. Dhiman, L. Su, A. R. A. Palmans. Facilitating functionalization of benzene-1,3,5-tricarboxamides by switching amide connectivity, *Org. Biomol. Chem.* **2021**, 19, 8281.

- [99] R. P. M. Lafleur, S. M. C. Schoenmakers, P. Madhikar, D. Bochicchio, B. Baumeier, A. R. A. Palmans, G. M. Pavan, E. W. Meijer. Insights into the Kinetics of Supramolecular Comonomer Incorporation in Water, *Macromolecules* **2019**, *52*, 3049.
- [100] X. Lou, S. M. C. Schoenmakers, J. L. J. van Dongen, M. Garcia-Iglesias, N. M. Casellas, M. Fernández-Castaño Romera, R. P. Sijbesma, E. W. Meijer, A. R. A. Palmans. Elucidating dynamic behavior of synthetic supramolecular polymers in water by hydrogen/deuterium exchange mass spectrometry, *J. Polym. Sci.* **2021**, *59*, 1151.
- [101] N. M. Matsumoto, R. P. M. Lafleur, X. Lou, K.-C. Shih, S. P. W. Wijnands, C. Guibert, J. W. A. M. van Rosendaal, I. K. Voets, A. R. A. Palmans, Y. Lin, E. W. Meijer. Polymorphism in Benzene-1,3,5-tricarboxamide Supramolecular Assemblies in Water: A Subtle Trade-off between Structure and Dynamics, *J. Am. Chem. Soc.* **2018**, *140*, 13308.
- [102] S. M. C. Schoenmakers, C. M. A. Leenders, R. P. M. Lafleur, X. Lou, E. W. Meijer, G. M. Pavan, A. R. A. Palmans. Impact of the water-compatible periphery on the dynamic and structural properties of benzene-1,3,5-tricarboxamide based amphiphiles, *Chem. Commun.* **2018**, *54*, 11128.
- [103] M. Lin, H. Liu, P. W. Miller, J. Zhang, C.-Y. Su. Surface modification of supramolecular nanotubes and selective guest capture, *New J. Chem.* **2014**, *38*, 3755.
- [104] A. D. Lynes, C. S. Hawes, E. N. Ward, B. Haffner, M. E. Möbius, K. Byrne, W. Schmitt, R. Pal, T. Gunnlaugsson. Benzene-1,3,5-tricarboxamide n-alkyl ester and carboxylic acid derivatives: tuneable structural, morphological and thermal properties, *CrystEngComm* **2017**, *19*, 1427.
- [105] H. Misslitz, K. Kreger, and H.-W. Schmidt. Supramolecular Nanofiber Webs in Nonwoven Scaffolds as Potential Filter Media, *Small* **2013**, *9*, 2053.
- [106] A. Iwan, H. Janeczka, B. Kaczmarczyk, J. Jurusik, Z. Mazurak, D. Sek, P. Rannou, J.-P. Bonnet, A. Pron. Supramolecular associations of poly(ketani)s with sulfonic acid derivatives of benzenetricarboxamide via Brønsted acid–base interactions: Preparation, spectroscopic, morphological and thermal investigations, *Synth. Met.* **2009**, *159*, 282.
- [107] N. Huang, J. Tao, S. Wei, W. Huang, and D. Wang. Positional Order in the Columnar Phase of Lyotropic Chromonic Liquid Crystals Mediated by Ionic Additives, *ACS Omega* **2020**, *5*, 9937.
- [108] W. Huang, S. Wei, D. Frenkel, N. Huang. The pathway and kinetics of hierarchical assembly of ionic oligomers into a lyotropic columnar phase, *Soft Matter* **2019**, *15*, 4460.
- [109] H. Qui, Z. M. Hundson, M. A. Winnik, I. Manners. Multidimensional hierarchical self-assembly of amphiphilic cylindrical block comicelles, *Science* **2015**, *347*, 1329.

- [110] J. Xu, H. Zheng, H. Liu, C. Zhou, Y. Zhao, Y. Li, Y. Li. Crystal Hierarchical Supramolecular Architectures from 1-D Precursor Single-Crystal Seeds, *J. Phys. Chem. C* **2010**, *114*, 2925.
- [111] Y.-J. Choi, D.-Y. Kim, M. Park, W.-J. Yoon, Y. Lee, J.-K. Hwang, Y.-W. Chiang, S.-W. Kuo, C.-H. Hsu, K.-U. Jeong. Self-Assembled Hierarchical Superstructures from the Benzene-1,3,5-Tricarboxamide Supramolecules for the Fabrication of Remote-Controllable Actuating and Rewritable Films, *ACS Appl. Mater. Interfaces* **2016**, *8*, 9490.
- [112] S.-C. Lin, R.-M. Ho, C.-Y. Chang, C.-S. Hsu. Hierarchical Superstructures with Control of Helicity from the Self-Assembly of Chiral Bent-Core Molecules, *Chem. Eur. J.* **2012**, *18*, 9091.
- [113] M. Burgard, D. Weiss, K. Kreger, H. Schmalz, S. Agarwal, H-W. Schmidt, A. Greiner. Mesostructured Nonwovens with Penguin Downy Feather-Like Morphology—Top-Down Combined with Bottom-Up, *Adv. Funct. Mater.* **2019**, *29*, 1903166.
- [114] A. Frank, C. Hils, M. Weber, K. Kreger, H. Schmalz, H.-W. Schmidt. Hierarchical Superstructures by Combining Crystallization-Driven and Molecular Self-Assembly, *Angew. Chem. Int. Ed.* **2021**, *60*, 21767.
- [115] F. A. Woodruff. Developments in Coating and Electrostatic Flocking, *J. Coat. Fabr.* **1993**, *22*, 290.
- [116] S. W. Bolgen. Flocking Technology, *J. Coat. Fabr.* **1991**, *21*, 123.
- [117] A. McCarthy, R. Shah, J. V. John, D. Brown, J. Xie. Understanding and utilizing textile-based electrostatic flocking for biomedical applications, *Appl. Phys. Rev.* **2021**, *8*, 41326.
- [118] Maag Flock GmbH, *How do I flock correctly?*, <https://maagflock.com/en/flock-school/wie-beflocke-ich-richtig/>, 04.11.2024, 19:38 Uhr.
- [119] A. Walther, A. Bernhardt, W. Pompe, M. Gelinsky, B. Mroziak, G. Hoffmann, C. Cherif, H. Bertram, W. Richter, G. Schmack. Development of Novel Scaffolds for Tissue Engineering by Flock Technology, *Text. Res. J.* **2007**, *77*, 892.
- [120] A. McCarthy, K. L. M. Avegnon, P. A. Holubeck, D. Brown, A. Karan, N. S. Sharma, J. V. John, S. Weihs, J. Ley, J. Xie. Electrostatic flocking of salt-treated microfibers and nanofiber yarns for regenerative engineering, *Mater. Today Bio* **2021**, *12*, 100166.
- [121] P. Balasubramanian, A. R. Boccaccini. Bilayered bioactive glass scaffolds incorporating fibrous morphology by flock technology, *Mater. Lett.* **2015**, *158*, 313.

- [122] R. H. Gong (Ed.), *Specialist yarn and fabric structures: Developments and applications*, Woodhead Publishing, Oxford, Cambridge, Philadelphia, New Delhi **2011**.
- [123] Z. Yu, S. Wei, J. Guo. Fabrication of aligned carbon-fiber/polymer TIMs using electrostatic flocking method, *J. Mater. Sci.: Mater. Electron.* **2019**, *30*, 10233.
- [124] A.-F. M. Seyam, Y. Cai, B. Wendisch, Y. K. Kim. Disc-shaped fibreweb formation with controlled fibre orientation using electrostatic forces: Theoretical analysis and experimental verification, *J. Text. Inst.* **2008**, *99*, 375.
- [125] X. Pan, Z. Huang, W. Jin, Y. Zhou, L. He. Calculation of Minimum Plate Distance in Electrostatic Flocking Process Based on Dynamics Research, *Fibers Polym.* **2024**, *25*, 383.
- [126] V. A. Semenov, S. P. Hersh, B. S. Gupta. Maximum Fiber-Packing Density in Electrostatic Flocking, *Text. Res. J.* **1981**, *51*, 768.
- [127] M. V. Vellayappan, S. K. Jaganathan, E. Supriyanto. Review: unraveling the less explored flocking technology for tissue engineering scaffold, *RSC Adv.* **2015**, *5*, 73225.
- [128] A. McCarthy, J. V. John, L. Saldana, H. Wang, M. Lagerstrom, S. Chen, Y. Su, M. Kuss, B. Duan, M. A. Carlson, J. Xie. Electrostatic Flocking of Insulative and Biodegradable Polymer Microfibers for Biomedical Applications, *Adv. Healthc. Mater.* **2021**, *10*, e2100766.
- [129] A. Probst, R. Facius, R. Wirth, C. Moissl-Eichinger. Validation of a nylon-flocked-swab protocol for efficient recovery of bacterial spores from smooth and rough surfaces, *Appl. Environ. Microbiol.* **2010**, *76*, 5148.
- [130] X. Chen, Y. Gu, J. Liang, M. Bai, S. Wang, M. Li, Z. Zhang. Enhanced microwave shielding effectiveness and suppressed reflection of chopped carbon fiber felt by electrostatic flocking of carbon fiber, *Compos. - A: Appl. Sci. Manuf.* **2020**, *139*, 106099.
- [131] K. Uetani, S. Ata, S. Tomonoh, T. Yamada, M. Yumura, K. Hata. Elastomeric thermal interface materials with high through-plane thermal conductivity from carbon fiber fillers vertically aligned by electrostatic flocking, *Adv. Mater.* **2014**, *26*, 5857.
- [132] J. Luo, N. Ji, W. Zhang, P. Ge, Y. Liu, J. Sun, J. Wang, Q. Zhuo, C. Qin, L. Dai. Ultrasensitive airflow sensor prepared by electrostatic flocking for sound recognition and motion monitoring, *Mater. Horiz.* **2022**, *9*, 1503.
- [133] X. Li, J. Wang, K. Wang, J. Yao, H. Bian, K. Song, S. Komarneni, Z. Cai. Three-dimensional stretchable fabric-based electrode for supercapacitors prepared by electrostatic flocking, *Chem. Eng. J.* **2020**, *390*, 124442.

- [134] M. Li, L. Qin, K. Ou, Z. Xiong, H. Zheng, Y. Sun. Electrostatic flocking MnO₂ nanofiber electrode for long cycling stability supercapacitors, *Int. J. Energy Re.* **2022**, *46*, 7946.
- [135] D. Weiss, D. Skrybeck, H. Misslitz, D. Nardini, A. Kern, K. Kreger and H-W. Schmidt. Tailoring Supramolecular Nanofibers for Air Filtration Applications, *ACS Appl. Mater. Interfaces* **2016**, *8*, 4885.
- [136] M. Weber, F. Bretschneider, Felix, K. Kreger, A. Greiner, H.-W. Schmidt. Mimicking Cacti Spines via Hierarchical Self-Assembly for Water Collection and Unidirectional Transport, *Adv. Mater. Inter.* **2024**.
- [137] U. Schlegel. The composite structure of cactus spines, *Bradleya* **2009**, *27*, 129.
- [138] J. Ju, H. Bai, Y. Zheng, T. Zhao, R. Fang, L. Jiang. A multi-structural and multi-functional integrated fog collection system in cactus, *Nat. Commun.* **2012**, *3*, 1247.
- [139] D. Gurera, B. Bhushan. Passive water harvesting by desert plants and animals: lessons from nature, *Phil. Trans. R. Soc. A* **2020**, *378*, 20190444.
- [140] F. T. Malik, R. M. Clement, D. T. Gethin, M. Kiernan, T. Goral, P. Griffiths, D. Beynon, A. R. Parker. Hierarchical structures of cactus spines that aid in the directional movement of dew droplets, *Philos. Trans. Royal Soc. A* **2016**, *374*.
- [141] F. T. Malik, R. M. Clement, D. T. Gethin, D. Beysens, R. E. Cohen, W. Krawszik, A. R. Parker. Dew harvesting efficiency of four species of cacti, *Bioinspir. Biomim.* **2015**, *10*, 36005.
- [142] J. Wang, S. Yi, Z. Yang, Y. Chen, L. Jiang, C.-P. Wong. Laser Direct Structuring of Bioinspired Spine with Backward Microbarbs and Hierarchical Microchannels for Ultrafast Water Transport and Efficient Fog Harvesting, *ACS Appl. Mater. Interfaces* **2020**, *12*, 21080.
- [143] H. Chen, T. Ran, Y. Gan, J. Zhou, Y. Zhang, L. Zhang, D. Zhang, L. Jiang. Ultrafast water harvesting and transport in hierarchical microchannels, *Nat. Mater.* **2018**, *17*, 935.
- [144] M. K. Chaudhury, G. M. Whitesides. How to Make Water Run Uphill, *Science* **1992**, *256*, 1539.
- [145] S. Mettu, M. K. Chaudhury. Motion of drops on a surface induced by thermal gradient and vibration, *Langmuir* **2008**, *24*, 10833.
- [146] J. Zhang, Y. Han. Shape-gradient composite surfaces: water droplets move uphill, *Langmuir* **2007**, *23*, 6136.

- [147] H. Chen, P. Zhang, L. Zhang, H. Liu, Y. Jiang, D. Zhang, Z. Han, L. Jiang. Continuous directional water transport on the peristome surface of *Nepenthes alata*, *Nature* **2016**, 532, 85.
- [148] Y. Zheng, H. Bai, Z. Huang, X. Tian, F-Q. Nie, Y. Zhao, J. Zhai, L. Jiang. Directional water collection on wetted spider silk, *Nature* **2010**, 463, 640.
- [149] É. Lorenceau, D. Quéré. Drops on a conical wire, *J. Fluid Mech.* **2004**, 510, 29.
- [150] D. Gurera, B. Bhushan. Designing bioinspired surfaces for water collection from fog, *Philos. Trans. Royal Soc. A* **2019**, 377, 20180269.
- [151] H. Lu, W. Shi, Y. Guo, W. Guan, C. Lei, G. Yu. Materials Engineering for Atmospheric Water Harvesting: Progress and Perspectives, *Adv. Mater.* **2022**, 34, e2110079.
- [152] D. Nioras, K. Ellinas, V. Constantoudis, E. Gogolides. How Different Are Fog Collection and Dew Water Harvesting on Surfaces with Different Wetting Behaviors?, *ACS Appl. Mater. Interfaces.* **2021**, 13, 48322.
- [153] Y. Si and Z. Dong. Bioinspired Smart Liquid Directional Transport Control, *Langmuir* **2020**, 36, 667.
- [154] T. Young. III. An essay on the cohesion of fluids, *Phil. Trans. R. Soc.* **1804**, 95, 65.
- [155] M. Liu, S. Wang, L. Jiang. Nature-inspired superwettability systems, *Nat. Rev. Mater.* **2017**, 2, 17036.
- [156] R. N. Wenzel. Resistance of Solid Surfaces to Wetting by Water, *Ind. Eng. Chem.* **1936**, 28, 988.
- [157] A. B. D. Cassie and S. Baxter. Wettability of porous surfaces, *Trans. Faraday Soc.* **1944**, 40, 546.
- [158] United Nations World Water Assessment Programme (WWAP), *The United Nations World Water Development Report 2015: Water for a sustainable World*, UNESCO, Paris **2015**.
- [159] B. Bhushan. Design of water harvesting towers and projections for water collection from fog and condensation, *Phil. Trans. R. Soc. A* **2020**, 378, 20190440.
- [160] B. Bhushan. Bioinspired water collection methods to supplement water supply, *Phil. Trans. R. Soc. A* **2019**, 377, 20190119.
- [161] O. Klemm, R. S. Schemenauer, A. Lummerich, P. Cereceda, V. Marzol, D. Corell, J. van Heerden, D. Reinhard, T. Gherezghiher, J. Olivier, P. Osses, J. Sarsour, E. Frost, M. J. Estrela, J. A. Valiente, G. Mussie Fessehaye. Fog as a fresh-water resource: overview and perspectives, *Ambio* **2012**, 41, 221.

- [162] C. Hiatt, D. Fernandez, C. Potter. Measurements of Fog Water Deposition on the California Central Coast, *ACS* **2012**, *02*, 525.
- [163] K. Stephan, *Heat transfer in condensation and boiling*, Springer, New York **1992**.
- [164] F. Bai, J. Wu G: Gong, L. Guo. Biomimetic “Cactus Spine” with Hierarchical Groove Structure for Efficient Fog Collection, *Adv. Sci.* **2015**, *2*, 1500047.
- [165] J. Ju, K. Xiao, X. Yao, H. Bai, L. Jiang. Bioinspired conical copper wire with gradient wettability for continuous and efficient fog collection, *Adv. Mater.* **2013**, *25*, 5937.
- [166] Y. Liu, J. Liu, C. Chen. Preparation of a Bioinspired Conical Needle for Rapid Directional Water Transport and Efficient Fog Harvesting, *Ind. Eng. Chem. Res.* **2023**, *62*, 10668.
- [167] X. Heng, M. Xiang, Z. Lu, C. Luo. Branched ZnO wire structures for water collection inspired by cacti, *ACS Appl. Mater. Interfaces* **2014**, *6*, 8032.
- [168] M. Cao, J. Ju, K. Li, S. Dou, K. Liu, L. Jiang. Facile and Large-Scale Fabrication of a Cactus-Inspired Continuous Fog Collector, *Adv. Funct. Mater.* **2014**, *24*, 3235.
- [169] S. Yi, J. Wang, Z. Chen, B. Liu, L. Ren, L. Liang, L. Jiang. Cactus-Inspired Conical Spines with Oriented Microbarbs for Efficient Fog Harvesting, *Adv. Mater. Technol.* **2019**, *4*, 1900727.
- [170] H. Zhou, M. Zhang, C. Li, C. Gao, Y. Zheng. Excellent Fog-Droplets Collector via Integrative Janus Membrane and Conical Spine with Micro/Nanostructures, *Small* **2018**, *14*, 1801335.
- [171] Y. Choi, K. Baek, H. So. 3D-printing-assisted fabrication of hierarchically structured biomimetic surfaces with dual-wettability for water harvesting, *Sci. Rep.* **2023**, *13*, 10691.
- [172] Y. Guo, Y.-Q. Luo, L. Liu, C. Ma, C. Liu, J. Wang, X. Gao, X. Yao, J. Ju. Bioinspired cone structures with helical micro-grooves for fast liquid transport and efficient fog collection, *J. Mater. Chem. A* **2023**, *11*, 12080.
- [173] X. Li, Y. Yang, L. Liu, Luyang, Yi. Chen, M. Chu, H. Sun, W. Shan, Y. Chen. 3D-Printed Cactus-Inspired Spine Structures for Highly Efficient Water Collection, *Adv. Mater. Interfaces* **2020**, *7*, 1901752.
- [174] D. Chen, J. Li, J. Zhao, J. Guo, S. Zhang, T. A. Sherazi, Ambreen, S. Li. Bioinspired superhydrophilic-hydrophobic integrated surface with conical pattern-shape for self-driven fog collection, *J. Colloid Interface Sci.* **2018**, *530*, 274.
- [175] C. Luo. Theoretical Exploration of Barrel-Shaped Drops on Cactus Spines, *Langmuir* **2015**, *31*, 11809.

- [176] B. Thiel, *Variable Pressure Scanning Electron Microscopy: in: Hawkes, P.W., Spence, J.C.H. (eds), Springer Handbook of Microscopy*, Springer, Cham, **2019**.
- [177] M. Brugnara. Using the ESEM for the Measurement of Contact Angles on Flat Samples, *Microsc. Anal.* **2007**, *21*, 17.
- [178] R. L. Hoffman. A study of the advancing interface, *J. Colloid Interface Sci.* **1983**, *94*, 470.
- [179] O. Breitenstein, W. Warta, M. C. Schubert, *Lock-in Thermography*, Springer, Cham **2018**.
- [180] A. Salazar. On thermal diffusivity, *Eur. J. Phys.* **2003**, *24*, 351.
- [181] S. Winograd. On Computing the Discrete Fourier Transform, *Math. Comput.* **1978**, *32*, 175.
- [182] T. Tran, C. Kodisch, M. Schöttle, N. W. Pech-May, M. Retsch. Characterizing the Thermal Diffusivity of Single, Micrometer-Sized Fibers via High-Resolution Lock-In Thermography, *J. Phys. Chem. C* **2022**, *126*, 14003.
- [183] C. Pradere J. M. Goyheneche J. C. Batsale S. Dilhaire R. Pailler. Thermal diffusivity measurements on a single fiber with microscale diameter at very high temperature, *Int. J. Therm. Sci.* **2006**, *45*, 443.
- [184] A. Mendioroz, R. Fuente-Dacal, E. Apiñaniz, A. Salazar. Thermal diffusivity measurements of thin plates and filaments using lock-in thermography, *Rev. Sci. Instrum.* **2009**, *80*, 74904.
- [185] J. F. Bisson, D. Fournier. Influence of diffraction on low thermal diffusivity measurements with infrared photothermal microscopy, *J. Appl. Phys* **1998**, *83*, 1036.
- [186] J. A. Cape, G. W. Lehman. Temperature and Finite Pulse-Time Effects in the Flash Method for Measuring Thermal Diffusivity, *J. Appl. Phys* **1963**, *34*, 1909.
- [187] R. Fuente, A. Mendioroz, A. Salazar. Revising the exceptionally high thermal diffusivity of spider silk, *Mater. Lett.* **2014**, *114*, 1.
- [188] G. L. Vignoles, G. Bresson, C. Lorrette, A. Ahmadi-Sénichault. Measurement of the thermal diffusivity of a silica fiber bundle using a laser and an IR camera, *J. Phys.: Conf. Ser.* (**2012**, *395*, 12079.
- [189] S. W. Kieffer, I. C. Getting, G. C. Kennedy. Experimental determination of the pressure dependence of the thermal diffusivity of teflon, sodium chloride, quartz, and silica, *J. Geophys. Res.* **1976**, *81*, 3018.
- [190] T. Katsura. Thermal diffusivity of silica glass at pressures up to 9 GPa, *Phys. Chem. Minerals* **1993**, *20*, 201.

References

- [191] H. Günzler, H. Böck, *IR-Spektroskopie*, Verlag Chemie, Weinheim **1983**.
- [192] H. Volkmann, *Handbuch der Infrarot-Spektroskopie*, Verlag Chemie, Weinheim **1972**.
- [193] J. F. Bisson, D. Fournier. The coupled influence of sample heating and diffraction in thermal diffusivity estimate with infrared photothermal microscopy., *J. Appl. Phys.* **1998**, *84*, 38.
- [194] C. L. Choy, K. W. Kwok, W. P. Leung, F. P. Lau. Thermal- Conductivity of Poly(Ether Ether Ketone) and Its Short-Fiber Composites, *J. Polym. Sci., Polym. Phys.* **1994**, *32*, 1389.
- [195] A. Salazar, A. Mendioroz, R. Fuente, R. Celorrio. Accurate measurements of the thermal diffusivity of thin filaments by lock-in thermography, *J. Appl. Phys.* **2010**, *107*.

Danksagung

Zu Beginn möchte ich mich herzlichst bei Herrn Prof. Dr. Hans-Werner Schmidt für die Möglichkeit meine Dissertation am Lehrstuhl MCI zu verfassen, bedanken. Besonderer Dank gilt den motivierenden und zielführenden Diskussionen nach jeder Vorstellung meiner Forschungsergebnisse und der daraus resultierenden Wertschätzung. Ich möchte mich zusätzlich für die gewährte Freiheit bedanken, meine Themen der Dissertation mitzugestalten und ihr Vertrauen hinsichtlich meiner Arbeiten. Danke für Ihren Zuspruch und Ihre Unterstützung über den gesamten Zeitraum meiner Promotion.

Ein großes Dankeschön geht an dich Dr. Klaus Kreger. Danke für deine Zeit, deinen Input, deinen Erfahrungsschatz und deine konstruktive Kritik für jegliche meiner Anliegen in den letzten drei Jahren. Es war mir eine Freude so viel von dir Lernen zu können.

Einen großen Dank spreche ich allen Mitarbeiter/-innen der Makromolekularen Chemie I aus. Ihr habt es mir leicht gemacht, sich bei euch wohl zu fühlen. Danke an alle Kollegen und Kolleginnen am Lehrstuhl, die meine Zeit in der MCI bereichert haben und die ich in guter Erinnerung halten werde. Vielen Dank geht hier besonders an Petra Weiss, für deine tolle Unterstützung bei allen administrativen und organisatorischen Fragen. Mit deiner herzlichen Art hast du dafür gesorgt, dass ich mich jeden Tag am Lehrstuhl willkommen gefühlt habe. Danke an Alex Kern, für all deine Hilfestellungen bei technischen Problemen. Ein großes Danke auch an Sandra Opel und Jutta Failner für eure wertvollen Ratschläge in jeglicher Hinsicht und die synthetischen Hilfestellungen und die gemeinsamen Mittagspausen. Ein großes Danke auch an dich Dennis, als letzte Doktoranden und dem immer leerer werdenden Lehrstuhl, haben wir gemeinsam die Stellung gehalten. Ohne dich wäre die Zeit in Bayreuth nicht annähernd so schön gewesen! Du bist eine Bereicherung für jede Gruppe und du warst es auch besonders für unserem Lehrstuhl.

Ein weiteres Dankeschön möchte ich Dr. Ulrich Mansfeld und Martina Heider für die Hilfestellungen am Rasterelektronenmikroskop aussprechen.

Bedanken möchte ich mich auch bei Nadine Raßmann für die Kooperation und das erfolgreiche Verfassen einer gemeinsamen Publikation.

Danksagung

Ebenfalls möchte ich mich bei Ina Klein bedanken. Unsere Kooperation im letzten Jahr hat mir sehr viel Spaß bereitet und es war stets eine Freude mit dir zu diskutieren und Ideen umzusetzen. Vielen Dank für all deine Mühen und Zeit, die du in das Projekt investiert hast.

Ein besonderer Dank geht an Felix Bretschneider. Aus einer spontanen Idee, unsere Systeme zu kombinieren, ist ein großartiges Projekt entstanden. Deine Kreativität, dein Wissensreichtum und deine Ruhe in jeglicher Situation haben das Arbeiten mit dir in der Kollaboration über die ganze Promotionszeit hinaus bereichert. Es hat mir unfassbar viel Spaß gemacht mit dir zusammen zu arbeiten, zu diskutieren, Problemstellungen zu lösen und uns gemeinsam zu unterstützen und an gleichen Zielen zu arbeiten. Ich freue mich, dass all unsere Mühen in einer gemeinsamen Publikation resultierten.

Ein weiteres großes Danke geht an Christina und Andi, ihr habt mich von Anfang an mit offenen Armen am Lehrstuhl empfangen. Über die vielen gemeinsamen Stunden am Lehrstuhl hinaus hat sich eine tolle Freundschaft entwickelt. Dankeschön für eure Unterstützung über all die Jahre. Durch deinen Sonnenschein Christina hast du den Lehrstuhl und meine Zeit vor Ort sehr bereichert. Danke dir Andi für alles was ich von dir in meiner Masterarbeit lernen durfte und erfolgreich in der Promotion anwenden konnte.

Vielen Dank an dieser Stelle an alle, die mein Leben außerhalb der Universität bereichert haben. Ich bedanke mich bei meiner Familie für all die Unterstützung über die gesamten Jahre des Studiums und der Promotion. Danke an Luisa und Bibi, auf die ich mich trotz der Distanz seit über einem Jahrzehnt verlassen kann. Danke dir Jenny, für all die gemeinsamen Trainingsstunden und die daraus entwickelte Freundschaft. Danke für deinen unermüdlichen Support und dein offenes Ohr über die letzten Jahre.

Zu guter Letzt danke ich dir Romano, für deine Unterstützung all die Jahre trotz der Distanz. Dein Zuspruch und Glauben an mich ist unermüdlich und war mir die größte Stütze in der ganzen Zeit. Deine Art und unsere gemeinsame Zeit haben mich jeden Stress vergessen lassen und einen großen Teil dazu beigetragen, dass ich die Dissertation mit so viel Elan und Freude abzuschließen konnte. Ich freue mich nun auf unseren gemeinsamen Weg.

(Eidesstattliche) Versicherungen und Erklärungen

(§ 9 Satz 2 Nr. 3 PromO BayNAT)

Hiermit versichere ich eidesstattlich, dass ich die Arbeit selbstständig verfasst und keine anderen als die von mir angegebenen Quellen und Hilfsmittel benutzt habe (vgl. Art. 97 Abs. 1 Satz 8 BayHIG).

(§ 9 Satz 2 Nr. 3 PromO BayNAT)

Hiermit erkläre ich, dass ich die Dissertation nicht bereits zur Erlangung eines akademischen Grades eingereicht habe und dass ich nicht bereits diese oder eine gleichartige Doktorprüfung endgültig nicht bestanden habe.

(§ 9 Satz 2 Nr. 4 PromO BayNAT)

Hiermit erkläre ich, dass ich Hilfe von gewerblichen Promotionsberatern bzw. -vermittlern oder ähnlichen Dienstleistern weder bisher in Anspruch genommen habe noch künftig in Anspruch nehmen werde.

(§ 9 Satz 2 Nr. 7 PromO BayNAT)

Hiermit erkläre ich mein Einverständnis, dass die elektronische Fassung meiner Dissertation unter Wahrung meiner Urheberrechte und des Datenschutzes einer gesonderten Überprüfung unterzogen werden kann.

(§ 9 Satz 2 Nr. 8 PromO BayNAT)

Hiermit erkläre ich mein Einverständnis, dass bei Verdacht wissenschaftlichen Fehlverhaltens Ermittlungen durch universitätsinterne Organe der wissenschaftlichen Selbstkontrolle stattfinden können.

Ort, Datum

Unterschrift